Prifysgol Abertawe
Swansea University

Investigating the potential for detecting Oak Decline
using Unmanned Aerial Vehicle (UAV) Remote Sensing

Jakob Iglhaut

Submitted to Swansea University in fulfilment of the requirements
for the degree of Doctor of Philosophy (PhD)

Department of Geography, College of Science, Swansea University

March 2023

PhD Supervisors

Jacqueline Rosette
Department of Geography
College of Science
Swansea University
Singleton Park, SA2 8PP, Swansea, UK

Peter North
Department of Geography
College of Science
Swansea University
Singleton Park, SA2 8PP, Swansea, UK

Juan Suárez
Forest Research
Northern Research Station
EH25 9SY, Roslin, UK

Abstract

This PhD project develops methods for the assessment of forest condition utilising modern remote sensing technologies, in particular optical imagery from unmanned aerial systems and with Structure from Motion photogrammetry. The research focuses on health threats to the UK's native oak trees, specifically, Chronic Oak Decline (COD) and Acute Oak Decline (AOD).

The data requirements and methods to identify these complex diseases are investigated using RGB and multispectral imagery with very high spatial resolution, as well as crown textural information. These image data are produced photogrammetrically from multitemporal unmanned aerial vehicle (UAV) flights, collected during different seasons to assess the influence of phenology on the ability to detect oak decline. Particular attention is given to the identification of declined oak health within the context of semi-natural forests and heterogenous stands. Semi-natural forest environments pose challenges regarding naturally occurring variability. The studies investigate the potential and practical implications of UAV remote sensing approaches for detection of oak decline under these conditions.

COD is studied at Speculation Cannop, a section in the Forest of Dean, dominated by 200-year-old oaks, where decline symptoms have been present for the last decade. Monks Wood, a semi-natural woodland in Cambridgeshire, is the study site for AOD, where trees exhibit active decline symptoms. Field surveys at these sites are designed and carried out to produce highly-accurate differential GNSS positional information of symptomatic and control oak trees. This allows the UAV data to be related to COD or AOD symptoms and the validation of model predictions.

Random Forest modelling is used to determine the explanatory value of remote sensing-derived metrics to distinguish trees affected by COD or AOD from control trees. Spectral and textural variables are extracted from the remote sensing data using an object-based approach, adopting circular plots around crown centres at individual tree level.

Furthermore, acquired UAV imagery is applied to generate a species distribution map, improving on the number of detectable species and spatial resolution from a previous classification using multispectral data from a piloted aircraft. In the production of the map, parameters relevant for classification accuracy, and identification of oak in particular, are assessed. The effect of plot size, sample size and data combinations are studied. With optimised parameters for species classification, the updated species map is subsequently employed to perform a wall-to-wall prediction of individual oak tree condition, evaluating the potential of a full inventory detection of declined health.

UAV-acquired data showed potential for discrimination of control trees and declined trees, in the case of COD and AOD. The greatest potential for detecting declined oak condition was demonstrated with narrowband multispectral imagery. Broadband RGB imagery was determined to be unsuitable for a robust distinction between declined and control trees. The greatest explanatory power was found in remotely-sensed spectra related to photosynthetic activity, indicated by the high feature importance of near-infrared spectra and the vegetation indices NDRE and NDVI. High feature importance was also produced by texture metrics, that describe structural variations within the crown. The findings indicate that the remotely sensed explanatory variables hold

significant information regarding changes in leaf chemistry and crown morphology that relate to chlorosis, defoliation and dieback occurring in the course of the decline. In the case of COD, a distinction of symptomatic from control trees was achieved with 75 % accuracy. Models developed for AOD detection yielded AUC scores up to 0.98, when validated on independent sample data. Classification of oak presence was achieved with a User's accuracy of 97 % and the produced species map generated 95 % overall accuracy across the eight species within the study area in the north-east of Monks Wood.

Despite these encouraging results, it was shown that the generalisation of models is unfeasible at this stage and many challenges remain. A wall-to-wall prediction of decline status confirmed the inability to generalise, yielding unrealistic results, with a high number of declined trees predicted. Identified weaknesses of the developed models indicate complexity related to the natural variability of heterogenous forests combined with the diverse symptoms of oak decline. Specific to the presented studies, additional limitations were attributed to limited ground truth, consequent overfitting, the binary classification of oak health status and uncertainty in UAV-acquired reflectance values.

Suggestions for future work are given and involve the extension of field sampling with a non-binary dependent variable to reflect the severity of oak decline induced stress. Further technical research on the quality and reliability of UAV remote sensing data is also required.

Declarations and Statements

Declaration

This work has not previously been accepted in substance for any degree and is not being concurrently submitted in candidature for any degree.
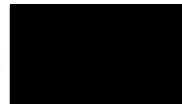
Signed ███████████ .... Date 09/05/2023 ....

Statement 1

This work is the result of my own independent study/investigation, except where otherwise stated. Other sources are acknowledged by footnotes giving explicit references. A bibliography is appended.
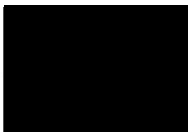
Signed ███████ .... Date 09/05/2023 ....

Statement 2

I hereby give my consent for my work, if relevant and accepted, to be available for photocopying and for inter-library loan, and for the title and summary to be made available to outside organisations.

Signed ███████ .... Date 09/05/2023 ....

Statement 3

The University's ethical procedures have been followed and, where appropriate, that ethical approval has been granted.

Signed ███████ .... Date 09/05/2023 ....

Authorship statement

The following people and institutions contributed to the publication of work undertaken as part of this thesis:

Author 1	Jakob Iglhaut	Department of Geography, Swansea University, Singleton Park, SA2 8PP, Swansea, UK
Author 2	Carlos Cabo	Department of Mining Exploitation and Prospecting, Polytechnic School of Mieres, University of Oviedo
Author 3	Stefano Puliti	Division of Forestry and Forest Resources, Norwegian Institute of Bioeconomy Research (NIBIO), P.O. Box 115, 1431, Ås, Norway
Author 4	Livia Piermattei	Department of Geosciences, University of Oslo, Sem Sælands vei 1, Geologibygningen, 0371, Oslo
Author 5	James O'Connor	Department of Natural and Built Environment, Kingston University, Penrhyn Road, Kingston upon Thames, KT2 1EE, Surrey, UK
Author 6	Jacqueline Rosette	Department of Geography, Swansea University, Singleton Park, SA2 8PP, Swansea, UK

Paper: Structure from Motion photogrammetry in forestry: a review
Located in Chapter 1: Introduction

Author 1 (candidate) was invited to contribute to the Current Forest Reports journal. The above publication was led by the candidate. The candidate invited co-authors based on their expertise and coordinated the collaboration. Revisions of co-author contributions were undertaken by the candidate to form a cohesive paper.

Author 2 contributed to the Theoretical Principles section, the creation of figures and contributed to revising the manuscript.

Author 3 contributed to the Aerial Inventory section and contributed to revising the manuscript.

Author 4 contributed to the Terrestrial Inventory section, the creation of figures and contributed to revising the manuscript.

Author 5 contributed to the SfM in Practise section, the creation of figures and contributed to revising the manuscript.

Author 6 contributed substantially to the revision of the manuscript.

All authors approved the final manuscript before publication.

We the undersigned agree with the above stated "proportion of work undertaken" for each of the above published peer-reviewed manuscripts contributing to this thesis:

Signed

Author 1 ████████████████████ _____

Author 2 ████████████████████ _____

Author 3 ████████████████████ _____

Author 4 ████████████████████ _____

Author 5 ████████████████████ _____

Author 6 ████████████████████ _____

Contents

X

Acknowledgements

There are many people whom I'd like to thank for their contributions to this dissertation, both directly and indirectly. First and foremost, I'd like to thank my supervisors, without whom I would not have been able to complete this research. Thank you to Dr Jacqueline Rosette, who supported me with all possible intellectual and financial services resources. I also thank Dr Juan Suárez and Prof Peter North for provided academic opportunities, their insight and feedback. 23/03/2023

My appreciation goes out to the PuRpOsE project members: Dr France Gerard, Mr Charles George, Dr Cecilia Chavana-Bryant, Dr Kevin White, Dr Karsten Schonrogge and Mr Duncan Ray. Much of the interest in investigating oak decline is owing to their impulse. Their support during field surveys has made a great contribution towards my research at Monks Wood.

I thank my co-authors of the Structure from Motion photogrammetry in forestry review paper that is featured in the introduction of this dissertation: Dr Carlos Cabo, Dr Livia Piermattei, Dr Stefano Puliti and Dr James O'Connor. Thank you for sharing the passion for SfM photogrammetry, the fruitful discussions and your contributions to the paper. I could not have done this without you.

I'd like to thank my parents for their endless support during 10 years of studies. Elke, Barny, I am forever grateful for your patience and understanding. A special thanks to my sisters, who were there for me during the highs and lows of the past years. Thank you, Lotte, for your generally great energy and expressing confidence in my abilities. Thank you, Clara, for your statistical expertise and helping me re-gain momentum in writing this thesis. I thank my wife Katrin for always believing in me. The great adventures we have had over the past years were the best compensation for the tedious writing task I could have asked for. Finally, I would like to thank Ronja, my daughter, for motivating me to complete this dissertation.

List of Tables

XIII

XVI

Abbreviations

AGL   Above Ground Level
ALS   Airborne Laser Scanning
AOD   Acute Oak Decline
ARI   Anthocyanin Reflectance Index
AUC   Area Under the Curve
CCCI   Canopy Chlorophyll Content Index
CHM   Canopy Height Model
CI   Coloration Index
COD   Chronic Oak Decline
CORS   Continuously Operating Reference Station
CSF   Cloth Simulation Filter
CV   Cross Validation
CVI   Chlorophyll Vegetation Index
DAI   Decline Acuteness Index
DLS   Downwelling Light Sensor
DSM   Digital Surface Model
DTM   Digital Terrain Model
FN   False Negative
FP   False Positive
GCP   Ground Control Point
GIS   Geographic Information System
GLI   Green Leaf Index
GNSS   Global Navigation Satellite System
GPS   Global Positioning System
GSD   Ground Sample Distance
HFOV   Horizontal Field of View
IMU   Inertia Measurement Unit
ITC   Individual Tree Crown
MVS   Multi View Stereo
NDRE   Normalized Difference Red Edge Index
NDVI   Normalized Difference Vegetation Index
NGRDI   Normalized Green Red Difference Index
NIR   Near Infrared
OBIA   Object Based Image Analysis
OCA   Overall Classification Accuracy
OS   Ordnance Survey
PDI   Phenotypic Decline Index
PPK   Post Processing Kinematic
RANSAC   Random Sample Consensus
RE   Red Edge
RF   Random Forest
RMSE   Root Mean Square Error

ROC	Receiver Operator Characteristic
RS	Remote Sensing
SD	Standard Deviation
SfM	Structure from Motion
SIFT	Scale Invariant Feature Transform
SNR	Signal to Noise Ratio
SURF	Speeded Up Robust Features
TGI	Triangular Greenness Index
TN	True Negative
TP	True Positive
UAS	Unmanned Aerial System
UAV	Unmanned Aerial Vehicle
VARI	Visible Atmospheric Resistant Index

CHAPTER 1:

INTRODUCTION

1.1 Forests in a changing climate

Forest ecosystems around the world are expected to experience increased stress due to changing climatic conditions (Shukla *et al.*, 2019). Tree mortality caused by extreme weather conditions, such as wind damage or forest fires can be identified and quantified with relatively high confidence, due to the sudden and dramatic forest loss.

However, increased vulnerability to forest insects and pathogens, given predisposing abiotic factors leads to more subtle changes and long-term growth reduction. In addition, as the climate changes, new pests and diseases may invade, placing native ecosystems under increased pressure. Such protracted damage is difficult to detect and measure given the spatiotemporal heterogeneity and complexity of associated stress effects. These impacts are not necessarily lethal but may drive the loss of ecosystem function, biodiversity and ultimately limit the natural ability of forests to act as carbon sinks. As humans, however we rely directly on functioning forests to supply materials, food and energy. Additionally, intact forests indirectly provide essential ecosystem services for regulating climate and water budgets, preventing soil erosion, enhancing soil fertility and supporting biodiversity as well as offering an important source of recreation and associated health and well-being benefits.

In the future, extreme weather events are predicted to increase, both in frequency and severity under our changing climate, in turn causing increased forest disturbance and vulnerability from pests and diseases (Anderegg *et al.*, 2015). Our increasing recognition of the importance of functioning forests for a healthy planet, signifies the necessity to detect and monitor declining forest health.

1.2 Monitoring of forest condition

Monitoring forest condition provides vital information to improve research knowledge on cause-and-effect relationships about forest decline. A good

understanding of these interactions is crucial to determine thresholds beyond which gradual deterioration may transition into rapid decline, ultimately leading to forest loss. Ideally, these evaluations are performed at a range of spatial scales, from individual tree level to stand level and even on a global level. Observations over large temporal scales and at adequate intervals help to identify resistance as well as resilience of forests across all spatial scales (Gauthier *et al.*, 2015).

Monitoring forest health enables comprehension of the general trajectory of forests, given the intensification of stresses on these ecosystems. It is only by quantifying forest condition that the complex implications of their decline and loss can be assessed. Planning and managing mitigation measures, such as efforts to contain pathogens, are only possible given the availability of forest health data. Therefore, monitoring forest condition enables informed management decisions on counteracting and compensating forest loss. Information on forest health facilitates policy development, adherence to international reporting obligations and silvicultural planning.

1.3 The current state of forests in the UK

13 % of Great Britain's land area is covered with forest, totalling 3.2 million hectares (Forest Research - Forestry Statistics 2020). Approximately half of Britain's woodland area (51%) consists of conifers, however their distribution between the individual nations is uneven; the proportion of coniferous cover ranges from 74 % in Scotland to 26 % in England. Principal coniferous species are Sitka spruce (*Picea sitchensis*), comprising 51 % of UK conifer area, Scots pine (*Pinus sylvestris*) 17 %, and Larches (*Larix spp.*) 10 %. Less dominant species are Lodgepole pine (*Pinus contorta*), Norway spruce (*Picea abies*), Douglas fir (*Pseudotsuga menziesii*) and Corsican pine (*Pinus nigra*).

The UK's most common deciduous species by area are birch (*Betula spp.*) comprising 18 %, oak (*Quercus spp.*) 16 % and European ash (*Fraxinus excelsior*) 12 %. Other widespread broadleaf species are sycamore (*Acer pseudoplatanus*), hazel (*Corylus spp.*), hawthorn (*Crataegus spp.*), willow (*Salix spp.*), alder (*Alnus spp.*) and sweet chestnut (*Castanea spp.*). While in Scotland birch dominates, occupying 43 % of the total broadleaf area, in the southern countries oak is the dominant broadleaf tree, accounting for 19 % of deciduous forest area of England and Wales.

Currently, government agency Forest Research identifies 25 diseases and 23 insects as threats to UK trees species (Forest Research, 2020). In additional to these biotic stressors, climate change and linked environmental impacts like drought are recognised as hazards to British forests (Collier and Thomas, 2016).

Some examples of diseases with detrimental impacts on forests in the UK have received widespread attention due to their socioeconomic impacts. The severity and rapidity of progression of these diseases has led to attention beyond the scientific community (Woodward and Boa, 2013; BBC News, 2018). One such example is, *Phytophtora ramorum,* an algae-like organism which has been causing severe damage to forests across the country (Sketchley, 2019). The disease can infect conifer and broadleaf species. In the UK however, the Ramorum disease has had the greatest impact on Japanese larch (*Larix kaempferi*) plantations. Infected larch stands and susceptible hosts are required to be felled, as mandated by Statutory Plant Health Notices (SPHNs). Felling and disposal of infected timber have caused enormous economic losses to forest owners.

A further ravaging disease is caused by the fungus *Hymenoscyphus fraxineus* and has affected ash populations across Europe. The disease, known commonly as ash dieback is often called "Chalara" from the asexual phase of the fungus's life cycle, *Chalara fraxinea*. First discovered in the UK in 2012, ash dieback has now spread across the country and is not containable, resulting in widespread felling due to safety concerns. Similar to the rest of Europe, the disease is expected to kill the majority of ash trees, causing significant financial damage to forest owners and posing a serious threat to biodiversity.

A tree whose health has recently come to public and scientific attention is the native British oak. Oak is affected by complex syndromes, caused by a multitude of factors, which together present a serious threat to the species in the UK. These decline diseases, can lead to rapid deterioration of tree condition and mortality. The decline of this iconic tree species, the classification of oak and the detection of oak condition are the focus of the research within this thesis. The importance of oak and the challenges they face are represented in the following subsections.

1.4 The relevance of oak to the UK

Oak is a tree of tremendous importance in Britain. Interwoven with the UK's history oaks present great cultural, societal and economic value to this day. The deeply rooted connection to the tree species is evidenced by the third most common pub name in the UK: "Royal Oak" (Pubs Galore - Most Common Names of Open Pubs, 2019), named after a legendary tree in the Battle of Worcester.

In Britain, oak timber has been, and still is, an important resource for construction due its high wood density, offering great load capacity yet providing flexibility. A famous example of oak wood used in construction is the roof of St Paul's Cathedral, re-built after the Great Fire of London in 1666 and still existing today. In the 1600s oak was also in high demand for building ships. The demand was so high in fact, that some forests were greatly thinned of this high quality wood, prompting Queen Elizabeth I to order replanting of oak, with some trees from this period currently still standing (Melby, 2008; Hight *et al.*, 2019).

Oaks are also well represented in British culture and literature. The Major Oak, a tree in Sherwood Forest, Nottinghamshire, England, is said to have served Robin Hood and his Merry Men as their hideout and still stands today, at nearly 1000 years old. Another iconic tree in English Folklore is a particular oak that is supposedly haunted by Herne the Hunter, also mentioned in William Shakespeare's 1597 play *The Merry Wives of Windsor*. Shakespeare himself reportedly used ink made from "oak apples" - the galls formed on oak leaves caused by grub wasps (Edmondson, 2015).

Oaks support vast biodiversity. In fact, oaks sustain more species of wildlife than any other native tree in the UK. A recent study (Mitchell *et al.*, 2019a) has found that mature oaks are is associated with a total of up to 2300 species: 38 bird species, 229 bryophytes, 108 fungi, 1178 invertebrates, 716 lichens and 31 mammals. As an important habitat, oaks hold a crucial ecosystem function for British landscapes.

Two species of oak are native to Britain: the pedunculate oak, *Quercus robur*, and sessile oak, *Quercus petraea*. Recently, Britain's native oak trees have been receiving increased attention due to observations of declining tree condition (Forestry Commission, 2018). Particular focus lies on new threats corresponding with well-known stressors. These concerns are predominantly centred around the effect of novel pests and diseases in the context of environmental impacts caused by changing climatic conditions.

One of the more recent stressors to British oaks is powdery mildew (Day, 1927). The fungal disease causes infestation of leaves and significantly reduces foliar absorption capacity (Thomas, 2008; Thomas, Blank and Hartmann, 2002). Powdery mildew can be particularly impactful when the prolonged effect of reduced absorption capacity is combined with short-term insect defoliation.

One such insect that causes heavy defoliation is the oak processionary moth, *Thaumetopoea processionea*. The moth was accidentally introduced to the UK in 2005 and has been causing severe disturbance since, particularly in Greater London (Townsend, 2013). The pest has received widespread attention due to the hazard posed to human health. The moth's caterpillars are capable of shedding fine hairs that can cause serious skin irritations and respiratory issues. The moth's larvae feed on the foliage, in some cases leading to complete defoliation of an affected tree.

Adding to these new threats there is a growing recognition of declining oak condition caused by complex interactions of environmental factors with cooccurring biotic stressors. Such diseases create great risk to the UK's native oak population and fall into the category of oak declines. This is discussed in the following subsection.

1.5 Oak declines

The category of decline diseases was first mentioned by Sinclair in 1965, who defined tree declines by the presence of three types of interacting factors: predisposing, inciting and contributing. Typically, a tree is affected by a decline when concurrence of (multiple) predisposing factors and causal agents are present. Both biotic and abiotic factors are associated with decline diseases and these cause greatly varying response patterns. Symptoms of a decline disease may develop over several years while the rate of symptom appearance may fluctuate within this period. Additionally, trees may show periods of remission once affected by a decline. Due to these variable effects on tree health and the great heterogeneity in pathology, declines are complex diseases to define and quantify.

Over the last three centuries, there have been increasing reports worldwide of declining oak condition (Gottschalk and Wargo, 1996). In Europe archival records bear evidence of emerging oak decline in Germany between the years 1739 and 1748 (Thomas, 2008). Since then, oak declines in Europe have been known to occur in periodic episodes characterised by increased tree mortality. These episodes can last

for up to ten years and are often preceded by phases of predisposing growth reduction (Thomas *et al.*, 2002). While this decline process remains unchanged, the set of stressors and causal agents involved varies depending on the geographical region and oak species.

Generally, European oak trees are experiencing combined stress from one or several abiotic factors, such as climatic extremes (drought and frost), and abiotic factors, like insect infestation and defoliation as well as pathogenic fungi (Thomas *et al.*, 2002). Within the oak decline complex, regional differences in stressors and pathology are often regarded as separate decline syndromes (Gottschalk and Wargo, 1996). Despite these distinctions, all oak decline syndromes exhibit the commonality that tree health is greatly reduced (with probable eventual mortality), causing ecosystem damage and measurable economic impacts on forestry.

In the UK, oaks have been affected by decline for more than a century (Day, 1927). Periodic episodes of decline have impacted British oak populations, causing dieback and reduced health to native Pedunculate oak (*Quercus robur*) and Sessile oak (*Quercus petrea*). Two separate decline syndromes have been identified to affect native oaks: chronic and acute oak decline (Denman and Webber, 2009; Brown *et al.*, 2016). Chronic Oak Decline (COD) and Acute Oak Decline (AOD) are discriminated by their associated causal agents, presence of symptoms and most predominantly in the speed of the decline (Denman *et al.*, 2014; Denman and Webber, 2009).

COD is defined as continued degradation of health over many years and is thought to be caused by pathogens attacking the roots of predisposed mature trees (Denman and Webber, 2009). The most predominant visible symptom of COD is a reduction of crown condition, with affected trees exhibiting a loss of foliage and dieback of fine twigs. Drought stress paired with root rot fungi are suspected to drive this complex disease. Affected trees may remain in this chronic state of decline for decades. Although COD affected trees have died in some localised areas, COD "on its own does not currently pose a serious threat to the United Kingdom's overall oak tree population" (*Forest Research*, 2020). However, trees weakened by COD may be more susceptible to other health threats. Such additional threats may stem from environmental stresses like severe drought and flooding, insect infestations like oak processionary moth and AOD.

Figure 1-1 Examples of AOD symptoms on the stem of sample trees at Monks Wood. On the left, an active stem bleed is shown, the centre shows lesions at several locations along the stem, and the right image shows a dried lesion in late summer.

AOD, in contrast to COD, is characterised by a rapidly declining tree health, often leading to mortality within a few years. Distinctive symptoms of AOD are cracks in the bark and lesions seeping dark fluid (also known as stem bleeds). These symptoms are visible on the stem of mature trees (see Figure 1-1) and originate from areas of necrosis in the cambial tissue underneath the bark plate. The bacterial species *Gibbsiella quercinecans* and *Brenneria goodwinii* have been isolated from symptomatic tissue and fluid (Brady *et al.*, 2017). Their presence is consistent for AOD symptomatic trees and has not been detected on healthy trees, thus implying a causal role of these bacteria (Sapp *et al.*, 2016; Denman *et al.*, 2016). Additionally, larval galleries and exit holes of the *Agrilus biguttatus* beetle always occur in conjunction with other AOD symptoms. It is however still unclear whether the Buprestid beetle acts as AOD causal agent or simply makes an opportunistic appearance on trees weakened by the decline (Brown *et al.*, 2017, 2015; Denman, 2019). Further indication for a biotic cause of the disease is that AOD affected trees often appear in clusters with newly symptomatic trees at the edge of declining groups (Brown *et al.*, 2016; Denman, 2019). It is however very likely that AOD susceptible trees have been weakened by abiotic predisposing factors and/or COD. Thus AOD is often referred to as specific "syndrome within the wider Oak Decline complex in Britain" (Denman *et al.*, 2016; Denman, 2019).

Generally, while presence of biotic factors has been demonstrated in COD and AOD, little is known on the specific effects of these, potentially interacting, factors on

oak trees. The complexity of the declines has left large gaps in the understanding of the nature of causes and dispersal of these diseases. With increasing pressure from changing climatic conditions and accumulated severe weather events, further knowledge on oak declines is essential to adapt the management of Britain's native oak stands and potentially mitigate the risk of mortality.

1.6 Remote sensing of forests

1.6.1 Remote sensing of forest species

Identifying tree species with remotely sensed data has been an active field of research for several decades (Fassnacht *et al.*, 2016) and information derived on species distribution has been shown to be highly valued by forest practitioners (Felbermeier *et al.*, 2010). This section provides an overview of the current state of research on tree species classification with remotely sensed data, including the methods used, the potential applications and challenges faced.

Remote sensing is a useful for tree species classification because it provides an efficient way to map and monitor large forest areas and is motivated by forest management and conservation applications. Additionally, the potential complete inventory that remote sensing provides would not be possible to achieve using traditional ground surveys. A comprehensive understanding of the distribution and diversity of tree species has great value for estimating the ecological and economic parameters of the forest and for making informed decisions related to conservation, management, and land use planning. Applications for species distribution maps include forest inventory and biomass estimations, monitoring of invasive species, habitat mapping, biodiversity conservation, and to assess the impact of land use change, forest management practices, and climate change on forest ecosystems (Breidenbach *et al.*, 2010; Fassnacht *et al.*, 2016; Pham *et al.*, 2016; Puliti *et al.*, 2017; Xie *et al.*, 2019).

The use of remote sensing in forest species classification has a long history dating back to the early days of aerial photography and satellite imagery. Initially, forest species were classified using visual interpretation of aerial photographs (Sayn-

Wittgenstein, 1978), which provided a broad overview of the distribution and composition of forest cover.

With the advent of new remote sensing technologies, such as multispectral and hyperspectral imaging and LiDAR (Light Detection and Ranging), the ability to classify forest species at finer scales and with greater accuracy has improved.

Multi- and hyperspectral imaging captures a range of wavelengths of light, which can provide information on the chemical and structural properties of vegetation, such as leaf chemistry and canopy structure. Inter-species differences in these properties are used to distinguish between species. LiDAR, on the other hand, can provide information on the height and structure of vegetation. LiDAR has thus been shown to be particularly useful for delineating individual trees.

In addition to advances in sensor systems delivering data at higher spatial and spectral resolutions, the use of remote sensing in forest species classification has increased with the advancement of machine learning techniques in recent years, becoming more sophisticated and accurate.

Common remote sensing approaches that have been used for tree species classification can be summarised as follows:

- Spectral-based methods: These methods use the reflectance properties of tree species in different wavelength ranges to classify them. Multi- and hyperspectral imagery is often used in this type of classification.

- Structure-based methods: These methods use the structural properties of trees, such as crown shape and canopy height, to classify them. LiDAR is a frequently used technique for this type of classification.

- Fusion-based methods: These methods combine the information from multiple remote sensing data sources, such as optical imagery and LiDAR, to improve the accuracy of tree species classification.

- Machine learning-based methods: These methods use various machine learning algorithms such as Random Forest, Support Vector Machine, Neural Network etc. to classify tree species based on the remote sensing data. With the advent of deep learning techniques such as convolutional neural networks, the accuracy of tree species classification has been further improved.

- Object-based methods: Opposed to pixel-based approaches, these methods classify tree species by analysing the properties of individual trees or groups of trees within a given image. This approach is based on the segmentation of an image into homogeneous regions (i.e. object based image analysis - OBIA) and then assigns the class labels based on the characteristics of the segmented regions. Object-based methods are particularly beneficial with high spatial resolution imagery when pixel-based approaches suffer in accuracy due to high spectral variability.

A combination of these methods is also possible and is typically exploited to pursue an increase in classification accuracy (Fassnacht *et al.*, 2016; Hologa *et al.*, 2021). An example of a possible approach (given data availability) is an object-based classification using a machine learning algorithm on fused data. Using such an approach, (Alonzo *et al.*, 2014; Dalponte *et al.*, 2012, 2014; Sarrazin *et al.*, 2011) demonstrated that a combination of the above methods can improve species classification results in terms of spatial detail and classification accuracy.

The use of remote sensing for forest species classification has been applied to both natural and managed forests. It has been used to map and monitor the distribution and diversity of forest species at various scales, from individual trees (Chen *et al.*, 2021; Lee *et al.*, 2016; Plesoianu *et al.*, 2020; Shi *et al.*, 2018, 2021; Zhang, 2016), to stands (Grabska *et al.*, 2019; Wan *et al.*, 2021) and entire forests (Bolyn *et al.*, 2022; Welle *et al.*, 2022). The demands regarding the spatial resolution of the species distribution map vary with the final application. The choice of remote sensing approach depends on the specific goals of the study, the type of forest being studied, and the available data. However, in many cases, the spatial scale of the final species map is determined or constrained by the available spatial resolution of the sensor used.

According to the chosen remote sensing method and spatial unit of the species classification, a suitable ground sampling density needs to be determined. Typically, requirements for ground sample density and ground survey accuracy are higher with an increased spatial resolution of the remotely sensed data. However, this will depend on the main objective of the species classification, i.e. whether the desired information is an estimate of forest stand composition or explicit information on the location of species and / or individual trees. Remote sensing-derived species distribution maps are

used as standalone products or in further analysis where species distribution is a prerequisite, such as biomass estimations.

Challenges in tree species classification using remotely sensed data include the similarity of reflectance properties among different tree species, the complexity of forest structure often with interlocking crowns, and the high cost of acquiring and processing remote sensing data. Additionally, the accuracy of tree species classification can be affected by factors such as the quality of the remote sensing data, the size of the study area, and the environmental conditions.

1.6.2 Remote sensing of forest health

Traditionally, forest condition surveys and monitoring of health involves ground-based inspections by trained experts. These inspections are mostly based on visual assessments of symptoms and estimations of crown condition. Traditional condition surveys however are very labour intensive and have downsides regarding the achievable spatial coverage and the subjectiveness between surveyors. Supplemental to ground-based surveys, remote sensing offers potential to negate these issues: remote sensing enables the provision of comprehensive geodata that can be assessed objectively. These data offer higher consistency than traditional surveys, greater spatial accuracy and coverage as well as enabling automated or semi-automated analysis of forest health. Yet there is no direct conflict between these survey techniques. As such, field survey data support the generation of tools (e.g. models) for the detection and monitoring of declined forest/tree condition. Furthermore, remote sensing surveys that precede ground surveys can help in locating affected areas, that can be further assessed in the field. The combination of both information sources is what ultimately enables the creation of wall-to-wall surveys of forest condition which would be impossible by ground measurements alone. In this way, these spatially-inclusive data provide a greatly improved basis upon which to manage threats to forests compared with traditional field-based point sampling alone (Tuominen *et al.*, 2009; Solberg *et al.*, 2012).

Earliest attempts of remote sensing-based forest condition assessments took place at the beginning of the 20th century. These surveys were undertaken by visual interpretation of analogue aerial photographs to "extract […] information […] such as the estimation of the extent of stresses in forests" (Laar and Akça, 2007). Since then,

optical imaging technology has progressed and the focus has shifted towards the analysis of digitally-recorded spectral information. Ever since multispectral satellite imagery has become broadly available (e.g. Landsat) researchers have been developing methods to quantify vegetation abundance, growth, health and change (Allen and Richardson, 1968; Curran, 1980; Cui *et al.*, 2013; Hobbs, 1990; Botkin *et al.*, 1984). These methods generally rely on the correlation between the physical properties of plants and their spectral reflectance properties (Stone and Mohammed, 2017). As such, the visible portion of the electromagnetic spectrum is indicative of chlorophyll and pigment content (Peñuelas and Filella, 1998). Information on cell properties can be inferred from the near-infrared (NIR) (Knipling, 1970) and water content from the short-wave infrared part of the spectrum (Seelig *et al.*, 2008; Penuelas *et al.*, 1993). Most commonly, these relationships are exploited through the calculation of wavelength ratio indices which are sensitive to physiological properties and allow the estimation of vegetation characteristics (Jackson and Huete, 1991).

To date, most research on forest condition has utilised medium to coarse (5-30m) multispectral satellite imagery to derive spectral signals for reduced tree health at scales ranging from forest to landscape and even global level (Achard *et al.*, 2011; Meigs, Kennedy and Cohen, 2011; Fraser and Latifovic, 2005; Franklin *et al.*, 2003). The majority of these studies are focused on quantification of the spatial extent of forest damage. An example where such analyses have found widespread application is the United Nations programme for Reducing Emissions from Deforestation and forest Degradation (REDD; www.un-redd.org).

High resolution satellite imagery (< 5 m) has been shown to enable within-stand analysis of forest condition and assessment of individual trees (Wulder *et al.*, 2008; White *et al.*, 2005; Meng *et al.*, 2016; Hicke and Logan, 2009). The finer spatial resolution facilitates a more precise localisation of damaged or dead trees than medium to coarse satellite imagery. Likewise, high resolution imagery has been shown to characterise small outbreaks or other spatially-limited forest damage better than coarser imagery, indicated by improved classification accuracies (Dash *et al.*, 2017). High resolution information is also a key requirement for the detection of specific forest pathogens. Therefore to date, remote sensing-based disease detection has mainly applied imagery from piloted aerial platforms (Leckie *et al.*, 2004; Stone and Mohammed, 2017).

Subtle changes in forest condition or long-term growth reduction are generally difficult to identify and require multiple observations over time. Change detection methods have proven most suited to identify these slow impacts as their spatiotemporal patterns are revealed (Verbesselt *et al.*, 2009; Chen and Meentemeyer, 2016; Fernandez-Carrillo *et al.*, 2020). Similarly, multitemporal data can improve the detection of forest disturbances as the temporal aggregation has been shown to enhance the signal-to-noise ratio. Atmospheric influences and other environmental factors that introduce noise are reduced when sites are observed over longer time frames (Rullan-Silva *et al.*, 2013).

The early detection of compromised tree and forest health with remote sensing is an active field of research (Dash *et al.*, 2017; Ortiz, Breidenbach and Kändler, 2013). Multiple airborne campaigns using piloted aircraft are costly. As a consequence, they are unable to provide surveys at sufficiently-short intervals that would facilitate the near-continuous monitoring of forests necessary for early-stage detection of declining condition. The medium-to-coarse resolution of these platforms does not allow the detection of small, isolated outbreaks and individuals in decline, which is a requirement in forests with high species diversity and heterogenous structure.

1.7 UAV remote sensing

Contrary to spaceborne and manned airborne sensor platforms, unmanned aerial systems (UAS) present a new and emerging technology that offers a) cost-effective, b) frequent, c) high-resolution and d) rapid response data capture. A UAS consists of a ground control station (GCS) and an unmanned aerial vehicle (UAV), that can be either a fixed wing or rotary wing aircraft. Developments in miniaturisation of technology have enabled UAVs to be equipped with flight controllers accommodating global navigation satellite systems (GNSS) and inertia measurement units (IMU) as well as sensor payloads. While most publicly available UAVs remain in the sub 25 kg category, most commercial UAVs weigh between 1 kg and 10 kg. Driven by the consumer market consisting of hobbyist, photography, and cinema use cases, UAV hardware and software have experienced impressive technological advances over the past decade. Concurrently, UAV production rates have vastly increased causing the price for this technology to drop (Crutsinger *et al.*, 2016).

The accessibility of UAS has led to greatly increased interest from the scientific community (Anderson and Gaston, 2013; Manfreda *et al.*, 2018). Widespread use of UAS in natural sciences is indicated by the exponential increase of "UAV" publications since 2005, totalling 414 papers in the agriculture and forestry domain until 2017 (Raparelli and Bajocco, 2019). The emergence of UAS in research derives from a multitude of benefits provided by this modern survey tool.

First and foremost, modern UAS facilitate autonomous flying with planned and repeatable trajectories for mapping purposes. The autonomy makes these systems approachable for non-experts and enables surveys to be replicated exactly, an important requirement for multitemporal data acquisition. Concurrently, the majority of UAS used for mapping are compact and affordable for most research projects. These characteristics translate to great flexibility in deployment and reduce logistical constraints that are common for piloted aerial surveys, such as aircraft and pilot availability as well as weather conditions. Reduced time and effort required to undertake mapping flights allow the collection of geodata at short notice, using specified spatial parameters, and providing time series observations with high temporal resolution.

Flight altitude of UAVs is constrained by legal limitations to < 120 m above ground level (AGL) in most countries (Cunliffe *et al.*, 2017). Consequently, the small survey range delivers hyperspatial resolution imagery (Michez *et al.*, 2016), defined as a ground sample distance (GSD) of ten centimetres or less, enabling detailed imaging of individual trees. Additionally, as distance between sensor and subject is reduced, atmospheric influences drastically decrease. The low flight altitude also means that a UAV can be operated below cloud cover making UAS surveys less weather dependent than piloted aircraft or satellite image acquisitions.

However, the small-scale platforms and miniaturised payloads bear their own respective challenges. Wind is a major limiting factor for UAS surveys (Duffy *et al.*, 2017). Due to their low take-off weight, most UAVs cannot be flown in winds above 40 km/h (e.g. DJI Phantom 4 pro). Furthermore, as high resolution imagery captures wind-induced movement of vegetation, the final data quality is impacted (Iglhaut *et al.*, 2019). In addition, sensor payloads for UAVs are under active development and generalised calibration procedures and quality assurance methods are not yet established and standardised as is the case with satellite and airborne imagery.

Data acquisition and processing can be undertaken by researchers themselves rather than by specialised remote sensing survey technicians. As a consequence, since the technology and data processing are accessible to the general public, new sources of error may be introduced that lead to degraded data quality. Flight survey design, data collection, and image processing therefore require knowledge and technical rigor to be applied in order to produce data which are in equal in quality to professional airborne or satellite remote sensing campaigns.

Despite these challenges, the impact of UAS as a survey tool in research is regarded as so significant that the technology is believed to be "revolutionizing natural science observations […] similar to those transformations that GIS and GPS brought to the community two decades ago" (Watts *et al.*, 2012).

1.8 Structure from Motion (SfM) photogrammetry

The emergence of UAS as a surveying tool is in part owing to parallel advances in photogrammetry. Digital photogrammetry has been undergoing a methodological revolution over the last decade, allowing automated 3D reconstruction from unordered images. These vast developments are driven by the integration of advanced computer vision algorithms in a photogrammetric workflow. In traditional stereophotogrammetry, the exact camera position and orientation as well as surveyed ground reference points were essential to derive 3D information from imagery. Current image matching algorithms eliminate this requirement and this modern approach is commonly called Structure from Motion photogrammetry (SfM). The technology, its emergence and application in forestry are thoroughly discussed in *SfM photogrammetry in forestry: a review* authored by Iglhaut *et al.* (2019)*. The following introduction to SfM photogrammetry includes paragraphs and figures from the published work. As SfM presents the key data acquisition method in research presented in this thesis, the photogrammetric technique is introduced in greater detail and practical implications are given in the sections that follow.

1.8.1 SfM photogrammetry: theoretical principles

Traditional stereophotogrammetry methods are based on an analogy of the binocular human vision. Depth can be perceived from two points whose relative position is known. However, depth, volumes, or 3D features can also be perceived from a single observing point if either the observer or the object is moving (Bolles *et al.*, 1987; Ullman, 1979). SfM is a photogrammetric technique that is based on both these principles: (i) the binocular vision and (ii) the changing vision of an object that is moving or observed from a moving point (Koenderink and van Doorn, 1991). SfM is used for estimating 3D models from sequences of overlapping 2D images. SfM became of great interest in recent years due to its ability to deal with sets of unordered and heterogeneous images without prior knowledge of the camera parameters (Westoby *et al.*, 2012).

SfM differs from traditional photogrammetry mainly in three aspects: (i) features can be automatically identified and matched in images at differing scales, viewing angles and orientations, which is of particular benefit when small unstable platforms are considered; (ii) the equations used in the algorithm can be solved without information of camera positions or ground control points, although both can be added and used; and (iii) camera calibration can be automatically solved or refined during the process.

SfM can thus automatically deliver photogrammetric models without requiring rigorous homogeneity in overlapping images, camera poses and calibrations (Fonstad *et al.*, 2013; Micheletti, Chandler and Lane, 2015; Skarlatos and Kiparissi, 2012). Please refer to Figure 1-2 for the data processing workflow.

A set of overlapping images is the main input requirement for SfM photogrammetry. In a first step of the SfM workflow (Figure 1-2), features in the images are detected (see also Figure 1-3). This process is also referred to as keypoint extraction. Keypoints are features offering high probability of recognition in different images such as where the texture of the scene has clear changes, e.g. corners, intersecting edges. Common algorithms used for the identification of keypoints mainly stem from the computer vision domain. Scale Invariant Feature Transform (SIFT) and Speeded Up Robust Features (SURF) are two of the most used open-source feature detection and matching algorithms and are integrated in several software packages (Lowe, 2004).
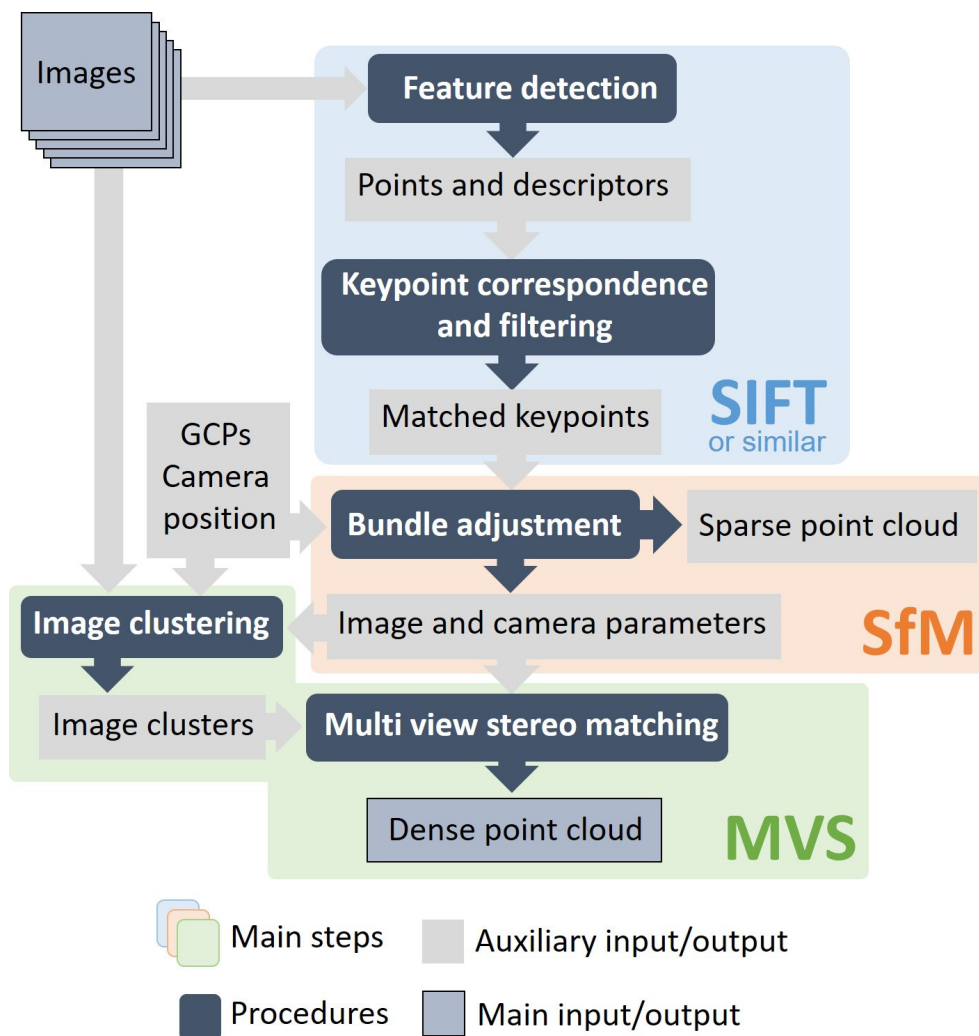
Figure 1-2 Schematic workflow of the Structure from Motion (SfM), Multi View Stereo (MVS) process. Individual stages are shown from input image set, to feature identification and matching by algorithms such as the common Scale Invariant Feature Transform (SIFT), to the bundle adjustment phase where the scene is reconstructed in three dimensions, and finally the MVS stage densifying the spare point cloud. The dense point cloud is georeferenced by providing positional information for images and/or ground control points. (Iglhaut *et al.*, 2019)

Proprietary SfM software solutions do not publicly share the information about their underlying feature detection algorithms, although Agisoft Photoscan (renamed Metashape) is reported to utilise a "SIFT-like" algorithm (Dandois and Ellis, 2013).

For every keypoint, a complex descriptor is then computed in order to find corresponding points across multiple images. Typically, a filtering step follows the recognition of corresponding keypoints to discard geometrically inconsistent matches.

At this stage the common keypoints of any image pair are tested for their collinearity, where all points that lie on a single line remain aligned in this way. The relationship between the two images is hereby specified in the fundamental matrix (F-matrix) calculated by the Eight-point algorithm (Longuet-Higgins, 1987). While other methods are applicable, a common approach for the evaluation of the F-matrices, hence the collinearity validation, is the RANdom SAmple Concensus (RANSAC) method (Fischler and Bolles, 1981). The sampling step is iterated until there is a 95 % chance that only inlier keypoints remain.

The actual SfM stage starts after the keypoint filtering stage using the remaining, geometrically correct feature correspondences. Here the 3D geometry (structure) of a scene, the camera position and orientation (extrinsic parameters) and the camera's intrinsic parameters are simultaneously estimated employing bundle adjustment algorithms (Ullman, 1979). In this situation, bundle refers to bundles of rays connecting the camera centres to points in 3D space and adjustment refers to the minimisation of a cost function that reflects measurement errors in the location of image features in the object space, also known as reprojection errors. The minimisation of the cost function concurrently optimises the 3D structure of the scene as well as the camera parameters. Traditional photogrammetry, in contrast, requires known ex- and intrinsic camera parameters. The SfM phase outputs the camera models and poses along an arbitrarily scaled 3D point cloud, referred to as sparse cloud. In order to georeference and scale this cloud, either ground control points (GCPs) with known XYZ coordinates can be used or the camera location and orientation can be exploited (Smith *et al.*, 2015; Carbonneau and Dietrich, 2016). Once a sparse georeferenced point cloud along with the camera parameters is obtained, a typical subsequent step in the workflow is the densification of the cloud by the means of a multi-view stereo (MVS) algorithm. Hereby a densification of at least two orders is achieved. The SfM-MVS workflow and respective results are illustrated in Figure 1-2 and Figure 1-3.
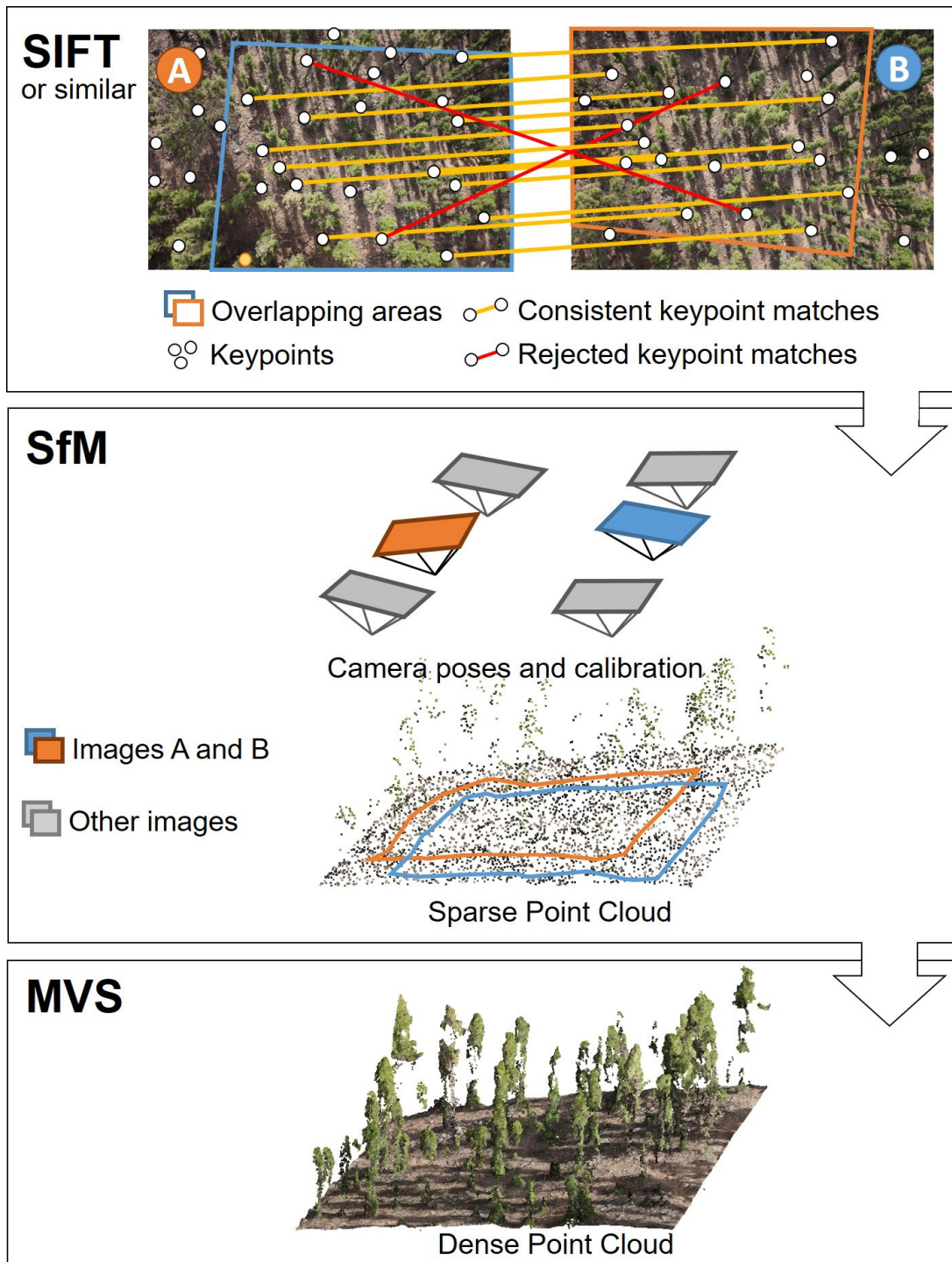
Figure 1-3 The three key stages in a SfM-MVS workflow illustrated on two hypothetical images of a Canary Island pine forest: 1) keypoint identification and matching (e.g. SIFT), 2) SfM with camera parameters and a sparse point cloud as output, and 3) the densified point cloud following MVS. (Iglhaut *et al.*, 2019)

A dense point cloud, with colour/spectral information derived from the input images, represents the primary output of the SfM-MVS workflow. Subsequent processing steps (for aerial surveys) typically involve the derivation of a digital surface model (DSM) and an orthomosaic. The orthomosaic holds the spectral information of the input imagery and is geometrically corrected with the SfM-derived surface information.

1.8.2 SfM photogrammetry in practice

Today, multiple software packages integrate SfM-MVS algorithms for fully automatic creation of point clouds. At the forefront of proprietary SfM solutions are Agisoft Photoscan, later renamed to Metashape (www.agisoft.com) and Pix4D (www.pix4d.com). Established open-source software packages are VisualSFM (www.ccwu.me/vsfm), Bundler (www.cs.cornell.edu/~snavely/bundler) with lesser-known alternatives like Apero/MicMac (logiciels.ign.fr/?Micmac) and SURE (www.ifp.uni-stuttgart.de/publications/software/sure). The rapid and largely automated processing of imagery using a software package such as this, allows the reconstruction of 3D scenes with relatively little hardware requirements, although processing is intensive and may take considerable time on less powerful machines.

Input imagery can be obtained from almost any camera system. Suitable sensors range from consumer-grade digital cameras to professional multi- and even hyperspectral sensors. The availability of high-resolution off-the-shelf compact cameras with low weight makes SfM photogrammetry particularly suited for UAS applications. The low cost and flexibility of such a system makes it an attractive alternative to LiDAR, in particular when frequent surveys are needed. In contrast to a LiDAR approach, photogrammetry however does not penetrate features, due to the passive nature of the sensor. A SfM derived point cloud therefore only represents the "seen" surface and has limitations when detection of ground topography is a requirement, e.g. under dense canopy forest. However, SfM photogrammetry holds the advantage over LiDAR that all spectral information of the original imagery is attached to points. Since the spectral information and the point geometry both have the same imagery origin, a temporal mismatch is avoided.

SfM algorithms have substantially changed digital-photogrammetry and ultimately enabled the use of drone imagery. Some proprietary SfM software packages

have made UAV photogrammetry very accessible, even to unexperienced users. However, practitioners seeking to apply SfM-photogrammetry professionally and specifically as a research tool still require substantial knowledge of "traditional" photogrammetry and understanding of technical fundamentals to collect high quality data for rigorous scientific analysis. Additionally, photography basics and the camera technology need to be well understood to gather unflawed imagery. The reconstructed scene will exhibit gaps where texture is not reliably displayed due to low resolution imagery, motion blur, over- and underexposed images or features with smooth or glossy surfaces. Insufficiently textured areas and patches where visibility is constrained by occlusion are filtered out during the MVS phase and result in gaps in the model. Such "holes" in a reconstructed scene, where data is essentially missing due to a lack of clear texture in the imagery, is a key restriction of a SfM-MVS approach. Provision of quality input imagery by careful consideration of texture limiting factors is hence essential for the creation of a point cloud without gaps. Therefore, a well and evenly illuminated scene is critical to capture texture. This is required to contrast surface spectral differences in the imagery, especially when UAVs equipped with consumer grade cameras are considered. Weather conditions at the time of flight are therefore an important consideration, e.g. changing illumination due to the sun emerging from or disappearing behind clouds during flight impedes both image matching and subsequent spectral data analysis. In a highly-variable cloudy climate such as Britain's, this can be problematic.

In every circumstance, the camera settings need to be considered to ensure optimal image data are acquired given a set of constraints, namely (i) those from the environment (lighting conditions), (ii) the platform (UAV, pole, tripod or handheld) and (iii) the camera and lens combination (the exposure triangle, focal length, sensor size) and is discussed in detail in O'Connor *et al.* (2017).

Within image acquisition and SfM photogrammetric workflows, users have many parameters which they can vary depending on the equipment and software used. For some, users can have near full control (e.g. the 'exposure triangle'; ISO, shutter speed and aperture), though there are several which will only be estimated prior to performing a survey (such as the exact camera positions images will be acquired from). Other influential factors, which cannot be manipulated (e.g. light conditions), will have to be carefully considered when planning a SfM-based survey. The success

of reconstruction is ultimately dependent on factors that can be broken down into five categories, presented in Table 1-1.

Table 1-1 Overview of variables influencing the results of a SfM survey. (Iglhaut *et al.,* 2019)

Domain	Variable		Recommendation
Scene	Texture	-	High surface contrast to allow for feature-point detection
	Pattern Repetition	-	Increase overlap and increase accuracy of geotags
	Moving Features	-	Avoid!
	Occlusions	-	Increase overlap and viewing angles
Lighting Conditions	Sun Angle	-	High! Solar noon is ideal
	Weather	-	Overcast provides even lighting (ambient occlusion) for structural (RGB) surveys. For spectral surveys little atmospheric influence may be required, clear skies.
	Changing Illumination	-	Avoid!
Camera Parameters	Focal Length	-	Wide but not too wide to minimize distortions. 28-35 mm is a good basis (James *et al.* 2012)
	Exposure Δ	-	Well exposed
	- Aperture	-	Small for max depth of field*, f/8 an advisable default
	- Shutter Speed	-	High for reduced motion blur*, ground speed (m/s) * exposure time (s) = blurred pixel length
	- ISO	-	Low for min noise*, auto-ISO an advisable default
			*ideal scenario, but will always be a compromise between these three parameters
	Pixel Pitch	-	As high as is practical. Physical pixel size positively influences dynamic range and sensitivity
Survey Characteristics	Overlap	-	High (>80% forward and lateral) as rule of thumb for forests to increase redundancy and matchability in scenes with high pattern repetition, moving features and/or occlusions. As a rule of thumb a UAV-SfM data acquisition should be planned so that each point will be visible at least in 4-5 images.
	View angles	-	Convergent for reduction of systematic errors (RGB) Parallel (Nadir) for spectral sensing (reflectance)
	Survey Range	-	With increasing distance to the object/scene (decreasing GSD) survey precision degrades. Increased GSD requires higher overlap.
Processing Parameters	SfM – matching		
	- Image scale	-	If matching isn't successful at full image scale ½ or ¼ may promote matchability
	- Keypoints	-	The number may be reduced for large datasets to reduce processing time
	MVS - densification	-	Densification may not always be required at full image scale/maximum point cloud density
	Secondary Products	-	Multitude of algorithms for meshing, gridding etc. (results will depend on specific method)

To apply SfM photogrammetry in forestry, important aspects to achieve a successful survey are that (i) the scene is covered with overlapping images from multiple locations and angles (high overlap to increase redundancy and multiple viewing angles of the same object to reduce occlusions and systematic errors), (ii) any feature to be reconstructed should be visible in at least three images (five or six images for dense vegetation) and the angular divergence between neighbouring images should not exceed 10 - 20 degrees, (iii) the scene is sufficiently illuminated (constant lighting is preferable, e.g. overcast or cloud free conditions), and (iv) the object of interest is fixed (preferably no movement from branches in wind) (Iglhaut *et al.*, 2019).

To use SfM-photogrammetry surveys as a method in quantitative research, careful consideration of all parameters involved is essential to realise the full potential of the approach, as well as to enable sources of error to be traced.

1.8.3 SfM photogrammetry for forest species mapping

Analogous to forest species classification with remotely sensed data from piloted aircraft or satellite platforms (see 1.6.1), UAV imagery can be used to map species, offering several advantages for forest species classification, including high spatial resolution, flexibility, and low cost.

Spatially continuous spectral mapping used to be exclusive to the satellite or piloted airborne surveying domains. However, in recent years, lightweight sensors with discrete narrow spectral bands suitable for UAV mounting have become commercially available, allowing researchers to collect their own aerial spectral data (Dash *et al.*, 2017; Näsi *et al.* 2015; Minařík and Langhammer, 2016; Aasen and Bareth, 2019). Such 2D spectral imagers may be used for SfM-based photogrammetric reconstruction and orthophoto generation, which can then be used to classify tree species.

With the technological possibilities improving for researchers to collect and process spectral UAV data, there has naturally been increased interest in using these data for classification of tree species. Early examples of studies demonstrate potential for classification of tree species (Baena *et al.*, 2017; Gini *et al.*, 2014; Lisein *et al.*, 2015; Michez *et al.*, 2016) classifying between three and five different tree species in open forest scenarios. Despite their use of NIR-modified RGB cameras, that exhibit undesired band overlap (Pauly, 2016), these early publications on UAV-based tree species classification achieved classification accuracies over 70 %.

Michez *et al.* (2016) highlighted that an object-based image analysis approach together with machine learning models are well suited for high-resolution UAV imagery. In later publications on UAV-based tree species classifications, a combination of these methods is widely adopted. Further notable studies are Alonzo *et al.*, 2018 who used UAV imagery and machine learning algorithms to classify five tree species in a temperate forest in Mexico. They achieved an overall accuracy of 90 % in identifying the species. Kattenborn *et al.*, (2019) used UAV imagery and object-based image analysis to classify six tree species in a mixed forest in Germany.

They achieved an overall accuracy of 86 % and highlighted the importance of choosing appropriate image segmentation methods to improve classification accuracy. Wang *et al.* (2020) used UAV imagery and deep learning algorithms to classify four tree species in a tropical rainforest in China. They achieved an overall accuracy of 91.4 % and demonstrated the effectiveness of deep learning methods in overcoming the challenges of complex forest structures and varying lighting conditions.

More recent research employs data fusion from multiple UAV sensors to further enhance classification accuracy and improve segmentation for an object-based approach (Moura *et al.*, 2021; Qin *et al.*, 2022; Schiefer *et al.*, 2020; Zhong *et al.*, 2022). The authors of these publications recognise that the high information content of UAV data, while allowing for refined intra-species distinction, can potentially introduce background noise and uncertainty in choosing a suitable segmentation approach that avoids over- or under segmentation. Individual tree segmentation algorithms generally require LiDAR data as input and are less suited for dense broadleaf forests where crowns often overlap. Segmentation of UAV imagery in different forest scenarios is thus an active field of research.

Further challenges associated with using UAVs for forest species classification are the variability in lighting and weather conditions, which can affect the quality and consistency of UAV imagery. The accuracy of species classification can also be influenced by the quality and resolution of UAV cameras, the flight parameters, and the complexity of forest structures. Another challenge is the need for accurate ground truth data for training and validation of machine learning algorithms. This requires extensive fieldwork to collect samples of different forest species, which can be time-consuming and labour-intensive.

It remains the case that most species classification studies using remote sensing utilise data acquired by sensors on board piloted aircraft. Relatively speaking, the use of UAVs as platforms for this purpose is in its infancy, with challenges and requirements associated with calibration, survey design, and interpretation needing to be identified, investigated and recommendations made to account for these. This is the equivalent of establishing good practice at the advent of airborne studies in past decades, permitting consistent applications to be made. The research presented in this thesis incorporates each of the remote sensing analysis techniques listed in section 1.6.1 to investigate and inform the potential of UAV remote sensing data for species classification.

1.8.4 SfM photogrammetry for forest health assessments

Opposed to the field of precision agriculture, where SfM-based processing of spectral image data is widely applied for plant health analyses (Hunt and Daughtry, 2018), in forestry there are currently only few examples where SfM-derived mapped spectral products have found application to assess forest health. Early UAV/SfM-based studies of forest health made use of off-the-shelf RGB cameras, modified to capture NIR images. Lehmann *et al.* (2015) and Michez *et al.* (2016) used an object based image analysis (OBIA) approach to segment and classify their scenes in order to identify declining tree health caused by biotic stress agents on both alder and oak. They achieved good overall classification accuracies (79.5 - 84.1 % and 82.5 – 85 % at their respective study sites) across five classes. However, they acknowledged limitations of NIR modified RGB cameras namely that, since visible and NIR spectra are not separable on the same sensor, there is spectral contamination due to broad and overlapping bands (see also Pauly, 2016) as well as the inability to correct for changing light conditions (as downwelling irradiance is not captured).

Näsi *et al.* (2015) used hyperspectral image data combined with the SfM-derived DSM for bark beetle damage detection at the individual tree level, achieving an overall classification accuracy of 76 % when distinguishing between healthy, infested and dead trees. In a follow up study Näsi *et al.* (2018) concluded that the individual tree-based approach, facilitated by the combination of 3D and spectral data, provides a promising and cost-efficient alternative to field-based assessments of pest infestation. Minařík and Langhammer (2016) also used a UAV-SfM based mapping approach to map bark beetle forest disturbance and found that bands from the red-edge (RE) and NIR part of the spectrum were most suited for stress detection. These findings are consistent with the results by Dash *et al.* (2017), who assessed the potential of a commercially available multispectral sensor, the Micasense RedEdge (Micasense Inc., Seattle, WA, USA), for the detection of early signs of stress during a simulated disease outbreak in a pine plantation. In their random forest classification of time-series data, normalized difference vegetation index (NDVI) was shown to be the best performing predictor variable to map physiological stress symptoms indicative of the declining tree health. Further late examples of forest health monitoring are Baena *et al.* (2017) and Brovkina *et al.* (2018), both successfully

applying an OBIA approach on SfM mapped NIR image data stemming from a modified consumer RGB sensor to separate between dead and living trees.

The UAV SfM-based research on forest health to date illustrates the great potential to utilise the method for user-led remote sensing data acquisition. The ability to use UAVs as an acquisition platform has been shown to be particularly valuable. However, unique challenges that relate to employing high-resolution photogrammetry in forested environments need to be well understood and mitigated where possible. These forest-specific challenges predominantly relate to repetitive texture, moving objects (branches in wind), spatial heterogeneity, structural complexity and inability to place GCPs underneath canopy (Table 1-1). To apply SfM-photogrammetry in the studies presented in this thesis, these challenges are addressed in further detail in the general methods section.

1.9 Potential in UAV remote sensing to identify trees affected by oak decline

Despite the aforementioned link between tree health indicators and optical properties obtainable by remote sensing, to the author's knowledge, there have been no studies published on AOD or COD employing remote sensing technology. This research opportunity coupled with the recent increase in availability of miniaturised optical sensors and known advantages of UAVs (low-cost, flexibility and high-resolution imagery) has motivated the proposition to investigate the potential of UAV remote sensing for AOD and COD detection.

COD is thought to be driven by drought stress and the loss of fine roots due to fungal infection (Denman and Webber, 2009) while stem lesions in AOD are potentially linked to bacterial infection (Gathercole *et al.*, 2021). Although these key causal factors within the respective decline syndrome complex are not directly measurable with remote sensing, the impact of either disease syndrome on a tree will cause stress responses and interference of physiological processes that will ultimately translate to changes within the crown and foliage. With UAV remote sensing crowns can be recorded and assessed for indicators of reduced tree health.

In COD, the pathology is already partly defined by reduced crown condition including foliage loss and dieback of fine twigs. In AOD necrosis of cambial tissue and/or damage from larval galleries is expected to disrupt vascular flow, hampering the allocation of nutrients and water availability. Despite differing expression of

symptoms, prolonged stress by AOD or COD will translate into changes in the physical appearance and biochemical changes in the foliage, indicating decreased crown vigour and compromised overall health (Denman *et al.*, 2010). These altered spectral and structural characteristics of trees in decline present the key opportunities to detect AOD or COD inflicted stress with UAV remote sensing.

Declining oak tree health can be inferred spectrally, as coherently photosynthetic activity is declining. Oak foliage may even appear to be chlorotic due to the lack of chlorophyll (Denman and Webber, 2009). With multispectral sensors available to use on UAVs it is possible to record parts of the electromagnetic spectrum that are sensitive to these foliar changes (Carter and Knapp, 2001). Healthy, photosynthetically active leaves absorb most radiation in the visible range while greatly reflecting the NIR portion of the spectrum. If chloroplasts are degrading and changes in leaf pigmentation are occurring this relationship is moderated, with a greater absorption in the NIR and higher reflection in the visible part of the spectrum (Rouse, Haas and Deering, 1973; Bannari *et al.*, 1995; Croft *et al.*, 2016).

Leaf water content, an indicator for drought stress, is best assessed in the water absorption bands, in the short-wave infrared region of the electromagnetic spectrum (Seelig *et al.*, 2008). Most multispectral UAV sensors on the market today do not include bands in these respective wavelengths. Hyperspectral sensors may offer wavelengths not covered by multispectral cameras but are linked to higher purchasing and operational costs. Also, UAV-specific hyperspectral sensors currently still offer less spatial resolution and more complex and error-prone image processing pipelines than their multispectral counterparts (Näsi *et al.*, 2015; Hakala *et al.*, 2018). As leaf water content is essential for photosynthesis, multispectral sensors may still give valuable insight into water stress using a combination of visible and NIR bands (Easterday *et al.*, 2019).

Expected differences in crown structure between healthy and declining trees, such as loss of foliage and/or branch dieback, are well represented in high-resolution UAV imagery, allowing for resolutions of 10 cm per pixel or higher. Gaps in the crown are typically depicted by shadowed pixels in the imagery where less solar radiation is hitting. Structural crown characteristics can be assessed with OBIA (Blaschke, 2010) and/or texture metrics (Haralick, Dinstein and Shanmugam, 1973; Sayn-Wittgenstein, 1978; Gini *et al.*, 2018).

Temporal/phenological aspects may also influence the potential for a UAV remote sensing detection of AOD and COD stressed trees. For oak trees undergoing stresses interference of regulated growth processes is likely. Early or delayed bud burst in spring and/or early or delayed autumnal senescence are potential consequences (Kuster *et al.*, 2014). However, there is little known about AOD and COD and their effect on phenological patterns. On heavily weakened trees delayed bud burst and early senescence are probable but early bud burst and delayed senescence may also occur. The latter effect was demonstrated when drought-stressed oak seedlings were re-watered, which can be interpreted as attempt to recover once given the opportunity (Mijnsbrugge *et al.*, 2016). An additional compensation method for hampered growth is the ability of oaks to have a second leaf flush, also called Lammas growth (Denman *et al.*, 2014).

Differences in bud burst, senescence and Lammas growth between declining and healthy trees can in principle help in distinguishing affected trees, given correct timing of UAV image acquisitions. Together with previously mentioned spectral and structural aspects there is theoretical potential to monitor oak tree health with UAV remote sensing. This potential has motivated the research presented in this thesis, to gain a baseline understanding of the practical implications for oak decline detection utilising UAV remote sensing in the UK.

1.10 Scope and motivation for research

Research on forest health analysis by UAV remote sensing is still sparse, despite there being obvious benefits of the approach. Prominent benefits of UAV remote sensing are the potential to collect spatially inclusive information at high spatiotemporal resolution and allowing great independence in the acquisition of these data. Theoretically these survey characteristics present UAV remote sensing as an appropriate tool for near-continuous monitoring of forests and/or detection of subtle changes in forest condition. Yet, most UAV remote sensing research on forest condition and tree health to date has been undertaken in monocultures or orchards with explicit pest/disease impacts and distinct pathology (Dash *et al.*, 2017; Minařík and Langhammer, 2016; Brovkina *et al.*, 2018; Baena *et al.*, 2017). These scenarios have the advantage that trees are even-aged, often composing of a single species and in the case of orchards, trees are often widely spaced, greatly simplifying crown delineation

efforts and offering a distinct per-tree spectral response (Șandric *et al.*, 2022). In a natural environment however, tree physiology and morphology can exhibit great variation. Stress symptoms provoked by complex diseases, such as oak decline, may vary from tree to tree. Additionally, factors beyond the disease impact can have influence on a tree's appearance such as site conditions as well as any biotic, abiotic or anthropogenic disturbances, that are not directly linked to a disease. To steer towards operational use of UAV remote sensing in forest condition assessments, it is essential to also examine the approach in realistic scenarios that depict heterogenous mixed species forests and trees with ambiguous stress symptoms.

1.11 Thesis aims and objectives

The research presented in this dissertation seeks to investigate the use of UAV remote sensing for assessing forest condition, and specifically for detecting declined oak condition in natural woodlands with mixed species composition. The potential application of UAV remote sensing as a data source is evaluated for the detection of AOD and COD. Building on the discussions in the previous sections, the underlying principle explored in this research is whether AOD and COD induced stress translates to structural and biochemical changes within the crown and foliage that are detectable within UAV obtained imagery of the forest canopy.

1.11.1 Aims

In collaboration with the Forestry Commission, this research aims to determine whether UAV remote sensing is a suitable tool for the detection of the complex and little-understood AOD and COD in two semi-natural woodlands and to investigate the requirements to best achieve this. This is achieved through the following objectives.

1.11.2 Objectives

- To investigate the necessary UAV and camera system parameters, flight mission design and site considerations to achieve highest accuracy image data collection to enable differentiation between symptomatic and asymptomatic oak trees.

- To experimentally determine which remote sensing data (raw spectra, vegetation indices or textural metrics), alone or in combination, produce highest classification accuracy of trees affected by oak decline. This will include bands, vegetation and textural indices using parts of the electromagnetic spectrum which are known to be sensitive to biological processes or structural properties expected to be impacted by oak decline e.g. foliage discolouration due to reduced photosynthetic capacity or deterioration of crown integrity.
- To evaluate the ability to conduct a multiple species classification with UAV imagery in order to ascertain the distribution of oak within the mixed-composition, closed-canopy forest, to enable wall-to-wall prediction of oak condition. To optimise for detection of oak, assessment is undertaken of how classification results are influenced by varying image acquisition and analysis parameters.
- To determine the optimal period(s) of flight by assessing the influence of phenology on the ability to classify species and to detect oak decline. This is achieved through multitemporal flight campaigns within the growth season and aims to take account of seasonality e.g. whether transitional periods inform oak decline detection if stressed trees exhibit a phenology offset from that of healthy individuals.
- To assess the potential for wall-to-wall predictions of oak health status with machine learning.
- To provide insights on the potential to operationally apply these methods, synthesising both theoretical results and practical implementation issues.

1.12 Thesis structure

Chapter 1, Introduction (this chapter), has provided an overview of the importance of tree health monitoring, and in particular oak decline that will be examined in this thesis. The potential of UAV remote sensing is presented, along with considerations and requirements to ensure that high quality SfM photogrammetry data are collected.

Chapter 2, Materials and Methods, presents the two study sites in the Forest of Dean and Monks Wood which respectively exhibit COD and AOD. The parameters used for the acquisition of UAV remote sensing data and post-processing procedures which are common to all Chapters are specified in this Chapter. The methods are subsequently applied to the investigations in Chapters 3-5.

Chapter 3, examines the potential for identifying COD with UAV imagery using the example of Speculation Wood. RGB, multispectral data and derived vegetation indices are assessed for their explanatory value in discriminating trees with COD symptoms from those without. This chapter provides fundamental knowledge on the feasibility for a UAV-based detection of oak decline.

Chapter 4, describes the application of the previously-used data collection and analysis techniques to produce a high-resolution species classification map for Monks Wood, Cambridgeshire, a highly diverse mixed deciduous woodland. The importance of multitemporal datasets, individual spectral channels and sample size is discussed.

Chapter 5 investigates the distinction and species-specific prediction of AOD symptomatic and asymptomatic trees. Binary classification models, that separate AOD affected from healthy trees are generated from multitemporal data and their performance as well as individual features are assessed. The species distribution map, generated in Chapter 4, is utilised to identify individual oak trees at the site and predict their condition with trained models.

In Chapter 6, Discussion, the potential of identifying declining oak health and to monitor oak condition with UAV remote sensing data is critically discussed. Observed opportunities of applying UAV remote sensing in the context of health assessments in natural forests are illustrated alongside identified shortcomings. General challenges in remotely assessing forest condition with UAVs are highlighted and discussed separately to limitations of the current experimental designs.

Chapter 7, Conclusion, summarises the collective outcome of the research undertaken. The utility of UAV remote sensing for the identification of oak decline is summarised on the basis of the current results and experience gained through these studies. The chapter concludes with recommendations for future work.

CHAPTER 2:

MATERIALS AND METHODS

2.1 Study sites

The research presented in this thesis focuses on two study sites, Speculation Cannop in the Forest of Dean which contains COD symptomatic trees and Monks Wood in Cambridgeshire where AOD symptoms were examined. The following section provides background context to the sites and their characteristics. Relevant information on sample trees at these sites is provided in the respective research chapters.

2.1.1 Speculation Cannop

The Forest of Dean is in the western part of the county of Gloucestershire, England, near the Welsh border. The Forest of Dean comprises 110km² of ancient woodland (Hart, 1966) and has a long history of forestry as well as formerly iron and coal mining.

In the early 1900s, Pedunculate (*Quercus robur*) and Sessile oak (*Quercus petrea*) were planted throughout the forest though failed to establish on steeper slopes and unsuitable soils. Today, the mixed woodland is comprised of deciduous and coniferous trees, with oak remaining the predominant deciduous species. Beech (*Fagus sylvatica*) and Sweet chestnut (*Castanea sativa*) are other deciduous species that have been prevalent at the Forest of Dean for centuries. Following World War I, conifers were planted excessively at the Forest of Dean. The key coniferous species today are Douglas fir (*Pseudotsuga menziesii*), Norway spruce (*Picea abies*), European larch (*Larix decidua*) and Corsican pine (*Pinus nigra*).

Situated within the Forest of Dean is Speculation Cannop, an area with a notable history of timber production, mining, quarrying and chemical manufacturing. At the site, oak was planted around the year 1812 over an area of 156 hectares. The history of forestry management of Speculation Cannop is only partially recorded. However, it is known that thinning of the stand was undertaken shortly after World War II, in the 1970s and most recently in 2010/11.

Speculation Cannop is regarded as "wet-wood" due to the seasonally waterlogged soils, which corresponds with the occurrence of Pedunculate oak. Concentrated in the southern forest compartment but situated throughout the site, drainage ditches are present, thought to be dug in the 1950s for management purposes to alleviate the challenges of seasonal inundation.

Mining at Speculation Cannop ceased production in 1883 though several shafts are present today. Additionally, numerous shallow pits can be observed and are visible in an airborne LiDAR derived terrain model (Figure 2-9). These pits are believed to relate to unregulated small scale mining operations that took place during the Depression between 1929 and 1939.

Root systems at Speculation Cannop wood might have been damaged by extensive diggings (personal communication through collaboration with PhD student Neil Matthews, Swansea University), potentially contributing to declined oak health. Symptoms of COD have been present at the site for the last decade (Gagen *et al.*, 2019). A survey by Forest Research in 2008 selected and tagged sample trees to study this disease. A total of 39 COD symptomatic and asymptomatic trees have since been monitored by the dendrochronology focus group at Swansea University (Gagen *et al.*, 2019) and research projects (Finch *et al.*, 2019) in collaboration with Forest Research and the Forestry Commission (Denman, 2019). These sampled trees are utilised for the research in this thesis, and the related study is presented in CHAPTER 3: UAV remote sensing for the identification of Chronic Oak Decline.

2.1.2 Monks Wood

Monks Wood is one of Britain's best-known lowland woods with a recorded history of over 900 years. The woodland is located 10 km northeast of Huntingdon in Cambridgeshire. In 1953 Monks Wood was established as a National Nature Reserve. Since then, the site has been managed solely to maintain and enhance its biodiversity. The 157 hectares of ancient mixed deciduous woodland are home to over 400 species of plants as well as a rich population of birds, mammals and insects including over 1000 identified beetle species.

The highest part of Monks Wood lies at 46 m above mean sea level. Higher sections of the wood are situated along the southern edge and separated from the central basin by slopes with an average angle of seven degrees. The lowest section of

Monks Wood is in the north-east with approximately 7.5 m above mean sea level elevation. Two streams run through the woodland in a south-west to north-east direction. The streams meet in the lower, north-east corner. The natural drainage system has been enhanced with artificial ditches which follow the edges of ridges (Steele and Welch, 1974).

Prior to WWI, Monks Wood was managed as coppice-with-standards. The woodland falls into the ash-oak category as specified by Tansley (1949). This woodland type is typical for calcareous soils and marked by an abundance of oak, ash and occurrence of field maple and potentially a mixture of other trees like birch, aspen, elm and shrubs such as hazel, sallow, dogwood and more. In the pre-war period, oak at the site was presumably managed as standards while ash, hazel and other shrub species were coppiced, as was the case with most ash-oak woods in southern England (Steele and Welch, 1974).

During WWI, heavy fellings were made at Monks Wood, reportedly leading to more than half of the woodland being cut (Steele and Welch, 1974). After the war, until Monks Wood was declared a National Nature Reserve, little to no systematic management took place and the woodland regenerated naturally. Today the woody vegetation of Monks Wood is heterogeneous regarding species composition, age, density and vertical structure. The dominant tree species at Monks Wood are oak, ash, elm and Field maple. Other species found in the upperstory are birch, aspen and the occasional Wild service tree and Crab apple.

Ash (*Fraxinus excelsior*) is spread throughout the whole woodland and is mainly present in the form of coppice stems. Today, a significant fraction of ash trees at the site are affected by ash dieback, a widespread disease caused by the fungus *Chalara fraxinea.* Like ash, the Field maple (*Acer campestre*) is abundant and occurs as standards and coppice stems. Its occurrence is particularly visible along the edges of the woodland. Elm (*Ulmus carpinifolia*) occurs in pure stands in the eastern section of the woodland. These patches are dominated by the dense canopy cover of the elm trees and show little undergrowth. Today the elm trees are the tallest trees at the site. Birch is present as Downy birch (*Betula pubescens*) and Silver birch (*Betula verrucosa*) and mainly occurs as solitary trees or in smaller patches. Similarly, aspen (*Populus tremula*) forms smaller patches of pure stands and is mainly present on wetter soils in the centre and eastern part. The Wild service tree (*Sorbus torminalis*) is present as individuals throughout the woodland, although its' main occurrence is in the central

belt. The Crab apple (*Malus sylvestris*) is of rare occurrence, with few individual trees visible during spring due to their white flowers. The understory and shrub layer at Monks Wood are composed of hazel (*Corylus avanella*), blackthorn (*Prunus spinosa*), dogwood (*Thelycrania sanguniea*) and willows (*Salix caprea* and *cinerea*).

Steele and Welch (1974) characterise the oak found at Monks Wood as Pedunculate oak (*Quercus robur*) hybrids. It is most likely that introgressive hybridisation has occurred between Pedunculate and introduced Sessile oak (*Quercus petrea*). Emerging hybrid forms could have crossed further with the predominant Pedunculate oak (Wigston, 1975). Older oak trees that were managed as standards are found throughout the entire woodland. Younger oaks, present mainly in the centre and east of Monks Wood, are of coppice origin dating back to the fellings undertaken in WWI. Symptoms of AOD (e.g. stem bleeding) have been identified on oaks throughout the site. To study AOD pathology and the impact of a potential loss of these trees on the ecosystem sample trees were selected and tagged by the PuRpOsE project (Mitchell *et al.*, 2019b). PuRpOsE is a multidisciplinary research project to "PRotect Oak Ecosystems" in the UK (www.forestresearch.gov.uk/research/protect-oak-ecosystems-purpose). The overall aim of the project is to gain better understanding of recent threats to oak, the consequences of declined tree health and to provide adaptation strategies for future climates. A key focus of the project is investigating the causes and dynamics of AOD. At Monks Wood, 20 sample trees, ten AOD symptomatic and ten asymptomatic, were established by the PuRpOsE project. These trees are studied in the current investigations presented in CHAPTER 5: UAV remote sensing for the identification of Acute Oak Decline and species-specific prediction of tree health.

2.2 UAS

An unmanned aerial system (UAS) comprises an unmanned aerial vehicle (UAV) and a ground station that controls the vehicle. In the case of the current studies, the ground station presents an integral part in the acquisition of remote sensing data to plan, control and monitor flights. The ground station is comprised of a transmitter to control the vehicle and a computer or tablet to plan missions and monitor in-flight telemetry data. For all survey missions for the purpose of this research project, UAVs

were flown with a direct connection to the ground station operated and attended by a pilot. Therefore, the terms UAV and UAS are used analogous throughout the thesis.

remote sensing surveys were carried out with two types of UAVs. A fixed-wing UAV (section 2.2.1.1) was used to gain coverage of the 23 ha large Monks Wood study site. Monks Wood is surrounded by agricultural fields that provided ample options for take-off and landing as well as a position to observe the aircraft and monitor the flight. Speculation Cannop does not offer sufficient space to launch and land the fixed wing aircraft safely. Therefore, multirotor UAVs (sections 2.2.1.2 and 2.2.1.3) were used to enable vertical take-off and landing. In the following section, the UAVs and their respective payloads are described.

2.2.1 UAVs

2.2.1.1 Bormatec Maja - fixed wing

The Bormatec Maja is a fixed-wing aircraft designed explicitly for the use as UAV. It is constructed from expanded polypropylene, which offers a simple yet sturdy airframe structure. The Maja is a single propeller aircraft with the motor in a push configuration at the T-tail. With its 2.2 m wingspan, flight times of one hour are possible in the current configurations. The fuselage is constructed to allow the top to fold away, giving access to the payload bay, flight controller and other electronics. To control the aircraft, a Pixhawk PX4 flight controller was used. The Pixhawk is a widely used open-source flight controller that enables fully autonomous flights with GNNS/IMU navigation and real-time telemetry. The UAV is pictured with the ground station in Figure 2-1.

The maximum payload capacity lies at around 500 g, which brings the total take-off weight to 3 kg. For the current studies, the aircraft was equipped with two separate swappable payloads. An off-the-shelf RGB camera (section 2.2.2.1) was used in conjunction with a GNSS receiver to collect high-resolution RGB imagery at high accuracy. This configuration features a total weight of 470 g. The second payload consists of a narrow band multispectral sensor (section 2.2.2.2) with a corresponding downwelling light sensor and GNSS receiver. The total weight of the multispectral payload is 170 g.

Figure 2-1 Bormatec Maja fixed-wing UAV, pictured with transmitter and laptop as ground control station.

Mapping missions with the fixed-wing UAV were initiated by hand-launching the aircraft. The remote sensing survey was performed fully autonomously based on pre-programmed flight missions. Upon completion of the mission, the aircraft was landed manually.

2.2.1.2 DJI Phantom 4 pro - quadcopter

The DJI Phantom 4 pro (P4p) is an off-the-shelf quadcopter (DJI, Shenzhen, China). The multirotor UAV is equipped with a permanently installed and gimbaled RGB sensor. With a total take-off weight of 1380 g the P4p reaches maximum flight times of 30min. The aircraft is controlled by its dedicated transmitter that connects to a mobile device, acting as the ground station. The P4p is frequently used for mapping purposes, mainly due to its one-inch 20 Mp CMOS sensor featuring a mechanical shutter, making it ideal for high quality photogrammetric surveys (Peppa *et al.*, 2019). The ease of use and minimal set-up time makes the P4p an attractive solution for

spontaneous mapping missions and surveys to produce RGB overviews (orthophotos) and canopy models.

2.2.1.3 DJI M600 pro - hexacopter

The DJI Matrice 600 pro (M600) is a hexacopter designed for professional applications like aerial cinematography and industrial purposes. The modular platform allows for variable payloads, making it highly suitable for research purposes. Its weight without payload is 10 kg, and the maximum payload capacity is 5.5 kg, totalling a maximum take-off weight of 15.5 kg.

Depending on the payload weight, the M600 has a maximum flight time of 20-30 mins. Similar to the P4p, the M600 is controlled with a dedicated DJI transmitter and mobile device. The big difference to the consumer market-oriented P4p is that the M600 features triple redundancy regarding GNSS and IMU units. This combined with the weight bearing capacity makes the M600 UAV particularly suited for carrying costly sensors. For the current investigations, the M600 was flown with a DJI Ronin gimbal stabilizing the multispectral sensor. A thermal sensor was also used onboard the M600 though these data did not find application in the current studies due to image quality issues.

2.2.2 Sensors

2.2.2.1 RGB

RGB camera sensors were primarily utilised for the photogrammetric generation of detailed canopy models and orthophotos with high spatial resolution. Two different sensors were used to acquire RGB images, the consumer Sony a6000 camera and the P4p UAV. The Sony a6000 camera was equipped with a 16 mm focal length lens which produces an almost equal field of view compared to the P4p, 73 ° and 74 ° horizontal field of view (HFOV), respectively. Image resolutions are similar between the sensors, 6000 x 4000 px for the Sony a6000 and 5472 x 3648 px for the P4p. These parameters mean that both sensors produce a similar GSD of around 3 cm when flown at 120 m AGL.

However, physical sensor size and the lens construction differ between the cameras, rendering the Sony a6000 advantageous regarding sharpness, sensitivity and

reproduction of micro-contrast. The Sony a6000 features an APS-C sized sensor (23.5 x 15.6 mm) while the P4p has a smaller one-inch sensor (13.2 x 8.8 mm). The 16 mm lens used for the Sony a6000 is constructed from glass elements, while the P4p is equipped with a plastic lens. Despite these qualitative differences, both sensors are perfectly suited for photogrammetric surveys and UAV mapping (Peppa *et al.*, 2019; O'Connor *et al.*, 2017; Fraser *et al.*, 2016). Both sensors were typically flown with 80 - 90 % overlap (front and side) depending on the complexity of the scene. The primary reason for the use of the Sony a6000 camera over the P4p in some scenarios was the ability to read an exact shutter signal off the flash hot-shoe. This signal was used in conjunction with a GNSS receiver to retain precise time stamps and image locations (see Direct Georeferencing (PPK)). A detailed comparison of sensor parameters is given in Table 2-1.

Table 2-1 Overview of sensor specifications and calculated airborne acquisition parameters. The table shows the three sensors used the current PhD research project. All calculated specifications are based on a flight of 120 m AGL.

		Micasense RedEdge	Sony a6000	DJI P4 pro	Sensor
		40	24	24	~ 35mm equivalent focal length
Given	Sw	4.8	23.5	13.2	= the sensor width of the camera (mm)
	Sh	3.6	15.6	8.8	= the sensor height of the camera (mm)
	FR	5.5	16	8.8	= the focal length of the camera (mm)
	H	120	120	120	= the flight height (m)
	imW	1280	6000	5472	= the image width (px)
	imH	960	4000	3648	= the image height (px)
Calculated	Dw	105	176	3.29	= width of single image footprint on the ground (m)
	DH	79	118	180	= height of single image footprint on the ground (m)
	HFOV	47	73	74	= angle of horizontal field of view (degrees)
	VFOV	36	52	53	= angle of vertical field of view (degrees)
	GSD	8.18	2.94	3.29	= Ground Sampling Distance (cm/px)

2.2.2.2 Multispectral

Multispectral imagery was collected with a MicaSense RedEdge 3 camera (Micasense Inc., Seattle, WA, USA). The narrowband multispectral sensor captures five separate bands as simultaneous snapshots. In the sensor array, each band is captured by an individual sensor with a global shutter. Each band features an image resolution of 1280

x 960 px (1.2 Mp) and is recorded in 12-bit raw format (TIFF). Imagery is captured at ~ 8 cm GSD (per band) at 120 m AGL flying height (see Table 2-1). The sensor offers the wavelengths and respective bandwidths, presented in Table 2-2.

Table 2-2 Bands and respective bandwidths of the Micasense RedEdge sensor.

Band Name	Centre Wavelength (nm)	Bandwidth (nm)
BLUE	475	20
GREEN	560	20
RED	668	10
RE	717	10
NIR	840	40

The RedEdge sensor system features an external downwelling light sensor (DLS) recording solar irradiation for every frame capture during flight. As part of the DLS, which is placed on top of the UAV, an inertia measurement unit (IMU) capture the sensor angle for each image. Physical radiometric targets with diffuse properties (near Lambertian) are imaged prior to every flight for radiometric calibration (see Figure 2-2). Calibration takes place within SfM photogrammetry software by adopting calibration coefficients (Table 2-3) of the individual channels, determined in a laboratory setting. In this way, raw pixel values are converted to absolute reflectance. In-flight illumination changes are counteracted by incorporating irradiance information and sun angle data linked with the recorded aircraft orientation. Calibration coefficients, as provided by Micasense, are given in Table 2-3 and the per-band calibration is illustrated in Figure 2-2. A study assessing the radiometric performance of the RedEdge sensor has found a strong correlation between remote sensing-acquired reflectance and in-field spectrometry (Cao *et al.*, 2019).

Table 2-3 Calibration coefficients of the Micasense calibration panel. The average reflectance for the panel is determined in the laboratory and applied per band to convert raw pixel values to reflectance.

Band Name	Average	Min	Max
BLUE	0.64	0.633	0.638
GREEN	0.64	0.637	0.641
RED	0.64	0.633	0.638
RE	0.63	0.629	0.631
NIR	0.59	0.576	0.603

| BLUE | GREEN | RED | RE | Near IR |
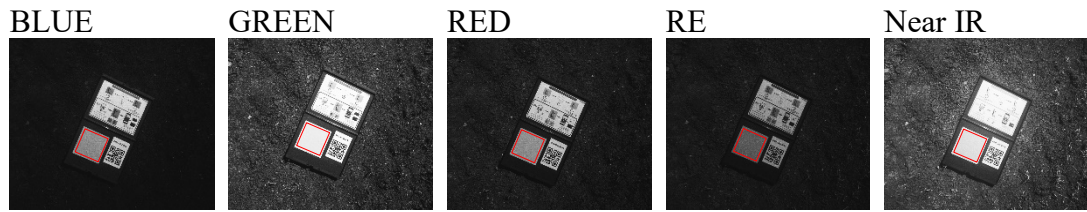
Figure 2-2 Radiometric calibration targets that were imaged prior to multispectral UAV flights. The diffuse (near Lambertian) area is selected in SfM photogrammetry software to provide the coefficients for the calibration.

2.2.3 Direct georeferencing (PPK)

Unlike traditional photogrammetry, a SfM approach requires neither known camera position orientation nor the surveyed location of ground control points as input. Triangulation and hence creation of a 3D model in SfM-photogrammetry can be undertaken by the automated identification of matching features in the imagery alone. Reconstructed scenes calculated in this way will have an arbitrary scale and orientation. To register the model to real-world coordinates however surveyed ground control points or the camera (sensor) location for every image are needed. In the case of UAVs as mapping platforms, every image is tagged with the respective geolocation based on the GNSS receiver on board. In addition to the position, the orientation of the UAV is retrieved from the inertial measurement unit built into every modern flight controller. Utilising this information in the bundle adjustment is called direct georeferencing. The theoretical advantage is that with an accurate sensor exterior orientation, surveyed ground control points (GCPs) are no longer a requirement. However, the GNSS receivers typically used for navigation on-board a UAV resolve camera position in the air to 3 m accuracy at best. While these GNSS coordinates may not be used to accurately define the sensor's location for direct georeferencing, these positional estimations may still be used as an initial "guess" as to which images are overlapping and hence tell the algorithm where to seek matching features first. To make full use of direct georeferencing however, the sensor's position and orientation during image capture needs to be determined with high accuracy. If this is achieved (e.g. positional knowledge < 10 cm), the benefits of a direct georeferencing approach in the context of forested scenes are manifold: 1) improved absolute and relative accuracy of photogrammetric products, 2) enhanced image matching in SfM photogrammetric processing and 3) shortened processing time. All the advantages

mentioned above are achieved by solving the bundle adjustment with high weight placed on pre-determined sensor positions.

Constraining the positional uncertainty of the images translates directly to an improved absolute and relative accuracy of SfM derived products. Obtaining an accurate location of reconstructed features is crucial for precise links to validation data (ground truth) and the collection and analysis of multitemporal data.

Associated with this, direct georeferencing is particularly relevant for scenes where extensive GCPs placement is unfeasible, such as forests with dense canopy cover. Interrelated, uncertainty in image matching is reduced by direct georeferencing with accurately known image locations. This is especially important for scenes of repetitive texture, as is the case in densely forested areas. A direct georeferencing approach facilitates a complete reconstruction and prevents noise under challenging scenes (Mokros and Surovy, 2019).

For the research projects within this thesis, a direct georeferencing approach was deemed very important for the successful SfM-based processing of UAV acquired imagery. The objective to collect multitemporal data at very high spatial resolution called for a complete reconstruction and correct alignment between datasets. Obtaining high absolute and relative accuracy was considered crucial for this undertaking.

Dense canopies at Speculation Cannop and at Monks Wood interfere with the placement of GCPs, and photogrammetric reconstruction is hampered by the repetitive texture of these forests. To circumvent the aforementioned issues, a direct georeferencing approach was applied, utilising a post-processing kinematic (PPK) method with a GNSS receiver capable of recording raw data. The Emlid Reach GNSS was used in raw logging mode onboard the UAV. A precision time stamp was recorded for each shutter event of the sensor. Post-processing of the GNSS log was undertaken in conjunction with correction data by the nearest Ordnance Survey (OS) Net station providing hourly logs in ETRS89 as RINEX files. Corrected coordinates were transformed from ETRS89 latitude and longitude to OSBG36 National Grid eastings and northings using the Ordnance Survey's Transformation OSTN15. GPS ellipsoid heights were converted to the Ordnance datum Newlyn for mainland Britain using the National Geoid model OSGM15.

Using the proposed PPK approach for image locations, resulting geotags are expected to be within decimetre accuracy, in all three dimensions. However, the

accuracy of geotags obtained in flight cannot be validated directly. Thus, validation was undertaken by holding PPK-supported directly-georeferenced SfM outputs against 14 independently surveyed GCPs. This permitted an understanding of the achievable accuracy of the PPK system. The setup and results of this testing phase are described in Appendix A.

2.2.4 Autonomous mapping missions - flight planning

The critical objectives for every UAV survey are continuous coverage and maximised image quality. SfM-based photogrammetric processing requires sufficient and consistent overlap between images. Therefore, flight mission planning is essential to obtain reproducible photogrammetric results with controlled quality. During flight planning, the specific survey targets are determined and implemented while incorporating hardware limitations like UAV flying speed and minimum trigger intervals of the sensor. Consequently, in the current studies all UAV mapping missions were planned and performed autonomously to guarantee that survey quality objectives were met.

Specialised software was used to plan, program and execute the flights. In the case of the fixed-wing UAV, the open-source software Mission Planner was used to program the Pixhawk flight controller. Mission Planner offers a PC-based user interface for mission planning and execution. This allowed requirements specific to fixed-wing aircraft and the use of different sensors in the aerial surveys undertaken to be met. One such requirement is the increased turning radius of fixed-wing aircrafts compared to multicopters. The ability to adapt virtually any flight characteristic and aircraft parameters made this software solution ideal for the fixed-wing mapping missions performed for the current studies.

As the multirotor UAVs utilised in this research do not accommodate open-source flight controllers, the software Ground Control Station (UgCS) was used to perform mission planning for the DJI aircraft. UgCS is a sophisticated UAV mission planner that enables the implementation of complex survey missions for the multirotor UAVs, allowing custom payloads. The ability to incorporate topography (terrain following), thus remaining a constant height AGL, particularly at the Speculation Cannop site, was crucial to the success of the missions.

An example of mission planning for the study site at Monks Wood, covering an area of 23 ha in a single survey, is given in Figure 2-3. The mission was planned for the Bormatec Maja fixed-wing UAV with the Micasense RedEdge payload. The camera's intrinsic parameters were entered in Mission Planner to allow for the correct calculation of flight lines and sensor trigger intervals based on a given overlap. Due to the dense vegetation at the scene, a forward overlap of 85 % and a side overlap of 85 % were chosen. A flying height of 120 m AGL, thus at the legal limit, was selected to counter the somewhat narrow field of view (47 ° HFOV) of the sensor, simultaneously minimizing flight time. As a safety precaution, flight lines were oriented so that the first flight line was parallel to the road, thereby increasing the distance from the road with every consecutive flight line. In the given scenario slight wind was expected with westerly direction. To allow the aircraft to make a complete 180 ° turn, correctly aligning with the following flight line before entering the survey area again, overshoot was set to 80 m and lead-in was 150 m. Programmed flight lines and corresponding waypoints are presented in Figure 2-3. The flight controller was programmed with a flying speed of 12 m/s.

Figure 2-3 Example UAV mission planned for the Monks Wood study site. The study site boundary is illustrated in red, flight lines in yellow and waypoints are shown in green.

With these parameters a total flight time of 37 minutes was calculated, covering the area in 28 flight lines, 17.8 m apart from each other. At intervals of 18 m the sensor is triggered, capturing images with an estimated footprint of 104.7 x 78.5 m (less due to canopy height) and 8.18 cm GSD. Within the survey area, a photo was taken every 1.05 seconds resulting in 1081 images captured. The minimum shutter speed to avoid motion blur > 1 pixel is estimated as $1/300^{th}$ of a second. However, the actual sensor-to-scene distance differs from the flying height AGL due to the canopy height, decreasing the GSD and conversely increasing the potential for motion blur. To counteract this effect a minimum shutter speed of $1/500^{th}$ of a second was chosen for the sensor. Relevant mission parameters for the exemplified case are summarised in Table 2-4.

Table 2-4 UAV mission parameters for an example mission at the Monks Wood study site with the Micasense RedEdge sensor payload. At a flying altitude of 120 m above ground level (AGL) the ground sampling distance (GSD) of collected images is estimated at 8.18 cm.

Given	Area	23 ha
	Overlap	85/85 %
	Height AGL	120 m
	Overshoot	80 m
	Lead In	150 m
	Distance	21.31 km
	Speed	12 m/s
Calculated	Flight Time	36:59 min
	Distance between lines	17.8 m
	No of Strips	28
	Distance between images	13 m
	Pictures	1081
	GSD	8.18 cm
	Footprint	104.7 x 78.5 m
	Photo every	1.05 s
	Min Shutter Speed	1/300 s

2.3 Photogrammetric processing

All UAV acquired images were photogrammetrically processed in a SfM-MVS pipeline as described in the Introduction. During remote sensing data acquisition flight campaigns for the current studies were undertaken between the years 2016 and 2019. During this time advances in SfM software were made which led to the use of two different commercial products throughout the investigations. Pix4D Mapper (Pix4D SA, Lausanne, Switzerland) and Agisoft PhotoScan (AgiSoft LLC, St. Petersburg, Russia; PhotoScan was renamed Metashape in 2018) were used for SfM photogrammetry. Both desktop-based processing solutions apply proprietary algorithms in an automated and semi-automated workflow to reconstruct scenes from images. Both software packages were used with RGB and multispectral imagery. Earlier versions of Agisoft PhotoScan (versions < 1.4) did not allow the simultaneous processing of multispectral imagery bands or for a radiometric calibration procedure. For this reason, Monks Wood data, collected in 2017 and 2018 were processed with Pix4D Mapper (version 4.3.12). However, Speculation Cannop data from 2018 and 2019 were processed in Agisoft Metashape (version 1.6), allowing faster processing and better fine-tuning of parameters than Pix4D.

The typical workflow for both software solutions consisted of:

1) Initial image alignment on reduced image scale (1/2 or 1/4th) with a low key and tie point limit (e.g. 10000 key points, 5000 tie points).

2) Identification of matching errors and further potential issues.

3) Fine alignment of images on full image scale incorporating identified issues for parameter refinement. In some cases, a lower than full image scale was used to support matching in areas of repetitive texture.

4) Densification of the sparse point cloud generated in the image alignment in the case of RGB imagery. This step is skipped for multispectral imagery.

5) Generation of a DSM by interpolating the sparse (multispectral) or dense (RGB) point cloud.

6) Generation of an orthophoto from the original imagery integrating the previously derived surface information.

7) Accuracy assessment based on reference information and visual quality inspection.

For RGB imagery, the final products generated in the SfM-photogrammetry software are a dense point cloud ($\sim$ 500 pts/m²), a high-resolution DSM ($\sim$ 5 cm resolution) and an orthophoto ($\sim$ 3 cm resolution). Intermediate products produced in the SfM-pipeline were not used for multispectral image sets. Only the radiometrically calibrated multi-band orthophotos ($\sim$ 8 cm resolution) were relevant and applied to the current investigations.

2.4 Post-processing

2.4.1 Hybrid SfM/ALS canopy height models

In each research chapter of the thesis, Canopy Height Models (CHMs) were used, calculated as the difference between ground elevation and maximum canopy height throughout the scene. CHMs were mainly applied for the automated detection of trees by individual tree crown (ITC) algorithms. These algorithms generally require normalised canopy height as input information. However, particularly for dense vegetation, UAV acquired photogrammetric products solely describe the outer canopy surface since SfM is based on photographic images and does not penetrate vegetation. Therefore, the CHMs used for these studies were derived from a hybrid form of SfM and airborne laser scanning (ALS) point clouds. In this approach the ALS data provide the required topographic information while the canopy surface is represented by the SfM-derived point cloud.

The hybrid approach was adopted (rather than using the LiDAR data exclusively to create the CHM) to avoid potential discrepancies resulting from canopy changes between the date of ALS acquisition and the UAV flights. The CHM therefore represents the current state of the canopy at the time of this study.

Additionally, due to the much higher point density of the SfM point cloud the canopy surface is depicted in greater detail than is typically possible with ALS data.

To generate the hybrid CHMs, SfM data were combined with formerly acquired ALS data which are freely available and were captured by the Environment Agency in 2012 (publicly available from Defra's Data Services Platform: environment.data.gov.uk). A good alignment between SfM and ALS data is essential

and this requirement is best fulfilled by high global accuracies of both data sources. In the case of the UAV surveys, the demand of high absolute accuracy is facilitated by the PPK direct georeferencing approach and the use of GCPs described above.
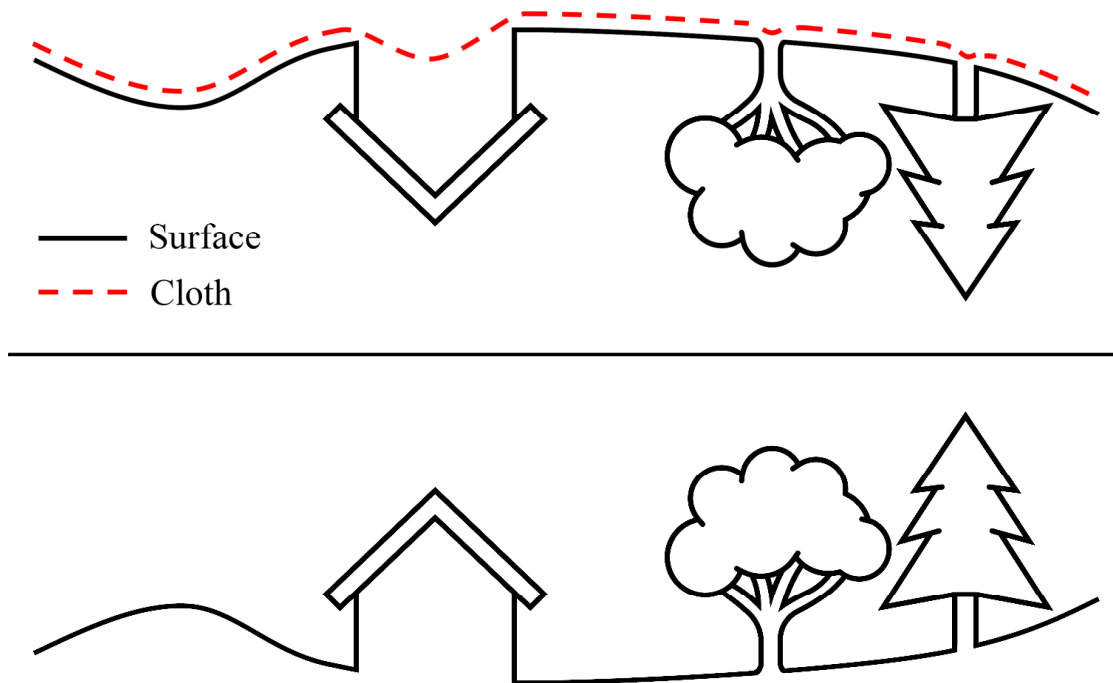
Figure 2-4 Visualisation of the basic principle behind the Cloth Simulation Filter (CSF) for identification of ground in point clouds. Cloth rigidity can be adjusted. Ground points are selected based on the distance threshold to the cloth. Figure adapted from Zhang *et al.* (2016).

For the normalisation of SfM-derived canopy height, ground information was extracted from ALS data. To filter ground points the Cloth Simulation Filter (CSF) was applied which has shown high performance on ALS and SfM point clouds in non-complex terrain (Serifoglu Yilmaz, Yilmaz and Gungor, 2018; Klápště *et al.*, 2020), as is the case at both study sites. The CSF was chosen over other common ground filtering algorithms, such as progressive triangulated irregular network densification filtering, as it requires only few known parameters and computational time is low. The CSF simulates a draped cloth on the inverted (upside-down) point cloud (Zhang *et al.*, 2016; Cai *et al.*, 2019). The basic principle behind this very effective ground filtering method is illustrated in Figure 2-4. Based on a cloth rigidity factor and a distance threshold to the cloth, points are labelled as ground or non-ground. CSF parameters were optimised manually in iterations by inspecting intermediate results visually.

Ground points identified with optimised parameters were subsequently interpolated to generate a continuous ground surface. Holes in the ALS-derived ground point cloud were closed by meshing (Delaunay triangulation), and points were sampled on the resulting mesh. In this case, the sampled point density was chosen to adequately match the point density of the SfM point cloud, e.g. 5 cm point spacing. Ground points were then merged with the SfM point cloud. The resulting hybrid point cloud facilitates the normalisation of surface heights above ground level and consequently enables the derivation of a CHM. An example of a hybrid SfM/ALS point cloud and normalised canopy height is given in Figure 2-5. The subsequent generation of CHMs was implemented by the "spike-free" algorithm (Khosravipour *et al.*, 2016) available through the point cloud processing software LAStools (M. Isenburg, "LAStools - efficient LiDAR processing software", version 141017).
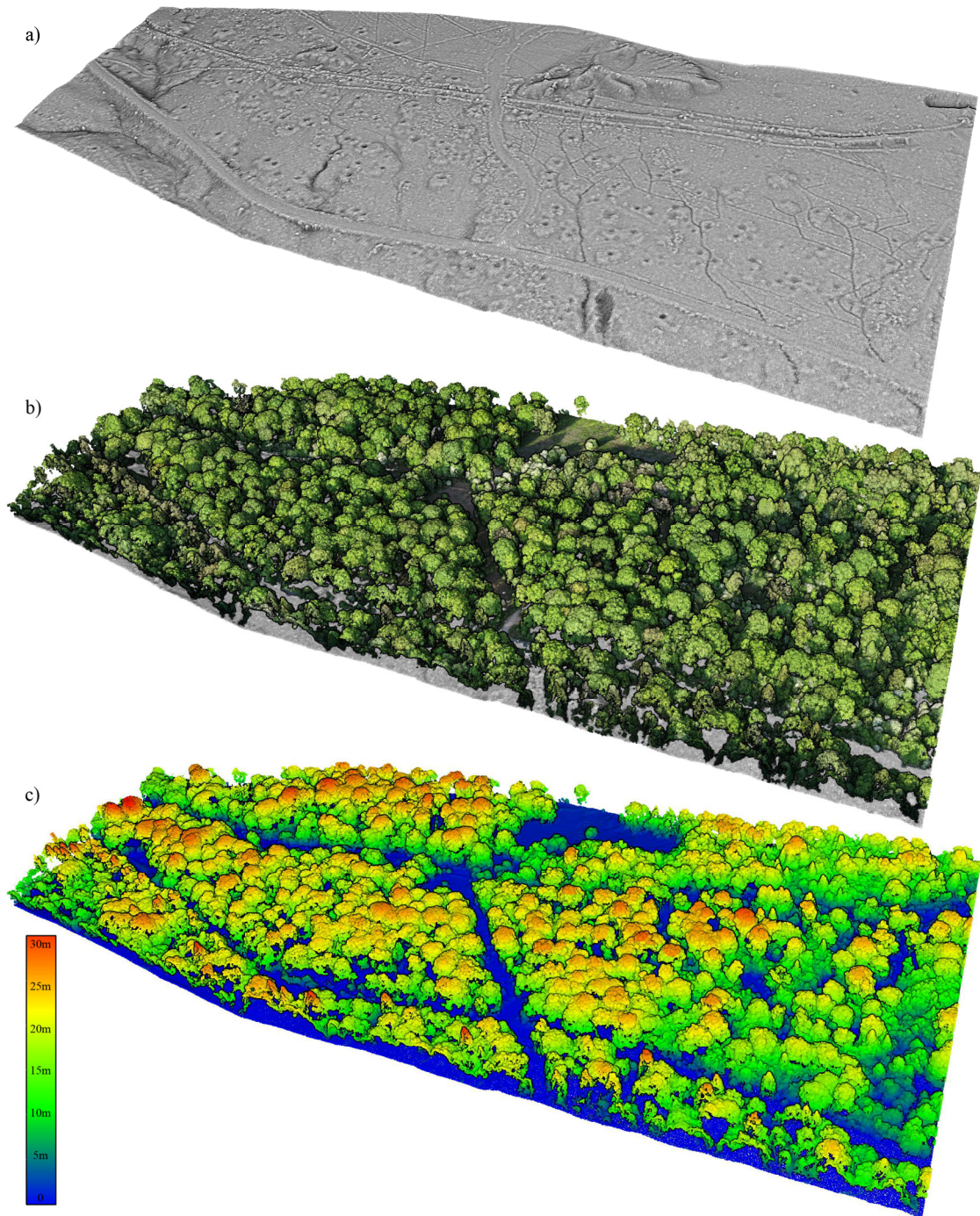
Figure 2-5 Perspective view of the of stages in the generation of hybrid SfM-ALS point clouds and the subsequent normalisation of canopy height. a) ALS extracted ground information generated by the CSF algorithm and interpolation, b) RGB coloured SfM point cloud merged with ALS ground points and c) merged SfM-ALS data with normalised height as colour scale. Data presented were acquired for CHAPTER 3, at Speculation Cannop, Forest of Dean. The area illustrated in the oblique 3D rendering spans approximately 750 m x 350 m.

2.4.2 Derivation of vegetation indices

Following the photogrammetric reconstruction and generation of orthophotos, vegetation indices were derived from the UAV data. Vegetation indices have been successfully applied in evaluations of vegetation presence, condition and change and have a long history in forest remote sensing (Myneni *et al.*, 1995; Jackson and Huete, 1991). They exploit the sensitivity of different parts of the electromagnetic spectrum to biophysical attributes, allowing indices to be derived which can act as a proxy for these. Resulting indices often combine visible light radiation and non-visible spectra and can be used for the quantitative and qualitative assessments of vegetation.

A further justification for the use of vegetation indices is the reduced sensitivity to radiometric calibration accuracy. Most vegetation indices are based on normalised band ratios. Inaccuracies or inconsistencies in the calibration, converting from radiance to raw reflectance values, were eliminated by using normalised ratio-based vegetation indices. This also facilitated direct comparison of data acquired within a single survey and over time. The reduced impact of calibration procedures on data quality was particularly beneficial for UAV-based acquisition of radiometric information. Cao *et al.* (2019) presented work illustrating the variability in UAV acquired reflectance measurements over time. With their low flight altitude, UAVs are inherently more impacted by atmospheric conditions and illumination changes than piloted aircraft. The chosen vegetation indices for the current study aim to, in part, prevent differences in the acquired multitemporal data that can be attributed to calibration issues. However, the vegetation indices used here were primarily determined by available input bands, from the UAV sensor and their potential for forest health assessment.

For the investigations presented in this thesis, vegetation indices were chosen by querying the Index DataBase (www.indexdatabase.de, Henrich *et al.*, 2009) based on three criteria: 1) the required wavelengths match the bands of the UAV sensor, 2) the index is classified as sensitive to vegetation vitality, stress or water stress, and 3) the index is not specific to satellite remote sensing data, thus does not feature weather correction components. The vegetation indices selected for the assessment of oak decline in this research all relate to indicators that are relevant to tree condition and showed successful application in other plant health studies (Brovkina *et al.*, 2018;

Easterday *et al.*, 2019; Bannari *et al.*, 1995). An overview of vegetation indices utilised in the current investigations is given in Table 2-5.

2.4.2.1 Multispectral vegetation indices

Multispectral vegetation indices used in this research were derived from orthophotos acquired with the Micasense RedEdge sensor and based on the multispectral data make use of the RED, GREEN, RE and NIR bands.

- Normalised Difference Vegetation Index (NDVI)

   The NDVI is perhaps the most prominent vegetation index. First mentioned by Rouse *et al.* in 1973, the index is well known by the remote sensing community today and widely used for estimating vegetation abundance and photosynthetic capacity of plants. The index enhances the contrast of reflectance in the RED and NIR channels. Chlorophyll in healthy plant matter strongly absorbs solar radiation in the visible spectrum. In contrast, NIR light is strongly reflected by the cell structure of vegetation to prevent overheating. Unlike visible radiation, a portion of NIR light is transmitted though foliage and reflected by lower parts of the canopy, thus revealing information about vegetation density. By utilising the ratio between these absorbed (RED) and reflected (NIR) spectra, the presence of photosynthetically active plant matter can be estimated. As a proxy for photosynthetic activity NDVI consequently carries information related to physiological stress. Less light is reflected in the NIR range if vegetation is stressed or dead, resulting in a lower NDVI value. It is for this reason and its established use in vegetation science (Bannari *et al.*, 1995) that NDVI was included in the analysis of oak decline.

- Normalized Difference Red Edge Index (NDRE)

   The NDRE is an alteration of the NDVI that utilises the RE band, a narrow spectrum at the edge of the chlorophyll absorption feature. Leaf-level investigations have shown a better response to chlorophyll content (Gamon and Surfus, 1999; Gitelson and Merzlyak, 1994) by replacing the RED band in the NDVI by the RE band. NDRE has found application with high resolution imagery (Potter *et al.*, 2012; Cundill *et al.*, 2015) and was adopted in the current studies for the UAV-captured imagery.

- Canopy Chlorophyll Content Index (CCCI)

The CCCI combines the NDVI and NDRE as ratio in a single metric. The fundamental idea behind the index lies in the utilisation of the NDRE as an indicator for stress, however normalising by vegetation quantity estimated by the NDVI (Barnes *et al.*, 2000). In theory, the index therefore provides a better measure of vegetation stress in scenarios with varied vegetation density than NDVI or NDRE alone and was thus included in the investigations presented here.

- Chlorophyll Vegetation Index (CVI)

The CVI was proposed by Vincini *et al.*, 2007 as an indicator for leaf-level chlorophyll concentration estimated from broadband multispectral imagery (e.g. QuickBird) at the canopy scale. The index is a development of the "Green Simple Ratio" (NIR/GREEN) where the GREEN band is included as an estimator for pigment content. The CVI is expanded by the introduction of a RED/GREEN band ratio originally intended to reduce the influence of variable leaf quantities in open canopies, through normalising by vegetation density (Vincini *et al.*, 2008). However, the index has shown to be sensitive to chlorophyll content in closed canopies also.

- Anthocyanin Reflectance Index (ARI)

Anthocyanins are pigments that are present in very young as well as in senescing leaves(Gitelson and Merzlyak, 1994). Stressed vegetation can also exhibit increased anthocyanin concentration (Murakami *et al.*, 2008; Gitelson, Chivkunova and Merzlyak, 2009; Gitelson *et al.*, 2001; Chalker-Scott, 1999). The GREEN band, thus spectra around 550nm are most sensitive to anthocyanin content. However, these spectra are also highly sensitive to chlorophyll. To isolate and quantify the anthocyanin content, the RE band, that is insensitive to anthocyanins but responds to chlorophyll, is subtracted. The ARI was included in the present studies as a multispectral vegetation index that may indicate vegetation under stress but is not aimed at chlorophyll content quantification. Furthermore, with respect to imagery acquired in autumn, ARI was assessed to determine whether it provides an indication of early and/or accelerated senescence in stressed trees.

2.4.2.2 RGB vegetation indices

In addition to the vegetation indices based on narrowband multispectral imagery, several common vegetation indices were derived from broadband RGB imagery. The broad bandwidth and overlapping of bands compound the information on physical plant properties: chlorophyll content, pigment content and canopy architecture. Despite the lack of calibration and the expected aforementioned combining of vegetation characteristics, RGB vegetation indices can potentially enhance within-site variability in the visible domain and were thus evaluated with particular regard to the applicability of lower-cost commercial RGB sensors for vegetation stress detection.

- Visible Atmospheric Resistant Index (VARI)

  The VARI was initially developed to quantify vegetation fraction in space borne remote sensing imagery, reducing atmospheric effects and varied illumination (Gitelson *et al.*, 2002). However, today VARI is also used with UAV imagery and is offered in several UAV software platforms to emphasise greenness and to provide a relative view of vegetation condition (Anon, n.d.). VARI was included in the current investigations to evaluate its explanatory power in a forest health context.

- Triangular Greenness Index (TGI)

  The TGI correlates with chlorophyll content and is designed to work with broad- and narrowband RGB data (Hunt *et al.*, 2011). It is sensitive to chlorophyll content at leaf and at the canopy scale (Hunt *et al.*, 2012). Its application with broadband RGB information was tested for sensing physiological status with regard to declining oak trees.

- Green Leaf Index (GLI)

  The GLI is specifically designed to work with broadband RGB sensors (Gobron *et al.*, 2000). Its original intended use was to determine crop cover (Louhaichi *et al.*, 2001), though it has also found use in other vegetation study scenarios (Hunt *et al.*, 2011).

- Normalized Green Red Difference Index (NGRDI)

  The NGRDI utilises the GREEN band in place of the NIR band in the NDVI. This index was proposed by Tucker in 1979 to estimate biomass, leaf water content and chlorophyll content. It showed lower significance in estimating these properties than RED and NIR combinations (Tucker, 1979). However, it

is still included in the current study to assess its performance compared with other RGB vegetation indices.

- Coloration Index (CI)

  The CI has also found use with UAV imagery (Anon, n.d.). It is the only RGB vegetation index that solely uses the BLUE and RED band in the expression and was added to the analysis for comparison against other RGB vegetation indices.

Table 2-5 Overview of vegetation indices adopted in the current studies. Indices were selected from the Index DataBase (www.indexdatabase.de, Henrich *et al.*, 2009) *based on their proven application in vegetation research and available channels from the RGB sensor (DJI Phantom 4 pro) and multispectral sensor (Micasense RedEdge).*

	Vegetation Index	**Formula**	**Reference**
RGB-based vegetation indices	Visible Atmospheric Resistant Index	$VARI = \dfrac{GREEN - RED}{GREEN + RED - BLUE}$	(Gitelson *et al.*, 2002)
	Triangular Greenness Index	$TGI = GREEN - 0.39 * RED - 0.61 * BLUE$	(Hunt *et al.*, 2011)
	Green Leaf Index	$GLI = \dfrac{2 * GREEN - RED - BLUE}{2 * GREEN + RED + BLUE}$	(Gobron *et al.*, 2000)
	Normalized Green Red Difference Index	$NGRDI = \dfrac{GREEN - RED}{GREEN + RED}$	(Tucker, 1979)
	Coloration Index	$CI = \dfrac{RED - BLUE}{RED}$	(Escadafal *et al.*, 1994)
Multispectral-based vegetation indices	Normalized Difference Vegetation Index	$NDVI = \dfrac{NIR - RED}{NIR + RED}$	(Rouse *et al.*, 1973)
	Normalized Difference Red Edge Index	$NDRE = \dfrac{NIR - REDEDGE}{NIR + REDEDGE}$	(Barnes *et al.*, 2000)
	Canopy Chlorophyll Content Index	$CCCI = \dfrac{\frac{NIR - REDEDGE}{NIR + REDEDGE}}{\frac{NIR - RED}{NIR + RED}}$	(Barnes *et al.*, 2000)
	Chlorophyll Vegetation Index	$CVI = NIR\dfrac{RED}{GREEN^2}$	(Vincini *et al.*, 2008)
	Anthocyanin Reflectance Index	$ARI = \dfrac{1}{GREEN} - \dfrac{1}{REDEDGE}$	(Gitelson *et al.*, 2001)

2.5 Analysis

Standard exploratory statistics were deployed throughout all research chapters. Random Forest with cross validation was predominantly implemented to gain a deeper understanding of the data generated within these studies.

2.5.1 Random Forest

Random Forest (RF) is a non-parametric ensemble method that uses decision trees (Breiman, 2001). Decision trees predict a target value based on a series of binary decision rules learned from the input information. The decision tree algorithm learns decisions based on a defined set of criteria. The procedure begins with an evaluation of the dataset, followed by the identification of the most suitable feature to partition the data into two subsets, with the objective of attaining subsets that possess a high level of purity. For each subset this process is repeated recursively until a stopping criterion is met. The current research employs the Gini impurity technique as the criterion for splitting (Breiman *et al.*, 1984). The stopping criterion can be based on the minimum improvement in Gini impurity, the maximum tree depth, the maximum number of leaf nodes or the minimum number of samples per leaf. These criteria can be used to control the growth of the tree, thus regulating the complexity of the tree to prevent overfitting.

RF further reduces the risk of overfitting by training a series of decision trees on sub-samples of the input data deriving the final decision from the "forest" of decision trees. Training data are split into small subsets (often randomly drawn with replacement), known as bootstrap samples. For each bootstrap sample, a new decision tree is separately trained. All decision trees together form the RF ensemble. The final solution to the classification problem is determined by a majority vote from all decision trees, a process referred to as Bagging or Bootstrap Aggregation. This method improves the robustness of the final decision, by reducing the impact of variability in the input data (e.g. noise).

Parameters influencing the performance of the RF can be adjusted to fit the data and/or purpose of the prediction. Key parameters, also called hyperparameters, that were adjusted in the current study are: 1) the number of decision trees in the forest, 2) the maximum depth in each decision tree, 3) the minimum number of data points required for a node split and 4) whether bootstrapping is performed or instead features

are randomly selected to build a decision tree. In some cases, the ability to fine-tune these parameters can be a great advantage, e.g. if the sample size is small or the feature set is large (Bogner *et al.*, 2018). However, in most cases RF requires little parameter tuning and works well on a large range of data and feature sets. In remote sensing this reliability has made RF a suitable classifier for a great range of applications (Pal, 2005; Belgiu and Drăgu, 2016).

Another benefit of RF is that features can be ranked based on their ability to discriminate between target classes, also known as feature importance. By disregarding features of low importance, model robustness can be further improved while processing time is reduced. In the case of the current investigations, feature importance was also used to determine the general relevance of specific features in the prediction/detection of studied diseases.

2.5.2 Cross validation

Cross validation (CV) was used as a technique to assess and validate the accuracy, and thus the explanatory power of RF models in the current studies. Generally, validation techniques are applied to gain an understanding of how well a model would perform on an independent dataset. This is typically achieved by splitting the input data into a subset for training the model and a testing subset, against which the model is tested. However, the sample sizes were relatively small in the current investigations and a split into training and testing subsets would have further reduced the data available for training. With a decreasing number of samples used in training the effect of outliers increases, potentially incorporating bias in the model. Another risk is that the randomly chosen training data predicts the chosen test data well. In any other constellation of train/test samples, however, the model would not perform well. To prevent these issues k-fold CV was applied. In the basic procedure of k-fold CV the entire dataset is split into k subsets of equal size. A model is then trained on a k-1 fraction of the data and tested on the remainder. This process is repeated iteratively until each of the k folds was used as a test dataset. Thus, a k number of models is trained and validated. The overall performance of the model is then expressed as the average of the scores across the entire loop. K-fold CV offers a way to utilise all available samples while providing a robust measure of model performance. Both

characteristics were particularly important for the assessment of tree samples in the presented research.

———————

This chapter has presented the study sites, data collection and analysis methods that are common throughout this thesis. Site- and context- specific methods for the investigations at the study sites are described in the three research chapters that follow.

CHAPTER 3:

ASSESSING THE POTENTIAL OF UAV REMOTE SENSING FOR

DETECTING TREES AFFECTED BY CHRONIC OAK DECLINE

3.1 Introduction

This study addresses the use of UAV remote sensing to detect COD-induced stress on mature trees in a natural woodland. UAV flights were performed at Speculation Cannop at the Forest of Dean, where symptoms of COD have been present on oak trees for the last decade (Gagen *et al.*, 2019). The research investigates whether reduced crown vigour, as a consequence of COD induced stress, can be observed in remotely sensed spectra. The main focus of this work was to determine whether the acquired UAV remote sensing data hold information to differentiate between COD and control trees, and to explain any differences detected.

Denman *et al.* (2009) describe that trees with COD may exhibit chlorotic canopies and, in advanced stages of the decline, experience defoliation and branch dieback. These changes are expected to translate directly to changes in reflectance properties, observable with remote sensing. The expected outcome is a shift in the reflection pattern of the vegetation in the visible spectrum, with a decrease in the reflection of green light and an increase in the reflection of red and blue light, as opposed to high green light reflection and low red and blue light reflection in healthy vegetation (Hunt *et al.*, 2012). A similar shift occurs in the NIR region of the electromagnetic spectrum, which is highly sensitive to chlorophyll at the leaf and canopy level (Allen and Richardson, 1968; Sellers *et al.*, 1992). Leaves that have decreased photosynthetic capacity tend to absorb more NIR light (Croft *et al.*, 2016). Additionally, when there is an increase in presence of non-photosynthetically active material in the crown due to defoliation and dieback, it is anticipated that the NIR reflectance will decrease overall.

The connections between vegetation characteristics and remotely sensed data led to an initial inquiry on the practicality of utilising UAVs as a detection method for oak decline, specifically COD. Should a distinction of affected trees from healthy trees be possible with UAV remote sensing data, this would provide a baseline upon which to build further research. An example of potential advanced application of work in this

field would be the prediction of tree health status to enable the detection of declining oak to be upscaled, aiming to ultimately inform forest management. It is thus important to understand the relationship between remote sensing-derived metrics and decline symptoms that are observable from the ground.

To explore the information content of remote sensing-derived metrics regarding oak health, raw spectral channels and derived vegetation indices from four UAV flights, two with an RGB sensor and two with a multispectral sensor, were analysed. Particular focus was given to the spectral channels and vegetation indices which are sensitive to reduced foliage, photosynthetic capacity and water content. The explanatory value of these data was quantified in the binary classification case of symptomatic versus asymptomatic trees. Given that a significant difference between the two groups can be detected in the remote sensing data, it was further explored where the link between remote sensing data and tree health status is the strongest: namely, the importance of individual raw spectral channels and vegetation indices and their potential relation to COD symptoms observable from the ground.

In addition to the assessment of individual remote sensing-derived variables in the detection of declined health, the role of data distribution was assessed. UAV imagery provides hundreds of data points (pixels) per tree crown, therefore this study investigates whether declined oak health is expressed in the spectral means of tree crowns (i.e. less chlorophyll or change of pigmentation of the crown overall) or whether spectral outliers in the remote sensing data characterise COD-affected trees (i.e. dead branches or extreme changes in parts of the crown). Per-tree data distribution was therefore considered in the analysis.

The research additionally explored questions directed at wider adoption and accessibility for a UAV-based approach of COD detection including whether remote sensing data in the non-visible spectrum are a requirement for the identification of COD-stressed trees.

Field surveys for COD are typically carried out by visual inspection of crown condition. The study therefore examined whether remote sensing data from a consumer-grade RGB UAV sensor would suffice for the identification of reduced crown health, potentially providing a more accessible alternative to multispectral image acquisitions. To determine this, and despite the overlapping and broad-band characteristics, RGB imagery was included in the analysis to quantify the theoretical

disadvantage compared to a multispectral sensor and assess whether lower-cost RGB sensors can still provide sufficient information content for oak health assessments.

Furthermore, a multispectral flight undertaken with changing illumination was also included to evaluate its value for monitoring of forest condition in a realistic scenario, where optimal conditions for remote sensing data collection are not always guaranteed.

Lastly, practical implications, such as model transferability and sensor calibration, were examined. From an operational perspective, a remote sensing approach is of great interest if stress-detection models can be used to extrapolate, applied to the same site at a later stage for continuous monitoring or applied on a different site for tree health mapping. Thus, the potential for such an undertaking was assessed and considered with regard to feasibility in real-world applications.

3.2 Methods

3.2.1 Study site

Speculation Cannop is located in the Forest of Dean, in the western part of the county of Gloucestershire, England. The site and its' history are described in further detail in CHAPTER 2. The section of Speculation Cannop chosen as the study site is dominated by over 200-year-old oak trees. Other tree and shrub species are present, however mainly as individuals or as a shrub layer, predominantly along the edges of the woodland. Oaks at Speculation Cannop have been known to exhibit symptoms of COD for the last decade (Gagen *et al.*, 2019). The condition of oaks at the site has been assessed by the dendrochronology focus group at Swansea University (Gagen *et al.*, 2019) and research projects (Finch *et al.*, 2019) in collaboration with Forest Research and the Forestry Commission (Denman, 2019).

3.2.2 Field data

Field data were provided through a collaboration with the dendrochronology team at Swansea University. The sample trees used in the current study are and have been subject to several research projects investigating COD and its underlying causes. Initially, oak trees at Speculation Cannop were tagged and selected for coring by

Forest Research staff in 2008. Core samples were collected between 2009 and 2016 from a total of 39 trees (Gagen *et al.*, 2019). During field observations in 2009/2010, and 2016 these trees were assessed for external COD symptoms and classified as either symptomatic or control. This assessment predominantly relies on visual crown inspections, as COD-induced stress often shows in the crown first.

A conglomeration of three methods was used to assess crown condition: 1) estimation of crown loss based on photographs in the Forestry Commission Field book 12: Assessment of Tree Condition (Denman and Webber, 2009), 2) the diagnostic method ARCHI (Architecture) developed by the IDF (Institut pour le Développement Forestier, France) and 3) a crown morphology assessment taken from the Hessian Forest Research Institute, Germany. The Forestry Commission's method for defoliation estimation is carried out in summer while the ARCHI and the Hessian method are winter assessments.

A further assessment of COD status took place in 2017 when the location of trees was surveyed by Nathan Brown as part of Defra's Future Proofing Plant Health (FPPH) project. This dataset, providing tree locations along with the binary COD class, formed the basis for the current remote sensing study at Speculation Cannop presented in this chapter. 18 of these trees and their classification regarding COD symptoms were used in research on decline severity (Finch *et al.*, 2019). They recorded phenotypic descriptors including stem bleeds and cracks, insect defoliation and exit holes and fungal fruiting bodies, resulting in a Phenotypic Decline Index (PDI) value being allocated. The PDI value is mainly influenced by crown size and condition, and in the case of the 18 trees studied, (Finch *et al.*, 2021) their results confirm the binary COD status adopted for this study.

From the total of 39 tagged sample trees, 31 trees were selected as suitable for remote sensing-based examination of COD status. At the time of the study, the remaining tagged trees were either standing dead, fallen or their crown was not visible in the imagery and thus excluded. Ten sample trees used in this study show signs of COD (symptomatic), and 21 trees are considered healthy control trees (asymptomatic). For the analysis, a clear ID was assigned to every tree, as previous studies had used identical numbers for some trees from the symptomatic and asymptomatic classes (e.g. tree ID 45). This was achieved by adding a digit in front of the original tree ID: 1 for symptomatic trees and 2 for asymptomatic trees, allowing for a simple separation of the two classes (e.g. < 200 for symptomatic). An overview of the sample tree data

provided by previous studies, the respective COD classification and the tree ID system are given in Table 3-1.

The locations of sample trees were recorded in 2017 with handheld GNSS receivers (Garmin, Trimble) with varying levels of accuracy (~ 1 - 15 m). This geolocation uncertainty is not sufficient for the purposes of this current study. Therefore, to ensure a good fit between field-based observations and remote sensing data required for this PhD research, the central crown locations of the sample trees were re-surveyed in May 2019. A mobile mapping approach, utilizing a previously acquired UAV RGB orthomosaic (05/05/2019), was used in conjunction with a recorded and post-processed GNSS track (PPK with 2 min observation time at the stem of a sample tree, < 10 cm accuracy). Tree centres were then manually digitised on-site using the previously acquired information. In this way all 31 trees were mapped with high certainty of their location – precisely aligning with the UAV imagery (Figure 3-1).

Table 3-1 List of tree samples as assessed by research groups involved at Speculation Cannop. Data for the current study were provided by the Dendrochronology team at Swansea University, specifically Prof. Mary Gagen, Neil Matthews. Further tree observations were provided by Nathan Brown (Department of Computational and Systems Biology, Rothamsted Research, Harpenden AL5 2JQ) and Jasen Finch (Department of Biological, Environmental and Rural Sciences, Aberystwyth University, Ceredigion, SY23 3FL) as part of Sandra Denman's task force on oak declines (Centre for Forestry and Climate Change, Forest Research, Alice Holt Lodge, Farnham GU 4LH, UK).

Dendrochronology Swansea				Nathan Brown 2017		Jasen Finch 2018			Jakob Iglhaut 2019	
ID	class	2009/2010	2016	ID	FPPHtype	ID	class	PDI	ID	class
		crown condition								
SC2M	COD	4	5	2	COD	2	Symptomatic	0.876545	12	symp
SC12M	Control	1	3	12	COD	12	Symptomatic	0.776833	112	symp
SC21M	COD	2	5	21	COD	21	Symptomatic	0.91287	121	symp
SC24M	COD	2	3	24	DendroOnly_COD				124	symp
SC30M	COD	2	3	30	COD	30	Symptomatic	0.810003	130	symp
SC37M	COD	-	3	37	DendroOnly_COD				137	symp
SC39M	COD	-	3	39	COD	39	Symptomatic	0.937514	139	symp
SC44M	COD	-	3	44	COD	44	Symptomatic	0.904023	144	symp
SC45D	COD	-	2	45	COD	45	Symptomatic	0.550919	145	symp
SC47D	COD	-	2	47	COD	47	Symptomatic	0.732294	147	symp
SC11M	Control	1	1	11	Healthy	11	Non-symptomatic	0.130888	211	asymp
SC14M	Control	1	1	14	Healthy	14	Non-symptomatic	0.272105	214	asymp
SC18M	Control	2	3	18	DendroOnly_H				218	asymp
SC20M	Control	2	2	20	Healthy	20	Non-symptomatic	0.425076	220	asymp
SC26M	Control	1	2	26	Healthy	26	Non-symptomatic	0.231132	226	asymp
SC28M	Control	1	1	28	Healthy	28	Non-symptomatic	0.230442	228	asymp
SC29M	Control	1	1	29	Healthy	29	Non-symptomatic	0.166426	229	asymp
SC31M	Control	1	1	31	Healthy	31	Non-symptomatic	0.416824	231	asymp
SC35	Control	-	1	35	DendroOnly_H				235	asymp
SC36	Control	-	1	36	DendroOnly_H				236	asymp
SC38	Control	-	1	38	Healthy	38	Non-symptomatic	0.347936	238	asymp
SC40	Control	-	1	40	DendroOnly_H				240	asymp
SC41	Control	-	1	41	DendroOnly_H				241	asymp
SC42	Control	-	1	42	Healthy	42	Non-symptomatic	0.297829	242	asymp
SC43	Control	-	1	43	Healthy	43	Non-symptomatic	0.245506	243	asymp
SC45	Control	-	1	45swan	DendroOnly_H				245	asymp
SC47	Control	-	1	47swan	DendroOnly_H				247	asymp
SC48	Control	-	1	48	DendroOnly_H				248	asymp
SC49	Control	-	1	49	DendroOnly_H				249	asymp
SC50	Control	-	1	50	DendroOnly_H				250	asymp
SC51	Control	-	1	51	DendroOnly_H				251	asymp

Crown condition categories
1 Healthy = <10% crown loss
2 Early Decline = 11-30% loss
3 Moderate Decline = 31-55% loss
4 Advanced Decline = 56-80% loss
5 Severe Decline >80% loss
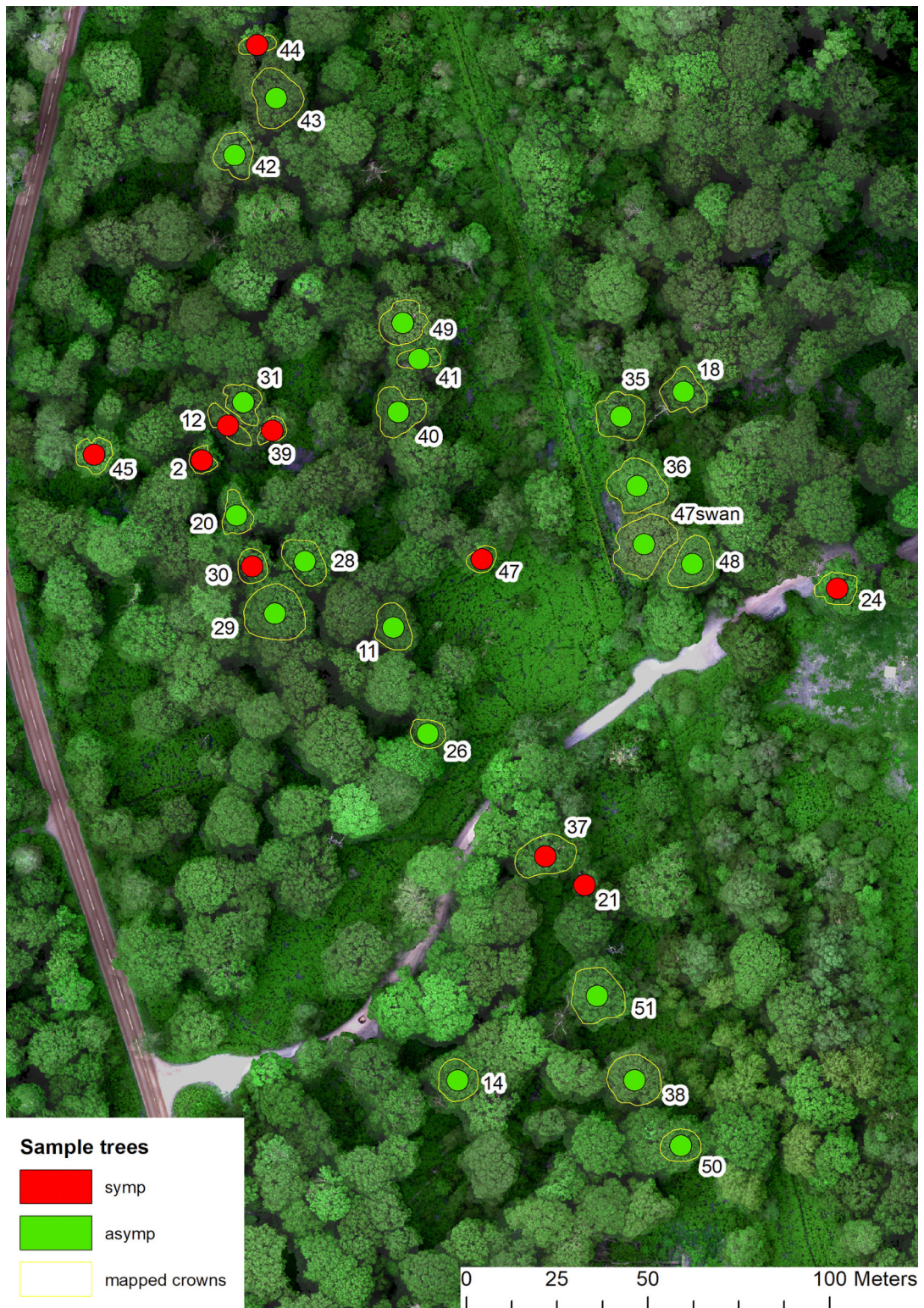
Figure 3-1 Overview of the study site and the 31 sample trees surveyed in this study. 10 COD symptomatic and 21 asymptomatic trees. The outline of the tree crowns is shown in yellow. The crown outline was mapped in the field using a mobile GIS with reference to a UAV orthophoto (~ 3 cm GSD) previously generated as part of this study. In the overview, tree labels are depicted as they are physically marked in the field. For this study, existing tree labels were adapted – symptomatic tree IDs received a 1 as the leading digit and asymptomatic trees a 2.

3.2.3 UAV remote sensing data

The UAV dataset used in this study comprises multispectral and RGB data collected in early summer and mid-summer 2019 (Table 3-2). The RGB data were initially acquired with the sole purpose of generating surface models and site overviews. However, they were later included in the analysis to test their information content regarding tree health. RGB data were captured with a DJI Phantom 4 pro quadcopter (DJI, Shenzhen, China) that features an integrated and gimbaled sensor. The UAV was flown autonomously based on a pre-programmed flight plan (mapping grid) at 120 m AGL with 85 % lateral and longitudinal overlap.

Multispectral imagery was collected with a MicaSense RedEdge 3 camera (Micasense Inc., Seattle, WA, USA). The multispectral sensor and dedicated downwelling light sensor were mounted on a DJI M600pro octocopter (DJI, Shenzhen, China). The sensor was angled in such a way that would allow a near-nadir orientation of the resulting imagery according to the pitch angle of the flight. The autonomous flight was programmed at 120 m AGL with at least 75 % overlap between images. The acquisition of multispectral imagery was undertaken near solar noon to optimize reflectance response and to minimise shadowing. Further details on UAVs, sensors and flight planning are provided in CHAPTER 2.

Table 3-2 Overview of the UAV flight campaigns at Speculation Cannop, respective weather conditions and processing parameters.

Date	Time	Sensor	Bands	Conditions	GSD	Bit-Depth	Processing
05/07/2019	13:30-13:50	MicaSense RedEdge	R,G,B,RE,NIR	mostly overcast, clouds moved in mid-flight	~ 8 cm	16-bit	Agisoft Metashape, no DLS, calibrated with 3x3m 36 % reflectance tarpaulin
09/07/2019	14:50-15:10	MicaSense RedEdge	R,G,B,RE,NIR	fully overcast	~ 8 cm	16-bit	Agisoft Metashape, with DLS, calibrated with 3x3m 36 % reflectance tarpaulin
05/05/2019	12:00-12:15	DJI Phantom 4 pro	R,G,B	fully overcast	~ 3 cm	8-bit	Agisoft Metashape
22/05/2019	19:10-19:25	DJI Phantom 4 pro	R,G,B	fully overcast	~ 3 cm	8-bit	Agisoft Metashape

3.2.4 Photogrammetric processing

The images gathered on the four dates were processed in Agisoft Photoscan (version 1.6). Point clouds, surface models and orthomosaics were generated in an SfM-based photogrammetry pipeline. The multispectral data were calibrated with a 3 x 3 m, 36 % reflectance tarpaulin (Resonon Inc., Bozeman, MT, USA). Details on the reflectance properties of the calibration tarpaulin are given in Table 3-3 and Figure 3-2. The tarpaulin was placed in the largest forest opening at sufficient distance from surrounding trees to avoid shading.

Table 3-3 Reflectance coefficients of the 3 x 3m calibration tarpaulin used for calibration of multispectral imagery at Speculation Cannop.

Band Average Reflectance (%)		
420 - 700 nm	420 - 1050 nm	900 - 1700 nm
36.1	36.0	35.2
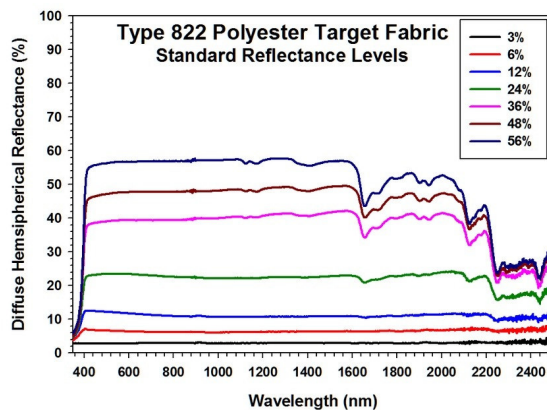
Figure 3-2 Spectral characteristics of the 3 x 3 m reflectance tarpaulin used for calibration of multispectral imagery at Speculation Cannop. The tarpaulin features an average reflectance of 36 % (pink line) and is provided by Resonon Inc., Bozeman, MT, USA.

The downwelling light sensor information was only utilised for data captured on 09/07/2019 in the reflectance calibration procedure. This is because the inclusion of downwelling light sensor information in the reflectance calibration for 05/07/2019 data caused small scale artefacts, due to changing light conditions during the flight. Therefore, downwelling light sensor information was excluded, basing the conversion from radiance to reflectance on the tarpaulin alone, resulting in an orthomosaic with visible banding only present at the edges of the site. The calibration procedure

provided in Agisoft Metashape can handle the conversion to reflectance based on the tarpaulin alone or using a combination of the tarpaulin and downwelling light sensor information. Both flights were calibrated and produced multispectral orthomosaics which store reflectance values in 16-bit format, where 100% reflectance corresponds to the centre of the value range (100% reflectance = 32768).

The high-resolution RGB imagery was captured with the intention of enabling detailed photogrammetric surface reconstruction. Due to the sensor`s broad and overlapping band characteristics, radiometric correction was not performed on these data. Orthomosaics were generated from the source images in 8-bit format. Although not captured in ideal light conditions, the RGB mosaics were included in the analysis to test their explanatory value for COD classification.

3.2.5 Post-processing

Spectral vegetation indices which are known to be sensitive to plant physiological stress were calculated. The indices were chosen based on the availability of spectral bands provided by the UAV sensors. Vegetation indices calculated from multispectral imagery are covered by a large body of research and have been successfully applied to assess vegetation presence, condition and change (Jackson and Huete, 1991; Bannari et al., 1995). A detailed description of vegetation indices can be found in the general methods chapter of this thesis (CHAPTER 2).

The NDVI is a widely used ratio, strongly correlated with photosynthetic activity, and a proven predictor of declining plant health (Tuominen et al., 2009). NDRE was included in the analysis as it is highly sensitive to chlorophyll content due to the inclusion of the REDEDGE band (Barnes et al., 2000). The CCCI is derived from the NDVI and NDRE together, thus calculated from NIR, RED and REDEDGE bands. Another chlorophyll-sensitive index, the CVI, was included to examine the benefit of utilising the GREEN band in addition to the NIR and RED band. The GREEN and REDEDGE portions of the spectrum are utilised to compute the ARI. The ARI was included in the analysis for its' response to pigments that are present in very young and senescing leaves (Gitelson et al., 2001).

The vegetation indices listed above are designed explicitly for narrowband multispectral data. In addition, vegetation indices were derived from the broadband RGB imagery. The calculated indices, VARI, TGI, GLI, NGRDI and CI all make use

of the three broadband channels of the RGB sensor to emphasise the visible characteristics of vegetation (Hunt *et al.*, 2011). These indices were included to quantify the explanatory value of RGB imagery for estimating plant health compared to costly narrowband multispectral imagery.

An overview of selected vegetation indices with their respective properties is provided in detail in CHAPTER 2. Following the calculation of chosen vegetation indices, the resulting vegetation index bands were stacked with the individual bands of the raw imagery. Every input band was resampled to ten-centimetre spatial resolution (nearest neighbour), aligned, and merged to create a multiband raster. This served as input for the generation of vegetation indices and as input for the analysis.

3.2.6 Analysis

The relationship between tree response to COD-induced stress and the remote sensing data was first explored with descriptive and inferential statistics. The data were then further analysed using a machine learning method to predict symptomatic and asymptomatic trees. The purpose of this prediction was to quantify the explanatory value of single acquisition dates and individual input variables. With this knowledge, the overall information content of the acquired remote sensing data for detecting COD-affected trees was assessed.

For the analysis, variable values were extracted from the multiband raster at the location of sample trees (ten symptomatic, 21 asymptomatic). At a three-metre radius around the manually mapped crown centre, pixel values were extracted and stored in a Pandas (version 0.24) data frame. The three-metre radius provides a sample of ~ 2900 pixels per tree from within the sunlit canopy. A smaller radius provides fewer pixels, thus less information for the class distinction. A larger radius increases the risk of including unwanted edge effects. A simple RF-model to test the separability of the two classes at radii from one metre to five metres confirms this (see Figure 3-3). With the chosen three-metre radius, variable values were extracted at a total of 91357 pixel locations for all 31 sample trees together. These data served as input for the following analysis, treating each UAV flight as an individual dataset.
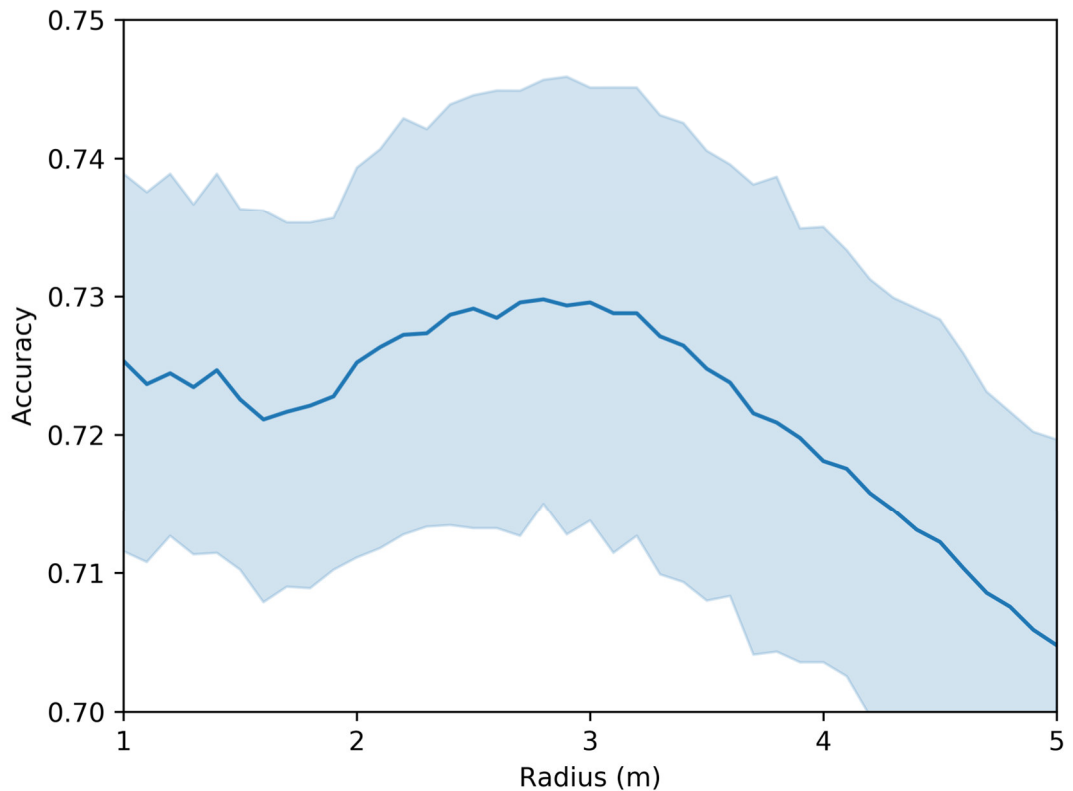
Figure 3-3 Overall classification accuracy according to plot size for a RF model based on raw band data from all four flights undertaken. Results are presented for parameters: (RF trees = 10, bootstrap iterations = 100). Accuracy was determined with 5-fold CV. Pixels were extracted around the centroid of manually mapped tree crowns. Plot radii were tested from one to five metres in ten-centimetre increments.

As a first step, the datasets were analysed in an exploratory manner. Boxplots of the individual datasets and variables within a dataset were visually assessed for differences between the symptomatic and asymptomatic groups. Subsequently, a Welch's t-test was applied to every dependent variable to assess whether a significant difference could be detected in the variable means of symptomatic and asymptomatic trees. The Welch's t-test was chosen as it can be applied to data with unequal sample sizes and variance (Ruxton, 2006). With large sample sizes, the Welch's t-test can also deal with non-normally distributed data (Delacre *et al.*, preprint), which was the case for some variables.

Additionally, t-tests were repeated with prior removal of outliers. A simple approach of removing data points which fall outside one standard deviation of the mean was chosen for outlier removal. T-test results with and without outlier removed

were compared to establish the role of spectral outliers in the distinction between symptomatic and asymptomatic trees, given that outliers hypothetically may be descriptive of canopy state (e.g. defoliation state and/or partial pigmentation by decline-induced senesce).

Having established the general ability of the remote sensing data to distinguish between the two sample groups (t-test), the following steps consisted of quantifying their significance in characterising COD-affected trees at Speculation Cannop in terms of 1) the individual datasets, 2) the features within each dataset and 3) the individual sample trees. A modelling approach based on Random Forest was chosen for these tasks. Each sample tree is represented in this modelling approach by summary statistics of pixel values extracted at three-metre radius. The arithmetic means and percentiles (at ten percent interval) of all available spectral channels and derived vegetation indices comprise the list of features incorporated in RF modelling.

As a final step in the analysis, the best performing RF model was used to predict the health status of samples trees with the remote sensing data of a second flight. This test was undertaken to assess whether the model remains valid on unseen data from a different point in time, investigating the potential for monitoring a location over time.

3.2.6.1 RF modelling

RF models were used to assess the capacity to detect stress symptoms with the remote sensing data. As a non-parametric method RF uses ensemble decision trees to predict a class (Pal, 2005; Belgiu and Drăgu, 2016; Breiman, 2001). The general method behind RF models is described in detail in CHAPTER 2 of the thesis.

In the RF modelling the raw band data and vegetation indices served as explanatory variables while the COD status of the sample trees served as response. An RF-based modelling approach is selected in this scenario because RF is comparatively less affected by small sample sizes (Cortijo and Blanca, 1999). As opposed to parametric techniques, RF demonstrates reduced sensitivity to the small sample size issue, also known as the Hughes effect (Hughes, 1968), which occurs when the number of training samples per category is less than the feature space's dimension.

Furthermore, RF models have been selected to examine the relationship between COD status and UAV remote sensing data owing to their relative insensitivity to feature

correlation (Dormann *et al.*, 2013). Combined models are used to evaluate both raw band data and vegetation indices in the analysis. Since the raw bands and vegetation indices can capture similar vegetation characteristics and vegetation indices are derived from raw band data, there is a natural correlation between these variables. Moreover, the percentiles and the mean of all variables were assessed as distinct features within a single model, which will inherently exhibit correlation among themselves.

RF models can help mitigate the impact of correlated features by combining outputs from multiple decision trees. Each tree in the forest establishes decision rules to partition the data on a randomly drawn subset of features. The final prediction is determined by aggregating the individual predictions of multiple decision trees. Specifically, each tree's prediction carries equal weight, and the class with the highest number of votes is chosen as the final prediction, in this case symptomatic or asymptomatic.

Chen and Liaw (2004) observed that RF models may exhibit a bias towards the class that has a greater number of samples. To address this issue of class imbalance, the majority class was down-sampled. Ten trees were selected from the total of 21 asymptomatic trees to match the number of symptomatic sample trees. A bootstrapping approach was adopted to enable the analysis of all 31 sample trees. This bootstrapping approach allows a) the balanced inclusion of all sample trees and b) the calculation of metrics that describe the certainty of the prediction (e.g. confidence intervals). 100 iterations were conducted where, in every run, ten symptomatic and ten asymptomatic trees were analysed. At every iteration model accuracy is assessed by performing a 50 / 50 split between training and testing data; the RF model is trained on ten trees (five symptomatic and five asymptomatic) and the prediction is tested on the remaining "unseen" ten trees.

The number of decision trees in the RF was set to 100, which has been acknowledged as offering a reasonable balance between model performance, robustness and computational efficiency across disciplines (Oshiro *et al.*, 2012). The parameter for minimum samples required at the leaf node of every tree was set to five, forcing each decision tree to establish a decision based on a single feature. Although it has been recognised that reducing the number of features in each decision tree can enhance classification accuracy (Immitzer *et al.*, 2012) in this specific case, it also enabled the documentation and evaluation of decision thresholds across features in a model.

No further hyper parameter tuning was undertaken as the RF model was primarily used as an analysis tool. The RF-based analysis was undertaken with each UAV acquisition date treated as an individual dataset. The four datasets, two RGB and two multispectral, were assessed regarding overall prediction accuracy and individual variables for their importance in the model.

The mean training accuracy across all 100 runs was assessed as an indicator for overfitting of the model, given the small sample set. The testing accuracy was employed as performance metric for explanatory value of a single dataset. The training and testing accuracies were recorded for each dataset at every bootstrap iteration. The standard deviation and confidence intervals across all iterations provide information about model robustness in the decision between symptomatic and asymptomatic trees. The dataset with the highest scoring testing accuracy, low standard deviation and small confidence interval was considered to be the best model. In evaluating the results, specific focus was given to the performance of multispectral imagery compared to RGB imagery.

Best performing datasets were assessed further regarding feature importance. Remote sensing-based predictors, thus spectral properties, that show high feature importance, are expected to be associated with tree biophysical attributes linked to stress. Feature importances were determined according to the adopted bootstrapping procedure, analysing all sample trees with balanced group samples, across 100 iterations. The importance of a feature is recorded across all runs and the mean feature importance score and standard deviation are analysed.

Representative decision trees that showcase the most significant features were illustrated. The decision thresholds were documented in all the decision trees within each of the 100 iterations. Typically, decision trees in RF models can have multiple nodes and chosen feature thresholds at these nodes do not split the input data evenly. The ensemble of decision trees replicates the process of a decision but is does not explain the original data in its structure. In this scenario however, where decision trees were forced to split the two balanced samples groups evenly, each decision tree in the random forest model consists of only one feature. The recorded decision thresholds thus do provide insight into the consistency of decisions across sample trees, considering that a new set of samples is selected in each iteration.

3.2.6.2 Further assessment of prediction results for individual sample trees: per-tree prediction confidence

Results for the RF-based prediction of symptomatic and asymptomatic sample trees were further scrutinised regarding the prediction accuracy of individual trees. Per tree accuracy was obtained as percentage, dividing the number a tree was correctly classified by the number a tree was predicted, across 100 iterations. This step was used to identify sample trees repeatedly classified incorrectly by the model. The prediction probabilities for each iteration were visualised to evaluate how confident the model is in its classification per tree. A low confidence, in this case, might imply that factors specific to this tree (e.g. a previously symptomatic tree in remission) prevents a correct class assignment.

3.2.6.3 Model transferability - predicting samples of a different time point

Finally, an investigation was undertaken to test how the determined best model performs on a separate flight. This test provided insights on model robustness, transferability and sensor calibration. These important aspects were assessed regarding practical implications and the general potential of UAVs for oak decline monitoring. The same approach as previously was adopted for the prediction of the health status of sample trees. 100 iterations were performed, where in every iteration, 50 % of the balanced sample set were used for training a model, which is then used to predict the remaining 50 % in the test sample set using the remote sensing-data of a separate flight, with the same spectral features. High testing accuracy is expected, given that flights have been undertaken in short succession, thus small to no changes within sample tree crowns should exist. A deviation from a high testing accuracy would be interpreted in terms of potential issues with remote sensing data quality.

3.3 Results

A total of four datasets, two RGB and two multispectral, were analysed for their explanatory value of COD induces stress. Field assessments of collaborating research projects provided the health status of the sample trees and served as a binary dependent variable (symp/asymp). The model features consisted of mean and percentiles of the raw band data together with respective vegetation indices.

3.3.1 Exploratory data analysis

Pixel values of raw data and spectral indices extracted at the sample locations show first signs of differences between symptomatic and asymptomatic trees, presented in the boxplots in Figure 3-4. The multispectral imagery from both acquisition dates exhibits higher reflectance values for control trees in the inner quartile range (IQR) and median of the NIR band. Lower reflectance can be observed in the control tree samples of the GREEN band. Across all multispectral raw bands, the range of reflectance values is larger for symptomatic trees than asymptomatic trees suggesting a higher variance in the spectral response of COD-affected trees. A separation between the health groups is present in the IQR, median and mean of all calculated multispectral vegetation indices. The separation is less noticeable in the vegetation indices and raw band information of the RGB imagery. However, both dates show higher values in the IQR, median and mean for GREEN, TGI, GLI, NGRDI and CI information extracted from asymptomatic trees.
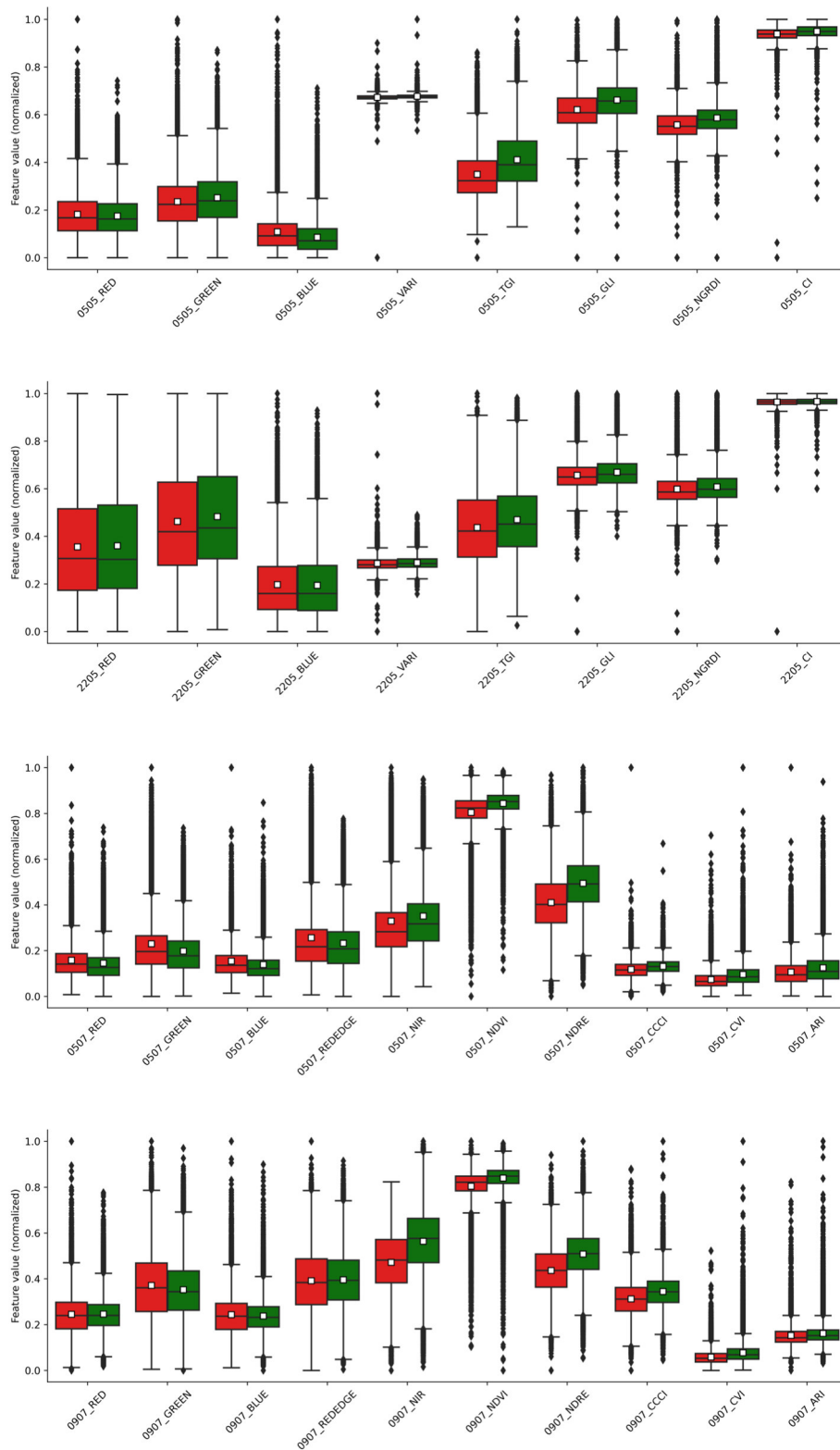
Figure 3-4 Box plots for raw band data and vegetation indices of the analysed datasets by date. RGB flights presented in two plots at the top, multispectral flights in the two plots at the bottom. Values were extracted at a 3 m radius from sample trees crown centre. Green for asymptomatic, red for symptomatic trees. Mean values for the groups are displayed as a white square.

The initial assessment of the datasets is supported by the Welch's t-test (see Table 3-4) These results show that mean variable values of the two health groups differ significantly (p-value < 0.05) for all bands but the RED band of the 09/07 multispectral imagery and the BLUE band of the 22/05 RGB imagery after outlier removal. The largest t-values occur for the NDRE feature of both multispectral flights, with and without outliers filtered. Overall, multispectral features delivered higher t-values than RGB features, suggesting an advantage of the narrow band sensor. The t-test shows significant separation of symptomatic/asymptomatic trees among calculated vegetation indices in the means of all dates and individual variables. Vegetation indices generally provided higher t-values than raw band data indicating an enhancement of tree health class separability based on their calculation.

Table 3-4 Results for t-tests on all model features. T-tests were undertaken on data with and without outliers. Outlier filtering was performed by rejecting all data points +/- 1 standard deviation. Features marked with $^{"x"}$ are not significant (p-value < 0.05).

	RGB features			
	0505		2205	
	with outliers	without outliers	with outliers	without outliers
RED	11.18	11.76	-2.65	-8.76
GREEN	-21.97	-26.70	-12.70	-20.59
BLUE	41.59	49.72	2.61	-0.29^{x}
VARI	-58.02	-67.37	-16.98	-24.83
TGI	-78.15	-86.34	-30.17	-40.84
GLI	-78.77	-90.24	-28.74	-33.97
NGRDI	-66.78	-79.58	-22.37	-29.93
CI	-54.35	-57.18	-16.39	-14.88

	Multispectral features			
	0507		0907	
	with outliers	without outliers	with outliers	without outliers
RED	22.38	19.44	-1.55^{x}	-14.65
GREEN	35.44	32.52	18.88	14.98
BLUE	27.65	24.75	9.81	-3.95
REDEDGE	22.78	19.29	-4.35	-10.41
NIR	-17.88	-20.66	-94.33	-102.11
NDVI	-71.82	-67.07	-71.37	-67.07
NDRE	-98.19	-115.75	-98.52	-110.57
CCCI	-54.13	-73.46	-60.18	-72.25
CVI	-74.01	-97.52	-73.44	-89.47
ARI	-39.52	-48.34	-28.75	-42.69

It is noticeable that t-values for the 22/05 RGB dataset achieve lower scores across indices than the 05/05 RGB data. This is potentially linked to the unfavourable time of the UAV acquisition at this date, being at sunset rather than solar noon.

Differences between t-test results with and without outlier filtering are minor, suggesting that spectral differences between COD affected trees and control trees tend to lie within the mean of the spectral features and are not considerably influenced by outliers. This phenomenon is further explored in RF modelling evaluating feature importance, specifically looking at the importance of feature percentiles.

3.3.2 RF modelling

3.3.2.1 Model accuracies – multispectral vs. RGB imagery

The potential of the UAV imagery to provide information about COD inflicted physiological stress was quantified by RF modelling. The datasets were tested individually for their explanatory power. Results are presented in Table 3-5.

All models show overfitting, since model training and testing accuracies differ between 17 and 22 percentage points. However, given the small sample set, this is not surprising. Mean training accuracies across the four datasets range from 81 to 91 %. Testing accuracies confirm the general ability to predict the class of trees in the validation group with better than random decision (a random decision is expressed by 50 % testing accuracy in the binary classification case with balanced samples). Training accuracies are expected to be high as the classifier is predicting the same trees it was learning from, and given the small training set, it does not have a wide variability of data points. However, training accuracy scores of less than 100 % and testing accuracies higher than 50 % imply that while the model overfits, it can generalise to unseen data to some degree.

The information content for the purpose of identifying declined trees is shown to be higher in multispectral imagery compared to RGB data. RGB imagery yielded testing accuracies of 59 % for the 05/05 flight and 64 % for the 22/05 flight, presenting poor discrimination of COD-affected trees from control trees. Test accuracy scores for multispectral data are more encouraging, yielding a mean accuracy of 74 – 75 % with 14 – 16 % standard deviation across the 100 iterations.

Low accuracies for models comprising RGB imagery support the theoretical disadvantage of broad and overlapping band information. Close inspection of individual tree crown maps (see Appendix C) further confirmed this result – RGB images show less information on tree condition status than images derived from the multispectral sensor. The RGB datasets were thus not considered in the subsequent analysis. Further assessment only took place with the two multispectral flights, 05/07 and 09/07.

Table 3-5 Results for RF models based on individual input datasets. The analysis is carried out with 100 iterations, an RF model with 100 trees and 50 / 50 training / testing split. The standard deviation (SD) is given across all iterations. The confidence interval (CI) is presented at the 95 % confidence level.

Data name	Training Accuracy mean %	Testing Accuracy mean %	Testing Accuracy SD %	Testing Accuracy CI % (95 %)
0505	81	59	13	56 - 62
2205	85	64	14	61 - 67
0507	91	75	14	72 - 77
0907	91	74	16	69 - 74

3.3.2.2 Feature importance

According to their mean feature importance values across 100 iterations, the top 20 features contained in the multispectral models are presented in Figure 3-5. Feature importance values showed very high relevance of NIR information in each model. The ten features with the highest mean importances in both flights consist of a vegetation index comprising the NIR band (NDRE, NDVI and CVI) or NIR as raw band information. Amongst the vegetation indices, the NDRE, NDVI and CVI were demonstrated to be most beneficial to the models.

The boxplots show that feature importance amongst the features with highest mean importance varies greatly across the iterations suggesting that most of the top-ranking features are equally important and depend on the training data.

Percentiles are represented, ranging from lower to upper end, indicating that differences between symptomatic and asymptomatic trees are displayed across the whole spectral distribution of pixels extracted from tree crowns.
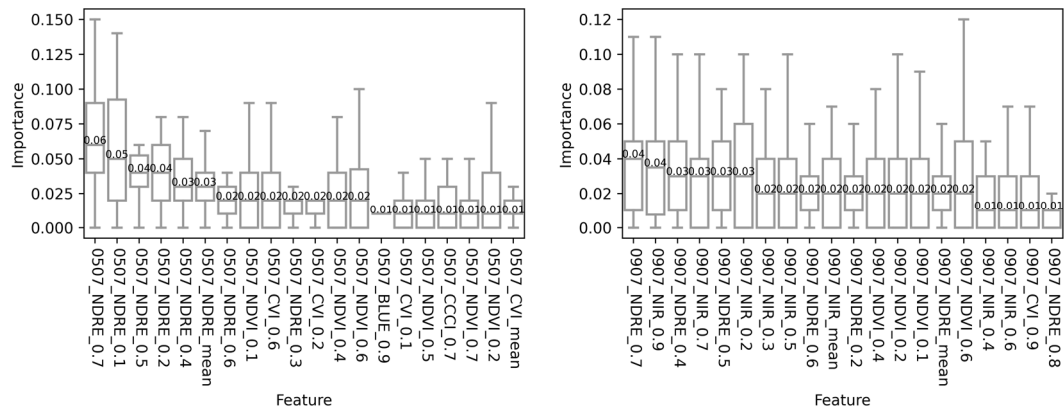
Figure 3-5 Mean decrease gini importance boxplots for the 20 features with the highest importance across 100 iterations, shown respectively for the two multispectral models: 05/07 on the left and 09/07 on the right. Mean feature importance scores are shown as labels.

3.3.2.3 Example decision trees for multispectral models

Example decision trees in Figure 3-6 illustrate the decision logic within the RF models used in the analysis. For every decision tree in the RF ensemble the two sample groups, five symptomatic and five asymptomatic trees, were split in a single feature based on their feature values. In these features with high importance, it is evident that the sample groups have little or no overlap in their values and can be separated by a single threshold with little misclassification. For example, the 60th percentile of CVI in the 05/07 model, the 70th percentile of NDRE in the 09/07 model and the 40th percentile of the NDVI in the 09/07 model do not exhibit overlap between symptomatic and asymptomatic trees (see Figure 3-6). The determined threshold for these decision trees thus separated these samples correctly in these examples. As the final decision is aggregated across 100 decision trees in each model and samples are evaluated across 100 model iterations, robustness is increased. Recorded thresholds for all 100 iterations showed little variation across features, indicating consistency across sample trees and their feature values (see Appendix D for reference).
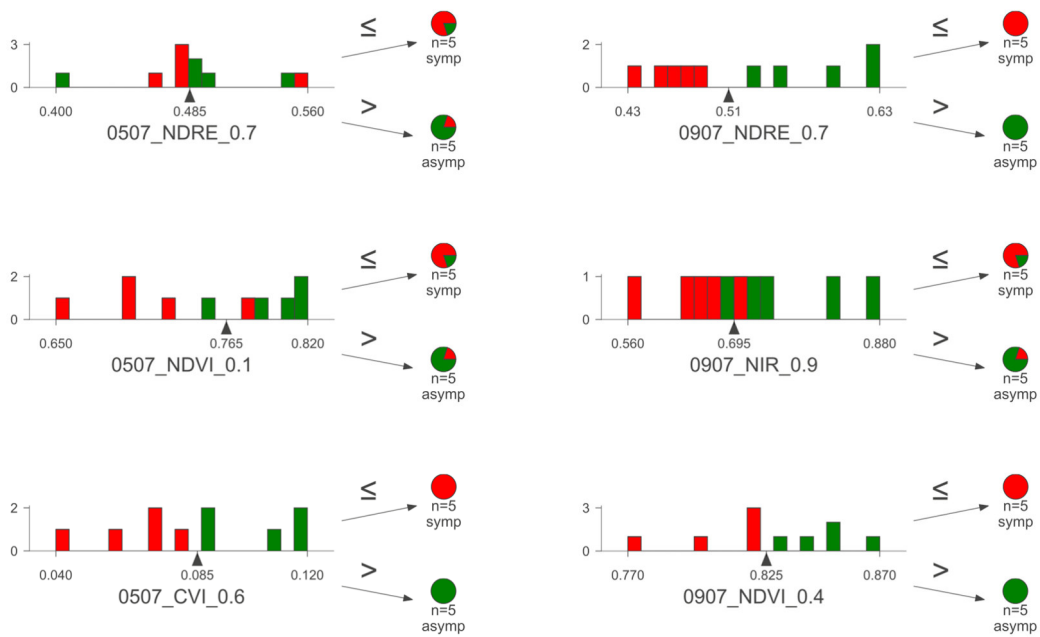
Figure 3-6 Example decision trees for features among the features with highest importance in the two multispectral models. Here three example trees and their decision threshold are presented. Each model in the 100 iterations is trained on 100 such trees. Histograms of the input samples show how the input data is distributed for this feature between the symptomatic (red) and asymptomatic (green) group. The prediction result of the learned threshold in each decision tree based on the training data is presented as pie charts indicating correctly and falsely classified condition.

3.3.2.4 Individual tree prediction/assessment

The prediction of the health status of individual trees provided an overview of their classification accuracy and the respective certainty of a model for their class prediction. The models demonstrate a high degree of certainty regarding class prediction for some individuals, for either the symptomatic or control class. Others showed low certainty in the class assignment, revealing a near random decision. Per tree accuracies are given in Table 3-6 and corresponding prediction probabilities across 100 iterations are depicted in Figure 3-7.

Trees 12, 121, 147, 211, 240, 245, 250, and 251 were classified correctly in all 100 runs of the 05/07 model and with high accuracy in the 09/07 model. Prediction probabilities are high for these trees, indicating high certainty in that decision of both models.

Trees 112, 235 and 236 showed very low accuracy scores. An inspection of their corresponding classification probability reveals a decision of both models for the opposite class with high certainty.

Tree 228 is notable, as it was predicted with 100 % accuracy and high certainty by the 09/07 model. However, the 05/07 model predicted its class with 48 % accuracy, presenting very low certainty and a nearly random decision.

Tree 220 was predicted as symptomatic by the 05/07 model, despite having the opposite class label, but the 09/07 shows a near random decision. The same applies to tree 242, which was assigned the opposite class by the 09/07 model, whereas the 05/07 dataset is indecisive regarding this tree.

Both models show low certainty for tree 145, which has low accuracy scores (63 – 65 %), being assigned the asymptomatic class 17 and 18 times, in 05/07 and 09/07 respectively, out of the 48 times it was predicted in both models. Tree 241 is borderline and shows medium accuracy in the 05/07 model but a near random decision by the 09/07 model. All remaining trees presented medium accuracies in both models.
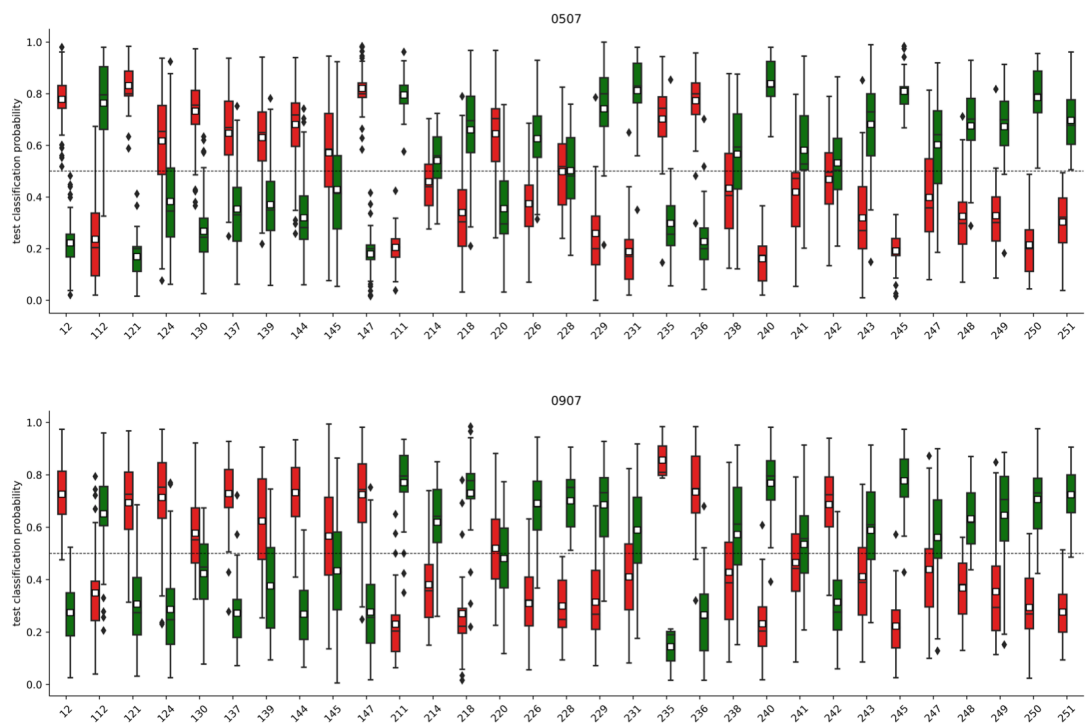
Figure 3-7 Per tree prediction probabilities for the two multispectral RF models, 05/07 and 09/07. Results presented for 100 iterations, with a new 50 / 50 training / testing split performed at every iteration.

Table 3-6 Per tree classification accuracies by the best performing models for the two multispectral RF models, 05/07 and 09/07. Results presented for 100 iterations, with a new 50 / 50 training / testing split performed at every iteration.

	Accuracy %	
treeID	05/07	09/07
12	100	95
112	10	16
121	100	82
124	71	88
130	88	64
137	85	96
139	83	67
144	88	93
145	65	63
147	100	89
211	100	90
214	68	84
218	79	88
220	18	47
226	86	97
228	48	100
229	89	83
231	96	69
235	9	0
236	7	9
238	61	69
240	100	96
241	75	56
242	53	16
243	83	73
245	100	96
247	69	69
248	86	78
249	85	88
250	100	89
251	100	95

3.3.2.5 Model transferability – predicting samples of a different time point

Sample tree status was predicted on unseen 09/07 data using the 05/07 dataset for training. Across 100 runs, with a newly trained model at every iteration, the mean testing accuracy was 52 % (standard deviation 6 %). The prediction probabilities for individual trees revealed the cause for the very low classification accuracy. By average prediction probability every tree fell into the asymptomatic group regardless of the class label (Figure 3-9). An explanation for this phenomenon was found in the higher absolute feature values of the 09/07 imagery. This difference between the data from the two flights is observable in the reflectance values and, consequently, in the derived

vegetation index values (for an overview of individual variables see boxplots in Appendix B). Thresholds for the distinction between asymptomatic and symptomatic trees learned from 05/07 data thus are not transferable to the 09/07 imagery.

Under the assumption that among pixels extracted from crown centres, areas of high and low reflectance did not change within the four days between the two multispectral flights, a min-max-scaling was performed to normalise both datasets. This procedure had little effect on raw spectral channels, but vegetation index values showed better alignment following normalisation. An example of the most important raw channel and vegetation index, before and after normalisation are given in Figure 3-8. The prediction was repeated with the normalised datasets, improving the testing accuracy to 71 % (standard deviation 13 %). After normalisation, prediction probabilities and class predictions for individual trees were closely aligned with the results for single date predictions (compare Figure 3-9 and Figure 3-7).
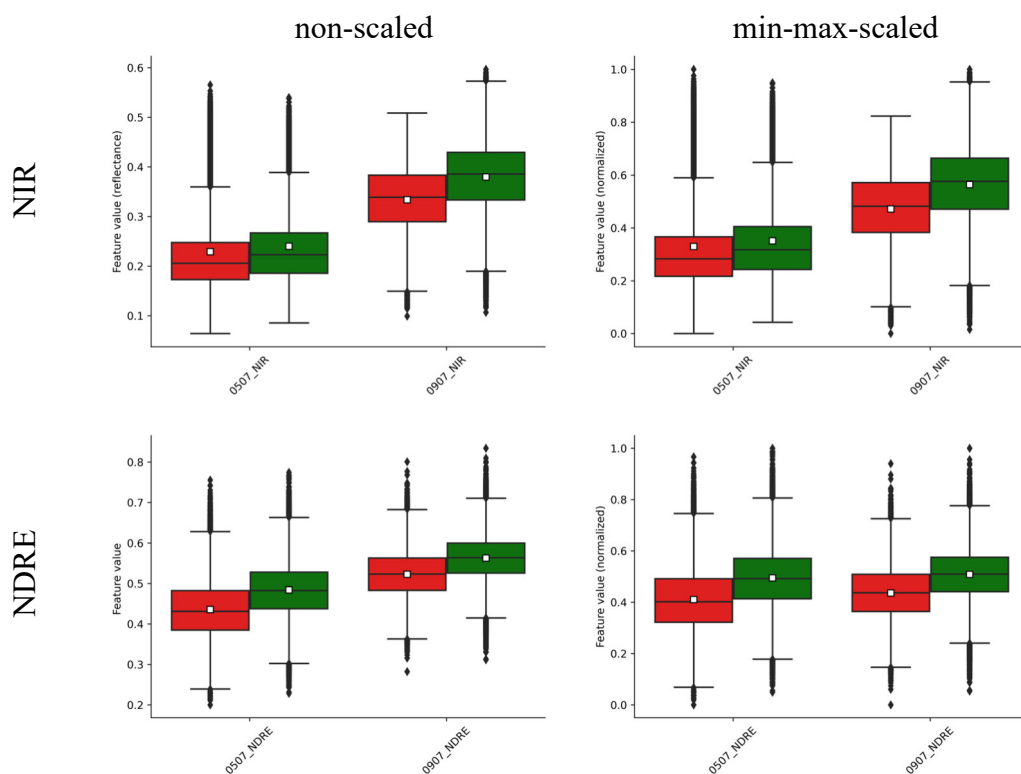
Figure 3-8 Boxplots for non-scaled (left) and min-max-scaled (right) feature values of the most important raw channel (NIR, above) and the most important vegetation index (NDRE, below). Scaling had little impact on the NIR reflectance values but has achieved better alignment of NDRE feature values between the two dates.
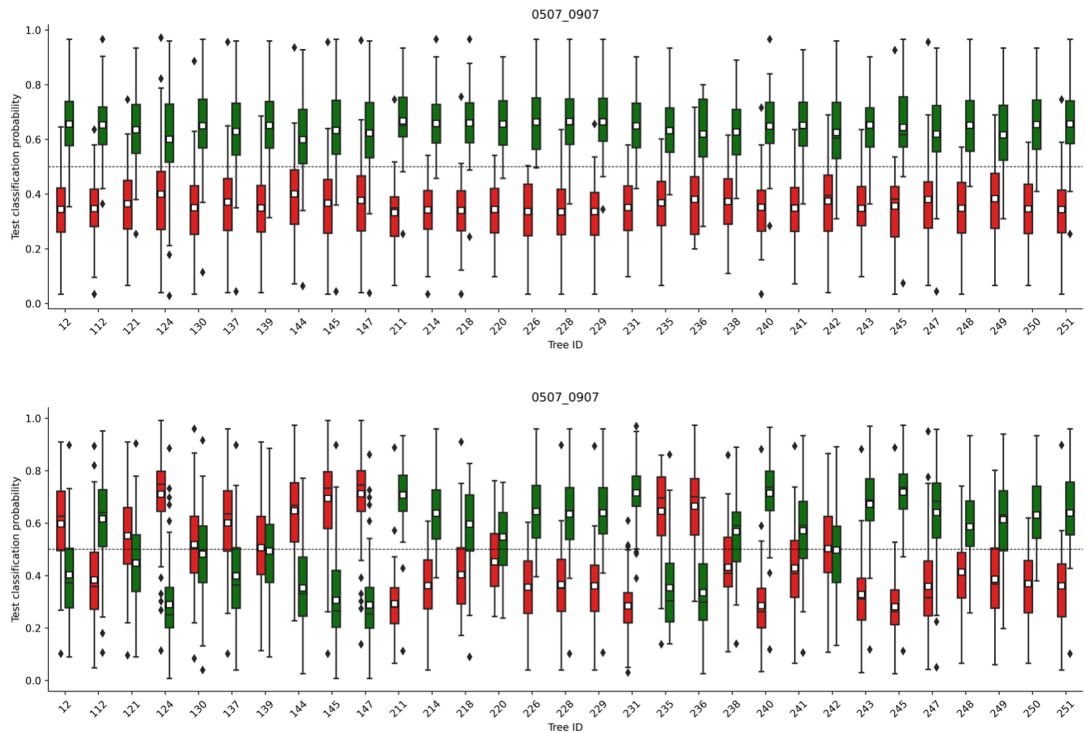
Figure 3-9 Per tree prediction probabilities across 100 runs using 05/07 for training and 09/07 for testing. The same test is performed for non-scaled data (above) and min-max-scaled data (below).

3.4 Discussion

The analysis conducted within this study demonstrated that UAV-acquired spectral data contain potential information to distinguish between COD-affected and control trees. As identified in the results, narrowband multispectral information was shown to be most suited to differentiate the classes.

RGB imagery, however, did not provide sufficient information content for a robust class distinction, despite visible symptoms of COD at the site, such as reduced foliage and dead branches. The key limiting factor of consumer-grade RGB sensors lies in the broad band characteristics. In comparison to narrow band multispectral imagery, RGB data covers large portions of the spectrum in a single band. These broad band characteristics lead to overlapping spectral channels, as it has been illustrated by (Pauly, 2016), rendering RGB imagery a sub-optimal choice for monitoring vegetation stress. The results, in this case, reinforce that RGB imagery is inadequate for detecting declining tree health.

Conversely, multispectral imagery provided a greater predictive capacity for the detection of declined trees. 05/07 multispectral imagery delivered the highest explanatory power, closely followed by the second multispectral dataset, 09/07. Illumination conditions were not ideal for either flight, being overcast and thus featuring a high amount of diffuse rather than direct light. Both flights were planned according to weather forecasts for clear skies, however, these conditions were not met. Though it is expected that decreased diffuse light delivers a cleaner spectral signal, increasing the potential for stress sensing, the data were still analysed to provide insights into the applicability of UAV-based COD monitoring in a realistic scenario, where ideal conditions cannot always be met, particularly in a highly variable climate such as in Britain. As such, it was found that, changing light conditions during the 05/07 flight did not appear to significantly affect the prediction performance, delivering a similar accuracy score as the 09/07 flight performed in stable conditions. However, it was found that the two calibrated orthomosaics, depicting the same site only four days apart, did not show similar reflectance values. Reflectance values of the 05/07 flight were significantly lower than those of the 09/07 flight. Both flights were successfully calibrated with a reflectance tarpaulin laid out in the centre of the site.

Only imagery of the 09/07 flight was additionally calibrated with downwelling light sensor information. For the 05/07 flight, the initial inclusion of downwelling light sensor information had led to large artefacts and was therefore neglected. Changing illumination at the start and end of the flight and missing downwelling light sensor information may explain some of the observed difference in reflectance values between the two flights, however does not explain the general shift to higher reflectance values of the second flight given that both flights were calibrated by reflectance tarpaulin.

Cao *et al.* (2019) reported that the specific multispectral sensor used in the current studies showed measurement variability over time, suggesting that differences in illumination between flights influence derived reflectance, despite a correct calibration procedure. This shows that further scrutinising of UAV-specific multispectral sensors and reflectance calibration procedures implemented in the SfM pipeline is critically needed. Confidence in reflectance values delivered by UAV remote sensing is crucial, for attempts to link spectral components to plant traits and for the generalisation of models, enabling model transfer and upscaling of results.

In the assessment of the multispectral datasets, was evident that the NIR signal is most relevant for a distinction of the two tree health classes. NIR spectra and associated vegetation indices showed consistently lower values for symptomatic trees compared to asymptomatic trees. In the model-based assessment this is also demonstrated by the thresholds determined in the features with highest importance, which in some cases delivered a distinct separation between the two groups (see also Figure 3-6).

NIR percentiles ranked among the 20 most important features for the 09/07 model and NIR information is contained in all vegetation indices with high feature importance. The analysis demonstrated that multispectral vegetation indices derived from bands in the near-infrared region can be an important predictor to separate symptomatic from asymptomatic trees, in the present study. NDRE and NDVI particularly have been shown to hold high explanatory value, indicated by the high feature importance of these vegetation indices. These results align the findings of Dash *et al.* (2017, 2018) and follow the underlying principle of a link between spectral reflectance and foliar properties.

Chlorophyll, pigment and water content decline under physiological stress (Hunt *et al.*, 2011; Easterday *et al.*, 2019; Jackson and Huete, 1991; Peñuelas and Filella, 1998; Spyropoulos and Mavrommatis, 1978). As a consequence, the spectral composition of foliage also changes. While healthy vegetation reflects more NIR light, it absorbs more RED light than stressed vegetation (Myneni *et al.*, 1995; Sellers *et al.*, 1992). As such, low NDVI values are indicative of leaves with reduced photosynthetic capacity. Present findings regarding the utility of NDVI are consistent with the wide use of the index in research assessing vegetation condition (Bannari *et al.*, 1995; Jepsen *et al.*, 2009; Spruce *et al.*, 2011; Dash *et al.*, 2017; Rullan-Silva *et al.*, 2013; Stone and Mohammed, 2017).

NDRE has a shorter history in stress detection than NDVI. The inclusion of the REDEDGE band in the newer generations of sensors was mainly driven by findings that suggest high sensitivity of this wavelength region to stress in dense vegetation scenarios (Carter and Knapp, 2001). Although it is also indicative of chlorophyll content, REDEDGE light can penetrate leaves deeper and is less likely to be absorbed entirely than RED light (Gitelson *et al.*, 2005).

In the best performing models of the present study, 05/07 and 09/07, NDRE received the highest importance scores, closely followed by NDVI features. The

higher importance of NDRE compared to NDVI may be explained by the aforementioned difference of REDEDGE light penetrating vegetation deeper than RED light. It is hypothesised that this may potentially provide a benefit for the detection of chlorophyll content in dense oak crowns where NDVI may become saturated.

Two vegetation indices, CVI and CCCI, showed less benefit in the detection of oak decline, compared with the higher feature importances of the well-established NDVI and NDRE indices. The indices are highly correlated with NDVI and NDRE as they are derived from common input bands. Both these indices have been developed to normalise vegetation stress with vegetation density. Although lower feature importances were identified in the current evaluation, in a different scenario (e.g. with reduced spatial resolution, different stand density and/or sample trees), the applicability of CVI and CCCI for assessing tree health should be re-evaluated.

ARI, with feature importance scores outside of the 20 best features, provided less evidence of holding important information on COD-stress symptoms. Foliar anthocyanin content is predominantly related to stress caused by low temperatures and/or strong light. However, changes in foliar anthocyanin have also been linked to compromised water and/or nutrient transport (Spyropoulos and Mavrommatis, 1978; Chalker-Scott, 1999) as is the case with COD affected trees. In the t-test analysis ARI showed a significant difference in mean values between the symptomatic and asymptomatic sample group for both multispectral datasets. Nevertheless, very low feature importance was assigned to ARI percentiles in the Random Forest modelling. A possible explanation is that a stress signal derived from the spectral range associated with ARI is not specific to COD-induced stress. In other words, changes in the foliar concentrations of these pigments are non-specific indicators of a tree's physiological status. Thus, foliar anthocyanin concentration is influenced by exposure to a broad range of stressful processes and/or damaging agents as well as from the normal leaf maturation processes.

The results suggest that vegetation indices indicative of chlorophyll content tend to perform better in the identification of COD-induced stress than an anthocyanin-based index. However, further studies that apply a higher number of sample trees are required to strengthen the significance of this hypothesis. Additional assessments should be undertaken at different times during the growing season. The current study collected remote sensing data in the early-mid growing season. However, anthocyanin

concentration in oak leaves is expected to increase as the growing season progresses (Gamon and Surfus, 1999; Spyropoulos and Mavrommatis, 1978). As such, it is conceivable that the ARI, and inferred foliar anthocyanin content, gains relevance for a COD-stress detection in the later stages of the growing season. Future investigations should recognise the phenological influence on reflectance characteristics and consider employing time-series image datasets to identify the optimal timing for the detection of COD.

Further assessment of feature importance showed that all percentiles of a single variable are important in the present case. Thus, feature importance shows less the importance of a particular percentile, but rather the importance of a variable itself. Through this result, with the addition of the t-tests results, and undertaken with and without outlier filtering, it may be inferred that the entire spectral distribution of extracted crown pixels is relevant for the distinction, more so than spectral outliers.

Overall, it was shown that, among the collected UAV imagery, spectra in the near-infrared region, expressed by the NIR and REDEDGE channels, are most suited for a distinction between symptomatic and asymptomatic trees. Given the sensitivity of the spectral region to photosynthetic capacity, it is plausible that a correlation with COD-inflicted stress exists.

Generally, stress in trees may show as chlorosis in the canopy (Lausch *et al.*, 2016). In addition, COD is defined by a thinning canopy (Denman and Webber, 2009). Chlorosis, defoliation and dieback all lead to a reduction of photosynthetically active foliage in the crown. As chlorophyll presence in the canopy reduces, less light is reflected in the near-infrared region (Knipling, 1970). This is consistent with the current findings as the decision process of Random Forest-based models was shown to be highly dependent on few chlorophyll-sensitive variables, such as the NIR band, and NDRE and NDVI indices.

However, it is possible that the importance of these variables was artificially inflated. As most variables are correlated and all percentiles of an individual variable were included in the model, feature redundancy is high, which can cause unreliability in the ranking of feature importances (Strobl *et al.*, 2008). To reduce this effect, a permutation importance method has been suggested and is adopted in CHAPTER 5. Future studies may also explore the option of using a single summary statistic to represent individual variables to reduce feature redundancy. Removing redundant

features as an additional feature selection technique could enhance the interpretability of a model by simplifying it and reduce overfitting.

The limited sample size in the current study contributed to the problem of overfitting in the models, which was evident from the difference in accuracy between their training and testing results. The small number of sample trees is one of the biggest shortcomings in the assessments undertaken and reduces the significance of the findings. The low variance in threshold values over the 100 iterations shows that decision rules do not deviate for subsets of the sample data (see Appendix D). However, given the small sample size, thresholds are most likely dataset specific and cannot be applied to classify trees of other study sites.

Combined with the uncertainties already mentioned, and stemming from less-than-ideal illumination conditions, reflectance calibration and overfitting, results only hold true for this particular site and the data assessed. Generalisation of the developed models, as required for a monitoring approach, is not considered feasible at this stage.

Currently, developed models can neither be robustly applied at a different site nor at a different point in time. In fact, it was shown that discrepancies between data of calibrated imagery from two consecutive flights were greater than the signal used for the distinction of symptomatic and asymptomatic trees. To reduce the issue, a normalisation procedure helped to gain better alignment of feature values between the two flights and improved the prediction accuracy. However, uncertainty in absolute reflectance values must be greatly reduced to draw meaningful conclusions and to enable model transfer. Therefore, to move forward with UAV remote sensing-based research on oak decline, and tree health in general, spectra collected from miniaturised sensors and respective reflectance calibration procedures should be reviewed.

Despite the aforementioned shortcomings, potential for use of multispectral UAV remote sensing data in a prediction of oak health status was demonstrated. Testing accuracies of 74 % and 75 % for the two multispectral models show that the collected remote sensing data contain information that correlate with ground observations to some extent.

The two multispectral models however, also revealed four sample trees that were predicted as the opposing class, in most of the 100 iterations. Tree 112 was identified as asymptomatic and trees 220, 235 and 236 were identified as symptomatic by both models, but had received the opposite class tag in the initial field sampling. An inspection of their data distribution confirms the choice of the models. Values

extracted from the crowns of these particular trees differ slightly from the other trees of the same class (see Appendix B). This difference is particularly visible in the NDRE feature, where tree 112 shows higher NDRE values in the 05/07 and 09/07 data than the remaining trees in the symptomatic group and trees 220, 235 and 236 exhibit lower NDRE values than the rest of asymptomatic trees. This explains the low certainty in the prediction of their status, as NDRE is a highly important feature in both models.

In personal communication with Neil Mathews (dendrochronology PhD student, Swansea University), it was later confirmed that tree 112 was classified as control in latest field sampling, which corresponds to the prediction results of the current models. The PDI value of 0.78 for tree 112, combined with a moderate decline in crown condition rating in 2016, suggests the possibility that this tree may have experienced more severe COD symptoms in the past but has since recovered. This observation aligns with the findings of Finch *et al.* (2021), who noted high PDI scores for multiple trees that were in remission.

Trees 220, 235 and 236 are still being considered COD control trees by the dendrochronology team for Oak Decline. Inspection of crown maps for those trees (see Appendix C) did not reveal any indications for COD symptoms for tree 220, but trees 235 and 236 do show some signs of dead branches in the RGB imagery, which may point to an early stage in the decline. Subsequent field assessment by Neil Matthews determined that trees 235 and 236 are indeed diseased, though with heartwood rot as opposed to COD. The trees spouted a foul-smelling liquid from the rotten centre when cored, and rotten lower branches were observed. The current study therefore correctly identified these trees as stressed, although the attribution of this is not COD.

Tree 220, which was predicted symptomatic by the multispectral RF models, depicts the highest PDI score (0.43) among the asymptomatic group according to Finch *et al.*'s (2021) assessment from field data collected in 2018. A progressively worsening crown condition could explain the predicted symptomatic status in the 2019 collected remote sensing data.

Similarly, the lowest PDI score (0.55) in the symptomatic group, may explain the uncertainty of the remote sensing models and associated low accuracy score, for tree 145. The tree is misclassified in about 45 % of instances in the binary prediction scenario. This could be because the tree falls within the early decline range, where symptoms may not be clearly evident, as indicated by the PDI score.

In other cases, PDI scores do not align with prediction results. Such is the case with tree 231 that shows a similarly high PDI score (0.42) in the asymptomatic group as tree 220, yet the prediction with multispectral data shows a high level of certainty. Similarly, tree 242 depicts a low PDI score (0.29), but was predominantly misclassified. Additional evaluation is needed in future research to explore the relationship between predictions based on spectral analysis and the output of the PDI model, which employs phenotypic characteristics.

Moreover, a greater number of sample trees with detailed information on decline severity is a crucial prerequisite for obtaining conclusive evidence regarding the health status of trees. The aim of the current investigation however, was to assess the overall potential for a remote sensing-based detection of COD. Potential was demonstrated for the distinction of health classes in the binary case. To increase the informative value of remote sensing research on COD, future studies should consider a continuous response variable in an analysis approach, such as regression. This will allow for improved quantification of the explanatory power of remote sensing-derived variables.

3.5 Conclusion

Evidence for potential of UAV remote sensing data in the detection of COD-stressed trees was demonstrated. A Random Forest-based modelling approach was implemented and the health status of trees was predicted in independent samples drawn from the same study site. Four UAV datasets were assessed and delivered testing accuracies between 59 % and 75 %, providing evidence for explanatory power of remote sensing data to distinguish between symptomatic and asymptomatic trees. The information content of narrow band multispectral imagery was shown to be far greater than broad band RGB imagery, confirming pervious findings. RGB imagery was thus considered unsuitable for an applied monitoring approach of oak tree decline and was excluded from further analysis.

Within collected multispectral data, the best performance in the distinction was achieved with near-infrared reflectance and the well-established vegetation indices, NDVI and NDRE. The relation of these remotely-sensed spectra to photosynthetic

activity illustrates a connection to a key symptom of COD, reduced crown vigour and loss of foliage.

The assessment of feature importance showed that important variables were represented by all percentiles. This indicated that the distinction of the health classes is not driven by spectral outliers but that differences are present throughout the data distribution of important individual variables, and may be expressed by their mean. The inclusion of all percentiles of a single variable in this study may have promoted overfitting, due to the high redundancy and correlation between features.

Further shortcomings relate to the limited number of samples and the binary classification of health status. Additionally, the study identified two trees which were diseased, although this was not due to COD. This supports the ability of the current approach to correctly identify stressed trees, however implies that COD may not be distinguishable from other forms of compromised condition.

Improvements to the current study design can be made by extending the field sample collection, providing a higher amount of groundtruth data and more detailed information on decline status, to use in a continuous response variable. This would allow for more definitive answers on the relationship between remotely-sensed spectra, derived vegetation indices and the decline status of trees.

Additionally, uncertainties in multispectral sensor calibration and respective reflectance maps prohibited assertions beyond the general potential for a distinction of the two health classes. It was shown that generalisation of the developed models is not possible at this stage and with the present data. A test for model transferability, training on a multispectral flight and testing on a multispectral flight four days later, revealed significant differences in absolute reflectance between the two datasets. Future work on forest health assessments by UAV remote sensing should strongly consider scrutinisation of technical aspects, such as sensor calibration, to improve confidence in UAV-acquired reflectance data.

CHAPTER 4:

CLASSIFICATION OF TREE SPECIES IN A MIXED BROADLEAF FOREST

USING MULTITEMPORAL MULTISPECTRAL UAV IMAGERY

4.1 Introduction

Forests with higher biodiversity have been found to be more resilient to stressors (Thompson *et al.*, 2009). Despite the known ecological advantage of heterogenous forests over pure stands, silvicultural systems resembling natural forests are uncommon in the UK (Forestry Commission, 2018). In large part this is due to the great challenge and cost that species rich and structurally heterogenous stands pose to forest inventory and management. A key factor contributing to this challenge is a seemingly trivial requirement: knowledge on tree species distribution. Forest inventories, biodiversity assessments, monitoring of invasive species and forest health as well as most forest management related activities, rely on information about the species composition, ideally in conjunction with spatially-explicit information on their distribution.

Mapping of tree species in the field is a time consuming and laborious task. Collection of comprehensive information on species distribution across large sites is typically too work and cost intensive. Additionally, in dense forests, the accuracy of GNSS surveys is restricted by multipath issues and the collection of accurate location information by total station is impractical due to logistical reasons. Consequently, efforts to produce spatially coherent tree species maps are often based on remote sensing data.

For the discrimination of tree species with optical remote sensing data, differences in spectral response (i.e. reflectance) are typically exploited. Species classification with optical imagery has been widely studied in the space- and airborne remote sensing domains (Fassnacht *et al.*, 2016). Limited by their spatial resolution, these image sources are typically unable to provide tree-level species information. However, in the case of the present study, motivation to map tree species stems from the need to separate oak signals from other species' signals in order to assess the health of individual trees. For the study site of this and the next chapter, Monks Wood, a tree species map exists from a previous study that utilised 2003 airborne multispectral

imagery (Hill *et al.*, 2010). In their species map of Monks Wood, Hill *et al.* (2010), separated six overstory species with 84 % overall classification accuracy (increased to 88 % with a clump and sieve procedure) with multitemporal Airborne Thematic Mapper imagery. However, for the current study, the spatial resolution of two metres for their final species map was considered insufficient to distinguish oak signal from other species with precision for conducting further research on AOD in this diverse woodland.

In order to fulfil the requirement of fine-scale class separation, tree species classification was undertaken with UAV imagery. Limited by their maximum legal flying height, UAVs inevitably enable capture imagery of very high spatial resolution. The close proximity of the sensor to the scene naturally holds the capacity of recording small GSDs, in turn providing more defined spatial borders between classes. Furthermore, by increasing spatial resolution, hypothetically the quantity of pixels with a pure class signal increases, thereby reducing spectral mixing. The present study thus intends to update the previous species map to improve on spatial class separation by increasing the spatial resolution to ten centimetres.

Using a supervised pixel-based classification approach, the ability to discriminate and map overstorey tree species, based on multitemporal UAV-acquired multispectral data (visible and NIR), was investigated across two growing seasons. Within this, several factors were explored with the objective of optimising future UAV acquisitions for tree species mapping in the context of mixed broadleaf forests. The study assessed how classification accuracy is affected by 1) the effect of random forest tree size, 2) the influence of plot size, 3) the number of training samples, 4) the timing of the acquisition and the combination of different acquisitions with specific focus on oak detection. Additionally, the value of tree height information was studied with respect to classification accuracy.

4.2 Methods

4.2.1 Study site

Monks Wood is an ancient woodland located north-west of Huntingdon, Cambridgeshire, UK, and is formed of native broadleaf species. As a National Nature

Reserve, Monks Wood is a species rich and diverse site (Massey and Welch, 1993). Prior to the establishment of the Nature Reserve in 1953, trees at the site were used as coppice (Steele and Welch, 1974). Since then Monks Wood has been maintained with the aim of promoting its natural biodiversity. Woody species at the site are heavily mixed both horizontally and vertically. More information on Monks Wood and its history can be found in CHAPTER 2. To achieve a remote sensing-based classification of upperstory species, Monks Wood is a particularly challenging site due to its mixed species composition, inter-species variability, high stand density and canopy with inter-locking crowns. The heterogeneity of the woodland is illustrated in a single nadir photograph (see Figure 4-1).

The woodland is primarily composed of oak, ash, elm and Field maple trees in the upperstory. Other species found in the upperstory are birch, aspen, Wild service tree and Crab apple. The primary focus of the current study lies on the north-east section of Monks Wood. In this ~ 22 ha large section of the wood, the two most dominant species are oak and ash. A cluster of elm trees is present in the southern part of the section. Field maple trees are heterogeneously spread throughout the section while birch and aspen trees are predominantly abundant in smaller patches.
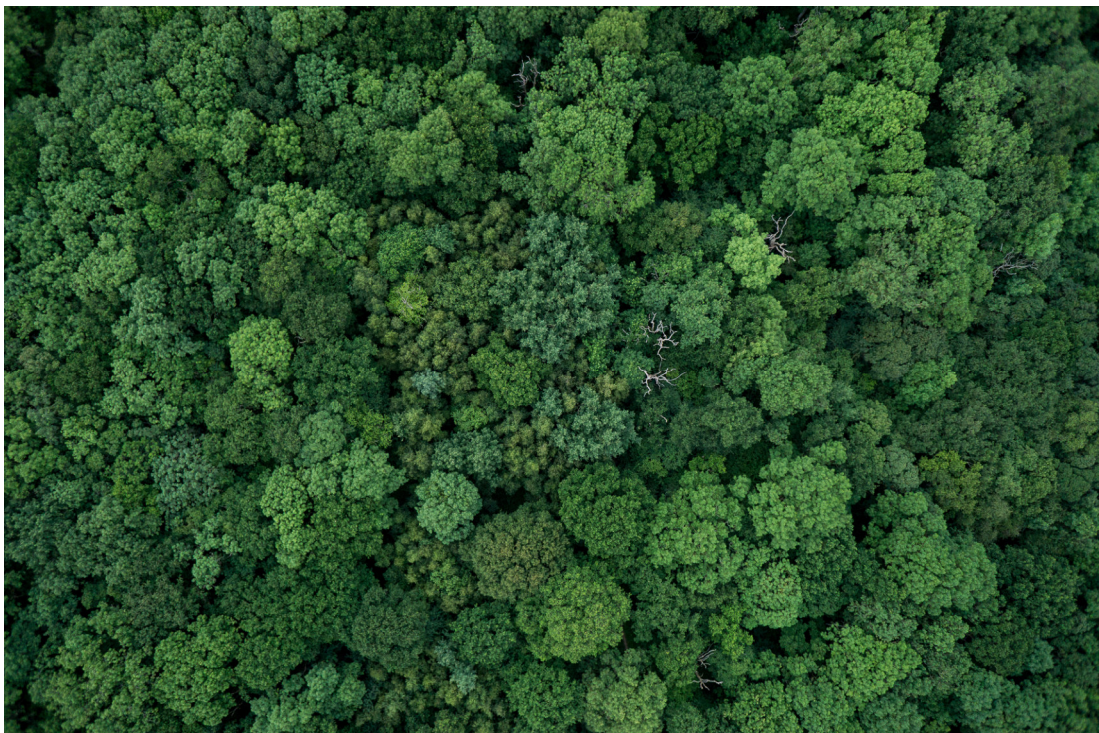
Figure 4-1 UAV image illustrating the natural diversity and dense canopy cover present at Monks Wood. The footprint of the photograph is approximately 150 x 100 m.

4.2.2 UAV remote sensing data

The remote sensing data used in this study consists of imagery collected at five separate dates over the course of two years. One RGB image set and four multispectral image sets were acquired. For the remote sensing-survey flights a fixed wing UAV was utilised. The UAV was equipped with a Sony A6000 camera with 16 mm lens for RGB image capture as well as a Micasense RedEdge 3 for narrowband multispectral acquisition. Due to the limited payload capacity, RGB and multispectral surveys were undertaken as separate flights. An extensive description of the acquisition protocol and further details on the UAV and sensors are given in CHAPTER 2.

The RGB image set, captured in June 2017, features a higher resolution (< 3 cm GSD) and higher positional accuracy (PPK) than the multispectral imagery. RGB images were captured synchronous to a raw GNSS log enabling PPK correction of their geolocation. PPK correction was enabled by the nearby Continuously Operating Reference Station (CORS) in Peterbrough (baseline < 20 km).

The RGB image set primarily serves the purpose of creating a photogrammetric reconstruction of the canopy surface and subsequent derivation of a CHM. A derived RGB orthomosaic also serves as georeference for the four multispectral image sets.

The multitemporal multispectral remote sensing data were collected during summer 2017, autumn 2017, spring 2018, and summer 2018. All flights were carried out at a height of approximately 120 m AGL resulting in a GSD of < 8 cm. All multispectral flights, except one, were undertaken within two hours of solar noon and featured clear or nearly clear sky conditions. The flight in July 2017 had to be undertaken before solar noon due to time restrictions (other field work). Furthermore, the NIR band of this specific flight has strong vignetting present in the lower right corner of the image (Figure 4-2). This was caused by unwanted sensor movement inside the airframe and led to the hatch obstructing part of the image. No significant quality issues are present in the other datasets.

An image of a calibrated reflectance panel was taken prior to every multispectral flight to allow the conversion of radiance to reflectance (see CHAPTER 2). In the case of the July 2018 flight the reflection panel was not imaged. Details on all flights undertaken are given in Table 4-1.
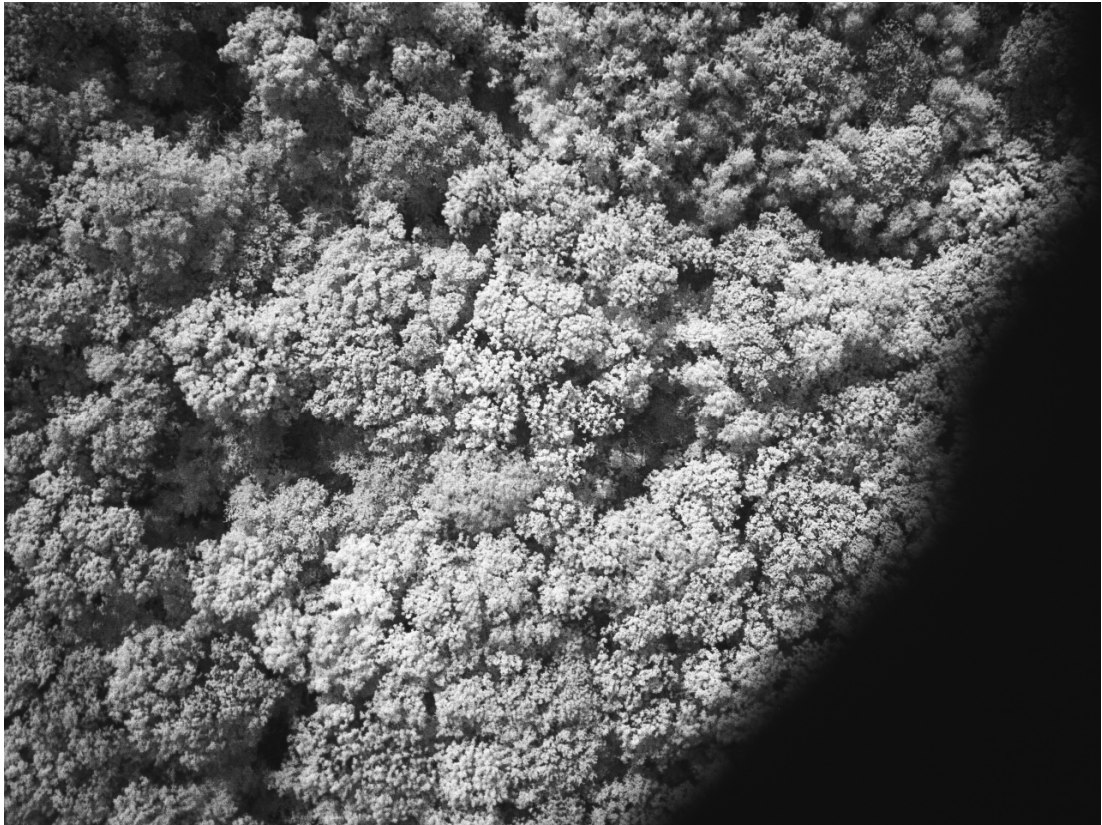
Figure 4-2 Vignetting present in the NIR band of the July 2017 flight caused by an obstruction of the sensor.

4.2.3 Photogrammetric processing

The UAV image datasets were individually processed in a SfM photogrammetry pipeline to generate surface models and orthophotos, respectively. The SfM photogrammetry software Pix4D (version 3.4.12) was used to process both the RGB and the multispectral imagery.

Photogrammetric reconstruction of the RGB data set was undertaken using a direct georeferencing approach exploiting the high location accuracy of the individual images. Using this approach, the global positional accuracy of the reconstructed model is expected to be < 1 m (see PPK section in CHAPTER 2). The applied PPK method allowed a complete reconstruction of the canopy surface providing a point cloud with an average point density of ~ 250 pts/m³. An RGB orthophoto, with 2.9 cm spatial resolution, was derived for subsequent use as visual reference.

The multispectral data were radiometrically corrected as part of the workflow in Pix4D. The calibrated reflectance panel information (acquired before the flight) was

used to convert raw digital number values to reflectance values. To adjust for minor lighting changes during the flight, the DLS data, associated with every image, were incorporated in the calibration procedure.

The NIR band of the July 2017 orthophoto shows visible banding (see Figure 4-3) due to the obstruction of the NIR sensor in this image set (Figure 4-2).

For the October 2017 dataset, inclusion of the DLS data caused bright spots on the northern border of the forest. These minor artifacts were potentially caused by sudden gusts of wind causing the UAV to bank away from the sun and the DLS to measure lower irradiance. An exclusion of the DLS data in the processing of the October 2017 dataset solved this issue.

As no reflectance panel was captured for the July 2018 dataset, only a radiometric conversion from raw digital number to radiance values was undertaken.

The final output of the photogrammetric processing chain yielded the following data: RGB point cloud (~ 250 pts/m³), RGB orthophoto (visual reference, 2.9 cm), multispectral orthophotos (reflectance, 8.0 cm) for July 2017, October 2017, May 2018 and multispectral orthophotos (radiance, 7.5 cm) for July 2018. An overview of produced multispectral orthophotos is provided in Figure 4-3 and Figure 4-4.

Table 4-1 Overview of UAV flights undertaken at the north-east section of Monks Wood.

Date	Time	Sensor	GSD	Bands	Conditions	Calibration
26/06/2017	16:41 - 17:00	Sony A6000	< 3 cm	R,G,B	Overcast, even lighting	-
17/07/2017	09:04 - 09:27	MicaSense RedEdge	< 8 cm	R,G,B,RE,NIR	Clear, slight haze at horizon	DLS, Panel
06/10/2017	10:44 - 11:08	MicaSense RedEdge	< 8 cm	R,G,B,RE,NIR	Clear, very few clouds and vapour trails	no DLS, Panel
14/05/2018	10:48- 11:22	MicaSense RedEdge	< 8 cm	R,G,B,RE,NIR	Clear, slight haze at horizon	DLS, Panel
13/07/2018	12:31- 12:52	MicaSense RedEdge	< 8 cm	R,G,B,RE,NIR	Clear	DLS, no Panel

4.2.4 Multispectral data preparation

An image stack was created containing the multispectral orthophotos of the individual flights. Spatial coherence, thus an alignment of features in the scene, was ensured by georectification, resampling and pixel alignment (snapping) of the orthophotos. The individual multispectral orthophotos were georectified using the RGB orthophoto as reference. Three points (distinct features like road markings) were manually selected to perform a first-order transformation, enabling a precise alignment. Georectification was performed in ArcMap (version 10.6), followed by band stacking in QGIS (version 2.18). In QGIS the georectified orthophotos were resampled to ten-centimetre cell size and stacked. A cubic function (4 x 4 kernel) was selected for the resampling process. The resulting stack consists of aligned pixels in 20 bands - five bands per date. To allow a direct comparison of information within the multitemporal image stack, pixel values of individual bands were rescaled to a 0 - 1 range (min-max-normalisation).

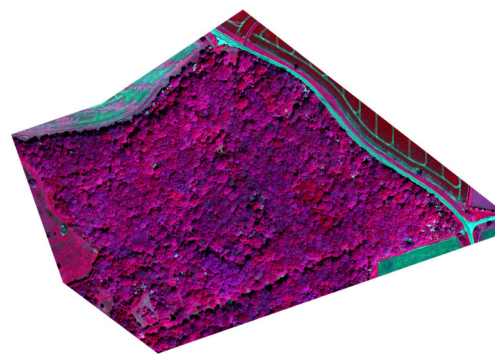|	
July 2017 – RGB	July 2017 – CIR
October 2017 – RGB	October 2017 – CIR
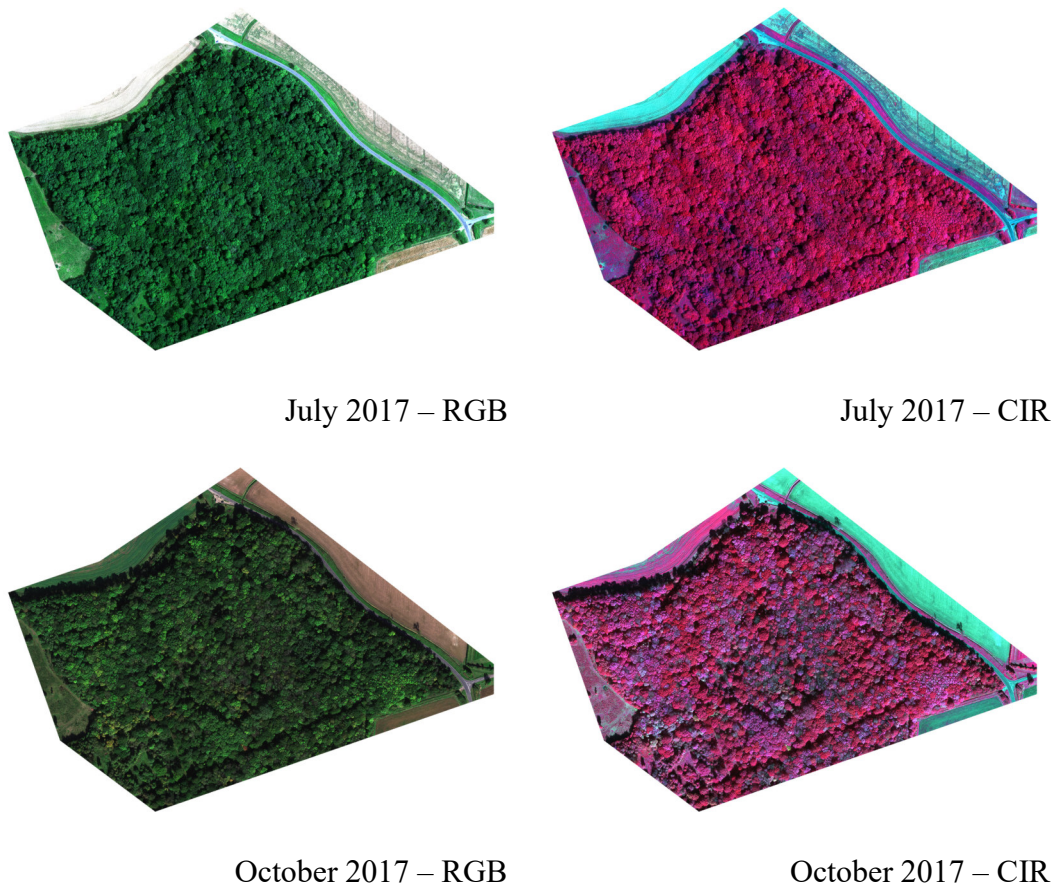
Figure 4-3 Overview of the multispectral imagery captured at Monks Wood in July and October 2017. RGB composites are shown on the left and false colour infrared orthophotos on the right. The July 2017 dataset shows banding due to an obstruction of the NIR band.
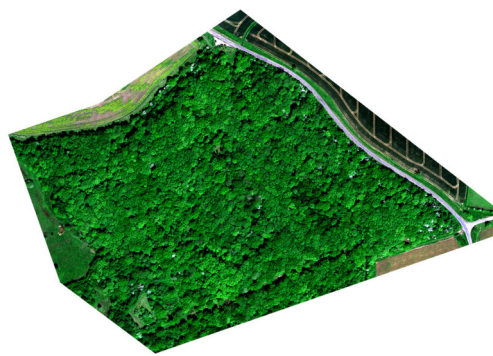
May 2018 – RGB	May 2018 – CIR
July 2018 – RGB	July 2018 – CIR
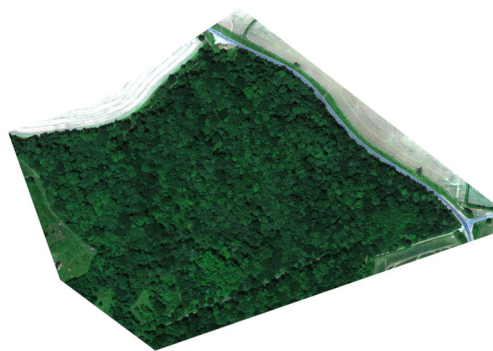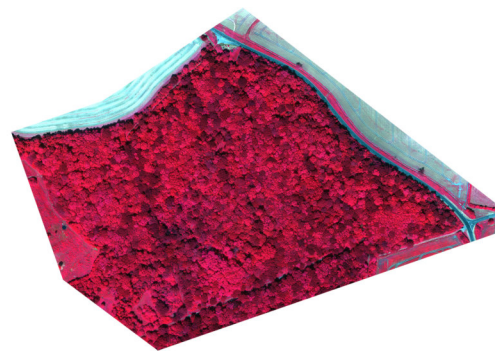
Figure 4-4 Multispectral imagery captured at Monks Wood in May and July 2018. RGB composites are shown on the left and false colour infrared orthophotos on the right.

4.2.5 Canopy height model computation

To assess the value of tree height information for species mapping a CHM was computed at ten-centimetre spatial resolution to match the resolution of the multispectral imagery. The SfM generated canopy surface model laid the basis for the CHM computation at such fine scale. The densified point cloud of the RGB dataset was combined with ground points extracted from 2014 ALS data (publicly available from Defra's Data Services Platform: environment.data.gov.uk). Ground points were determined with the previously introduced CSF method (see section 2.4.1). The hybrid SfM-ALS point cloud served as input for the CHM generation. To avoid pits and spikes in the CHM, the spike-free algorithm (Khosravipour *et al.*, 2016) implemented in LAStools (version 141017) was used with the beam-size parameter set to ten

centimetres. This delivered a CHM without artifacts at the desired spatial resolution. Finally, the CHM was added to the multispectral band stack to utilise canopy height as a feature in the subsequent analysis regarding species classification.

4.2.6 Field data

The ground reference dataset used for training and validation was obtained with a differential GPS (Leica Zeno 20) in January 2018. Leaf-off conditions allowed the collection of position and class samples without the typical multipath issues of dense-canopy forests. Sample locations were surveyed to < 1 m accuracy according to the reported RTK status of the dGPS unit. Positional samples of eight tree species were obtained by placing the dGPS under the perceived crown centre of a tree. A total of 316 individual tree samples were acquired. The alignment of the surveyed tree locations to the remote sensing data was validated with ground control points visible in the RGB orthomosaic. Next, using the RGB orthomosaic as visual reference, tree point samples that did not clearly fall within a tree crown were considered invalid and eliminated. This manual validation process reduced the total number from 316 to 297 tree samples. In addition to these samples, locations for three non-forest classes were picked manually from the imagery: road, agricultural land/soil and grass. As these features should be clearly distinguishable from each other, these classes act as a visual baseline to evaluate the classification performance. A total of 347 samples, consisting of point locations and respective class names, form the ground truth for the present study. The distribution of these samples is depicted in Figure 4-5.
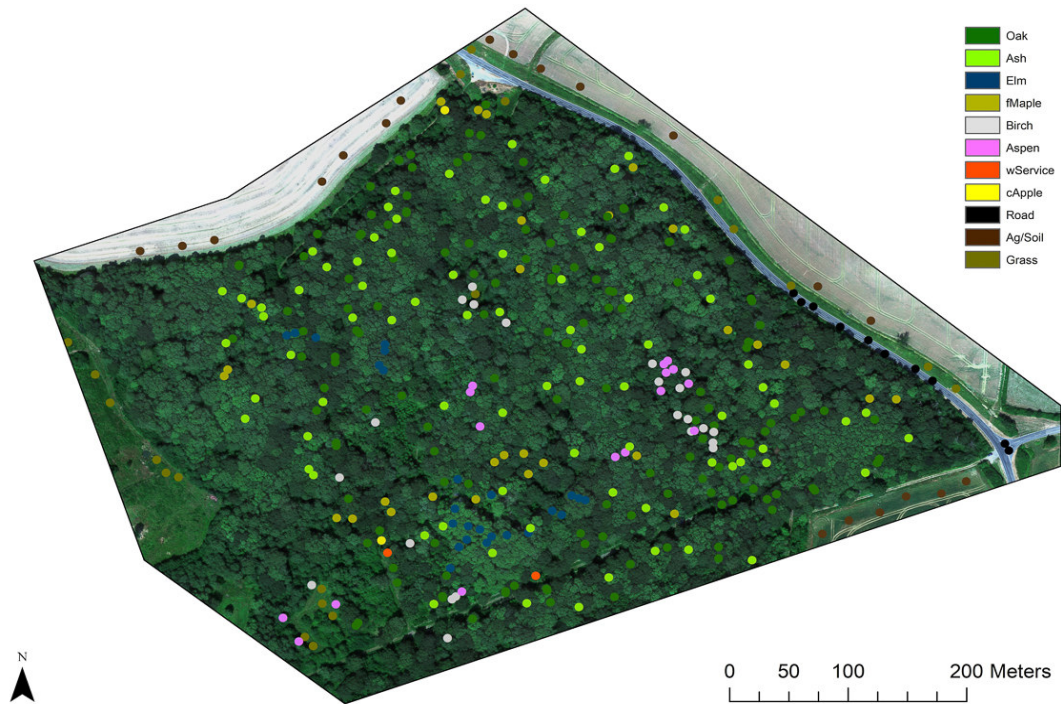
Figure 4-5 Location of the 347 class samples collected. Sample locations of the eight species classes and three background classes are overlaid on the RGB orthomosaic from June 2017.

4.2.7 Analysis

The species mapping was carried out using pixel-wise supervised classification. The underlying method consisted of a multi-class classification using a RF classifier and CV-based accuracy evaluation, with the aim of deriving a detailed species distribution map from the multispectral remote sensing data.

Intermediate steps towards this overall aim were set to test how classification accuracy is influenced by 1) the tree number of the RF classifier 2) the plot size for training sample extraction, 3) the number of training samples, and 4) the combination of multitemporal data. Four tests were conducted in the above order to inform on the impact of these factors and to ultimately optimise the accuracy of the classification. Classification accuracy is subsequently evaluated as the ratio of the number of correctly classified pixels to the total number of pixels, and all tests are scored with 5-fold CV.

The different species found at the study site were not present in equal numbers. To avoid a bias towards a class with higher number of samples (Chen and Liaw, 2004), the RF classifier was trained with "balanced" class weights for all tests. To

achieve this, class weights were adjusted inversely proportional to class frequencies. Specifically:

$$W_j = \frac{n}{kn_j}$$

where W_j is the weight applied to class j, n is the number of samples, n_j is the number of samples in class j and k is the total number of classes.

The pre-processed multitemporal multispectral data provided the independent variables for the classification. In addition to the raw multispectral information from the four flights, canopy height was employed as independent variable. This enabled the potential benefit for species classification to be quantified when used in conjunction with spectral data. However, to force an emphasis on spectral information the weight of canopy height in the class prediction was reduced. CHM data were binned so that individuals from separate species within the same height class are distinguished solely based on their spectral characteristics. CHM values were reclassified into six classes of manually selected height intervals (see Table 4-2 and Figure 4-6). Five metre intervals were chosen as, based on their data distribution most dominant tree species (oak, ash and elm) fall into the 15 – 20 m interval and most sub-dominant species (Field maple, birch, aspen, Wild service, Crab apple) fall into the 10 – 15 m interval. To still enable distinction of smaller bushes (< 2 m) and ground surfaces based on height alone, the 0 – 2 m and 2 – 5 m intervals were chosen. An overview of the per-class height distribution before and after binning is given in Figure 4-7. To rate the effect of binning, classification accuracy was determined for binned and un-binned CHM data in models that contain tree height (see Figure 4-12).

Table 4-2 Binning of CHM values to reduce the weight of canopy height information in the classification.

CHM value	Reclassified value
0 – 2 m	1
2 – 5 m	2
5 – 10 m	3
10 – 15 m	4
15 – 20 m	5
20 – 26 m	6

SfM/ALS CHM   reclassified canopy height
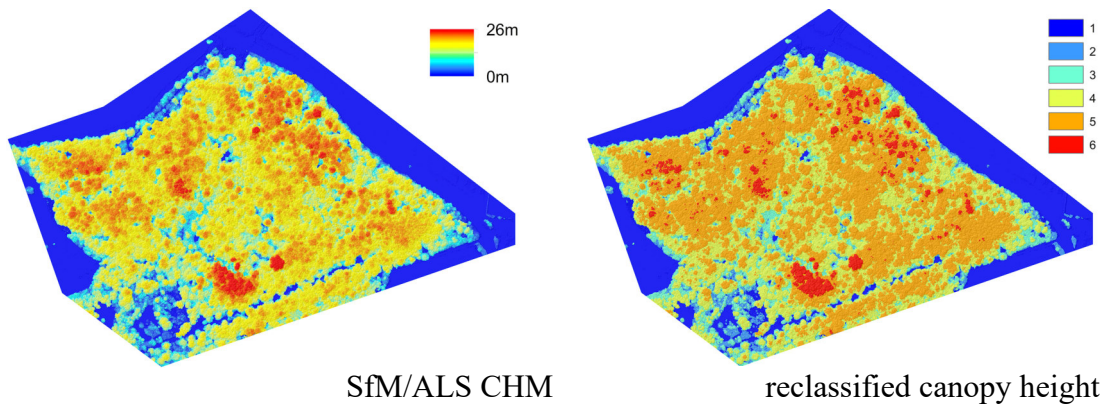
Figure 4-6 The CHM produced at 10 cm spatial resolution for the Monks Wood study site. The CHM is derived from a hybrid point cloud where ground is described by ALS data and the canopy surface is generated from UAV SfM-photogrammetric data. The CHM is displayed with its original values (left) and with the re-classified values (right) that were used in the classification to reduce the weight of tree height information.
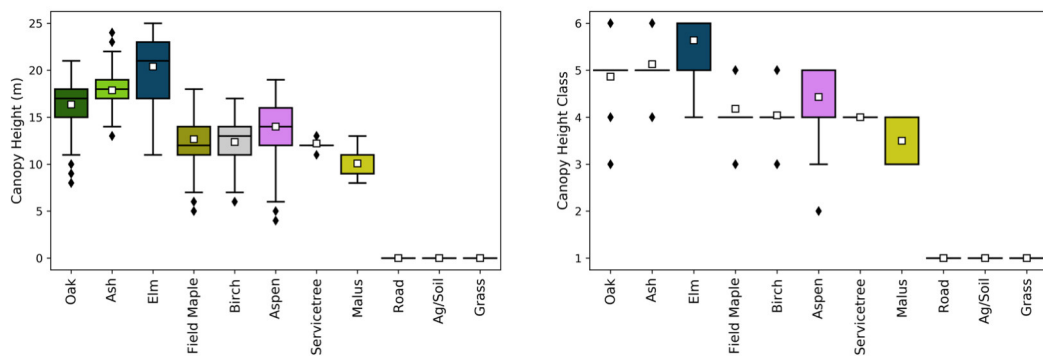
Figure 4-7 Per class canopy height of extracted sample pixels (left) and binned canopy height information (right).

A pixel-based method was used for the classification task. For the class samples, extraction of training and validation data was undertaken by retrieving pixel values from a circular plot around the surveyed tree location. The circular shape was chosen under the assumption that surveyed point samples are central to the crown and that crown shape is generally round. Point locations of the samples were buffered with a suitable radius size that was determined within the current work. Resulting polygons were then used to extract all raster cell values that fall within and intersect these boundaries. Extracted cell values were stored in Pandas (version 0.24) data frames and

tests were performed on only these data, avoiding the production of full-scale maps at intermediate stages, greatly reducing computational efforts.

4.2.7.1 Test 1: the effect of random forest tree size

Firstly, the influence of the number of trees in the RF on classification accuracy was evaluated. This was done to minimise the computational cost without decreasing the achievable classification accuracy. Tree numbers from ten to 1000 were implemented in the RF-based classification, iteratively increasing the number by ten. The influence on classification accuracy was determined using mean and standard deviation of the CV scores as performance metrics. In this test a one-metre radius was chosen as plot size parameter, providing $\sim$ 350 pixels per tree sample with minimal risk of border effects in smaller crowns.

4.2.7.2 Test 2: the effect of plot size

The objective of the test was to ascertain the buffer radius that maximises the quantity of information extracted. Simultaneously, the intention was to optimise the radius to reduce border effects and increase certainty of the signal originating from a single individual tree, thus enhancing classification accuracy. To accomplish this, an iterative process was implemented that tested buffer radii from one centimetre to five metres in five-centimetre increments. At every iteration, a RF-based classifier was trained with the extracted pixel samples for that radius. Classification accuracy was determined with CV. Finally, mean and standard deviation of the CV scores were recorded at every iteration to determine a suitable buffer radius.

4.2.7.3 Test 3: the effect of sample size

This test tested how the quantity of training samples affects the classification accuracy. For this purpose, the training sample size was increased iteratively, with one percent increment step size, providing a proportion of the full dataset at every iteration. A stratified sampling approach was applied to maintain the relative proportion of each class.

The previously-determined plot size was used for the extraction of training pixels from the total sample size of 347 trees. At every iteration, a RF classifier was trained on a proportion of the total number of pixels and the cross-validated classification accuracy

was derived. Mean and standard deviation of the CV scores were assessed to gain insight into the effect of sample size on classification accuracy.

4.2.7.4 Test 4: the effect of data combinations

Having determined suitable plot size, sample size and RF tree number, the final test of this study explored the importance of individual datasets and their combinations for species classification accuracy. This test assessed the role of phenology for tree species mapping at this spatial scale.

The study subsequently evaluated the effect of multitemporal flights to determine whether there is an optimal period during which a species exhibits characteristics that favour its detection and classification. This is particularly relevant for the use of UAVs for which the user has a high degree of autonomy in the decision of when to deploy the aircraft.

Within the general scope of the thesis, to assess the potential for monitoring oak decline, specific focus is given to oak classification performance in this test. The test was set up by training a RF classifier for 31 different input datasets: a dataset for each multispectral flight date and CHM, and datasets for all possible combinations between them (see Table 4-4). As with previous tests, performance was evaluated using mean and standard deviation of the cross-validated accuracy scores. For every date and/or combination Producer's and User's accuracies for all classes were produced, however for the purposes of this study, only the oak class is of relevance.

4.2.7.5 Species map production and assessment

Applying the information gained in the tests above, the previously determined ideal plot size, sample size, number of RF trees and input data combination were implemented to train the classifier and predict the class of every pixel within the entire study site. The importances of individual variables in the final model were assessed using a permutation feature importance approach with 5-fold CV. Per-class accuracies were derived from the confusion matrix and evaluated in terms of Producer's and User's accuracy.

Finally, "salt and pepper" noise, common in pixel-wise classification of imagery with very high spatial resolution, was filtered in the classified map image. This was carried out to improve spatial coherency of the final map by eliminating small specks and

patches of pixels within larger clusters of one species. A focal sieve operation was applied to the species map with a circular (r = 5 m) search window and a minimum pixel threshold per cluster of 1000. The operation firstly groups regions smaller than the minimum pixel threshold and in a following step these smaller regions are assigned the majority class within the set radius. The operation is achieved in ArcGIS using a combination of the tools Region Group, Focal Statistics (Majority) and Nibble available under the Spatial Analyst license. Unlike a majority filter which generalises the image, the focal sieve operation preserves the edges of larger polygons while eliminating patches of pixels that are smaller than the chosen threshold.

4.3 Results

4.3.1 Analysis

4.3.1.1 Test 1: the effect of random forest tree size

This RF specific parameter presented high (> 94 %) accuracies utilising more than 20 trees (see Figure 4-8). Little improvement of classification accuracy is gained using a higher number of RF trees. 100 RF trees was chosen as a practical compromise between accuracy and computational effort and was thus adopted as the method for the following analysis, making results comparable. Further enhancing the randomness and/or robustness by increasing the tree number was not considered necessary.
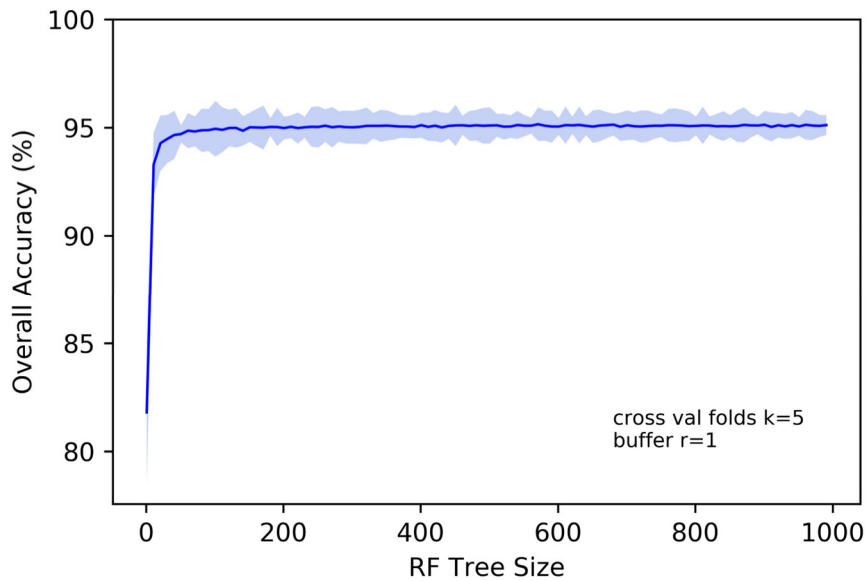
Figure 4-8 The effect of the number of RF trees on the classification accuracy. The blue line constitutes the mean cross-validated accuracy. 5 * standard deviation is depicted in faded blue.

4.3.1.2 Test 2: the effect of plot size

The extraction of training pixels provided the best classification (> 95 %) accuracy at plot sizes under one metre (see Figure 4-9). While radii below 0.6 metres show high mean accuracies, the CV score at every fold offers less consistency, indicated by the higher standard deviation. This is likely due less pixels being extracted at smaller radii, providing lower robustness in the class prediction.

With plot sizes over one metre radius the classification accuracy decreases slightly. This effect is anticipated to be the result of increased probability of including spectral information of neighbouring tree species with increasing buffer radii. Such an effect can introduce noise, contaminating the extracted sample of an expected pure class signal.
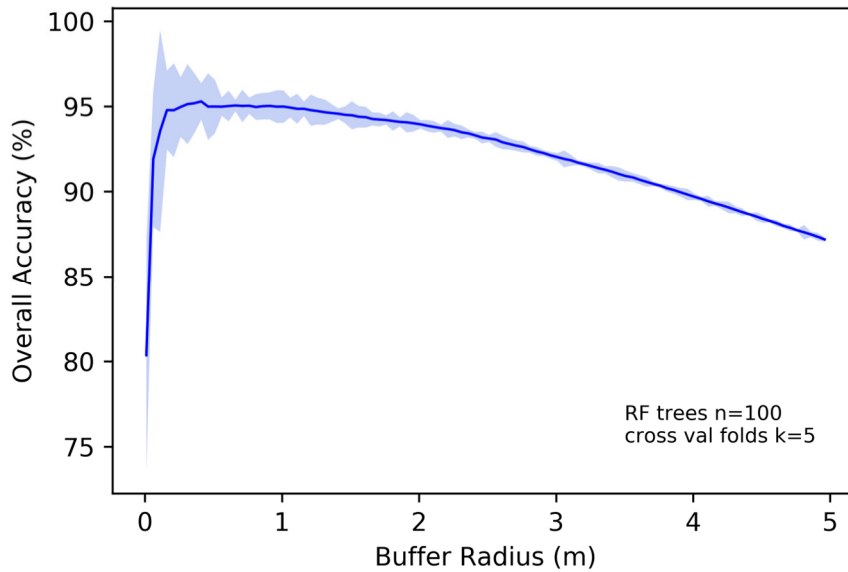
*Figure 4-9 Evaluation of the effect of plot size on classification accuracy. Plot size relates to the buffer radius around the surveyed sample locations used to extract pixel values. The blue line constitutes the mean cross-validated accuracy. 5 * standard deviation is depicted in faded blue.*

The highest classification accuracy in the current test was produced using a 0.45 metre radius, which yielded 95.3 % accuracy. A one-metre radius provided slightly decreased accuracy (95.0 %), but more than four times the number of pixel samples are extracted per plot, theoretically greatly improving model robustness. Therefore, in the following tests a plot size with a buffer radius of one metre was adopted. At this plot size a total of 123185 pixels are extracted across all classes. Wild service tree, as the smallest class, is represented with 709 pixels while oak, as the largest class, amounts to 42584 pixels. An overview of all classes and number of extracted pixels is provided in Table 4-3. Respective per-class feature values are depicted in Figure 4-7 and Figure 4-10.
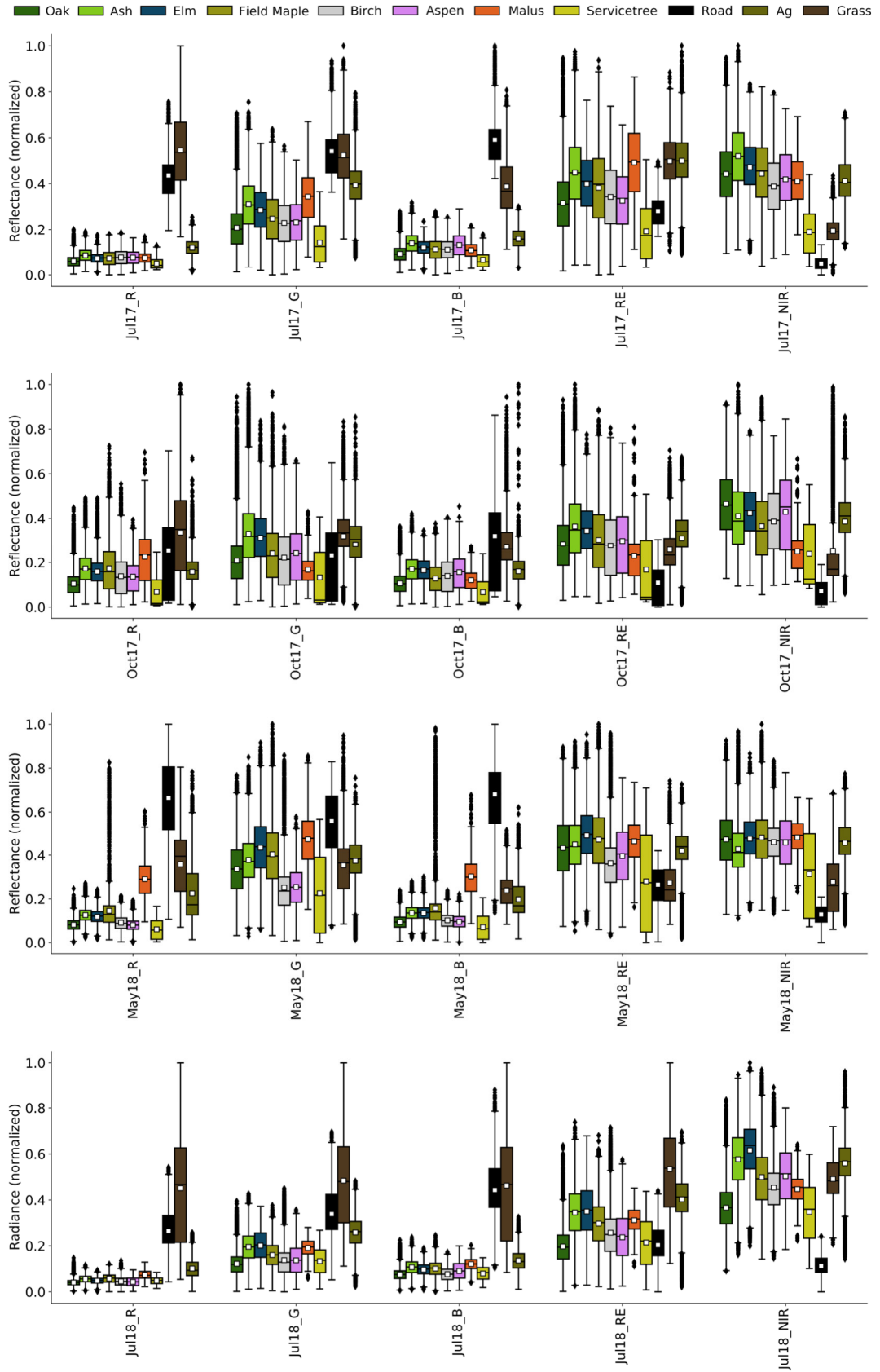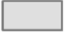
Figure 4-10 Boxplots for reflectance/radiance of the individual UAV acquisitions illustrated per class.

Table 4-3 Overview of classes and respective sample quantities. The number of surveyed sample locations is provided. Pixels extracted with the best performing plot size (r = 1 m) are also presented.

	Class	# of samples	# of pixels extracted at r = 1 m
	Oak	120	42584
	Ash	81	28757
	Elm	25	8882
	fMaple	29	10283
	Birch	22	7805
	Aspen	16	5690
	wService	2	709
	cApple	2	712
	Road	10	3552
	Ag/Soil	20	7096
	Grass	20	7115
	SUM	347	123185

4.3.1.3 Test 3: the effect of sample size

The test yielded the highest classification accuracy (95 %) using 100 % of available sample pixels (extracted at r = 1 m plot size) for training the classifier (see Figure 4-11). Though such behaviour is expected it is notable that, with the given input data, classification accuracy merely decreased by two percentage points (93 %) with half the amount of training pixels and by four percentage points (91 %) when training on 20 % of the available data.

As the objective of the present study was to produce a species map with high classification accuracy, the entirety of available sample pixels was used for further analysis.
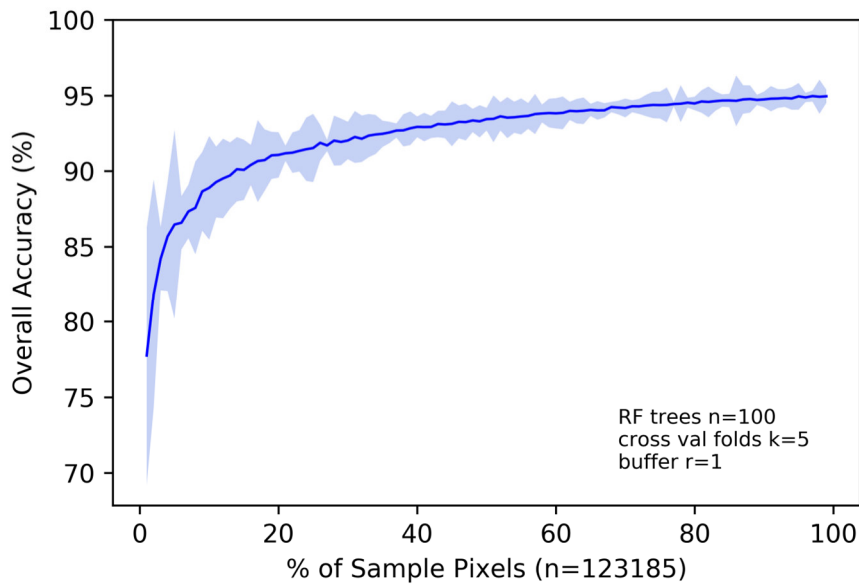
Figure 4-11 Assessment of classification accuracy relative to the proportion of pixels used in training the classifier. The blue line constitutes the mean cross-validated accuracy. 5 * standard deviation is depicted in faded blue.

4.3.1.4 Test 4: the effect of data combinations

The parameters established in the previous tests were applied in this final assessment: one-metre radius plot size, 100 % of available sample pixels and 100 RF trees. Using these parameters, the highest overall classification accuracy (95 %) was achieved when the model is trained on all available datasets, including multispectral information (raw band data) from four flights and binned canopy height information (Jul17-Oct17-May18-Jul18-SfMCHM). Results for all combinations of the datasets are presented in Figure 4-12 and Table 4-4. Overall classification accuracies report the accuracy across all classes, including non-tree classes that may be considered background. Separate reference is given to User's and Producer's accuracies of the oak class.
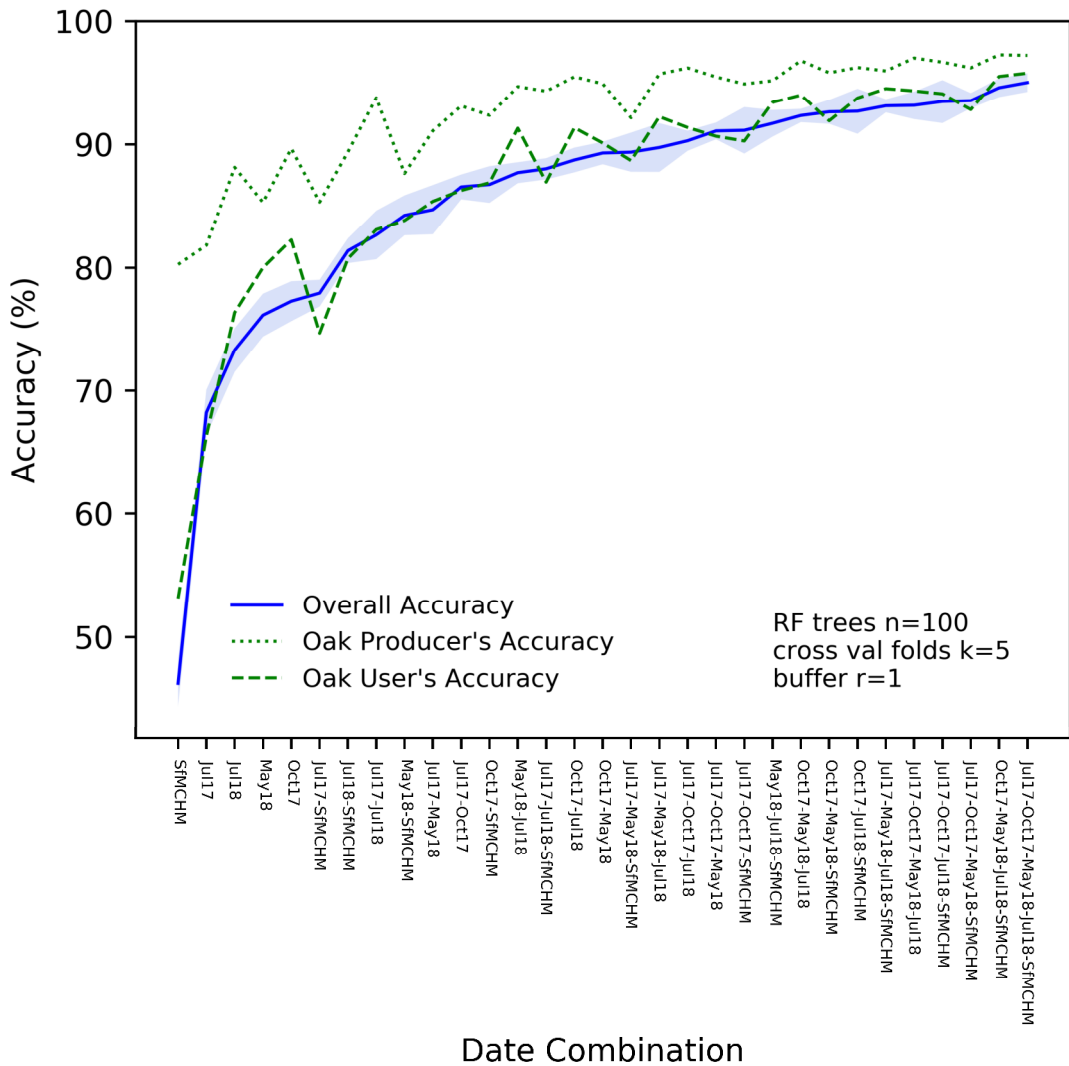
Figure 4-12 Classification accuracy achieved for different combinations of the available input datasets. The blue line constitutes the mean cross-validated accuracy. 5 * standard deviation is depicted in faded blue. User's and Producer's accuracies specific to the oak class are presented as separate line in green.

The lowest overall classification accuracy (46 %) was yielded by the canopy height information alone (SfMCHM). Un-binned canopy height information increased the accuracy to 50 %, reported in Table 4-4.

From the individual multispectral acquisition dates, the autumn imagery (Oct17) offers the highest overall classification accuracy (77 %). This is a sensible result as foliage characteristics, defining the derived reflectance, show the greatest difference between species during senescence. The autumn imagery captured for this study shows the forest at a mid/late senescence stage. At this phenological stage, Field maple, Wild service and Crab apple were conspicuous with a distinctive leaf tint. Ash, elm, birch

and aspen trees had begun to senesce and oak had not yet shown signs of discoloration. Of note is that many ash trees had already partly or fully shed their leaves due to the presence of the ash dieback disease.

With 76 % classification accuracy, the spring imagery (May18), closely followed the autumn imagery classification performance among the individual datasets. Similarly, to the autumn seasonal transition, inter-species differences are also enhanced during the early growth stage.

The contrary effect is observed for the mid-season growth stage when phenological differences between tree species are less apparent. Accordingly, the summer acquisitions' overall classification accuracy was lower, delivering 73 % for the Jul18 dataset and 68 % for the Jul17 dataset. The difference in classification accuracy between the two summer datasets is potentially caused by the technical difficulties that caused vignetting in the NIR band of the Jul17 imagery.

When combining two datasets, overall classification accuracy is increased to 83 - 90 % accuracy. Of the two-date combinations, the autumn imagery paired with the spring imagery (Oct17-May18) delivered the highest overall classification accuracy (90 %). These are also the two dates delivering the highest classification accuracy of the single date classifications. Their combination exploits the phenological phases when differences between species are most evident. Other combinations of two spectral datasets also yield high accuracies, from 83 % for the Jul17-Jul18 combination.

The combination of a spectral dataset with the binned height information (*-SfMCHM) provided an accuracy enhancement of around nine percentage points. Un-binned canopy height showed accuracy increases of up to 16 percentage points compared to spectral data alone. The highest accuracy of single-date spectral data combined with canopy height was achieved with autumn imagery (Oct17-SfMCHM). A combination of three or four datasets increases the overall classification accuracy further, although only marginally. Combining three datasets delivered overall accuracies between 88 % and 93 % while four datasets yielded overall accuracies between 93 % and 95 %. The combination of all available data provided the highest accuracy overall and was thus used in producing the final species map.

Classification accuracies for oak pixels are in general agreement with the overall classification accuracy though a slightly different pattern emerges (see Figure 4-12). Producer's accuracy was generally higher than the overall classification accuracy indicating that a high proportion of the oak reference samples were classified correctly

by every date and combination of data. Producer's accuracies for individual dates and the CHM presented were above 80 % with May18, Jul18 and Oct17 datasets scoring 85 - 90 %. User's accuracies closely follow the trend of the overall classification accuracy, with the lowest performing datasets being SfMCHM (53 %) and Jul17 (66 %). However, Jul18 and Oct17 present slightly elevated User's accuracies compared to the other datasets. This effect holds true when Jul18 and/or Oct18 are combined with other data.

Table 4-4 Combinations of available datasets with the achieved overall classification accuracy (OCA) and standard deviation (SD) across the 5 folds in CV. For models with SfM-CHM information, OCA for un-binned tree height data is indicated with*.

DATA	OCA (%)	SD (%)	Oak Producer's Accuracy	Oak User's Accuracy
SfMCHM	46.24 *50.78	0.19	80.26	53.15
Jul-17	68.40	0.22	81.82	66.31
Jul-18	73.46	0.26	88.14	76.36
May-18	76.26	0.18	85.31	80.00
Oct-17	77.47	0.15	89.65	82.27
Jul17-SfMCHM	78.17 *84.72	0.16	85.33	74.68
Jul18-SfMCHM	81.50 *86.47	0.07	89.38	80.74
Jul17-Jul18	82.98	0.20	93.75	83.10
May18-SfMCHM	84.32 *89.05	0.24	87.65	83.85
Jul17-May18	84.99	0.17	91.08	85.39
Jul17-Oct17	86.84	0.14	93.09	86.27
Oct17-SfMCHM	86.92 *91.31	0.12	92.34	86.89
May18-Jul18	88.01	0.06	94.67	91.29
Jul17-Jul18-SfMCHM	88.25 *91.10	0.13	94.30	86.95
Oct17-Jul18	89.05	0.12	95.47	91.33
Jul17-May18-SfMCHM	89.52 *92.11	0.17	94.91	90.10
Oct17-May18	89.56	0.08	92.14	88.68
Jul17-May18-Jul18	90.03	0.12	95.70	92.22
Jul17-Oct17-Jul18	90.56	0.02	96.19	91.35
Jul17-Oct17-SfMCHM	91.31 *93.53	0.15	95.46	90.65
Jul17-Oct17-May18	91.31	0.07	94.89	90.26
May18-Jul18-SfMCHM	91.80 *94.00	0.10	95.15	93.39
Oct17-May18-Jul18	92.62	0.13	96.78	93.98
Oct17-May18-SfMCHM	92.76 *94.66	0.09	95.80	91.89
Oct17-Jul18-SfMCHM	92.84 *94.67	0.15	96.23	93.74
Jul17-May18-Jul18-SfMCHM	93.26 *94.89	0.09	95.95	94.51
Jul17-Oct17-May18-Jul18	93.38	0.04	97.00	94.32
Jul17-Oct17-May18-SfMCHM	93.66 *95.06	0.08	96.66	94.08
Jul17-Oct17-Jul18-SfMCHM	93.67 *95.02	0.13	96.20	92.80
Oct17-May18-Jul18-SfMCHM	94.78 *95.96	0.12	97.26	95.49
Jul17-Oct17-May18-Jul18-SfMCHM	95.11 *96.02	0.08	97.21	95.77

4.3.1.5 Species map production and assessment

The best performing model, containing all four available spectral datasets combined with weighted canopy height information, was adopted to predict classes for all pixels in the study site. The feature importances determined for this model are presented in Figure 4-13. Binned canopy height is the most important feature in this model. NIR bands of all dates except Jul17 received high feature importance scores. The lower feature importance of Jul17_NIR can potentially be attributed to the previously described technical issue that had caused vignetting of this band. It is also notable that RE bands of all dates did not receive high feature importances in this final model.
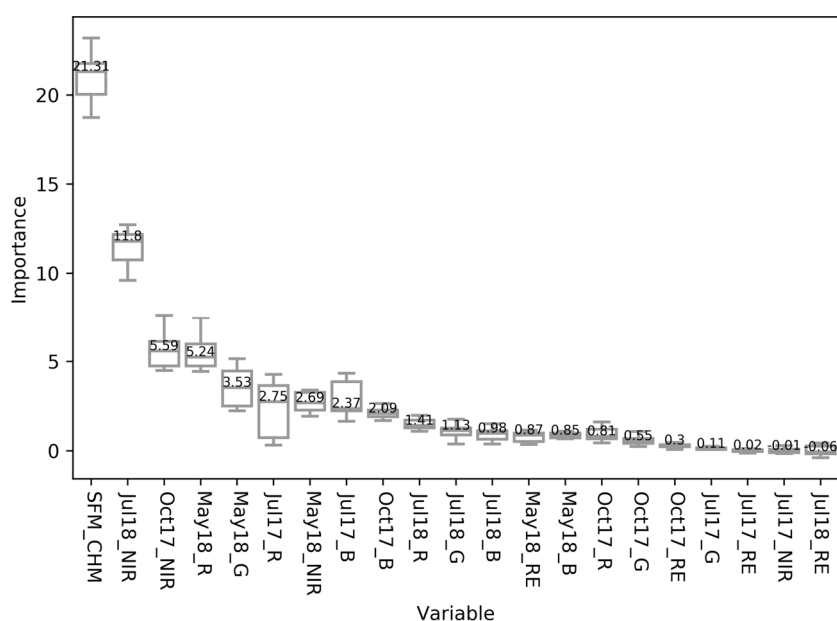
Figure 4-13 Permutation feature importances for all features included in the best model (Jul17-Oct17-May18-Jul18-SfMCHM). Feature importance determined from 5-fold CV.

Per-class Producer's accuracies ranged from 83 % to 100 % and User's accuracies from 90 % to 100 % across all classes (see Table 4-5). All non-forest classes (Road, Ag/Soil, Grass) were classified with 100 % accuracy. The lowest Producer's accuracy (83 %) was achieved for the Field maple class, whose pixels were most commonly misclassified as oak or ash (see Table 4-6). The two most abundant species at Monks Wood, oak and ash were classified with Producer's accuracies of 97 % and 96 % respectively. Their User's accuracies are 96 % for oak and 90 % for ash. Other classes were most commonly misclassified as ash as indicated by its lowest User's accuracy score of all the classes.

Table 4-5 Per-class classification accuracy presented as Producer's (Precision) and User's (Recall) Accuracy. Per class accuracies were derived from the confusion matrix for the best model (Jul17-Oct17-May18-Jul18-SfMCHM).
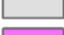
		Producer's Accuracy (%)	User's Accuracy (%)	Support: # of Pixels
	Oak	97	96	42584
	Ash	96	90	28757
	Elm	89	94	8882
	fMaple	83	95	10283
	Birch	98	96	7805
	Aspen	88	99	5690
	wService	96	100	709
	cApple	99	100	712
	Road	100	100	3552
	Ag/Soil	100	100	7096
	Grass	100	100	7115
Avg / Total		95	97	123185

Table 4-6 Confusion matrix for the final class prediction with the best model (Jul17-Oct17-May18-Jul18-SfMCHM), RF trees n = 100 and 5-fold CV.

						Predicted					
		Oak	Ash	Elm	fMaple	Birch	Aspen	wService	cApple	Road	Ag/Soil	Grass
Reference	Oak	41395	1084	63	23	7	12	0	0	0	0	0
	Ash	587	27487	433	236	2	12	0	0	0	0	0
	Elm	77	899	7836	47	9	14	0	0	0	0	0
	fMaple	884	739	10	8547	79	24	0	0	0	0	0
	Birch	106	23	0	26	7642	8	0	0	0	0	0
	Aspen	203	215	6	70	225	4971	0	0	0	0	0
	wService	1	0	0	31	0	0	677	0	0	0	0
	cApple	4	1	0	4	0	1	0	702	0	0	0
	Road	0	0	0	0	0	0	0	0	3552	0	0
	Ag/Soil	0	0	0	0	0	0	0	0	0	7096	0
	Grass	0	0	0	0	0	0	0	0	0	0	7115

The final species map produced from the RF-based classification features a spatial resolution of ten centimetres. The potential to precisely locate the tree species was thus greatly increased compared with the previous species map, derived from piloted aircraft data, that offered two-metre resolution (Hill *et al.*, 2010). Figure 4-14 demonstrates the enhanced resolution offered by the UAV-derived species map. The round shape of individual tree crowns can be distinguished in the current species map, illustrating better definition of borders to neighbouring species. Conversely, the coarser resolution data means that differentiation of species within the 2003 data is limited to larger clusters of trees.
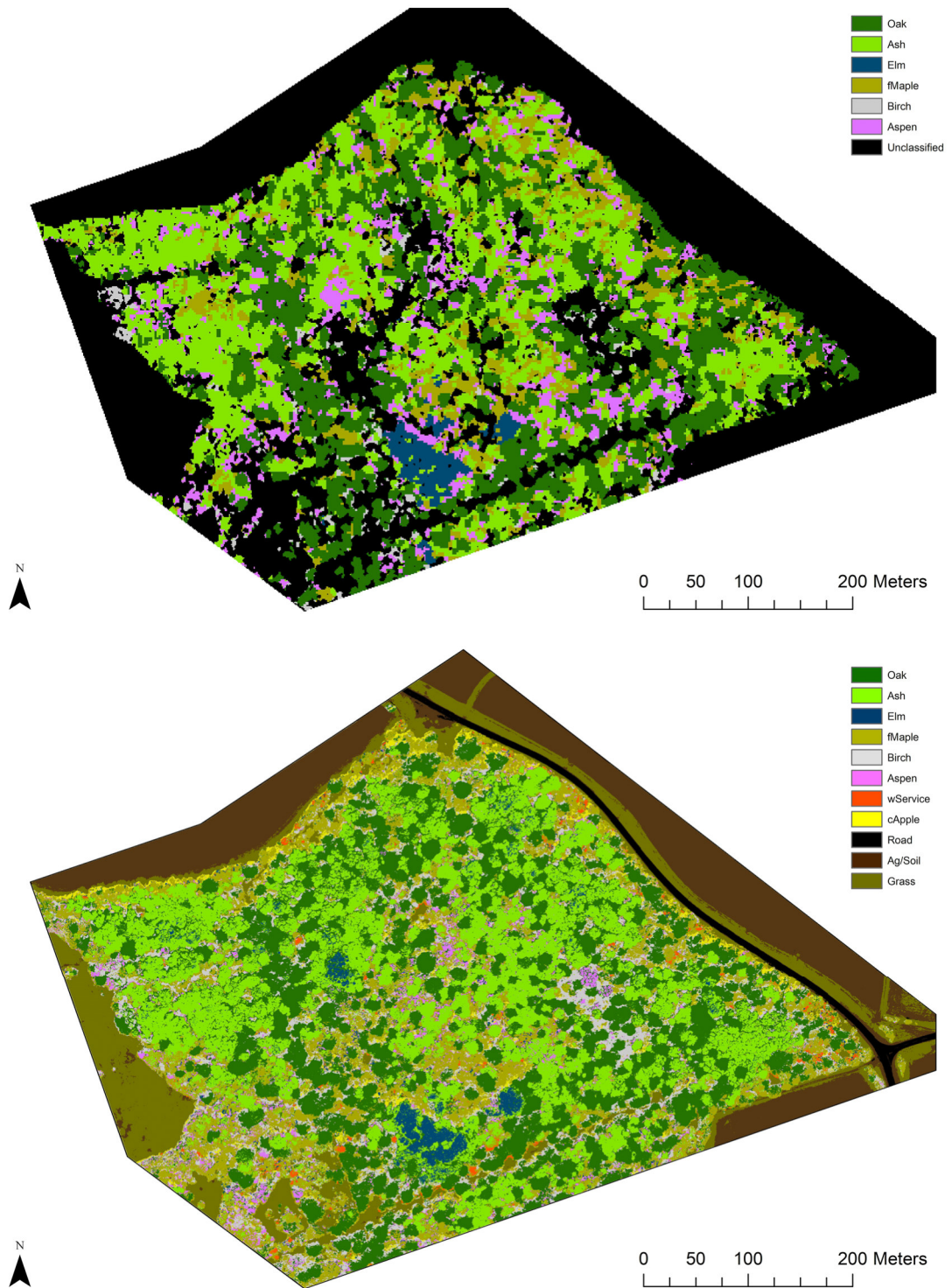
Figure 4-14 At the top: species map of Monks Wood NE section derived from 2003 Airborne Thematic Mapper timeseries at 2 m resolution (Hill et al., 2010). At the bottom: species map derived from 2017/2018 multitemporal multispectral UAV imagery, produced at 10 cm resolution.

The focal sieve operation undertaken on the pixel-based result smooths the species map assigning regions of 1000 pixels or less to adjacent classes. Removing the salt and pepper noise did not alter the overall classification accuracy, which remained 95 %, however, spatial coherence is visibly improved (compare Figure 4-14 and Figure 4-15). It is to be noted that the focal sieve operation introduced a minimum mapping unit of 10 m², which represses reproduction of objects smaller than this threshold. In the current application, to identify crowns and larger patches of oaks, the introduction of this minimum mapping unit was intended. The image resolution of 10 cm is maintained, allowing for clear representation of borders between classes.
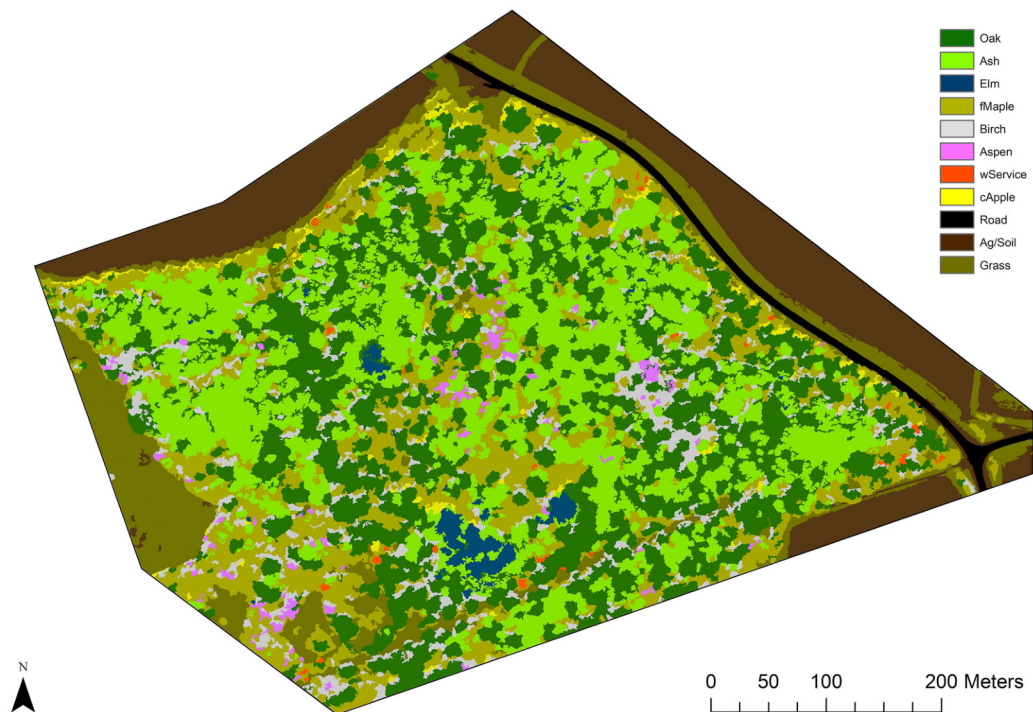
Figure 4-15 The final species map produced from 2017/2018 multitemporal multispectral UAV data, following a focal sieve operation for "salt and pepper" noise removal. In the focal sieve operations clusters few pixels were grouped to regions of 1000 pixels and above. This procedure improved spatial coherence while maintaining the original resolution of 10 cm, however introducing a minimum mapping unit of 10 m².

4.4 Discussion

This study used multitemporal UAV-derived datasets to update a pre-existing species map which had been produced from imagery captured from a piloted aircraft in 2003. The current study succeeded in increasing class separation from seven to eleven species, and improving spatial resolution from two metres to ten centimetres. This enabled greater definition of the canopy boundaries and facilitated class separation as a consequence of less spectral mixing.

The prediction of 11 classes yielded 95 % overall accuracy, utilising all available data. This improves the accuracy of the previous species map (Hill *et al*., 2010) that features 88 % OCA (84 % without clump and sieve). The high classification accuracy obtained in the current study can be attributed to the quantity of available data, both in terms of independent data (four dates of multispectral information plus canopy height information) and in terms of available training samples.

Multitemporal data can offer increased information content to enhance classification accuracy, however geometric calibration is required. This is critical for the correct alignment of features on the ground throughout the multitemporal image stack. Consequently, the need for locational and geometric accuracy increases with increased spatial resolution.

In the current study, repeated capture of high-resolution images of Monks Wood was enabled by a UAV equipped with a miniaturised multispectral sensor. SfM-photogrammetry allowed images from the non-calibrated sensor to be processed into geometrically-reliable orthophotos. As a result, the relative positional accuracy of orthophotos in this study is high. However, manual adjustments (affine transformations) were required to correctly align all datasets.

A direct georeferencing approach with PPK-computed image locations for the multispectral imagery and/or the incorporation of ground control point information in the SfM pipeline would lower the need for such manual adjustments. For future UAV-based acquisitions of multitemporal data, such approaches should ideally be considered to increase the achievable absolute positional accuracy of image-derived 3D models and respective orthophotos.

The overall accuracy score for the final model and map was determined to be 95 % using cross validation. Despite the high accuracy score, misclassifications are expected to have occurred. An example are thin elongated sections classified as Crab

Apple along the northern edge of the woodland where hedgerows are present. Species within hedgerows were not included in the collection of class samples, thus these areas are high potential of being misclassified. Pixels assigned to the Crab apple class within hedgerows possibly belong to species from the *Crataegus* genus, as these also exhibit white flowers in spring.

The species map, as produced by the classifier, also exhibits small scale misclassifications, that can be described as "salt and pepper" noise. In the present case study, utilising a multitemporal dataset, such noise can be attributed to small differences in crown morphology, canopy illumination and viewing angles, plus potential registration errors between the image acquisitions. "Salt and pepper" noise is predominantly present in shadowed areas between tree crowns and as few isolated regions where small gaps in the canopy occur. One such example of these misclassifications are thin lines of pixels classified as oak between individual ash trees (which in reality are canopy gaps and/or shadowed ash crowns). This can be observed in the most western and most eastern section of the species map where larger clusters of ash trees are present.

The previous species map was post-processed with a clump and sieve procedure to negate this issue (Hill *et al.* 2010). With such filtering the authors were able to increase the classification accuracy from 84 % to 88 % (Hill *et al.*, 2010). In the current study, a filtering stage, by a focal sieve operation, was also applied post-classification. The operation delivered the intended result of smoothing the output, removing small specks of isolated pixels, yet preserving the boundaries of the larger regions. Although pixels were assigned to other classes by the procedure, overall classification accuracy remained at 95 %.

The visual inspection of the smoothed species map, aided by the high-resolution RGB orthomosaic (~ 3 cm GSD), showed less small-scale artefacts and better spatial class coherency. However, it is to be noted that a minimum mapping unit of 10 m² was introduced. For some applications, such as the identification of larger regions belonging to a single species (a requirement in CHAPTER 5), the introduction of a minimum mapping unit is desired and the focal sieve procedure thus presents a useful post-classification procedure. However, depending on the application of the species map, the pixel-based result, where the spatial resolution matches the minimum mapping unit, may be preferred.

In this study, the tests provided highlighted the importance of parameter optimisation. The knowledge gained from these trials also provided important reference points to inform future studies attempting tree species classification with UAV acquired imagery. Specifically, it was found that a compromise between field and computational efforts and classification accuracy can be determined. The main parameter in RF modelling, the number of RF trees, showed no significant increase in classification accuracy above 20 trees with the current multitemporal UAV data. The chosen 100 RF trees in the current analysis presented a good trade-off between robustness and processing time and are in line with the results from other research fields, where it was found that between 64 and 128 trees are optimal (Oshiro *et al.*, 2012).

Further reference points for future work on species classification are regarding the quantity of the training data and the timing of UAV data acquisition. These parameters and their influence on classification accuracy are discussed in further detail in the following paragraphs.

The method devised for this study extracted pixels for training and validation from circular plots around the tree point locations that were collected in the field. Plot sizes between 0.1 metre and four metre radii generally yielded classification accuracies above 90 % for the species class samples. However, smaller plot sizes are less robust since they comprise fewer pixels and larger plot sizes exhibit higher risk of spectral contamination of samples by including pixels on the edge of the crown or outside the crown of a surveyed tree. Furthermore, computational efforts to train the RF classifier increase relative to radius size.

In the current case of a heterogeneous broadleaf forest mapped with ten-centimetre image resolution, the radius selected to apply going forward was one metre. Despite a 0.45-metre radius yielding the highest accuracy in the test, a one-metre radius provided a good compromise between accuracy, robustness and run-time. With ~ 350 pixels extracted per tree location, a one-metre radius provided more than four times the amount of training and validation information than a 0.45-metre radius. At one metre radius, spectral information is collected explicitly for every class sample, as overlapping of sample plots will occur only with radii above 1.25 metres in the present case. However, survey inaccuracies (GNSS multipath issues) remain a potential issue for the extraction of pure class signals. Nevertheless, in this case a

visual inspection of the one-metre radius sample plots showed good accordance with tree crowns depicted in the UAV imagery.

For sample pixels extracted from the one-metre plots, even 20 % of available training pixels provide a classification accuracy that is not far below the maximum achievable classification accuracy. Although this result indicates that fewer samples are needed to achieve high classification accuracy, it was possible to test a reduced quantity of training pixels, keeping the number of ground samples the same. To draw conclusions about required effort for future ground truth surveys, this test should be repeated in the form of an actual sample reduction. It was not possible to test this at the current site since, for some classes, very few samples were available (e.g. Wild service tree, only two samples available). A further interesting question is whether the use of less image data would require more training samples to achieve a similarly high classification accuracy. To minimise field efforts, in terms of ground truth and UAV data acquisition, future work should examine these factors in the scope of tree species classification.

The timing of UAV acquisitions showed a clear advantage of autumn and spring imagery for classification accuracy. These results are consistent with previous studies on tree species classification (Hill *et al.*, 2010). October and May data produced highest classification accuracies of single date acquisitions.

Although the phenological characteristics at these growth stages might be optimal for classification of tree species, they might not be as well suited for additional research based on the same remote sensing data (e.g. derivation of inventory metrics, health assessments, etc.). Furthermore, spring and autumn periods are typically not ideal for UAV acquisitions regarding unstable weather and unfavourable light conditions due to the low sun angle.

Consequently, a collection of mid-growth season imagery might be beneficial. If only one flight campaign is possible, these data, although offering lower class distinction on their own, can be complemented by structural information to enhance classification accuracy. The incorporation of binned canopy height information increased classification accuracy of a single dataset by approximately nine percentage points, yielding a higher classification accuracy for summer imagery combined with this information (82 %) than autumn imagery alone (77 %). These results are promising to produce species maps from a single sensor. Spectral derivatives such as vegetation indices may prove useful to further improve classification accuracy of a

single acquisition/dataset. Future work should investigate further the potential of classifying species from a single UAV acquisition, utilising vegetation indices.

Canopy height was demonstrated to be highly beneficial to classification performance in the present case. These findings align with earlier remote sensing work on species classification at broader scales (Holmgren *et al.*, 2008; White *et al.*, 2016; Wulder *et al.*, 2008; Xie *et al.*, 2019). When combined with single-date multispectral data, the inclusion of tree height information resulted in a significant improvement in classification accuracy. Moreover, the feature importance analysis highlighted the significance of canopy height, which outperformed all other tested features.

It is likely that the high importance of this feature can be attributed to the clear distinction between the dominant tree species (oak, ash and elm) and the sub-dominant species (Field maple, birch, aspen, Wild service, Crab apple) at this site using canopy height information (see Figure 4-7). Additionally, in the present classification task, the significance of canopy height may be overstated as non-forest classes are also included. The differentiation between forest and non-forest classes is facilitated by the fact that non-forest classes are located at ground level or close to it.

The results indicated that in order to enhance the accuracy of species and land cover classification using UAV data, canopy height should be considered. This is especially true when information regarding ground elevation is accessible, such as publicly available ALS data, which is the case for the majority of Britain. The approach demonstrated in this study, which combines the use of surface height obtained through SfM photogrammetry and ground elevation derived from LiDAR, can be valuable in obtaining canopy height with high spatial resolution. If the LiDAR data are acquired during a period of leaf-off conditions or are outdated, the hybrid approach provides an additional benefit by enabling the generated CHMs to correspond directly to the spectral data both structurally and temporally.

Although binning of canopy height information succeeded in increasing the influence of spectral data in the analysis, it has been demonstrated that for achieving the highest possible classification accuracy, using un-binned height data is more advantageous. Moreover, increasing the weight of spectral data would have been possible to accomplish internally within the random forest algorithm, resulting in a more objective approach to reducing the weight of canopy height, rather than relying on manually selected binning intervals. Future research may take this into consideration.

Considering the specific requirements of identifying oak trees for decline analysis, high Producer's and User's accuracies were achieved across all data combinations. The data combinations required to classify oak were similar to those observed across all classes. However, it was evident that autumn imagery is particularity well suited to the task of mapping oak within the mixed broadleaf canopy of Monks Wood. The single date model consisting of Oct17 imagery scored the highest Producer's and User's accuracies, and every combined model containing these autumn data produced slightly increased accuracy for the oak class. It is logical that discolouration of oak leaves due to autumnal senescence is especially appropriate for distinguishing from other classes. Whilst other tree species may show similar changes in leaf pigmentation, they may do so at a slightly different time.

Using the combination of all available datasets was found to deliver the highest oak classification accuracy, with 97 % Producer's and 96 % User's accuracy, enabling future AOD detection analysis to be targeted on oak.

Besides the production of a species map, the goal of the current study was to inform on species classification from a practical perspective, specifically the ease of using a single sensor/data source. Canopy height however, requires the normalisation of SfM-derived surface heights by a secondary data source such as ALS information. In future studies the incorporation of textural metrics rather than height information can be considered as these metrics do not require additional data sources and have been reported to significantly improve tree species classification from optical UAV remote sensing data (Gini *et al.*, 2018).

From the analysis of raw band data contained in the final model, NIR information exhibits high importance, likely due to its link to chlorophyll content. Spectral information in the visible range were also important variables for species classification, while RE information seems is less important for class distinction at this site.

———————

This study has explored important characteristics of survey design for implementation of UAV-remote sensing-based species mapping. Criteria have been identified to optimise species classification in diverse forests and offer a reference point for future similar studies.

However, results are valid at this study site using this ground truth dataset, and it is uncertain whether the same classifier would produce similar accuracies at a different site. Furthermore, it is to be noted that the "optimal" parameters determined in the current study, may not be universally applicable. Should, for example, trees have a more uniform crown size or if tree location ground truth is not available at high positional accuracy, then the plot size needs to be adjusted accordingly. With decreasing survey accuracy, it might be justified to decrease the plot size to avoid unwanted border effects and thus contamination of class signal.

4.5 Conclusion

UAV-acquired multispectral data were shown to be well-suited to tree species classification. An overall accuracy of 95 % was achieved for the pixel-wise classification, employing a random forest classifier. 11 classes were derived and a species map was produced at ten-centimetre spatial resolution. As additional result, the produced species map was filtered by a focal sieve procedure, introducing a minimum mapping unit of 10 m². A one-metre plot size was determined as optimal for the extraction of sample pixels at that resolution, given that the survey accuracy of ground truth is high. For the specific objective of classifying tree species with UAV-remote sensing data, imagery acquired in autumn and spring is most suited to differentiate between classes. Combining spectral and structural information as derived from the same source data shows promising results to produce high-accuracy species maps based on a single UAV flight.

CHAPTER 5:

UAV REMOTE SENSING FOR THE DETECTION OF ACUTE OAK DECLINE

AND SPECIES-SPECIFIC PREDICTION OF TREE HEALTH

5.1 Introduction

Acute Oak Decline is a recently defined disease posing a threat to native oak trees in the UK (Denman and Webber, 2009) and is complex in nature, currently still without all causes and implications known. A key symptom of AOD are stem bleeds in the form of dark fluid seeping lesions. Necrotic tissue beneath the bark plates creates cavities that eventually start leaking fluid through vertical cracks in the bark. Trees affected by AOD may die within three to five years as necrotic patches on the stem are believed to disrupt vascular flow, ultimately girdling the tree (Denman *et al.*, 2014). In the course of the disease, trees with stem bleeds also tend to exhibit poor crown condition (Brown *et al.*, 2016; Denman *et al.*, 2014). Reduced crown vigour is not specific to AOD but is rather a symptom of oak declines in general. However, decreased crown vitality in the case of AOD is likely to be associated with necrotic tissue present on the stem. This reciprocal effect underlies the investigation in this chapter, namely whether an onset and advanced state of AOD are identifiable in the crown of affected trees.

At Monks Wood National Nature Reserve in Cambridgeshire, numerous trees have been identified as showing symptoms of AOD, specifically actively bleeding stem lesions. Little is known about the relationship between the expression of symptoms on the stem and the manifestation of reduced health in the crown. However, in the course of the decline, stress induced by hampered vascular flow is expected to promote changes in leaf chemistry, defoliation and dieback. These expected differences between symptomatic and asymptomatic trees lay the basis for the current investigation. Multitemporal UAV-acquired multispectral data are evaluated regarding their spectral and textural characteristics and their ability to relate to differences in crown condition that are expected between AOD and control trees. The composition of Monks Wood, characterised by a dense canopy and a rich diversity of species, presents a significant challenge to the research project. Consequently, methods for extracting oak signals that are as pure as possible are elaborated.

5.2.1 Field data

A preliminary survey carried out by the PuRpOsE project (Mitchell *et al.*, 2019b) identified and tagged 20 oak trees at Monks Wood - ten AOD symptomatic and ten asymptomatic (control). Symptomatic trees are defined as such based on the presence of stem bleeds. six oak trees were tagged in the south-east corner of the woodland. This section of the woods, called the Old Wilderness, is a four-hectare plot that was abandoned as a potato field in 1963 and then left to naturally regenerate. This particular plot has a distinctly different history from the rest of the wood (see site description in CHAPTER 2). For this reason and the close vicinity to the former CEH buildings, which are now a police station, making UAV data collection unfeasible, image capture focused on the remaining 14 trees clustered in the north-east corner of the wood.

The locations of tagged trees were initially recorded by the PuRpOsE project using a handheld GPS device. The positional accuracy of the tree locations was up to 15 m from the true location of a tagged tree. This is likely to be due to multipath errors originating from the dense canopy cover present at Monks Wood. To allow precise alignment of tree locations and remote sensing data the positional accuracy of the tree survey had to be improved.

A method was developed to collect point samples from the centre of a tree crown with high location certainty and accuracy during the growing season (leaf-on conditions). A GNSS receiver was mounted on an extendable pole logging raw data at one Hertz interval. The pole and GNSS were was manually pushed through the canopy at the perceived centre of a sample tree crown. A minimum occupation time of ten minutes was undertaken per tree. Raw GNSS logs were then processed (PPK) with data from the nearby CORS, located in Peterborough (baseline < 20 km). The post-processed log reported a mean horizontal accuracy of 9.3 cm (RTKlib). In this log, every sample tree is represented by a cluster of points. In some cases, the points contained in a cluster are distributed over an area of up to ~ 60 cm radius due to slight wind movement of the crown during the occupation time. Finally, the centroid of each cluster was determined by applying the k-means algorithm with k = 14. This method provided a

central crown location, surveyed to high accuracy, of all 14 (nine symptomatic, five asymptomatic) tagged trees in the north-east corner of Monks Wood.

Additional tree samples were collected in the course of the field work undertaken for CHAPTER 4. Theses samples were surveyed from the ground near the stem with a RTK-GNSS device during leaf-off conditions (< 1 m accuracy). Of these additionally-surveyed trees, those that showed either clear symptoms of AOD or no symptoms were selected. Trees with ambiguous symptoms were disregarded, leaving six symptomatic and ten asymptomatic additional trees to be included in the analysis. With these additional trees, a total of 30 sample trees are analysed in this study, 15 symptomatic and 15 asymptomatic. The distribution of sample trees at the site is depicted in Figure 5-1.
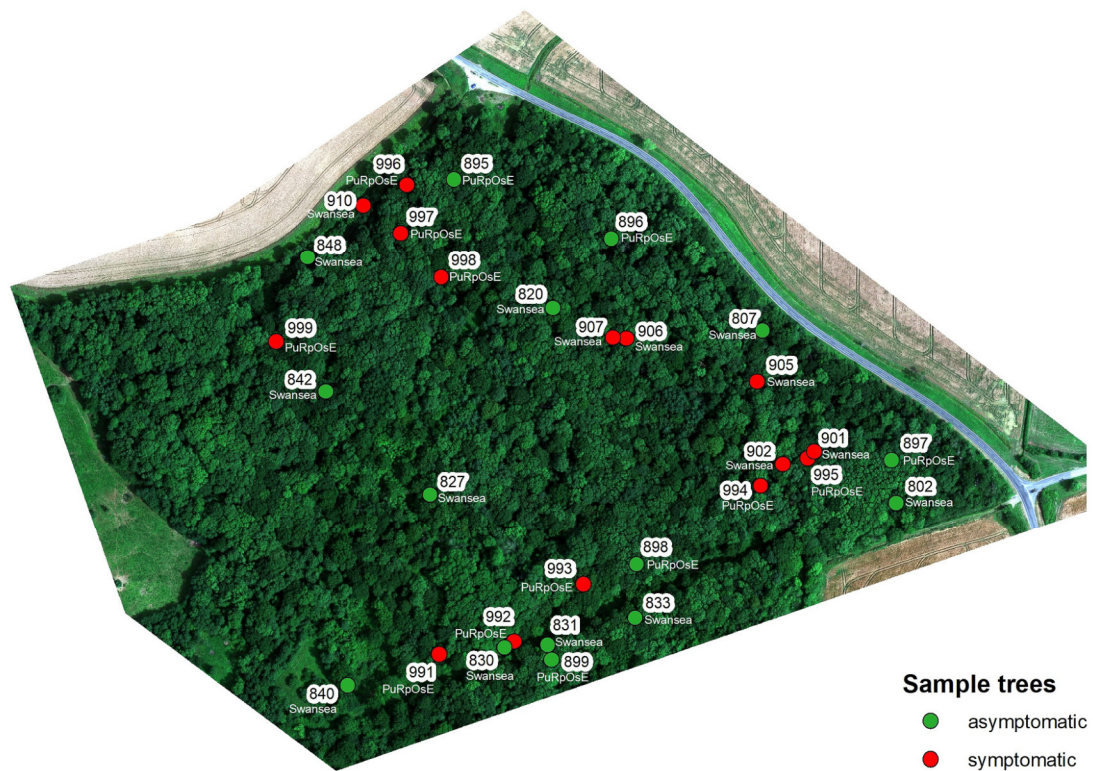
Figure 5-1 Overview of sample trees and their location at Monks Wood. Red represents trees with AOD symptoms and green shows asymptomatic trees. Labels show the tree ID and whether a tree was tagged by the PuRpOsE project or sampled by this author in the course of this PhD research project.

5.2.2 UAV remote sensing data

Remote sensing data for the current investigation comprises multitemporal multispectral imagery collected across the growing seasons of 2017 and 2018 at hyperspatial resolution. Multispectral orthophotos captured in July 2017, October 2017, May 2018 and July 2018 were derived from a SfM-photogrammetric pipeline (previously described) using images from the Micasense RedEdge sensor. All orthophotos were aligned with high accuracy to reference data (PPK 3 cm GSD RGB orthophoto) ensuring the alignment of features on the ground, i.e. individual trees, in all datasets. Following geometric calibration, a layer stack was generated from the orthophotos of all four dates resampled to ten-centimetre resolution. This layer stack of 20 multispectral bands serves as input for the analysis of AOD at Monks Wood. Further detail on the acquisition of UAV imagery and processing of coherent remote sensing data is given in CHAPTER 4, where the same multitemporal dataset is used for the generation of a species map.

5.2.3 Analysis

A pixel-based approach for the classification of oak tree health at Monks Wood was not considered suitable since a) within-class variance increases with increasing image resolution (decreasing GSD), thus lowering the achievable classification accuracy (Hay *et al.*, 1996). b) Accuracy of pixel-based AOD classification is further decreased in scenes exhibiting high background complexity, shadows or varying lighting conditions (Siebring *et al.*, 2019), which are given factors within the current multitemporal imagery. c) Finally, symptoms of declining condition can be present with varying severity, both at individual tree and at stand level. In this case, a pixel-based health classification is not appropriate as in-class variability is not captured. For these reasons, an object-based image analysis approach was adopted for the remote sensing-supported analysis of AOD at Monks Wood. At every sample tree location, spectral and textural feature values were extracted from a defined circular plot within the sunlit canopy and analysed using RF modelling.

5.2.3.1 Feature extraction

The location of a sample tree is described by the precisely-surveyed position of the crown centre (please see section 0). All pixel values were extracted within and touching the boundary of a one-metre radius surrounding these locations. This provides a sample of approximately 350 pixel values per tree. A one-metre radius is small enough to effectively reduce the risk of including cells from neighbouring trees (edge effect) and sources data from the canopy area with highest probability of being sunlit.

The feature set describing each tree in the sample set consisted of spectral features and textural features derived from the imagery of every date. Every tree is represented by 38 descriptive metrics based on the mean and standard deviation of 11 spectral features and eight textural features, calculated from pixel values within the one-metre radius crown plots described above. This method follows from the tests and results from CHAPTER 3.

- Spectral features

The Micasense RedEdge sensor captures five distinct bands. Narrow band width information is provided for three bands in the visible range of the electromagnetic spectrum (RGB) and in the RE and NIR range of the spectrum. In addition to the raw band data, spectral features in the form of vegetation indices were included in the analysis. The NDVI, NDRE, CCCI, CVI and ARI are calculated for every date in the multitemporal data as these indices have shown good response to declining (oak) tree health in a previous study (see CHAPTER 3: UAV remote sensing for the identification of Chronic Oak Decline). Vegetation indices are presented and discussed in more detail in CHAPTER 2.

- Textural features

Texture metrics were extracted from the brightness image of every date in the form of Haralick textures (Haralick *et al.*, 1973). These textural features describe the spatial distribution of intensities, in this case brightness, in the imagery. In the case of forest remote sensing imagery, texture information is related to crown morphological properties such as the density of foliage and branches (Sayn-Wittgenstein, 1978).

To quantify texture characteristics, eight statistical properties, as proposed by Haralick *et al.* in 1973, were derived from a Gray Level Co-occurrence Matrix (GLCM). The GLCM is a mathematical representation of the spatial relationship between different grey levels in an image, generated by recording the number of co-occurring pixel values in its neighbourhood. An overview of the eight texture metrics calculated and their interpretation is provided Table 5-1; corresponding formulas are given in Appendix E.

Table 5-1 Overview of the eight texture features, as proposed by Haralick et al. (1973), that were calculated in this study and their interpretation.

Texture metric	Interpretation
Energy	This provides a measure of uniformity or homogeneity. Higher values indicate greater textural uniformity.
Entropy	A measure of randomness or degree of disorder. High values indicate a heterogenous region.
Correlation	This measures correlation of a pixel value to its neighbourhood. A high value indicates a high dependency to neighbouring pixel values.
Inverse Difference Moment	Like Energy, this provides a measure for homogeneity but introduces a weighing factor for spatial proximity of pixels with similar grey values.
Inertia	Also known as contrast, this provides a measure for intensity contrast between a pixel and its neighbourhood
Cluster Shade	Describes the degree of asymmetry or skewness in the distribution of pixel values. A high value indicates an asymmetric region.
Cluster Prominence	This is a further measure of asymmetry. When cluster prominence is high the image is less symmetric.
Haralick Correlation	This shows the probability of two pixels in the GLCM having a similar value.

Due to computational constraints, texture metrics were not calculated for every band of every multispectral dataset, but rather for a combined brightness image of every date. Brightness was defined as the conglomerated intensity information across all spectral channels and calculated as follows:

$$brightness = \frac{R + G + B + RE + NIR}{5}$$

Eight Haralick texture metrics were calculated on the brightness image of every date, using the Orfeo Toolbox (version 6.6.0). A corresponding image is derived for each of these texture descriptors. For the computation, a 3 x 3 window size was chosen as it is the smallest possible neighbourhood. The reasoning behind this choice was to minimise the influence of neighbouring tree information in the description of texture variations, specifically at the border of tree crowns.

5.2.3.2 Model evaluation

In the first stage of the analysis, the dataset for each acquisition date was treated as an individual model. Each model consists of the previously described features: mean and standard deviation for raw spectra, derived spectral features and textural features.

To analyse whether a significant difference between symptomatic and asymptomatic trees lies within the acquired remote sensing data, a cross-validated prediction based on a RF was utilised. Prediction models were built on the basis of those sample trees that were initially tagged by the PuRpOsE project (n = 14). Trees with no tags, that were surveyed at a later stage as part of this PhD project, were retained as independent validation data (see 5.2.3.4). However, in order to balance sample quantities in the two groups, four of these additionally surveyed trees with no decline symptoms were added to the asymptomatic group.

Feature values were extracted from 18 sample trees, nine symptomatic (all tagged by PuRpOsE) and nine asymptomatic (five of these tagged by PuRpOsE and four surveyed within this study) serving as explanatory variables. The recorded AOD health status of the sample tree acted as response variable in the RF-based prediction.

The prediction was carried out with 100 RF trees, 3-fold CV and 100 iterations per model. Bootstrapping was not applied. For every decision tree in the forest and every iteration, the entire set of samples is used (18 trees). A random subset of features is used for every split and the minimum samples per node was set to four, to constrain decision tree depth and reduce overfitting. As an ensemble method, each RF model consists of 100 decision trees and the final decision is aggregated across all of them further preventing overfitting. In order to assess the performance and variability of the models across datasets and samples, each model was run 100 times and cross validation was applied. The model performance was recorded as cross-validated Area Under the Curve (AUC) value at every iteration. Explanatory power and consistency of a model was evaluated as the mean and standard deviation of the AUC value across the 100 runs.

5.2.3.3 Feature selection

Following the evaluation of the models with all features included, a feature selection process was undertaken. This was undertaken to improve model performance and to investigate the role of individual features in expressing signs of declining health, thus feature importance. Feature importance was calculated with the permutation importance approach. Hereby the model is run as previously to record a benchmark score (AUC value in this case). Values of the feature in question are then shuffled and the model accuracy with the permuted values is compared against the benchmark score. This permutation importance approach allows the actual benefit to the model's performance to be determined. Features with a negative permutation feature importance have negative influence in the models' explanatory power.

Permutation feature importance was determined based on 100 RF trees and scored with 3-fold CV. For each model, ten iterations of the permutation process were performed. The mean score across these ten iterations served as feature importance.

The ten best performing features were selected per model. An additional model was created consisting of the three best performing features of all models. This model was evaluated regarding potential benefits of using conglomerated multitemporal data for the prediction of oak decline. These five models were subsequently analysed in the same manner as in the model evaluation and interpreted by the mean and standard deviation of the AUC value across 100 iterations using 100 RF trees and 3-fold CV.

5.2.3.4 Validation

Following the feature selection, the refined models were tested on independent data to validate their performance in predicting AOD status. Of the total of 30 sample trees, 12 trees were held back for this purpose. These trees were surveyed within the scope of this PhD research and were not in the recorded trees tagged at an earlier date by the PuRpOsE project. For the validation of the models, six clearly symptomatic and six asymptomatic trees were used. The trained models post feature selection were applied to these 12 trees using the method described earlier, with 100 RF trees and 100 iterations per model, predicting their AOD health status. Model performance was evaluated using the mean and standard deviation of the AUC value.

5.2.3.5 Prediction

Finally, the applicability of a spatially-continuous determination of AOD status was assessed. Applying the knowledge from the previous evaluations, the models were used for a site-wide prediction. However, the method presented here predicts an AOD class at an individual tree level in an object-based manner. Since Monks Wood is a semi-natural site with heterogeneous species composition, the intended wall-to-wall prediction thus required the following pre-processing steps: a) classification of oak and b) identification of individual tree crowns within oak clusters.

A highly detailed species map for Monks Wood was created in CHAPTER 4. In this study a pixel-based classification was carried out on the basis of the same multitemporal data used in the current study. "Salt and pepper" noise present in final classification was filtered by a focal sieve operation. The focal sieve filtering stage removed small isolated regions and generalised the map output with segments containing 1000 pixels per class. The operation thus improved spatial coherency providing smoothed patches of predicted oak presence for the subsequent identification of AOD (compare Figure 5-2 b) and c)).

Subsequently, an individual tree crown (ITC) detection algorithm was applied to segment oak areas into individual crowns. A variable-area local maxima method was utilised as implemented in the rLiDAR package (Silva *et al.*, 2017). For this process, a CHM was derived from a hybrid SfM-ALS point cloud with 0.5 m cell size. To smooth the CHM, a gaussian filter with 3 x 3 window size and 0.6 sigma was applied.

For the local maxima detection (i.e. tree top), a fixed window size was used and a minimum tree height of ten metres was set. This ensured that the analysis focused on mature trees in the overstory where AOD symptoms are expected (sample trees by the PuRpOsE project range between 15 m and 23 m). The detected central crown locations then served as seed points to grow the individual tree crowns. In this case, a maximum tree crown radius of 8m was allowed. The resulting tree crown polygons and central crown points were then used in conjunction with classified oak areas in the species map produced in CHAPTER 4, to derive information from individual oak trees.
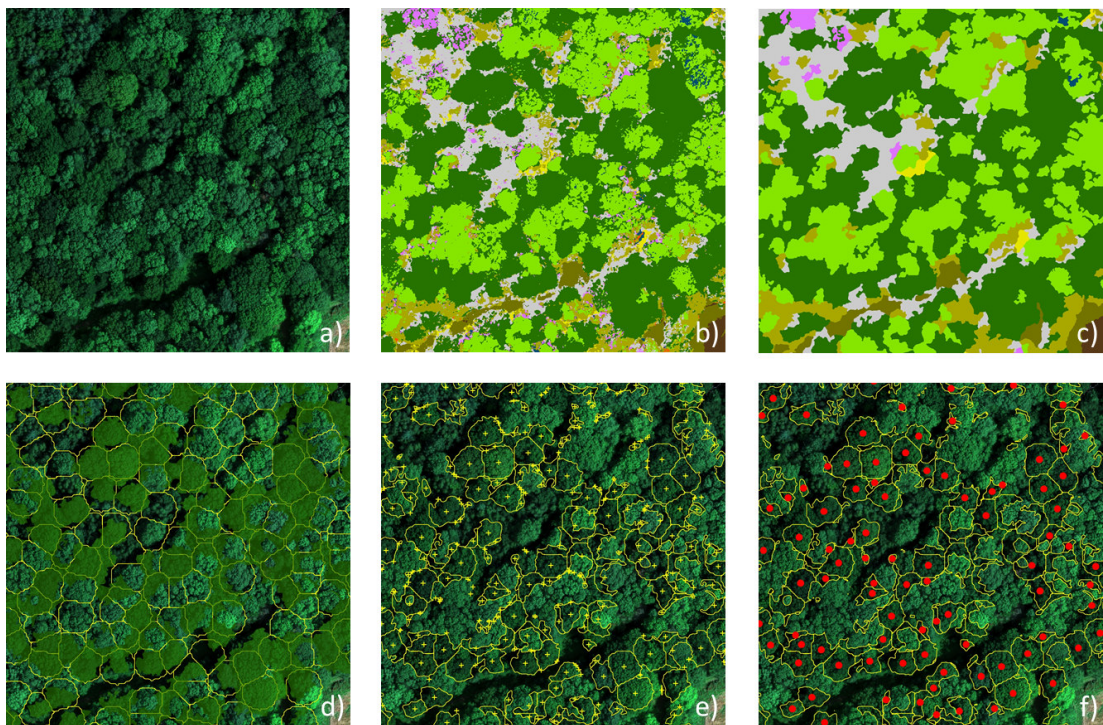
Figure 5-2 Pre-processing steps for the species-specific prediction of AOD status at individual tree level. a) Orthophoto, b) pixel-based species distribution map, c) focal sieve operation, d) ITCs, e) intersection of oak areas and ITCs, f) selection of central crown points where the crown shape is at least r = 1 m.

Oak tree regions from the species map and ITCs were intersected to retrieve polygons for individual oak trees. However, the intersection process leads to very small polygons due to the separate methodologies of identifying species (spectral) and identifying crowns (structural). Particularly at the edges of tree crowns, the intersection of these two datasets led to small, often elongated polygons that do not represent actual tree crowns and do not contain spectral information from the sunlit

canopy. To disregard these smaller polygons, a selection process was undertaken. First a buffer around all central crown locations was created with radius of one metre. Then only those trees that exhibit a crown larger than this circle were selected. The entire process of selecting suitable oak trees for the prediction is presented in Figure 5-2. The AOD status of selected trees was predicted with the established RF models (post feature selection). All trees identified as oak throughout the woodland with a crown radius of 1m or larger were classified as either symptomatic or asymptomatic. A comprehensive tree list providing ground truth for the entire forest was not feasible within this project, thus the explicit model accuracy was limited to the trees that had been surveyed. The evaluation of results therefore focused on statistical plausibility and were assessed regarding congruence between the results of the individual models (whilst acknowledging the possibility of these being consistently wrong).

5.3 Results

5.3.1 Analysis

5.3.1.1 Model evaluation

This analysis demonstrated that data acquired from UAV multispectral and RGB image analysis contain potential to differentiate between symptomatic and asymptomatic trees. Individual models, thus acquisition dates, differed in performance with mean AUC values between 0.36 and 0.86, ranging from none to high explanatory power. The standard deviation across 100 iterations ranged between 0.03 and 0.02 indicating consistency in these results. Results for all models are presented in Table 5-2.

Table 5-2 AUC values scored for individual date models. Results presented for 100 runs with 3-fold CV.

Date	AUC mean	AUC std
May18	0.86	0.02
Jul17	0.67	0.02
Jul18	0.56	0.02
Oct17	0.36	0.03

The highest AOD prediction accuracy was obtained using the data captured in May 2018 (AUC 0.86). Both models based on July data demonstrated poor separability between the two health groups (AUC 0.56 - 0.67). October data showed no explanatory power as the AUC value of 0.36 implies a worse-than-random model performance.

5.3.1.2 Feature selection

Model performance improved for all acquisition dates following feature selection. Combining the three best features of every date in a single model produced very high explanatory power (AUC 0.91) with high confidence (standard deviation 0.01). However, using the ten best features of the May 2018 data alone delivered results with the same level of explanatory value (AUC 0.91). Features derived from the July imagery of both years produced reasonable accuracy scores (AUC 0.66 - 0.77). Whilst data captured in October data continued to demonstrate poor ability to discriminate AOD (AUC 0.63). The results of the accuracy assessment post feature selection are summarised in Table 5-3.

Table 5-3 AUC values scored for individual date models after feature selection. The ten best features were selected for the individual dates and the three best from each date were combined. Results from across 100 runs with 3-fold CV.

	AUC mean	AUC SD
combined_3bestfeat	0.91	0.01
May18	0.91	0.01
Jul17	0.77	0.03
Jul18	0.66	0.01
Oct17	0.63	0.02

The feature selection analysis showed that best performing features are not consistent across models. Features based on the standard deviation however seem to dominate the highest scoring places in the feature selection. Only in the October 2017 model, were features based on the mean of variables predominantly amongst the ten best performing features. The best performing feature in the July 2017, October 2017 and May 2018 models is among the textural features. In the July 2018 model, the best performer is the standard deviation of the derived ARI.

Therefore, textural features and spectral features occur amongst the top ten features of every model. In most models, derived vegetation indices score higher feature importances than raw spectral information, with the exception of the May 2018 model where the standard deviation of the NIR and RE channel receive second and third place in the importance ranking respectively. The full list of features and their respective scores is in Appendix F. Boxplots, presented in Figure 5-3, demonstrate the data distribution between the sample groups for features comprised in the combined_3bestfeat model. Example decision trees for all models and corresponding features with highest importances are depicted in Figure 5-4 and give information on how the data is partitioned and how decision rules are applied based on the samples in this iteration. Although this gives indication of the processes involved in the partitioning, the depicted decision boundaries do not explain the input data in their structure.
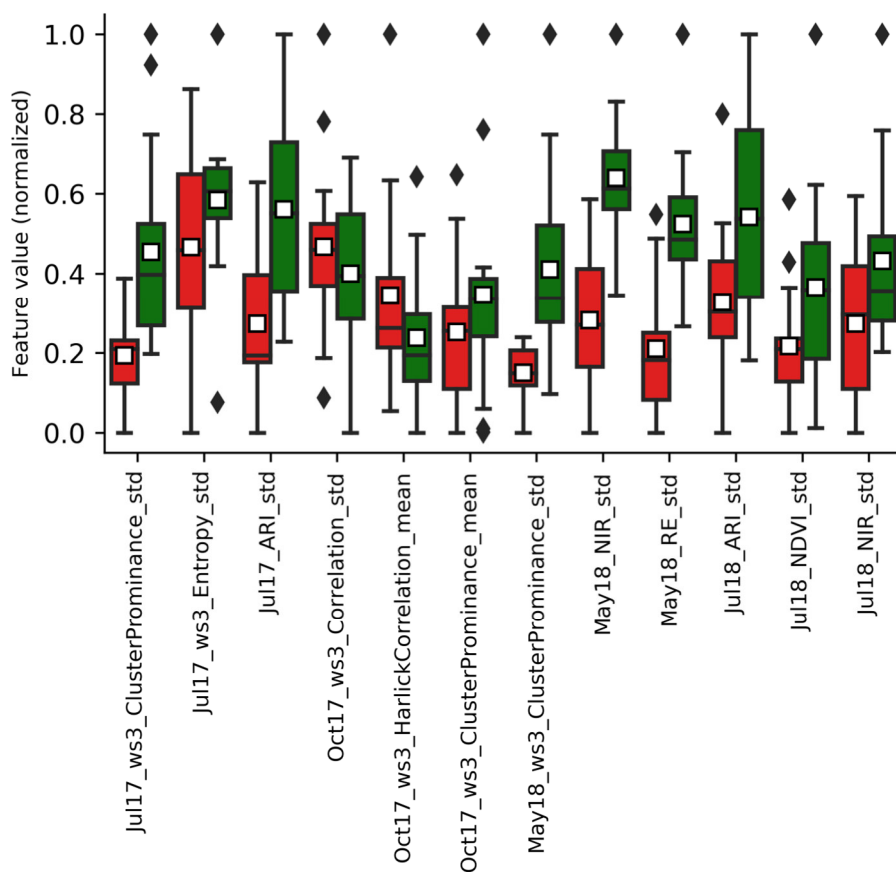
Figure 5-3 Boxplots for features comprised in the combined_3bestfeat model, that combines the three features with highest importance from each flight. Red presents symptomatic sample trees, green represents asymptomatic trees
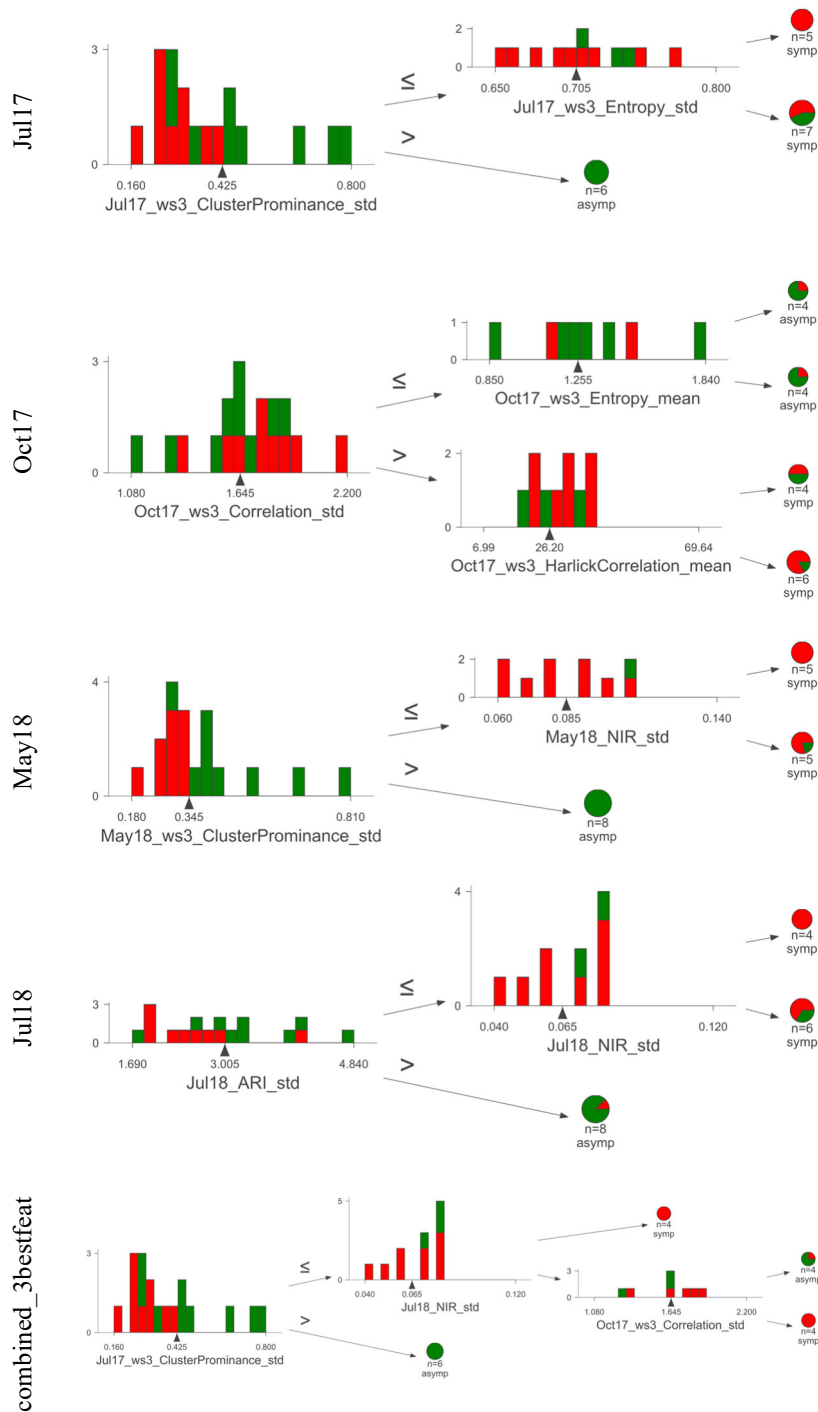
Figure 5-4 Example decision trees for all evaluated models. Examples are given for highest ranking features according to determined permutation feature importances. Each model in the 100 iterations consists of 100 decision trees. Histograms of the input data show the distribution at each node with symptomatic samples shown in red and asymptomatic samples shown in green. The stopping criterion in each decision tree is based on the minimum required samples at every leaf, four in this case, which prohibits excessive tree depth.

5.3.1.3 Validation

Validation of the model performance with independent test data (12 trees) demonstrated that the UAV-based remote sensing data capture significant information for the discrimination of AOD symptomatic and asymptomatic oak trees. July 2017 and May 2018 models produced high accuracies (AUC 0.98), as did the model combining the three best features of all dates (AUC 0.95). July 2018 data showed reasonable performance (AUC 0.73) while the analysis of the October 2017 data confirms that this dataset holds little explanatory value (AUC 0.65) for the prediction of AOD affected trees. All results for the validation of the model performance with independent samples are presented in Table 5-4.

Table 5-4 Model performances (AUC) evaluated on separate validation data (12 trees). Results presented from 100 runs with 3-fold CV.

	AUC mean	AUC SD
May18	0.98	0.01
Jul17	0.98	0.03
combined_3bestfeat	0.95	0.03
Jul18	0.73	0.02
Oct17	0.65	0.05

5.3.1.4 Prediction

A total of 673 locations for individual oak trees were predicted by applying the method described in 5.2.3.5. The previously determined best performing model was based on May 2018 data, and predicted 328 AOD symptomatic and 345 asymptomatic trees. All other models predicted more symptomatic than asymptomatic trees at the site - July 2018 model excessively so, predicting 81 % of identified trees to be AOD symptomatic. Results for all models are presented in Table 5-5. For a visual comparison between models, corresponding prediction maps are presented in Figure 5-5, Figure 5-6 and Figure 5-7.

Table 5-5 Number of predicted trees in each group for final models.

	asymptomatic	symptomatic
Jul17:	261	412
Oct17:	302	371
May18:	345	328
Jul18:	125	548
combined_3bestfeat:	306	367
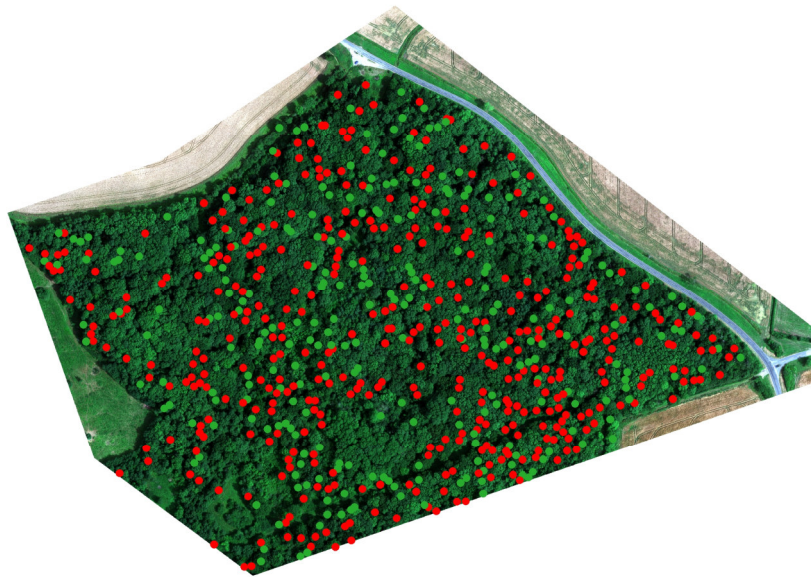
Jul17
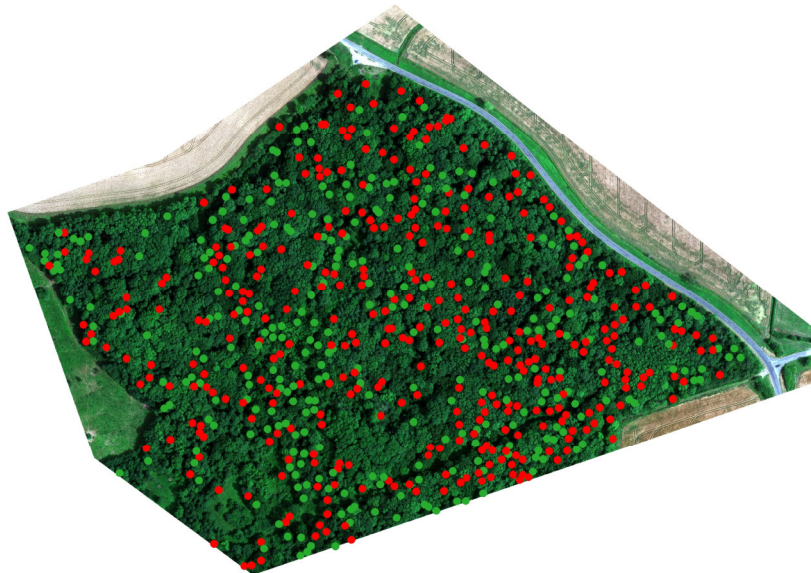
Oct17

Figure 5-5 Oak tree status as predicted by models built on 2017 UAV flights. A total of 673 oak trees are predicted throughout the NE section of Monks Wood. Trees predicted as asymptomatic are shown in green and trees predicted to be AOD symptomatic are shown in red.
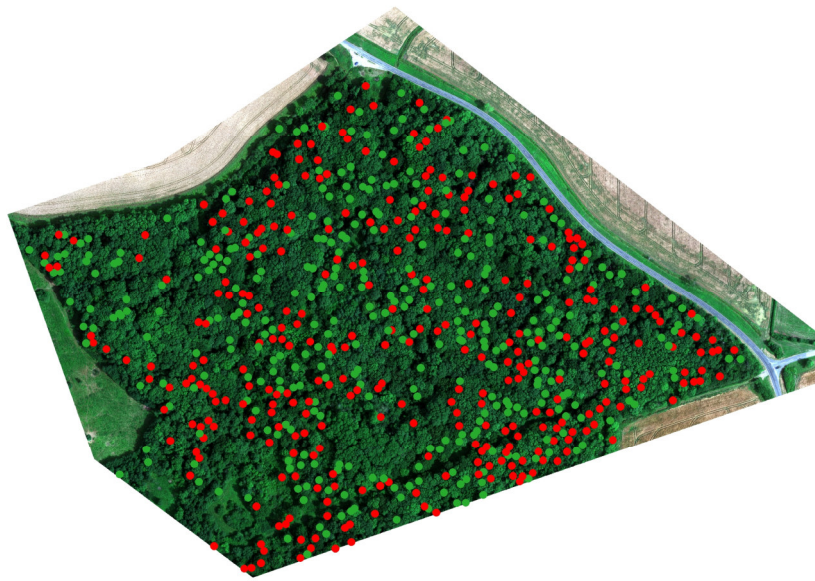
May18
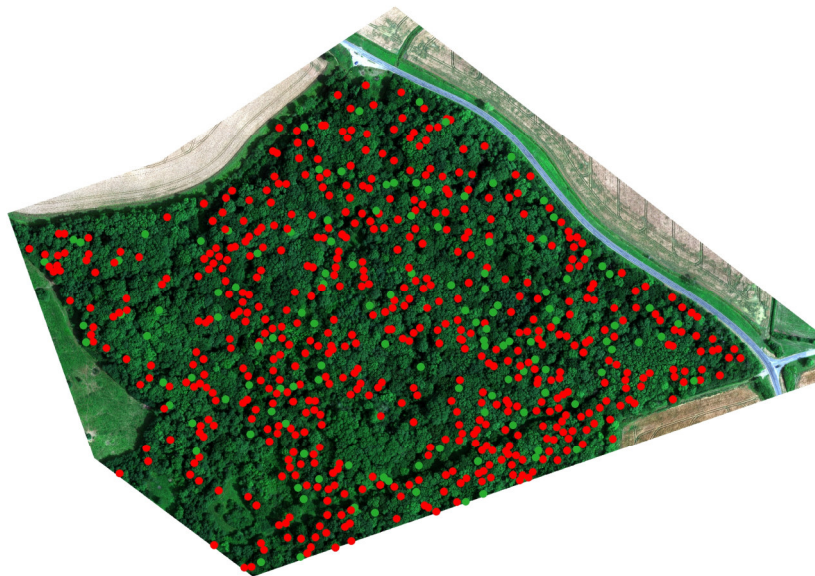
Jul18

Figure 5-6 Oak tree status as predicted by models built on 2018 UAV flights. A total of 673 oak trees are predicted throughout the NE section of Monks Wood. Trees predicted as asymptomatic are shown in green and trees predicted to be AOD symptomatic are shown in red.
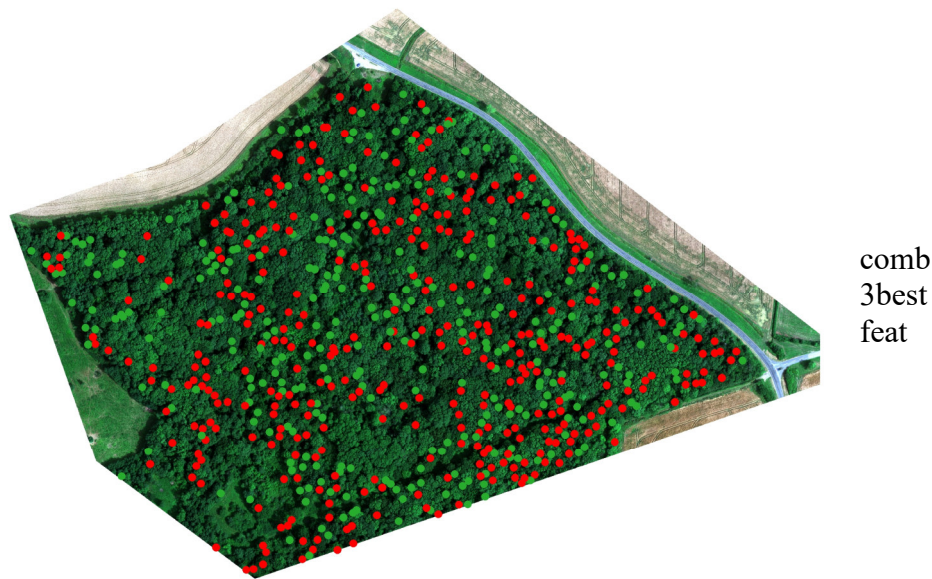
comb
3best
feat

Figure 5-7 Map showing the prediction result of the combined_3bestfeat model. A total of 673 oak trees are predicted throughout the NE section of Monks Wood. Trees predicted as asymptomatic are shown in green and trees predicted to be AOD symptomatic are shown in red.

5.4 Discussion

The method applied in this study demonstrated potential to differentiate between AOD affected trees and healthy trees using UAV acquired multispectral imagery. The use of multitemporal data provided insights into phenological effects on AOD detection accuracy. Spring imagery (May 2018) consistently offered the highest explanatory value. Both summer acquisitions (July 2017 and July 2018) delivered lower, although possibly acceptable, accuracies while autumn imagery (October 2017) held little to no information to successfully distinguish between AOD symptomatic and asymptomatic trees.

A possible explanation for the weak explanatory value of autumn data is that naturally-occurring differences between sample trees, such as age, site conditions and management history are more pronounced during senescence. Indicators for AOD could fall within this variability thus preventing the model from separating signals between normal senescence and decline-induced effects on foliage. An additional reason for the lower performance of the autumn imagery could be that textural features offer less information content compared to the other data due to light smearing effects

in the orthophoto. This smearing effect is a result of wind present on the acquisition day moving branches and foliage during the flight. In such conditions, during photogrammetric processing, when images are stitched and blended to create an orthomosaic, the inconsistent position of branches and foliage causes minor blur.

Summer imagery performed well in the distinction between AOD-affected and control trees. The two summer datasets however differed slightly in performance. Across all evaluation stages, higher AUC values were obtained with the July 2017 model compared to the July 2018 model. Reasons behind this difference are unclear, although phenological and/or meteorological discrepancies between the two years could have contributed. The UK's summer 2018 was significantly warmer and drier than the average (Kendon *et al.*, 2019) which could have caused stress amongst oak trees which are not symptomatic for AOD, thereby reducing the capacity for differentiation. A further potential contributing factor to observed differences could be that 2018 radiance data could not be converted to reflectance due to a lack of a calibration panel in the acquisition. Data from summer 2017 (reflectance) and 2018 (radiance) data were normalised for the current study, thus these data should be comparable. However, the possibility of the lack of calibration having an impact on the explanatory value cannot be ruled out completely.

May imagery in particular exhibited greatest explanatory value, delivering AUC values between 0.86 and 0.98 for all evaluations undertaken. In this year, bud burst had occurred in early April thus leaves were fully developed when the imagery was collected on the 14th of May 2018. However, at this early growth stage, foliage is unlikely to show phenomena such as gall or mildew development. While not necessarily having a negative impact on trees, such ailments will influence the appearance of the foliage, adding noise to spectral and textural properties. The early season data capture in May 2018 could therefore have prevented confusion between the spectral impacts of gall, mildew and AOD. A further possible explanation for the high accuracy AOD classification obtained by the May model is if AOD-derived stress modifies the growth process, since such stress-induced growth differences would be more pronounced during the early growth stages than later in the season. Further investigations are required to determine the effect of AOD on oak phenology.

High accuracy was also achieved by combining features of high importance from each date in the multitemporal dataset into a single model (combined_3bestfeat). In a previous study, combining the information of individual acquisitions, and

therefore different phenological states, provided higher accuracy than imagery from a single date alone (see CHAPTER 4). In the current study, although offering high explanatory power, the use of multiple datasets did not deliver an advantage over the use of single date acquisition (e.g. May 2018 model). Avoiding the necessity of multiple UAV acquisitions would greatly reduce efforts and thus costs. In an operational rather than a purely scientific context, this finding is certainly of interest when the future use of remote sensing-based techniques for forest condition assessments are considered.

30 samples were used in this study, 18 trees for model generation and 12 additional trees for independent validation. The robustness of the results could have been greatly improved if more samples were available. However, no more AOD affected trees were discovered within the study site thus limiting the total number of (balanced) samples.

Future UAV remote sensing investigations of AOD should aim to identify a site in which there are higher oak and/or AOD densities so that a greater number of samples can be measured within a similar area as the current study site (i.e. enabling UAV data capture in a single flight). Increasing the sample size in this way, and thereby increasing the significance of results, is crucial to fully understand the applicability and transferability of UAV-based assessment of AOD.

The complexity of Monks Wood makes it challenging as a study site. Being a nature reserve since 1954 and managed with little intervention, purely for conservational purposes, Monks Wood has a high diversity Being a semi-natural woodland, it is difficult to conclusively identify 'control' trees since trees not impacted by AOD, may nevertheless display the impacts of other conditions or previous management practices. Cause and effect are therefore difficult to determine.

The north-east section of Monks Wood (the focus of this study) contains eight tree species in the overstorey and several further species in the shrub layer. Trees at the site, including oak, have a history of coppicing (Steele and Welch, 1974). This management practice has potentially had, and may continue to cause, varied and unknown effects on tree growth. Furthermore, oak trees in Monks Wood comprise *Quercus robur*, *Quercus petraea* and their hybrid form (Steele and Welch, 1974). Genotyping data were unavailable and so it could not be ascertained how these genetic differences may influence the way in which they present AOD symptoms. Visually (and therefore subjectively) differences between individual oak trees were apparent,

particularly in the hue of foliage. However, the origin of these differences could be numerous, including varied site conditions at the micro scale. These factors combined could lead to spectral and textural variations that are inseparable from the characteristics utilised in this study to identify AOD.

For more conclusive results from UAV remote sensing assessment of AOD, a pure oak stand with even age distribution and site condition would be ideal. Additionally, the disease is mostly found amongst mature trees (Denman *et al.*, 2014). Such combination of factors, homogenous oak stands of mature age, are uncommon in the UK. To summarise, it is challenging to isolate the impacts of AOD from the effects of the multi-faceted heterogeneity present at Monks Wood.

Additionally, there remains the question of severity of AOD amongst the sample trees. The trees determined to be AOD symptomatic by the PuRpOsE project were classified in the field according to the presence of stem bleeds. However, the number of bleeds varied greatly amongst these symptomatic trees. Bleeds as well as additional symptoms indicative of AOD-induced stress were not recorded in a quantitative manner. Quantifying symptoms would have given insights into the stress level trees are experiencing and thus a more precise coding of AOD stage and the impact of this. A non-binary AOD classification, would permit AOD indicators to be aggregated in a continuous severity scale. Individual indicators could be weighted based on their importance for the detection of the disease. The resulting continuous severity metric would be very helpful to better understand the importance of remote sensing features (partial dependence) in the model, ultimately allowing models to be refined and enabling a more precise prediction. Future work aiming to study the remote sensing-based detection and prediction of AOD should strongly consider a ground survey design that enables the adoption of a continuous AOD (severity) scale as dependent variable rather than the current binary health classification.

An object-based image analysis approach was crucial to the successful algorithmic distinction between symptomatic and asymptomatic trees. A pixel-based approach for the analysis was deemed unfeasible due to high variability of the scene, the natural state of the sample trees and the severity of AOD symptoms. The high spatial resolution of UAV imagery captures this variability well, and thus intensifies the issue. The circular crown segmentation method utilised in this study, focuses on central crown pixels. Though being a relatively simple approach, the method has shown to deliver "clean" samples that represent sample trees well (see also CHAPTER

3 and CHAPTER 4). In the case of Monks Wood, the task of extracting information from sunlit portions of the crown of individual trees and avoiding edge effects, is aggravated by the high diversity and density, often with interlocking crowns. The ground-truth location sampling method described in CHAPTER 4 and adopted in the current study was crucial for the successful segmentation of individual tree information. The pole-mounted GNSS receiver was precisely positioned in the centre of the sample tree crowns, thus ensuring that the chosen 1m radius, for the extraction of pixels, did not touch neighbouring crowns. The disadvantage of this rigorous, high-certainty field tree location sampling method is the immense labour involved, particularly for a diverse, semi-natural forest like Monks Wood. Future remote sensing investigations of AOD require equal precision in field knowledge of oak tree geolocations, and should incorporate criteria that allow for an extensive ground truth survey.

A different segmentation method was also tested within this study, whereby tree sample locations were matched with automatically generated ITCs. Feature values were extracted from these ITC segments. This approach delivered considerably worse model performances and is likely due to the inclusion of unwanted edge effects and noise. Automatically generated ITCs were larger than the one-metre circular plot used in the current study and may include undesired information from shaded areas between crowns or incorporate information from neighbouring trees. Most ITC algorithms are designed for the application in homogenous coniferous forest and work on the basis of canopy height information while disregarding spectral information. It is therefore unsurprising that an ITC segmentation approach delivered subpar results for the semi-natural broadleaf forest of Monks Wood.

The current study utilised an analysis approach based on RF modelling. This method facilitated the quantitative analysis of feature importances. In three of the four single date models a textural feature was the best performing feature. It was clearly demonstrated that adding textural variables added to the overall performance of the models. Similarly, other studies have concluded that textural variables hold valuable information in forest classification, particularly so regarding very high resolution imagery as is the case with UAV acquisitions (Gini *et al.*, 2018; Yuan and Hu, 2016). An example for a well performing textural feature in the current study is the standard deviation of Cluster Prominence which expresses the local variation in brightness (within the 3 x 3 pixel window, in this case). It is likely that this texture metric contains

information on the presence of shadow, which would be an indicator for canopy gaps or a canopy thinning. Consequently, the standard deviation of this feature points to the uniformity of the brightness/shadow variation within the segmented crown centre of sample trees. In both models, where the standard deviation of Cluster Prominence is the best performing feature (July 2017 and May 2018), higher values for this variable are observed in asymptomatic sample trees (see Figure 5-3). It was expected that healthy trees exhibit a more uniform crown texture while AOD-impacted trees with partial crown damage would display a more heterogenous crown texture. The results obtained in this study however point to the opposite effect whereby the standard deviation of Cluster Prominence (ws3_ClusterProminance_std) has a negative impact on model performance in the July 2018 model, according to the permutation feature importances. This relationship, whilst producing highest classification accuracy, is difficult to explain and interpret in terms of the expected underlying biophysical factors and requires further investigation across a broader range of samples. The analysis on COD in CHAPTER 3 did not account for variability within the crown, but did show that class separability did not suffer from outlier removal. However, these results are not directly comparable as the outlier filtering undertaken does not test within-crown variance as a predictor variable. Moreover, the comparison is impeded by the anticipated deviations in variability caused by differences in crown symptom manifestation between COD and AOD, as well as discrepancies in variance resulting from dissimilar plot sizes used for pixel extraction (3 m for COD and 1 m for AOD). Nevertheless, considering the significance of variability established in this chapter, investigating the potential of within-crown variability and texture metrics as predictors for oak decline states presents interesting opportunities for future research.

It is to be noted that texture metrics included in the current models were calculated on the basis of a brightness image that combines all spectral channels. This was done to limit the quantity of features overall, reducing model complexity and computational effort. The benefit of textural features was demonstrated in general, however it remains unclear whether the input parameters for texture calculation were optimised for the application. By averaging intensity contrasts across all bands, merging the information into a single brightness image, it is possible that vegetation specific texture characteristics appear less pronounced than in individual bands. In a scenario where texture metrics describe contrast between foliage and background (e.g. branches or canopy gaps), texture computation on bands in the NIR region can

theoretically provide a greater amplitude in texture metric values than a visible band, due to the higher sensitivity to chlorophyll. To optimise information content of texture metrics for forest health analyses, further work should investigate individual spectral channels for their entropy regarding this target.

Among the spectral features, there was no clear pattern displayed across models with regard to feature importance (Appendix F). It is however noted that the near-infrared region is predominately represented amongst the best performing features of all models, as raw channel or in the form of a vegetation index. As demonstrated in CHAPTER 3: this further supports the utility of this region of the electromagnetic spectrum for the detection of reduced tree health. In the case of AOD the high importance of near-infrared spectra indicates differences in photosynthetic capacity between symptomatic and asymptomatic trees. However, of those remote sensing features that comprise near-infrared spectra, it is the standard deviation rather than the mean that received highest feature importance in the models. Thus, it appears that the models' decisions have greater dependence on the degree of near-infrared variation rather than an absolute difference in these spectra. Figure 5-3 illustrates that symptomatic trees exhibit a more uniform distribution of spectral values in near-infrared spectra and related vegetation indices than asymptomatic trees. Although, these spectra can be related to photosynthetic capacity and it is plausible that control trees at Monks Wood have greater variance in chlorophyll content, it remains to be determined how important this observed difference is in the general detection of AOD-stress. Further investigation was not feasible within the current study, due to a limited number of sample trees. For future work on oak decline with UAV remote sensing, it is however advisable to give particular focus to the near-infrared region of the electromagnetic spectrum.

The final analysis of this study, predicted AOD among classified oak species across the entire study site. Forest-wide ground truth data of individual tree level AOD status was not feasible within the scope of this study. Despite the limited validation data, the field data collection above suggests that it is highly likely that the model predictions do not reflect reality and overestimate the occurrence of AOD. Whilst remote sensing data may succeed in detecting declining health before visible symptoms appear, it is likely that this would only be the case at an early stage of the decline. It is unlikely that approximately half of the oak trees are in this early stage of the decline where other obvious and visible symptoms are not present yet.

Alternatively, it could be the case that trees do not display symptoms observable from the ground while AOD-inflicted stress is evident in the canopy (a characteristic of COD). This could potentially be the case with trees that were previously affected by AOD but have gone into remission, occluding stem lesions (Denman and Webber, 2009). However, the specific dynamics of remission in AOD and associated change in symptomology are not yet understood (Denman *et al.*, 2014). Whilst the uncertainty in knowledge and understanding of AOD means that it is not possible to determine conclusively the absolute accuracy of extrapolation of the model predictions across the entire forest, it is likely that the incidence of AOD is largely overestimated. It is possible that some of the trees incorrectly classified as suffering AOD are in fact afflicted with a different condition, however it is improbable that this accounts for the total overprediction.

Despite the ambiguities discussed above, it is of note that the three best performing models (July 2017, May 2018 and the model combining the three best features of all dates) agree in their prediction in 399 cases of the total 673 trees. Though it could be the case that all are equally wrong.

The predictions should be regarded as a workflow suggestion for future studies aiming to investigate remote sensing supported detection of declining tree health. The results of the proposed method are influenced by multiple parameters: species classification, ITC delineation, feature extraction (spectral and textural) and parameters of the chosen prediction algorithm. A quantification of the sensitivity of these parameters to prediction results would inform method design for UAV remote sensing assessment of AOD.

5.5 Conclusion

The object-based image analysis of spectral and textural information derived from UAV remote sensing data showed high explanatory value in the distinction of 15 AOD symptomatic and 15 asymptomatic trees in the NE of Monks Wood, Cambridgeshire (both May 2018 and three best features models produced accuracy AUC 0.91). Validation of the model performance with independent test field data collected as part of this study (12 trees) confirmed those results. Validation demonstrated that the best performing models, July 2017 and May 2018 datasets, plus

the three best features model of all dates, capture significant information to differentiate AOD symptomatic and asymptomatic oak trees (AUC 0.95 - 0.98).

It was established that, at this site, spring and summer imagery were most suited for distinguishing AOD status while autumn imagery provided poor information content. It was further identified that the combination of multitemporal data did not improve classification accuracy over single date spring and summer data. Feature importances showed high importance for NIR spectra and vegetation indices containing NIR information across models, indicating differences in chlorophyll presence between AOD and control trees. Within-crown spectral variance and texture metrics were among the highest-ranking features according to feature importance, suggesting potential to differentiate the sample groups based on within-crown variability. However, opposed to the expected effect of crown deterioration in symptomatic trees, it was shown that asymptomatic trees depict greater variability in the crown. Further investigation of this phenomenon is needed in future research, with an assessment of the role of crown variability in identifying oak decline across a broader range of samples.

Obtaining a complete tree list of individual oak trees' AOD status throughout Monks Wood was beyond the scope of this study. Conclusive accuracy assessment of extrapolated predictions across the forest was therefore not possible. However, it is inferred from the results that AOD is overpredicted when the model is applied throughout the remaining area of the forest. The predictions are confounded by several factors, not least of which the heterogeneous character of Monks Wood, and the lack of full understanding of the causes and effects of AOD.

Further studies aiming to apply UAV remote sensing supported detection of AOD should consider 1) a homogenous study site (pure stand, even and mature age oak, with consistent soil conditions), 2) data collection of a large number of sample trees with high geolocation accuracy 3) rating AOD status by severity on a continuous scale compiled from multiple symptom metrics.

CHAPTER 6:

DISCUSSION

6.1 Potential in UAV remote sensing to identify trees affected by oak decline

The studies presented in this thesis demonstrated potential for use of UAV remote sensing for the detection and assessment of trees affected by oak decline. It was shown that multispectral imagery holds information to successfully distinguish between symptomatic and asymptomatic trees – in the case of COD as well as for AOD. Remote sensing data acquired at Speculation Wood (COD) and Monks Wood (AOD) exhibited significant differences between the two sample groups - declined and healthy oak trees. Best performing RF models showed high explanatory power relative to individual multispectral datasets, indicated by high scores of the performance metrics (overall accuracy and AUC), when validated on independent data of the same dataset. However, generalisation of developed models, was demonstrated to be unfeasible with the current data. Predicting tree health from one UAV flight to the next and extrapolating decline status to all trees of the same site revealed several issues, related to sensor calibration and the natural variability of the studied areas. Currently, these issues still prohibit application of the presented methodologies beyond research and prompt further investigation.

6.2 Comparable work

Thus far, there are only few comparable studies that investigated UAV remote sensing for forest health assessments. Like the presented work, these studies have indicated potential for UAV-based forest health monitoring, despite varying analysis approaches and investigation subjects. Closely related to current method, Lehmann *et al.* (2015) and Lisein *et al.* (2015) used an OBIA approach to identify declining tree health on both alder and oak in natural forests. They achieved good overall classification accuracies (79.5 – 84.1 % and 82.5 – 85 % at their respective study sites). The current result for AOD and COD detection accuracies are in-line with these earlier findings. In fact, models presented in CHAPTER 5 yielded higher accuracies, suggested by AUC of up to 0.98, than those by Lehmann *et al.* (2015) and Lisein *et al.* (2015). The high accuracy reported in the current investigation may originate from

the utilisation of a narrow band multispectral sensor, whilst aforementioned 2015 studies made use of modified off-the-shelf RGB cameras. The benefit of multispectral imagery over RGB imagery in the context of forest health remote sensing were reaffirmed in CHAPTER 3. Differences of RGB and narrow band multispectral imagers are more thoroughly discussed in a dedicated section (see 6.3.2 RGB versus multispectral imagery).

Other studies were predominantly focused on the classification of decreased health and dead trees in coniferous stands (Brovkina *et al.*, 2018; Dash *et al.*, 2017; Minařík and Langhammer, 2016). However, coniferous forests (particularly managed plantation stands) are expected to present less natural variability than the mixed broadleaf study sites of the current investigations. Additionally, studies on coniferous stands have largely been focused on forest health threats with distinct pathology, such as clear signs of needle discoloration or tree death by pest infestation. These differences and the topic of "natural variability" in forest health assessments are further discussed in the Challenges section of the Discussion.

6.3 Findings

6.3.1 Remote sensing for assessing oak decline

The chapters present evidence supporting the feasibility of using UAV-based multispectral imagery to differentiate trees that are under stress from COD and AOD from control trees. The analysis of the most significant variables for differentiating between symptomatic and asymptomatic trees revealed that symptomatic trees have lower values in NIR reflectance and associated vegetation indices, and greater variation in both spectral and texture metrics within the crown.

From a plant physiological standpoint these results are sensible, as the dieback of fine roots in COD and necrosis on stems in AOD are expected to disrupt the transport of water and nutrients, causing stress on affected trees. When stress persists, leaves experience a decrease in their ability to perform photosynthesis and transpiration, resulting in loss of foliage and the eventual death of branches (Walthert *et al.*, 2021). According to Denman's (2010) report, trees affected by AOD may experience canopy

dieback similar to those impacted by chronic oak decline, although this may not occur until the tree is close to death.

Past research has recognised the NIR region's sensitivity to variations in chlorophyll presence (Carter and Knapp, 2001; Michez *et al.*, 2016; Raddi *et al.*, 2022; Sampson *et al.*, 2003) as well as in leaf and canopy structure (Hallik *et al.*, 2019; Peterson *et al.*, 1988), implying a crucial role in evaluating decline within the crown. This highlights the importance of the NIR region in assessing impacted tree condition associated with oak decline.

The identified importance of standard deviation across spectral and textural features are consistent with the notion that reduced crown condition in declined trees manifests in changes of spectrally observable intra-crown variability. For sample trees at Monks Wood, where crown variability measures were included in the analysis, AOD trees displayed reduced heterogeneity in their spectral characteristics. For features with high importance that are indicative of variability in the crown, i.e. standard deviation and texture metrics, data distributions showed higher values for asymptomatic trees and lower values for symptomatic trees (see Figure 5-3). These findings were opposite to what was anticipated based on the current understanding of the effects of AOD on trees and how it may result in symptoms such as leaf discoloration, defoliation, and dieback in the crown (Denman *et al.*, 2010), which theoretically promotes heterogeneity in declined trees. However, to understand and explain the observed opposite effect, it is necessary to evaluate the intra-variability across a much larger number of samples. Further work is also required on the reliability of variability measures for a detection of declined trees. Although the variability within the crown can account for the differences observed at the current study location, it would be incorrect to consider these indicators as conclusive. The aforementioned variability markers are significantly impacted by factors such as the forest's overall canopy structure, environmental conditions, and the lighting conditions present during data collection. These topics are discussed further in section 6.4.

The present investigations were unable to address questions regarding the severity of crown decline and the timing and magnitude of symptom manifestation, which indicates that there is still room for further research on these topics. Foliar discolouration, defoliation, and crown dieback can be common symptoms across a broad range of tree pathogens (Lausch *et al.*, 2016; Stone and Mohammed, 2017). For AOD specifically, the degree of correlation between stem symptoms and crown

symptoms remains uncertain. Due to the binary rating of tree condition in the available data, comprehensive analysis of this relationship is severely hampered. To address this issue in future research, it is recommended to collect more ground-level data and give due consideration to decline severity, as discussed in section 6.4.3.

It was discovered during the examination of multi-temporal UAV images that the spring and summer acquisitions were effective in differentiating AOD sample trees from control trees, as they held noteworthy explanatory power. On the other hand, autumn imagery was found to have limited discrimination accuracy. These findings are further discussed in section 6.3.5. However, it can be said that the temporal and seasonal dynamics of oak decline, observable with remote sensing data as well as in the field, are not yet understood.

Having a higher temporal resolution could allow the monitoring of the transition from earliest onsets of predisposing stress factors, such as drought, to the subsequent decline-induced stress phase. This could provide valuable information regarding the extent of predisposing stress required to trigger a tree's decline. Consistent with this, it is necessary to establish the thresholds at which stress in oaks can be detected with remotely sensed data. Dash *et al.* (2017) successfully demonstrated the ability to determine early-stage stress in Monterey pine (*Pinus radiata)* with UAV-acquired timeseries data, over the course of 21 flights. They performed their experiment in a plantation forest, manually poisoned trees and monitored these with a multispectral sensor. In this controlled environment, they concluded that NDVI and NDRE are most suited for an early detection of stress.

For conducting similar investigations on oak and detecting early signs of decline in natural environments, higher resolution spectral data over a broader spectral range are an important requirement. Limitations of the sensor used in the current studies are discussed in section 6.4.4. There is a recognised necessity for more extensive spectral information, such as full-spectrum data, and more dependable data quality to extract plant physiological traits (Reich *et al.*, 2003). Establishing a connection between plant traits derived from spectral analysis and the (early) stages of decline can enhance our comprehension of complex diseases (Hernández-Clemente *et al.*, 2019). Hornero *et al.* (2021) found that by using a radiative transfer model and analysing hyperspectral and thermal imagery from a piloted aircraft, they were able to accurately infer plant functional traits related to oak decline symptoms observed on Holm oak (*Quercus ilex*) in southern Spain. Although drought stress can predispose

trees, the main cause of Holm oak decline is the infection of *Phytophthora cinnamomi*, which sets it apart from the oak decline syndrome observed in Britain. In their study, Hornero *et al.* (2021) determined canopy temperature and chlorophyll fluorescence to be the most important plant functional traits in the detection of early decline symptoms. Their approach showed that remotely sensed identification of decline can precede field-based visual identification by two years. Using a machine learning-based model, they predicted the status of individual trees and achieved an overall classification accuracy of 81 %, which was compared to field observations.

Whilst the final prediction models developed in CHAPTER 5 are currently not operational, it is possible to apply the described method of model generation and individual tree detection to achieve wall-to-wall predictions. As mentioned above, improved quantity and depth in remotely sensed and ground sample data can enhance model robustness, making it possible to map the spatial distribution of the decline. Conducting repeated surveys can facilitate change detection and aid in assessing the spread of the decline. Such investigations have the potential to offer insights into spatial dynamics of the decline and may establish connections between spatial patterns, biological factors, and environmental conditions. In a study on ash dieback (*Hymenoscyphus fraxineus*) in Britain, Chan *et al.* (2021) used hyperspectral data to predict the severity of ash dieback in identified ITCs. In their prediction maps they identified that trees situated at the edge of the forest exhibited more severe symptoms of dieback, demonstrating the potential of the approach.

6.3.2 RGB versus multispectral imagery

In CHAPTER 3 RGB imagery was assessed and compared with narrow band multispectral data. As RGB information can be gathered with consumer-grade UAVs and sensors it was evaluated as a potential cost-efficient approach to oak decline detection. However, the results from Speculation Cannop clearly showed that RGB imagery is not suited for the identification of COD symptoms. Derived RGB-based vegetation indices only marginally improved explanatory power. These results were somewhat expected since RGB vegetation indices offer less contrast between visible bands compared to contrast between the visible and NIR range, as provided by a multispectral sensor. Previous studies have tackled this issue by modifying off-the-shelf cameras, replacing the hot mirror with a NIR filter (Brovkina *et al.*, 2018;

Lehmann *et al.*, 2015). These studies have demonstrated a successful detection of decreased forest health with modified RGB sensors. Yet, two inevitable constraints for the use of RGB sensors in plant stress sensing remain: broad bandwidth and overlapping bands. As illustrated by Pauly (2016) the spectral characteristics of digital sensors with a Bayer RGB colour filter array are primarily designed to create visually pleasing images. The broad bandwidth and overlapping individual bands of RGB sensors serve this purpose, however, in a remote sensing context, the overlap between bands causes spectral contamination leading to clumping of several vegetation characteristics such as chlorophyll content, canopy density and architecture. To extract vegetation stress dynamics, targeted information on these characteristics is a prerequisite. To build models on statistical inference between plant physiology and distinct reflectance properties, RGB sensors are thus a less-than-ideal choice for forest condition assessments. In agriculture, where slight changes in the visible range are more apparent in even-aged monocultures, the value of RGB sensors is arguably higher. Forests however exhibit far greater natural variability. In this aspect NIR modifications have increased the utility of RGB sensors, though their application remains restricted to relative assessments of a single dataset. The lack of calibration procedures and in-flight irradiance corrections of modified RGB sensors prevents knowledge transfer to spatiotemporally differing data. To progress from site-relative assessments towards widely applicable models, built on inference of plant traits, narrow band multispectral sensors become a fundamental requirement.

6.3.3 Raw spectra versus vegetation indices

Based on the results from CHAPTER 3, the importance of raw reflectance was consistently lower than the importance of derived vegetation indices. It was demonstrated that the use of vegetation indices improved the ability to distinguish declined trees from asymptomatic trees. NDVI and NDRE, were the best performing predictors for COD at Speculation Cannop. The vegetation indices have been shown to be sensitive to photosynthetic activity as well as water deficiency (Bannari *et al.*, 1995). Both are expected outcomes of COD-induced root damage and inflicted stress. Other studies have yielded similar results, confirming the utility of these vegetation indices in particular for remote sensing-based stress detection. As such, Easterday *et al.* (2019) found a strong relationship between measured leaf water content and UAV

acquired NDVI values. Brovkina *et al.* (2018) also reports on NDVI being the most suited index for monitoring spruce health condition. These studies confirm the successful adoption of the proven NDVI in the case of high-resolution UAV imagery. NDRE, a modification of the NDVI for dense vegetation, showed similar value in the current investigation. The NDRE penetrates the canopy deeper than the NDVI by replacing the RED band by the REDEDGE band (Gitelson *et al.*, 2005). The high importance of NDRE found in the current studies indicates the utility of the index in natural environments, where mature trees have thick crown layers. However, it may also point to the identification of reduced health in lower sections of the crown. Further work is required to assess this eventuality.

In CHAPTER 5 a multitemporal dataset, consisting of four multispectral flights, did not present clear results when comparing the performance of raw reflectance with that of vegetation index features in the individual models for the prediction of AOD. Amongst the ten best performing features, raw spectra and vegetation indices are represented across all four acquisition dates. While in both July models vegetation indices received higher feature importances, the contrast was found for May and October models, where raw reflectance features ranked higher than vegetation indices. It is uncertain why raw reflectances performed better than vegetation indices in spring and autumn imagery. A possible explanation is that individual raw reflectance channels showed low feature importance for specific dates. Correspondingly, vegetation indices that compromise those raw reflectance channels receive low scores (e.g. RED and NDVI in the May model, see Appendix F). Nevertheless, models used in the analysis of AOD consisted of a large array of features, including texture metrics. The complexity of the feature composition in these models makes interpretations of these results very difficult. However, overall, the inclusion of vegetation indices in models is beneficial, particularly so with respect to their normalising function: vegetation index values can typically be directly compared across acquisitions, without the requirement for rigorous calibration. This is of particular value in the context of UAV image acquisitions where lightweight platforms and miniaturised sensors pose a potential risk for degraded imagery. Sudden illumination and view angle changes may occur, that need to be accounted for by pre- and in-flight calibration procedures. The calibration and stitching of imagery in a SfM photogrammetric pipeline may introduce further errors. As such, Cao *et al.* (2019) reported on low accuracy of raw reflectance values stemming from UAV multispectral

sensors compared to field spectroscopy measurements. They also assessed UAV reflectance over a range of several days and documented significant deviations from absolute reflectance.

To reduce issues outlined above and to lower calibration uncertainties of UAV acquisitions, the use of vegetation indices is inevitable. Their use is particularly important when data are to be compared, as is the case for change detection or the adoption of models across datasets. In addition, vegetation indices can improve classification accuracy by amplifying the signal of those spectral characteristics that are indicative of plant health. Overall, the current findings are well in line with previous studies and highlight the advantage of using vegetation indices over raw imagery in forest condition assessments.

6.3.4 The importance of texture metrics

In addition to spectral characteristics, sample trees at Monks Wood were also examined by texture metrics in order to distinguish AOD-symptomatic from healthy trees. It was shown that textural variables can contribute explanatory power. Improved model performance was reported, which is in accordance with publications that have adopted texture metrics in UAV image classification (Gini *et al.*, 2018; Yuan and Hu, 2016; Siebring *et al.*, 2019).

In the analysis of multitemporal data in CHAPTER 5, the contribution of individual textural features varied greatly between individual datasets. This ambiguity is likely rooted in the interdependence of textural variations with the lighting of the scene, phenological stage and sensor characteristics. Texture metrics are derived from the spatial variation of the intensity values within a pre-defined neighbourhood (Haralick *et al.*, 1973). Feature values are thus highly dependent on the variability within the neighbourhood. While differences in this variability help to discriminate between AOD status of trees, probably due to changes in canopy architecture, representation of intensity variations can also be affected by other environmental factors, illumination and technical aspects regarding image acquisition. Some of these aspects, illumination in particular, are very difficult to control and may hinder knowledge transfer (trained models) throughout space and time. Models that incorporate texture may therefore not be suited for generalisation to other study sites or to monitor forest condition over time. Nevertheless, for site-relative assessments,

texture has proven to be useful in the detection of declined oak condition. Future work may investigate the utility of textural features further, quantifying the contribution of these metrics to forest health monitoring. Additional work that evaluates model performance with and without texture would provide such insights. Furthermore, the neighbourhood for texture computation should be analysed in more detail than the current study allowed. Here further knowledge would be beneficial to optimise moving window size for investigations of individual tree health with high-resolution UAV imagery.

6.3.5 The importance of timing the remote sensing acquisition

At the Monks Wood study site, UAV data were collected over the course of two growth periods, 2017 and 2018. In CHAPTER 4 and CHAPTER 5 the timing of the individual datasets was assessed regarding their informative power with respect to classification of species as well as for a detection of AOD status. For species identification, imagery obtained in May and October offered the highest accuracy in classification. These results are supported biologically as plant characteristics offer the greatest interspecies discrepancies at these growth stages. Mid growth season multispectral data, however, did not produce significantly lower accuracy scores and remain well-suited for species mapping.

In the identification of AOD symptoms, May imagery delivered the greatest explanatory power, closely followed by July imagery, while October imagery demonstrated low accuracy. A possible explanation for the poor performance of the autumn dataset is that the effects of senescence are similar for AOD symptomatic and asymptomatic trees and senescence had progressed to a point where the two groups could no longer be separated. However, there have not been explicit investigations on senescence dynamics linked to AOD stress. In this respect, further work is required to understand the general pathology and dynamics of this new disease. Likewise, it is not entirely clear why spring imagery performed better than summer imagery. There are many potential explanations for this phenomenon: delayed budburst of affected trees, amplified differences in foliar water and/or chlorophyll content between stressed and healthy trees at this growth stage as well as emphasised symptoms of AOD regarding pigmentation of leaves and canopy architecture. In addition to existing knowledge on AOD pathology, feature importances of the May model obtained in the current study

point to many of the above reasons for an enhanced potential for remote sensing-based AOD identification in spring, when compared to summer acquisitions. However, to unravel the exact cause and effect relationship between phenological stage, AOD and spectral remote sensing acquisitions, additional work is required that incorporates data with higher temporal resolution and a greater tree sample size than the current study.

Combining imagery from different acquisition dates was shown to improve classification results, although improvements were minor. Thus, collection of multitemporal data is not always advantageous with respect to cost and return nor is it sensible and/or feasible for every project. Of note is that the derivation of forestry metrics is often based on models that are built on and around data from mid-growth season. Additionally, spring and autumn may not present favourable conditions for optical UAV acquisitions since unstable weather conditions prevail during these seasons. Wind in particular can present difficulties with respect to moving foliage and branches in SfM-based processing (causing matching issues and blur in derived orthomosaics). Furthermore, in the northern hemisphere, illumination conditions are not ideal during spring and autumn as the sun angle is low, causing pronounced shadowing. Thus, until more research has been undertaken on the interaction between phenological stages and the ability to identify declined tree health, it is advisable to resort to UAV acquisitions in summer. Findings from the current investigations would recommend that, if possible, spring imagery is gathered in addition to mid-growth-season data.

6.3.6 The importance of species mapping

For species-specific identification of diseases and monitoring of forest condition, a species distribution map with high spatial resolution is an important prerequisite. Most work on UAV remote sensing assessments of forest condition to date has been undertaken for forests that exhibit homogenous species composition and structure. From an operational perspective, homogenous forests are still currently the most common domain to apply these technologies. However, when progressing the application of UAV-supported forest condition monitoring, including for natural and unmanaged woodland, heterogenous forests will require increased attention. In particular as climate impacts are expected to intensify, not only coniferous plantations but also mixed broadleaf forests will experience higher stress and decreased tree

health. Up-to-date and accurate species distribution maps are thus of utmost importance for remote sensing forest condition assessments. In the current study, it was demonstrated that UAV multispectral imagery is well suited for this task. More so, it was shown that the same data can be used for both purposes: species mapping and condition assessments. In practise, UAVs can therefore facilitate on-demand remote sensing forest condition surveys from a single source, even in heterogenous stands.

In CHAPTER 4 a species map was derived from a four-date multispectral dataset at ten-centimetre spatial resolution (95 % overall accuracy). While the use of the entire multitemporal data provided the best accuracy for species classification, it was shown that single-date data can also provide accuracy of 68 – 77 %. Species distinction was improved by the inclusion of tree height information as derived from hybrid SfM-ALS data.

In the applied pixel-based classification approach, it was shown that a dramatic reduction of training pixels did not severely affect classification accuracy. However, the number of individual tree samples required across the eight identified species to retrieve high classification accuracy was not analysed. In future work, optimising the quantity of ground truth data should be a central question to minimise surveying efforts in the field. In this context, it is important to note that the minimum required sample size for a robust wall-to-wall classification of tree species will vary according to the level of heterogeneity present at the site. With increased variability in site conditions as well as age distribution and structural composition, a greater sample number will be required. Additionally, as pointed out by Hill *et al.* (2010), in very diverse forests, spectral differences within species can be greater than between species. In such a case, multispectral species differentiation can be supported by tree height information as well as textural metrics. Texture metrics proved beneficial in the distinction of AOD symptomatic and asymptomatic trees, as presented in CHAPTER 5, however, were not considered for species mapping. Future work should consider investigating texture metrics for use in species identification also, particularly in regard to reducing the amount of ground truth data for training.

6.3.7 Wall-to-wall prediction of tree health

In CHAPTER 5, as a final feasibility test for AOD identification, developed models were applied to extrapolate decline status to all oak trees within the study site. This was done to provide a procedure aimed at the operational use of the approach: to utilise UAV remote sensing for the detection and future monitoring of oak decline. The prediction was limited to trees that were previously classified as oak and an identification of individual tree locations was performed on SfM-derived CHM with an ITC algorithm, thus theoretically predicting the health status of individual oak trees.

The presented approach demonstrated that UAV-acquired remote sensing data can be used for wall-to-wall predictions of individual tree health. However, results could not be validated due to lack of ground truth. Despite this limitation for validation, it became obvious that the quantity of symptomatic trees was overestimated. The prediction suggest that the number of symptomatic trees outweighs asymptomatic trees according to the undertaken predictions. Almost certainly, this does not reflect reality. At Monks Wood, extensive field sampling has been undertaken as part of the species classification work and all oak trees were visually inspected for symptoms. Only six further trees at the site were identified as exhibiting clear AOD symptoms in addition to the nine symptomatic trees previously tagged by the PuRpOsE project.

As model accuracy was determined to be high, through validation on independent samples, it remains difficult to explain the overestimation of AOD symptomatic trees across the site. However hereby lies a challenge of a study of this type, whilst it is difficult to determine the cause, this may be explained by factors other than AOD causing canopy stress symptoms or reduced condition. Sample numbers used in training the prediction models were balanced. Imbalanced data can thus be ruled out as the cause for overprediction. However, it is certain that binary labelling of samples is not ideal for prediction across larger areas. Thus, it could be that the learned decision threshold for oak decline status falls within the natural variability of remaining trees. A better approach, sensible for future work, would be if training and prediction are undertaken on samples with categorical or continuous health ratings. The method presented here for a wall-to-wall prediction of individual tree condition is applicable to samples classified in a non-binary way too, yet results would depict a much more nuanced estimation of tree health. Challenges originating in the natural

variability of forests and non-binary assessment of tree status are discussed in further detail below.

6.3.8 The value of UAV remote sensing for oak decline detection

Overall, it was demonstrated that UAV surveys and respective data can be successfully employed for the identification of trees affected by oak decline. However, the current research depicts the early stages of such work. While possibilities for a spatially continuous prediction of oak health were shown, it is still unclear whether detection of declined oak trees with a UAV remote sensing approach is plausible on broad scales. The presented studies were undertaken within the realm of remote sensing research and cost-benefit analyses were not performed. Although it currently appears that UAV remote sensing can be a useful tool for foresters, statements on the value of these technologies with regard to monitoring oak decline would be premature. To fully evaluate the potential and value of UAV remote sensing in an operational context, more studies are needed. Specifically, studies that incorporate a higher quantity of samples across broader spatial and temporal scales.

6.4 Challenges

In the course of the investigations on oak decline, several limitations and challenges in the presented approach were identified. These restrictions primarily relate to the sampling design of ground truth as well as to the general setting of study sites. Critical points that presented challenges throughout the studies and depict shortcomings of the current research relate to small sample sizes, binary rating of tree health and the heterogeneity of study sites.

6.4.1 Sample size

In the current studies, a key limitation in the oak decline assessments was the small number of sample trees. As small datasets are prone to overfitting, preventative measures were taken in RF modelling: cross-validation, repeated tests (e.g. 100 iterations), feature selection and use of independent validation data collected in the course of this study. However, overfitting cannot be ruled out completely.

A larger sample size would improve the analysis and enable a more robust interpretation of feature importances. Furthermore, wall-to-wall predictions would have benefitted from increased sample sizes in terms of model robustness as well as the option to validate and further analyse results.

Linked to the few samples, many aspects have remained unclear. To inform about the general practicability of UAV remote sensing for identification of oak decline, a larger set of sample trees is of utmost importance. Ideally, these samples would be distributed across several sites that are representative of COD and AOD found in the UK. A large set of samples from multiple sites will facilitate a more robust interpretation of the contribution of remote sensing-derived descriptors (e.g. spectra, texture) and whether these descriptors are suited to identify oak decline across broader spatial and temporal scales. A large sample set would also enable investigation of the optimal sample size for remote sensing-based assessments of oak decline as well as help answering site-relative questions, such as determining the proportion of training data required for a reliable extrapolation to the entire population.

For the above reasons, future studies should strongly consider sites that allows for the collection of a great number of samples. In the current investigations, the number of samples was not restricted by survey efforts but by the baseline condition of oak trees within the stand. Simply put, at the studied sites, there are only few trees with explicit COD and/or AOD pathology. At the study site at Monks Wood, for example, only 15 trees were found to have distinct AOD symptoms. The majority of remaining oak trees at the site did not show any signs of stress while few trees displayed mild damage that is not exclusive to AOD, such as reduced crown condition and beetle exit holes on the stem. Ideally, sites for future investigations on oak decline with remote sensing data exhibit a larger number of trees with clear symptoms, that can be confidently attributed to COD/AOD.

6.4.2 Natural variability

A substantial challenge for remote sensing forest condition assessments is finding the "stress signal" amongst naturally occurring variability in the scene. Thereby, remotely sensed data may contain information on plant physiological status and changes that are influenced by climatic events, environmental conditions (for example soil, moisture and competition) and phenology, in addition to potential noise

caused by atmospheric influences and survey characteristics. Additionally, in remote sensing, forests present a special subject matter, in that they are inherently heterogenous and complex. It has been recognised that with increased heterogeneity in forests the accuracy of remote sensing approaches tends to decrease (Lehmann *et al.*, 2015; Michez *et al.*, 2016). By their very nature, the two study sites therefore provide challenging conditions for developing and testing methods for species classification and oak decline detection.

UAV remote sensing-based identification of plant health is currently still more common in agriculture than in forestry (Hunt and Daughtry, 2018; Iglhaut *et al.*, 2019). While in modern agriculture remote sensing-based monitoring of crop condition has become a common tool, in forestry, the majority of applications thus far have remained in the conceptual stage. The reasons for these differences are manifold. Firstly, agricultural crops are typically present as monocultures. Finding stressed "outliers", that show discolouration and/or other symptoms relative to the remaining site, is thus facilitated. Though plantation forests are similar to agricultural crops in that sense, further key differences remain, that can hamper a straight-forward detection of stress. Unlike trees, agricultural plants are mostly simple and small in scale, where poor health is typically expressed in the upper section of the plants. Trees however, exhibit far greater structural diversity and stress may not always be apparent in (crown) sections visible to airborne remote sensing. In forests, this diversity is aggravated by varied site conditions, species mixture and the vertical structure of a stand. With time and growth, the contribution of these factors to the complexity of a scene increases, ultimately adding noise/blur to the detectable impact of a specific stressor. An additional temporal aspect is that forest decline and reduced tree health often develop over much longer time scales than crop damage. These differences become particularly apparent as growth periods of agricultural crops are compared with those of trees and forests.

To reduce the impacts of spectral and structural variability in forest stress sensing, it is advisable to perform controlled experiments on even-aged, single-species stands. Within such controlled experiments, ideally a disease or pest is manually introduced for calibration and validation of the proposed remote sensing method. This way, the physiological changes a tree undergoes due to the invoked stress can be closely monitored. As such, Dash *et al.* (2017) manually infected trees in pine plantation plots and monitored the progression of the stress signals with periodic UAV

surveys. However, such baseline surveys are not always feasible if a species or forest is protected, if the pest or disease is not endemic and there is a risk of non-containment or subsequent managed eradication. Furthermore, small scale experiments with young plants in nurseries or in growth rooms do not always accurately represent stress dynamics present in forests or mature stands, especially considering natural or near-natural forest ecosystems. As such, the oak declines studied in the course of this PhD are known to affect mature trees (Denman and Webber, 2009) and experiments with manual inoculations of AOD on young oak in a nursery have previously failed (personal communication with PuRpOsE project members). When controlled experiments are not possible, as was the case in the current studies, the high variability of (natural) forests underlines the need for increased sample sizes.

6.4.3 Description of symptoms - severity of the decline

The results presented here demonstrated potential of a remote sensing-based identification of oak decline. However, it was solely shown that trained RF models are able to distinguish between symptomatic and asymptomatic trees. The results of the current investigations are thus not revealing information on the decline stage and/or on the detection threshold. Rather than a binary classification of tree condition, a continuous or categorical scale would be better suited for a thorough assessment of oak decline identification with UAV remote sensing data. A progressive scale would provide a better reference against which to rate the performance of models. Furthermore, this would facilitate a more robust assessment of individual remote sensing-derived features and their contribution in the description of symptomatic and asymptomatic trees, e.g. in the form of partial dependence plots.

To accomplish a gradual estimation of oak decline affection, future approaches should consider a more nuanced description of symptoms, that ideally reflects the severity of the diseases. First efforts towards measuring decline severity in oaks have been published by Finch *et al.* (2021) whose Phenotypic Decline Index (PDI) combines field-based visual indicators, related to crown and stem condition, in a continuous scale to depict decline severity. An additional Decline Acuteness Index (DAI) places trees on a continuous decline spectrum between COD and AOD, thus differentiating between the two diseases. Not only does this present a big step forward in the clarification of AOD/COD pathology but also presents a great opportunity to

link PDI/DAI scores with remote sensing data. At the time of writing, PDI values were available for eight symptomatic trees at Speculation Cannop. However, this did not provide enough data to robustly apply in a regression-based approach with remote sensing information. Future studies will greatly benefit from the proposed continuous phenotypic descriptors, and thus should be incorporated in the experimental design for remote sensing-based assessments of oak decline.

6.4.4 Limitations in UAV multispectral sensing

The multispectral sensor used in the current studies offers five distinct spectral bands, three in the visible range and two in the NIR range of the electromagnetic spectrum. For vegetation analyses, observed reflectance in these regions predominantly relates to chlorophyll content. In both, AOD and COD, chlorophyll content is expected to decrease during the decline progress and in agreement with the presented results, spectra available from the narrowband Micasense RedEdge sensor thus offer indication of oak health status. However, changes in chlorophyll content are not the only physiological changes, traceable with spectral image data, that theoretically occur in declining trees. A disruption of vascular flow that occurs in both decline syndromes (Denman and Webber, 2009) likely translates to changes in leaf water content. The reflectance spectrum of vegetation is known to be strongly influenced by cellular water presence in the NIR and short-wave infrared regions (SWIR) of the spectral domain, between 900 nm and 2500 nm (Ceccato *et al.*, 2001; Hunt and Rock, 1989). In the water absorption bands, which appear at 970 nm, 1200 nm, 1450 nm and 1950 nm, correlation between remotely sensed spectra and leaf water content is particularly strong (Das *et al.*, 2021). This relationship can be exploited for the estimation of leaf and canopy water content (Tucker, 1980) and when normalised with the leaf area index, equivalent water thickness can be derived (Gao and Goetzt, 1995).

The role of water content in the prediction of decline status is missed in the current analysis due to the limitation in spectral range of the multispectral sensor, which offers information for five discrete bands between 475 nm and 840 nm. The narrow wavebands and mechanical shutter of the Micasense RedEdge sensor make it among the highest quality available multispectral sensors for UAV use. However, important opportunities for further research on oak decline lie in the spectral region

> 900 nm. Assessments of leaf water content would facilitate better understanding of the physiological processes a tree undergoes in the course of the decline and offer potential to study the main predisposing factor for oak decline: drought stress.

Multi- and hyperspectral data from air- and spaceborne sensors, offering wavelengths in the NIR and SWIR region, have successfully been used to study water content in vegetation (Clevers *et al.*, 2010; Colombo *et al.*, 2008; Gao and Goetzt, 1995; Riggs and Running, 1991; Vinod *et al.*, 2021). In comparison to the UAV-specific multispectral sensor used in the current study, most of these larger instruments offer wider spectral range and greater band selection. Hyperspectral imagery in particular can facilitate more advanced non-parametric modelling approaches and physically-based modelling approaches where vegetation traits are directly inferred from full-spectrum data, e.g. by inversion of radiative transfer models (Dorigo *et al.*, 2009; Hernández-Clemente *et al.*, 2019; Hornero *et al.*, 2021). Higher spectral resolution can thus enable more robust retrieval of biophysical and biochemical properties (Verrelst *et al.*, 2015). At this early stage of remote sensing research on the oak decline complex, finer resolution spectra recorded across a broader range would have been greatly beneficial to strengthen understanding of the impact on trees and processes involved.

A small selection of hyperspectral sensors is currently available for UAV application (Adão *et al.*, 2017). While these miniaturised sensors offer greater band selection than multispectral UAV sensors, they are typically more limited in their spectral range than hyperspectral instruments on piloted aircrafts or satellites. Efforts at Monks Wood were made to collect hyperspectral data from a UAV mounted Pika L instrument (Resonon Inc., Bozeman, USA), a pushbroom sensor that records 281 spectral channels at 2.1 nm bandwidth in the spectral range between 400 nm and 1000 nm. Unfortunately, these data were corrupted due to electronic interference onboard the UAV.

Currently there are only few published examples where hyperspectral UAV sensors were adopted in the domain of forest health remote sensing (Ecke *et al.*, 2022; Näsi *et al.*, 2015, 2018; Sandino *et al.*, 2018). Certainly, this is partly the case due to the high cost of these systems. Furthermore, the technical difficulty to obtain spectrally and geometrically correct data from UAV-mounted hyperspectral sensors is considerably higher than with multispectral sensors. The requirements for high precision IMUs to geometrically correct data collected by a pushbroom sensor

currently still favours piloted aircraft platforms where these instruments can be larger and heavier and have undergone vigorous calibration procedures.

Despite the demonstrated potential to assess declined oaks with multispectral UAV data, there remain many opportunities for investigation of the disease with remotely sensed data. Greater spectral resolution is highly desirable for further research efforts on oak decline, specifically to enable differentiated identification of spectral traits involved in the decline process. It has been shown that hyperspectral data are well suited to spectrally infer physiological indicators of plant health, such as water stress, chlorophyll content and leaf pigmentation (Hernández-Clemente *et al.*, 2019; Lausch *et al.*, 2016; Omari *et al.*, 2013; Sampson *et al.*, 2003). Requirements for advanced analysis methods, such as inverse radiative transfer modelling, are high radiometric accuracy and high spectral resolution over a broad range (covering the visible, NIR and SWIR part of the spectrum). These requirements may currently still place piloted aircraft campaigns in favour over UAV data acquisition.

6.4.5 SfM photogrammetry and tree height

In CHAPTER 4, tree height was employed as an additional independent variable for species classification, presented as a CHM. Similarly, in CHAPTER 5, a CHM was utilised for the recovery of ITCs. Although the digital surface models generated by SfM photogrammetry in the current studies offer a comprehensive depiction of the canopy surface, extracting tree height information solely from these data is not possible. As outlined in section 1.8, photogrammetrically derived data characterises only the surface of a scene, due to the passive nature of the sensor. In order to normalise canopy height and thus obtain tree height measurements, supplementary data regarding ground elevation is necessary. Ground elevation is commonly obtained through LiDAR. For forest inventory, where tree height is commonly used in allometric equations, it was found that LiDAR is fundamental for accurate tree height estimations with photogrammetric data (Goodbody *et al.*, 2019a, 2019b; Wallace *et al.*, 2016; White *et al.*, 2016). At sites where detailed information on ground elevation is not readily available, tree height data require an additional sensor or system to be deployed, which can add significant complexity and cost to the project.

In the present study locations, the ground elevation was obtained from publicly available ALS data. Such datasets are becoming more readily-available at regional or national scales, with increasing government recognition of the importance of frequently-updated topographic data for multiple purposes e.g. flood risk mapping and international reporting requirements like National Forest Inventory.

The inclusion of tree height information, obtained from hybrid SfM-CHMs, greatly aided species classification and facilitated the retrieval of ITCs. Nevertheless, if information on ground elevation and therefore tree height data cannot be attained, species classification can still be accomplished using spectral data exclusively (Fassnacht *et al.*, 2016). This was also exemplified in the analysis of classification accuracy for data combinations in CHAPTER 4.

CHAPTER 5 utilised identified ITCs of oak trees to predict their condition by computing summary statistics for plots located around the centre of the ITCs. The use of tree-centric plots in this study was primarily to predict a comparable segment of the tree crown that the models were trained on, and to minimise undesired border effects caused by adjacent trees. Nonetheless, the application of ITCs in a dense broadleaf forest can present challenges. The approach may lack accuracy in assessing individual trees with heterogeneous crown structures, and in cases where tree crowns are interlocked or overlapping (Lindberg and Holmgren, 2017). It is also recognised that the precision of SfM-CHMs in detecting individual trees is greatly influenced by seasonal variations in foliage (Nuijten *et al.*, 2019).

Given the challenges mentioned above, and particularly when ground elevation data are unavailable, future studies on tree health in dense broadleaf forests may benefit from exploring alternative approaches for object-based analysis that do not depend on tree height information. UAV imagery has been successfully analysed using common OBIA algorithms (Karydas *et al.*, 2017; Michez *et al.*, 2016; Yu *et al.*, 2016; Yuan and Hu, 2016) such as the multi-resolution image segmentation algorithm (Blaschke, 2010), which can be applied to spectral data alone. Although individual tree analysis may not be possible using this approach in dense canopy forests, it can still be utilised to detect clusters of spectrally similar regions that may correspond to crown sections exhibiting poor health conditions. From an operational standpoint, if robust model predictions can be made for these sections, it could be argued that determining tree health at the individual tree level may not be necessary.

6.5 UAVs and SfM photogrammetry for forest condition assessments

The results from the current studies along with published work have demonstrated potential of UAV remote sensing for forest condition assessments (Näsi *et al.*, 2018, 2015; Minařík and Langhammer, 2016; Michez *et al.*, 2016; Lehmann *et al.*, 2015; Dash *et al.*, 2017; Baena *et al.*, 2017; Brovkina *et al.*, 2018).

A key benefit of the technology is the high independence in remote sensing data capture. Compared to piloted aircraft campaigns, UAV surveys can be realised at a fraction of the cost and can be undertaken single-handedly by researchers with moderate expertise required. A further crucial advantage of UAVs, that was exploited in the current investigations, is their ability for rapid on-demand deployment. With minimal lead time, surveys can be undertaken when up-to-date data are required, the target phenological stage is reached and/or weather conditions are optimal. An additional benefit of optical UAV remote sensing stems from SfM-photogrammetric processing of imagery: i.e. that spectral data and information on canopy structure are provided by the same source. Temporal and spatial mismatches between these data are thus avoided. High spatial resolution SfM-derived surface models can then be combined with pre-existing ground information (e.g. ALS) to retrieve tree heights, as employed in the current investigation.

The highly detailed information content of UAV remote sensing data however holds its own challenges. Increased detail in UAV imagery raises the requirement for locational accuracy in ground truth data. This is essential to link features in the remote sensing data with field observations. In the current investigations, this condition posed a notable challenge due to dense canopy cover at both study sites. To tackle this challenge, three different methods were employed to collect accurate locations of sample trees: 1) in-field digitisation of features on the UAV orthophotos generated within this study, 2) crown-centric location mapping using a pole-mounted GNSS receiver inserted through the tree crowns and 3) RTK surveys during leaf-off conditions. While these techniques worked well for their purpose, they still require considerable efforts in the field. Winter surveys, utilising a RTK-GNSS receiver, proved to be the fastest, most straightforward of the above solutions and generated sufficient (< 1 m) accuracy for species mapping. However, not all information relevant to tree health and forest condition can be attained in winter. As such, oak decline

symptoms like crown condition and/or stem bleeds are best assessed within the growth season.

From an operational standpoint, the inevitable requirement for high accuracy field data represents one of the largest obstacles for cost-effective UAV-driven forest condition assessment. For this reason, better information on optimal sample quantities is required. Future research on forest condition should further investigate the relationship between sample size and model/prediction performance for specific forest health threats.

Linked to the requirement for high accuracy field surveys in UAV remote sensing lies a further, more fundamental question, of whether the spatial resolution of UAV imagery is too high. Some studies have reported that finer resolutions are more suited to detect stress symptoms (Easterday *et al.*, 2019) whilst others advise coarser resolutions, e.g. at GSD the same size as the crown (Dash *et al.*, 2017). In theory, an ideal spatial resolution should exist where the integration area of the sensor maximises information content while minimising noise – thus maximised signal to noise ratio (SNR). The typically very high resolution (< 10 cm) of optical UAV data captures a large amount of variation. As discussed, forests and particularly natural forests, inherently contain great spectral and textural variability. While some variability may explain the condition of trees (as shown in CHAPTER 5), identification of decreased tree health is possibly enhanced as spatial resolution is decreased. In UAV remote sensing however, spatial resolution is restricted by the legal flying height as well as SfM-based image matching that requires defined minimum detail and resolution. To negate this issue, smoothing operations could be applied and/or spatial resolution could be reduced in post processing, by resampling to a coarser resolution. Segmentation approaches, common from OBIA, should be explored in addition to spatial resampling and/or image smoothing. In the current studies the effect of spatial resolution was not tested. However, future studies should incorporate investigations on SNR in relation to resolution. Associated with SNR, the impact of smoothing algorithms on the detection of stress signals should also be assessed. Investigations should assess how these approaches compare for an identification of reduced health at the individual tree level: high resolution versus resampled/smoothed, high resolution versus coarse resolution versus OBIA.

Further aspects of UAV surveys that require increased research efforts lie in the data quality. Uncertainties in the quality of data produced need to be better

understood, with respect to calibration performance and replicability. For repeated UAV acquisitions, variations in illumination, atmospheric and phenological conditions are inevitable. Being a passive remote sensing approach, these variations have direct influence on collected data in optical imaging. To compensate for these influences, calibration and correction procedures are required. Unlike in air- or spaceborne sensing, where sensors undergo vigorous calibration and validation, UAV operators are mostly limited to trusting the manufacturers of miniaturised sensors to perform according to their specifications under a great range of conditions. Recent studies however have found that, while a linear relationship exists, UAV acquired reflectance measurements (obtained with a Micasense RedEdge sensor) may not accurately represent actual reflectance (Cao *et al.*, 2019; Tu *et al.*, 2018). Additionally, variability in UAV-sensed reflectance was detected over time, suggesting that varied illumination and atmospheric conditions influence derived reflectance values (Cao *et al.*, 2019), despite calibration procedures being undertaken (reference targets and in-flight irradiance). While normalised vegetation indices can present a way to reduce these uncertainties, further investigations on absolute reflectance derived from UAV sensors are necessary. Instead of unquestioningly relying on manufacturers claims more work on validating outputs of miniaturised sensors and respective processing chains is needed. Protocols need to be developed that facilitate collection of robustly calibrated data under a range of conditions and survey scenarios. This knowledge is critically needed towards comparable UAV data and reliable extraction of biophysical properties from these data. Reducing uncertainties in data calibration will further enable model transfer and multitemporal analyses.

Overall, UAV, sensor and processing technologies have undergone remarkable developments over the past decade. Their potential in the forestry domain is undisputable. For large forest stands, full coverage may not yet be reached in a single flight due to limitations in flight time and air law regulations. However, partial coverage of forest can be achieved and these data have the potential to represent the forest more accurately than sampling from traditional field plots. As an example, Puliti *et al.* (2017) found that only a quarter of sample plots are required in UAV assessments compared to field-based measurement to achieve the same precision in forest inventory metrics. As an added benefit in remote sensing surveys, feature explicit spatial information and locations of individual trees and plots may be remeasured, data can be reanalysed and directly compared. Tabular data from traditional field surveys

typically does not contain such information and multitemporal assessments are limited. Rapid on-demand deployment of UAVs and fast photogrammetric processing on personal computers have and continue to approximate effort and cost between remote sensing surveys and ground-based inspections of forests. In fact, UAV remote sensing data may be collected in addition to regular field survey data without great effort or cost involved. In these respects, UAVs are already blurring the lines between traditional field-based and remote sensing-based data capture.

CHAPTER 7:

CONCLUSION

The studies presented within this thesis demonstrated potential for the detection of declined oak condition with UAV remote sensing in semi-natural forests. UAV-acquired imagery was shown to contain information that reflects stress-induced changes within the crown and foliage of COD and AOD affected trees, and allowed the differentiation between declined and control oak trees. Narrowband multispectral imagery was proven to be most suitable for this task. Spectra in the near-infrared region of the electromagnetic spectrum in particular were shown to contain greatest explanatory value, indicating a detectable degradation of photosynthetic capacity under physiological stress caused by oak decline.

RGB imagery was shown to be greatly inferior compared to narrowband multispectral imagery in the context of the current forest condition assessments. Broad and overlapping bands from conventional RGB sensors were found to be unsuitable for the distinction of COD symptomatic and asymptomatic trees. Among the five available bands in the multispectral data, the spectra from the near-infrared region, specifically the RE and NIR bands, were found to be the most important in distinguishing between declined and control oak trees. The results emphasise the significance of near-infrared spectra and the sensitivity of the spectral region to chlorophyll content to infer biophysical factors related to crown deterioration, such as foliage discolouration and loss, in declining trees.

Furthermore, the calculation of vegetation indices instead of and/or in additional to raw spectra, was demonstrated to add explanatory value to models. In the model-based distinction of symptomatic and asymptomatic samples, the NDVI and NDRE, which both relate to photosynthetic activity, showed particular high importance. Texture metrics, as used in the analysis of AOD affected trees, ranked among the highest feature importances of all models. The significance of standard deviation as a summary statistic for individual tree crowns regarding spectral features is consistent with this observation. Although it was shown that texture metrics and the variance of spectral features, thus variability within the crown, can be important predictors, the reliability of these measures requires further work.

At Speculation Cannop in the Forest of Dean, where COD is present, two multispectral UAV acquisitions in summer delivered the highest symptomatic/asymptomatic classification accuracy using random forest modelling producing 74 % and 75 % accuracy respectively, validated on 50 % of available sample trees. Despite the high classification accuracy, a test for generalisation of the developed models failed. Applying the model from one flight to the subsequent flight, just four days apart, revealed reflectance calibration issues that outweigh the signal used for the differentiation between the two oak health classes.

At Monks Wood, the detection of AOD affected trees was investigated by the combined use of spectral data and texture metrics. Greatest model performance was equally achieved by spring imagery (AUC 0.91 - 0.98) and the combined use of features with highest importance from four separate acquisitions (AUC 0.91 - 0.98). Summer imagery of two consecutive years also showed high explanatory value, delivering AUC 0.77 – 0.98 for July 2017 data and AUC 0.66 – 0.73 for July 2018 data respectively. In this case, and in contrast to findings for COD at Speculation Cannop, October imagery did not provide robust differentiation between the two sample groups (AUC 0.63 – 0.65).

For the species-specific application of developed models, UAV remote sensing enabled species classification at Monks Wood. This analysis permitted an existing species distribution map of highly mixed deciduous woodland derived from piloted airborne remote sensing data to be greatly improved. The number of classes was increased from seven to 11, the spatial resolution was improved from two metres to ten centimetres and the overall classification accuracy was increased from 88 % to 95 %. Classification of oak was achieved with a User's accuracy of 97 %. It was shown that species classification can be supported by canopy height information, increasing classification accuracy further. Though it was demonstrated that a high-resolution CHM can be derived from a photogrammetric canopy model, this process requires a complementary DTM from a supplementary source in dense forests. Increasing availability of airborne LiDAR datasets at a national level will overcome the past limitation of ALS coverage.

For condition assessments and species mapping alike, it was shown that the use of combined multitemporal data had a marginal effect on classification accuracy. Therefore, when time and costs are limited, future studies may focus efforts on timing UAV acquisitions according to phenological stage as well as weather and illumination

conditions. The current investigations concluded that imagery is best collected mid growth season and, if possible, supported by spring imagery.

Finally, the developed models for AOD detection and the produced species map were implemented to predict decline status within the entire study site. This wall-to-wall prediction of decline status confirmed uncertainties in model robustness and the inability to generalise, also found in the investigations on COD. At Monks Wood the extrapolation to all identified oak trees yielded unrealistic results, with a high number of declined trees predicted. In part, the identified weaknesses of the developed models originate from the natural variability of heterogenous forests combined with the diverse symptoms of oak decline. Additional limitations however, are specific to the current studies and can be attributed to intensive ground truth yet limited sample size and the consequent overfitting of trained models. The binary classification of oak health status and uncertainty in UAV acquired reflectance values further reduces the models' ability to successfully adapt to new data.

Such limitations of transferability were common in past airborne and satellite data empirical studies, and the current challenges using UAV-derived data may in part be due to the relative youth of this technology and in particular its application for forest health assessment.

Despite encouraging results for the general feasibility to detect signs of decline-induced stress on oak trees, many challenges and opportunities remain. For UAV remote sensing to become an additional tool for forest condition assessments in operational forestry, research is required that specifically targets the robustness of these assessments. How the ability to detect stress signals and reduced forest condition is influenced by the complexity of a forest and varied environmental conditions need to better understood. Additional research is also required regarding the reliability of UAV acquired data. Sensor calibration and processing chains need to be scrutinised to establish confidence in gathered absolute reflectance values. A better understanding of data quality and reliability will provide a strong basis to establish links between stress-relevant plant traits and UAV data. Increased confidence in the accuracy of UAV-sensed reflectance will also facilitate multitemporal analyses, assessing forest condition in terms of spectral changes (change detection) rather than identifying stress from optical properties of a single UAV acquisition.

Studies of forest condition with UAV remote sensing data should also aim to incorporate a large set of sample trees across multiple sites. To increase precision, tree

status should be represented by a continuous dependent variable, expressing the severity of infection. With a larger set of samples, representing decline severity on a broader scale, the robustness of models can be improved and links between remotely sensed spectra and health relevant plant traits can be established further.

In general, UAVs paired with SfM photogrammetry have paved the way for independent remote sensing data capture. UAVs facilitate rapid and frequent deployment, allowing practitioners to respond to requirements of immediate tree health assessments and continuous forest condition monitoring. With great user control over the collected data, UAV remote sensing provides a cost-effective alternative to traditional sources of remote sensing data. These recent developments have democratised the use of remote sensing technology and will continue to do so. It is without question that UAV remote sensing will ultimately transition from forest health research to operational forest condition monitoring, providing a new source of information for forest management. While the requirement for field information will likely not be eliminated entirely, UAV remote sensing can complement these data, e.g. by extrapolating point samples to forest or stand level. In this regard UAV remote sensing is bridging the gap between coarse air/spaceborne assessments and infrequent, sparse ground observations.

UAV remote sensing technology is, relatively speaking, still in its youth and as such new discoveries are still being made to establish optimal sensor configuration, flight parameters and necessary calibration of datasets. This is similar to the situation found with airborne and satellite sensors in past decades. This study has informed users of UAV remote sensing technology of the requirements of calibration, comprehensive ground-based data and flight planning considerations to take account of sensitivity to environmental conditions at time of flight, in order to obtain robust, replicable datasets.

In forestry studies using remote sensing technology, especially in the initial stages of its development, researchers often concentrate on monoculture plantation forests, which are typically composed of conifers with structurally distinct crowns and exhibit relatively uniform spectral and structural characteristics. Conversely, the two study sites used within this project represent amongst the most challenging conditions to test this comparatively new technology, with highly-mixed, semi-natural species composition, predominantly broadleaves with dense, interlocking crowns.

Furthermore, there is still much that is unknown about the cause and effects, biophysical characteristics, pathology and progression-remission cycles of oak decline and this is the subject of ongoing research among specialist plant health scientists in Britain. The ability to identify trees under stress, potentially before symptoms become visible to the eye, provides the opportunity to monitor the onset and progression of these diseases to better understand their dynamics and manage them. The use of new UAV remote sensing technology for this purpose is not without its challenges, however this study has indicated the potential to achieve this. Accordingly, it is proposed to perform additional research on oak decline employing UAV remote sensing to expand on this potential and to ultimately inform the protection of the iconic oak species in Britain.

Bibliography

Aasen, H., and Bareth, G. (2019) Spectral and 3D nonspectral approaches to crop trait estimation using ground and UAV sensing. In Thenkabail, P. S., Lyon, G. J., and Huete, A. (Eds.), *Hyperspectral Remote Sensing of Vegetation (Second, Edition, Four-Volume-Set). Volume III Title: Biophysical and Biochemical Characterization and Plant Species Studies*. CRC Press - Taylor and Francis Group.

Achard, F., Brown, S., Brady, M., DeFries, R., Grassi, G., Herold, M., Mollicone, D., Pandey, D., and Jr., C. S. (2011) *Global Obervation of Forest and Land Cover Dynamics Report version COP17-1*.

Adão, T., Hruška, J., Pádua, L., Bessa, J., Peres, E., Morais, R., and Sousa, J. J. (2017) Hyperspectral imaging: A review on UAV-based sensors, data processing and applications for agriculture and forestry. *Remote Sensing* 9(11).

Allen, W. A., and Richardson, A. J. (1968) Interaction of Light with a Plant Canopy. *Journal of the Optical Society of America* 58(8): 1023.

Alonzo, M., Andersen, H.-E., Morton, D., and Cook, B. (2018) Quantifying Boreal Forest Structure and Composition Using UAV Structure from Motion. *Forests* 9(3): 119.

Alonzo, M., Bookhagen, B., and Roberts, D. A. (2014) Urban tree species mapping using hyperspectral and lidar data fusion. *Remote Sensing of Environment* 148: 70–83.

Altmann, A., Tolosi, L., Sander, O., and Lengauer, T. (2010) Permutation importance: A corrected feature importance measure. *Bioinformatics (Oxford, England)* 26: 1340–1347.

Anderegg, W. R. L., Hicke, J. A., Fisher, R. A., Allen, C. D., Aukema, J., Bentz, B., Hood, S., Lichstein, J. W., Macalady, A. K., Mcdowell, N., Pan, Y., Raffa, K., Sala, A., Shaw, J. D., Stephenson, N. L., Tague, C., and Zeppel, M. (2015) Tree mortality from drought, insects, and their interactions in a changing climate. *New Phytologist*. doi:10.1111/nph.13477.

Anderson, K., and Gaston, K. J. (2013) Lightweight unmanned aerial vehicles will revolutionize spatial ecology. *Frontiers in Ecology and the Environment* 11(3): 138–146.

Baena, S., Moat, J., Whaley, O., and Boyd, D. S. (2017) Identifying species from the air: UAVs and the very high resolution challenge for plant conservation. *PLoS ONE* 12(11): 1–21.

Bannari, A., Morin, D., Bonn, F., and Huete, A. R. (1995) A review of vegetation indices. *Remote Sensing Reviews* 13(1–2): 95–120.

Barnes, E. M., Clarke, T. R., Richards, S. E., Colaizzi, P. D., Haberland, J., Kostrzewski, M., Waller, P., Choi C., R. E., Thompson, T., Lascano, R. J., Li, H., and Moran, M. S. (2000) Coincident detection of crop water stress, nitrogen status and canopy density using ground based multispectral data. *Proc. 5th Int. Conf. Precis Agric* (July 2015).

BBC News (/2018) Tree-killer disease Phytophthora ramorum extends its reach. Accessed: 22nd December 2020 <https://www.bbc.com/news/uk-scotland-south-scotland-44494674. >.

Belgiu, M., and Drăgu, L. (2016) Random forest in remote sensing: A review of applications and future directions. *ISPRS Journal of Photogrammetry and Remote Sensing* 114: 24–31.

Blaschke, T. (2010) Object based image analysis for remote sensing. *ISPRS Journal of Photogrammetry and Remote Sensing* 65(1): 2–16.

Bogner, C., Seo, B., Rohner, D., and Reineking, B. (2018) Classification of rare land cover types: Distinguishing annual and perennial crops in an agricultural catchment in South Korea. *PLoS ONE*. doi:10.5194/essd-6-339-2014.

Bolles, R. C., Baker, H. H., and Marimont, D. H. (1987) Epipolar-plane image analysis: An approach to determining structure from motion. *International Journal of Computer Vision* 1(1): 7–55.

Bolyn, C., Lejeune, P., Michez, A., and Latte, N. (2022) Mapping tree species proportions from satellite imagery using spectral–spatial deep learning. *Remote Sensing of Environment* 280.

Botkin, D. B., Estes, J. E., MacDonald, R. M., and Wilson, M. V. (1984) Studying the Earth's Vegetation from Space. *BioScience* 34(8): 508–514.

Brady, C., Arnold, D., McDonald, J., and Denman, S. (2017) Taxonomy and identification of bacteria associated with acute oak decline. *World Journal of Microbiology and Biotechnology* 33(7): 1–11.

Breidenbach, J., Næsset, E., Lien, V., Gobakken, T., and Solberg, S. (2010) Prediction of species specific forest inventory attributes using a nonparametric semi-individual tree crown approach based on fused airborne laser scanning and multispectral data. *Remote Sensing of Environment* 114(4): 911–924.

Breiman, L, Friedman, J., Stone, C. J., and Olshen, R. A. (1984) *Classification and Regression Trees*. Taylor & Francis.

Breiman, Leo (2001) Random forests. *Machine Learning* 45(1): 5–32.

Brovkina, O., Cienciala, E., Surový, P., and Janata, P. (2018) Unmanned aerial vehicles (UAV) for assessment of qualitative classification of Norway spruce in temperate forest stands. *Geo-Spatial Information Science* 21(1): 12–20.

Brown, N., Inward, D. J. G., Jeger, M., and Denman, S. (2015) A review of Agrilus biguttatus in UK forests and its relationship with acute oak decline. *Forestry* 88(1): 53–63.

Brown, N., Jeger, M., Kirk, S., Williams, D., Xu, X., Pautasso, M., and Denman, S. (2017) Acute oak decline and Agrilus biguttatus: The co-occurrence of stem bleeding and D-shaped emergence holes in Great Britain. *Forests* 8(3).

Brown, N., Jeger, M., Kirk, S., Xu, X., and Denman, S. (2016) Spatial and temporal patterns in symptom expression within eight woodlands affected by Acute Oak Decline. *Forest Ecology and Management* 360: 97–109.

Cai, S., Zhang, W., Liang, X., Wan, P., Qi, J., Yu, S., Yan, G., and Shao, J. (2019) Filtering airborne LiDAR data through complementary cloth simulation and progressive TIN densification filters. *Remote Sensing* 11(9).

Cao, S., Danielson, B., Clare, S., Koenig, S., Campos-Vargas, C., and Sanchez-Azofeifa, A. (2019) Radiometric calibration assessments for UAS-borne

multispectral cameras: Laboratory and field protocols. *ISPRS Journal of Photogrammetry and Remote Sensing* 149(January): 132–145.

Carbonneau, P. E., and Dietrich, J. T. (2016) Cost-effective non-metric photogrammetry from consumer-grade sUAS: Implications for direct georeferencing of structure from motion photogrammetry. *Earth Surface Processes and Landforms*. doi:10.1002/esp.4012.

Carter, G. A., and Knapp, A. K. (2001) Leaf optical properties in higher plants: linking spectral characteristics to stress and chlorophyll concentration. *American Journal of Botany* 88(4): 677–684.

Ceccato, P., Flasse, S., Tarantola, S., Jacquemoud, S., and Grégoire, J. M. (2001) Detecting vegetation leaf water content using reflectance in the optical domain. *Remote Sensing of Environment* 77(1): 22–33.

Chalker-Scott, L. (1999) Environmental significance of anthocyanins in plant stress responses. *Photochemistry and Photobiology* 70(1): 1–9.

Chan, A. H. Y., Barnes, C., Swinfield, T., and Coomes, D. A. (2021) Monitoring ash dieback (Hymenoscyphus fraxineus) in British forests using hyperspectral remote sensing. *Remote Sensing in Ecology and Conservation* 7(2): 306–320.

Chen, Caiyan, Jing, L., Li, H., and Tang, Y. (2021) A new individual tree species classification method based on the resu-net model. *Forests* 12(9).

Chen, Chao, and Liaw, A. (2004) *Using Random Forest to Learn Imbalanced Data*.

Chen, G., and Meentemeyer, R. K. (2016) Remote Sensing of Forest Damage by Diseases and Insects. (November): 145–162. doi:10.1201/9781315371931-9.

Chronic Oak Decline - Forest Research (/2020). Accessed: 14th December 2020 <https://www.forestresearch.gov.uk/tools-and-resources/pest-and-disease-resources/chronic-oak-dieback/. >.

Clevers, J. G. P. W., Kooistra, L., and Schaepman, M. E. (2010) Estimating canopy water content using hyperspectral remote sensing data. *International Journal of Applied Earth Observation and Geoinformation* 12(2): 119–125.

Collier, R., and Thomas, B. (2016) Agriculture and Forestry Climate Change. *Forest Research - Agriculture & Forestry Report Card Paper* 9: 1–34.

Colombo, R., Meroni, M., Marchesi, A., Busetto, L., Rossini, M., Giardino, C., and Panigada, C. (2008) Estimation of leaf and canopy water content in poplar plantations by means of hyperspectral indices and inverse modeling. *Remote Sensing of Environment* 112(4): 1820–1834.

Cortijo, F. J., and Blanca, N. P. D. La (1999) The performance of regularized discriminant analysis versus non-parametric classifiers applied to high-dimensional image classification. *International Journal of Remote Sensing* 20(17): 3345–3365.

Croft, H., Chen, J. M., Luo, X., Barlett, P., Chen, B., and Staeble, R. (2016) Leaf chlorophyll content as a proxy for leaf photosynthetic capacity. *Remote Sensing of Environment* : 1–12. doi:10.1111/gcb.13599.

Crutsinger, G. M., Short, J., and Sollenberger, R. (2016) The future of UAVs in ecology: an insider perspective from the Silicon Valley drone industry. *Journal of Unmanned Vehicle Systems* 168(January): 1–8.

Cui, X., Gibbes, C., Southworth, J., and Waylen, P. (2013) Using remote sensing to quantify vegetation change and ecological resilience in a semi-arid system. *Land* 2(2): 108–130.

Cundill, S. L., der van Werff, H. M. A., and der van Meijde, M. (2015) Adjusting spectral indices for spectral response function differences of very high spatial resolution sensors simulated from field spectra. *Sensors (Switzerland)* 15(3): 6221–6240.

Cunliffe, A. M., Anderson, K., DeBell, L., and Duffy, J. (2017) A UK Civil Aviation Authority (CAA)-approved operations manual for safe deployment of lightweight drones in research. *International Journal of Remote Sensing* 00(00): 1–8.

Curran, P. (1980) Multispectral remote sensing of vegetation amount. *Progress in Physical Geography: Earth and Environment* 4(3): 315–341.

Dalponte, M., Bruzzone, L., and Gianelle, D. (2012) Tree species classification in the Southern Alps based on the fusion of very high geometrical resolution

multispectral/hyperspectral images and LiDAR data. *Remote Sensing of Environment* 123: 258–270.

Dalponte, M., Ørka, H. O., Ene, L. T., Gobakken, T., and Næsset, E. (2014) Tree crown delineation and tree species classification in boreal forests using hyperspectral and ALS data. *Remote Sensing of Environment* 140: 306–317.

Dandois, J. P., and Ellis, E. C. (2013) High spatial resolution three-dimensional mapping of vegetation spectral dynamics using computer vision. *Remote Sensing of Environment* 136: 259–276.

Das, B., Sahoo, R. N., Pargal, S., Krishna, G., Verma, R., Viswanathan, C., Sehgal, V. K., and Gupta, V. K. (2021) Evaluation of different water absorption bands, indices and multivariate models for water-deficit stress monitoring in rice using visible-near infrared spectroscopy. *Spectrochimica Acta Part A: Molecular and Biomolecular Spectroscopy* 247: 119104.

Dash, J. P., Pearse, G. D., and Watt, M. S. (2018) UAV multispectral imagery can complement satellite data for monitoring forest health. *Remote Sensing* 10(8): 1–22.

Dash, J. P., Watt, M. S., Pearse, G. D., Heaphy, M., and Dungey, H. S. (2017) Assessing very high resolution UAV imagery for monitoring forest health during a simulated disease outbreak. *ISPRS Journal of Photogrammetry and Remote Sensing* 131: 1–14.

Day, W. R. (1927) THE OAK MILDEW MICROSPHAERA QUERCINA (SCHW.) BURRILL AND ARMILLARIA MELLEA (VAHL) QUEL. IN RELATION TO THE DYING BACK OF OAK. *Forestry: An International Journal of Forest Research* 1(1): 108–112.

Delacre, M., Lakens, D., and Leys, C. (n.d.) Why Psychologists Should by Default Use Welch's t-test Instead of Student's t-test (in press for the International Review of Social Psychology). doi:10.31219/OSF.IO/SBP6K.

Denman, S, Kirk, S., and Webber, J. (2010) Managing acute oak decline. *Practice Note-Forestry Commission* (15).

Denman, S., and Webber, J. (2009) Oak declines: new definitions and new episodes in Britain. *Quarterly Journal of Forestry* 103(4): 285–290.

Denman, Sandra (2019) *Acute Oak Decline (AOD) Newsletter*.

Denman, Sandra, Brown, N., Kirk, S., Jeger, M., and Webber, J. (2014) A description of the symptoms of Acute Oak Decline in Britain and a comparative review on causes of similar disorders on oak in Europe. *Forestry* 87(4): 535–551.

Denman, Sandra, Plummer, S., Kirk, S., Peace, A., and McDonald, J. E. (2016) Isolation studies reveal a shift in the cultivable microbiome of oak affected with Acute Oak Decline. *Systematic and Applied Microbiology* 39(7): 484–490.

Dorigo, W., Richter, R., Baret, F., Bamler, R., and Wagner, W. (2009) Enhanced automated canopy characterization from hyperspectral data by a novel two step radiative transfer model inversion approach. *Remote Sensing* 1(4): 1139–1170.

Dormann, C. F., Elith, J., Bacher, S., Buchmann, C., Carl, G., Carré, G., Marquéz, J. R. G., Gruber, B., Lafourcade, B., Leitão, P. J., Münkemüller, T., McClean, C., Osborne, P. E., Reineking, B., Schröder, B., Skidmore, A. K., Zurell, D., and Lautenbach, S. (2013) Collinearity: a review of methods to deal with it and a simulation study evaluating their performance. *Ecography* 36(1): 27–46.

Duffy, J. P., Cunliffe, A. M., DeBell, L., Sandbrook, C., Wich, S. A., Shutler, Jamie. D., Myers-Smith, I. H., Varela, M. R., and Anderson, K. (2017) Location, location, location: Considerations when using lightweight drones in challenging environments. *Remote Sensing in Ecology and Conservation* : 1–13. doi:10.1002/rse2.58.

Easterday, K., Kislik, C., Dawson, T. E., Hogan, S., and Kelly, M. (2019) Remotely sensed water limitation in vegetation: Insights from an experiment with unmanned aerial vehicles (UAVs). *Remote Sensing* 11(16): 1–18.

Ecke, S., Dempewolf, J., Frey, J., Schwaller, A., Endres, E., Klemmt, H. J., Tiede, D., and Seifert, T. (2022/1/July) UAV-Based Forest Health Monitoring: A Systematic Review. *Remote Sensing*. MDPI.

Edmondson, P. (2015) *Shakespeare: Ideas in Profile*.

Escadafal, R., Belghith, A., and Ben-Moussa, H. (1994) Indices spectraux pour la dégradation des milieux naturels en Tunisie aride. In *6e Symp. Int. Sur Les Mesures Physiques et Signatures En Teledetection*.

Fassnacht, F. E., Latifi, H., Stereńczak, K., Modzelewska, A., Lefsky, M., Waser, L. T., Straub, C., and Ghosh, A. (2016) Review of studies on tree species classification from remotely sensed data. *Remote Sensing of Environment* 186: 64–87.

Felbermeier, B., Hahn, A., and Schneider, T. (2010) Study on user requirements for remote sensing applications in forestry.

Fernandez-Carrillo, A., Patočka, Z., Dobrovolný, L., Franco-Nieto, A., and Revilla-Romero, B. (2020) Monitoring bark beetle forest damage in central europe. A remote sensing approach validated with field data. *Remote Sensing* 12(21): 1–19.

Finch, J., Beckman, M., and Draper, J. (2019) *New generation research towards developing predictive tools for monitoring Oak health*.

Finch, J. P., Brown, N., Beckmann, M., Denman, S., and Draper, J. (2021) Index measures for oak decline severity using phenotypic descriptors. *Forest Ecology and Management* 485: 118948.

Fischler, M. a, and Bolles, R. C. (1981) Random Sample Consensus: A Paradigm for Model Fitting with Applicatlons to Image Analysis and Automated Cartography. *Communications of the ACM* 24(6): 381–395.

Fonstad, M. A., Dietrich, J. T., Courville, B. C., Jensen, J. L., and Carbonneau, P. E. (2013) Topographic structure from motion: a new development in photogrammetric measurement. *Earth Surface Processes and Landforms* 38(4): 421–430.

Forest Research (2020) Forestry Statistics 2020. (September).

Forest Research (n.d.) Pests and diseases. Accessed: 21st December 2020 <https://www.forestresearch.gov.uk/tools-and-resources/pest-and-disease-resources/.>.

Forestry Commission (2018) *Preliminary findings of the extent, composition, health and nature of woodland oak in Britain*.

Franklin, S. E., Wulder, M. A., Skakun, R. S., and Carroll, A. L. (2003) Mountain pine beetle red-attack forest damage classification using stratified Landsat TM data in British Columbia, Canada. *Photogrammetric Engineering and Remote Sensing* 69(3): 283–288.

Fraser, R H, and Latifovic, R. (2005) Mapping insect-induced tree defoliation and mortality using coarse spatial resolution satellite imagery. *International Journal of Remote Sensing* 26(1): 193–200.

Fraser, Robert H, Olthof, I., Lantz, T. C., and Schmitt, C. (2016) UAV Photogrammetry for Mapping Vegetation in the Low-Arctic. *Arctic Science* 102(June): 1–51.

Gagen, M., Matthews, N., Denman, S., Bridge, M., Peace, A., Pike, R., and Young, G. (2019) The tree ring growth histories of UK native oaks as a tool for investigating Chronic Oak Decline: An example from the Forest of Dean. *Dendrochronologia* 55(July): 50–59.

Galore, P. (n.d.) Most common names of open pubs. Accessed: 16th December 2020 <https://www.pubsgalore.co.uk/stats/pubs/pub-names/#Most. >.

Gamon, J. A., and Surfus, J. S. (1999) Assessing leaf pigment content and activity with a reflectometer. *New Phytologist* 143(1): 105–117.

Gao, B. C., and Goetzt, A. F. H. (1995) Retrieval of equivalent water thickness and information related to biochemical components of vegetation canopies from AVIRIS data. *Remote Sensing of Environment* 52(3): 155–162.

Gathercole, L. A. P., Nocchi, G., Brown, N., Coker, T. L. R., Plumb, W. J., Stocks, J. J., Nichols, R. A., Denman, S., and Buggs, R. J. A. (2021) Evidence for the widespread occurrence of bacteria implicated in acute oak decline from incidental genetic sampling. *Forests* 12(12).

Gauthier, S., Bernier, P., Kuuluvainen, T., Shvidenko, A. Z., and Schepaschenko, D. G. (2015) Forest health and global change. *Science* 349(6250): 819–822.

Gini, R., Passoni, D., Pinto, L., and Sona, G. (2014) Use of unmanned aerial systems for multispectral survey and tree classification: A test in a park area of northern Italy. *European Journal of Remote Sensing* 47(1): 251–269.

Gini, R., Sona, G., Ronchetti, G., Passoni, D., and Pinto, L. (2018) Improving Tree Species Classification Using UAS Multispectral Images and Texture Measures. *ISPRS International Journal of Geo-Information* 7(8): 315.

Gitelson, A. A., Chivkunova, O. B., and Merzlyak, M. N. (2009) Nondestructive estimation of anthocyanins and chlorophylls in anthocyanic leaves. *American Journal of Botany* 96(10): 1861–1868.

Gitelson, A. A., Kaufman, Y. J., Stark, R., and Rundquist, D. (2002) Novel algorithms for remote estimation of vegetation fraction. *Remote Sensing of Environment* 80(1): 76–87.

Gitelson, A. A., Merzlyak, M. N., Zur, Y., Stark, R. H., and Gritz, U. (2001) Non-destructive and Remote Sensing Techniques for Estimation of Vegetation Status.

Gitelson, A. A., Viña, A., Ciganda, V., Rundquist, D. C., and Arkebauer, T. J. (2005) Remote estimation of canopy chlorophyll content in crops. *Geophysical Research Letters* 32(8): 1–4.

Gitelson, A., and Merzlyak, M. N. (1994) Spectral Reflectance Changes Associated with Autumn Senescence of Aesculus hippocastanum L. and Acer platanoides L. Leaves. Spectral Features and Relation to Chlorophyll Estimation. *Journal of Plant Physiology* 143(3): 286–292.

Gobron, N., Pinty, B., Verstraete, M. M., and Widlowski, J. L. (2000) Advanced vegetation indices optimized for up-coming sensors: design, performance, and applications. *IEEE Transactions on Geoscience and Remote Sensing* 38(6): 2489–2505.

Goodbody, T. R. H., Coops, N. C., and White, J. C. (2019) Digital Aerial Photogrammetry for Updating Area-Based Forest Inventories: A Review of Opportunities, Challenges, and Future Directions. *Current Forestry Reports* (March). doi:10.1007/s40725-019-00087-2.

Gottschalk, K. W., and Wargo, P. M. (1996) Oak decline around the world. *USDA Interagency Gypsy Moth Research Forum* : 3–13.

Grabska, E., Hostert, P., Pflugmacher, D., and Ostapowicz, K. (2019) Forest stand species mapping using the sentinel-2 time series. *Remote Sensing* 11(10).

Hakala, T., Markelin, L., Honkavaara, E., Scott, B., Theocharous, T., Nevalainen, O., Näsi, R., Suomalainen, J., Viljanen, N., Greenwell, C., and Fox, N. (2018) Direct

reflectance measurements from drones: Sensor absolute radiometric calibration and system tests for forest reflectance characterization. *Sensors (Switzerland)* 18(5).

Hallik, L., Kuusk, A., Lang, M., and Kuusk, J. (2019) Reflectance properties of hemiboreal mixed forest canopies with focus on red edge and near infrared spectral regions. *Remote Sensing* 11(14).

Haralick, R. M., Dinstein, I., and Shanmugam, K. (1973) Textural Features for Image Classification. *IEEE Transactions on Systems, Man and Cybernetics* SMC-3(6): 610–621.

Hart, C. E. (1966) *Royal Forest: A History of Dean's Woods as Producers of Timber*. Clarendon.

Hay, G. J., Niemann, K. O., and McLean, G. F. (1996) An object-specific image-texture analysis of H-resolution forest imagery. *Remote Sensing of Environment* 55(2): 108–122.

Henrich, V., Götze, C., Jung, A., Sandow, C., Thürkow, D., and Cornelia, G. (2009) Development of an online indices database: Motivation, concept and implementation.

Hernández-Clemente, R., Hornero, A., Mottus, M., Penuelas, J., González-Dugo, V., Jiménez, J. C., Suárez, L., Alonso, L., and Zarco-Tejada, P. J. (2019/15/September) Early Diagnosis of Vegetation Health From High-Resolution Hyperspectral and Thermal Imagery: Lessons Learned From Empirical Relationships and Radiative Transfer Modelling. *Current Forestry Reports*. Springer International Publishing.

Hicke, J. A., and Logan, J. (2009) Mapping whitebark pine mortality caused by a mountain pine beetle outbreak with high spatial resolution satellite imagery. *International Journal of Remote Sensing* 30(17): 4427–4441.

Hight, C. J., Farjon, A., Mitchell, R., Quine, C., Elliot, M., and Hemery, G. (2019) Iconic Oak. *Wood Wise*.

Hill, R. A., Wilson, A. K., George, M., and Hinsley, S. A. (2010) Mapping tree species in temperate deciduous woodland using time-series multi-spectral data. *Applied Vegetation Science* 13(1): 86–99.

Hobbs, R. J. (1990) Remote Sensing of Spatial and Temporal Dynamics of Vegetation. Springer, New York, NY doi:10.1007/978-1-4612-3302-2_10.

Hologa, R., Scheffczyk, K., Dreiser, C., and Gärtner, S. (2021) Tree species classification in a temperate mixed mountain forest landscape using random forest and multiple datasets. *Remote Sensing* 13(22).

Hornero, A., Zarco-Tejada, P. J., Quero, J. L., North, P. R. J., Ruiz-Gómez, F. J., Sánchez-Cuesta, R., and Hernandez-Clemente, R. (2021) Modelling hyperspectral- and thermal-based plant traits for the early detection of Phytophthora-induced symptoms in oak decline. *Remote Sensing of Environment* 263.

Hughes, G. F. (1968) On the mean accuracy of statistical pattern recognizers. *IEEE Trans. Inf. Theory* 14(1): 55–63.

Hunt, E. R., and Daughtry, C. S. T. (2018) What good are unmanned aircraft systems for agricultural remote sensing and precision agriculture? *International Journal of Remote Sensing* 39(15–16): 5345–5376.

Hunt, E. R., Daughtry, C. S. T., Eitel, J. U. H., and Long, D. S. (2011) Remote sensing leaf chlorophyll content using a visible band index. *Agronomy Journal* 103(4): 1090–1099.

Hunt, E. R., Doraiswamy, P. C., McMurtrey, J. E., Daughtry, C. S. T., Perry, E. M., and Akhmedov, B. (2012) A visible band index for remote sensing leaf chlorophyll content at the Canopy scale. *International Journal of Applied Earth Observation and Geoinformation* 21(1): 103–112.

Hunt, E. R., and Rock, B. N. (1989) Detection of changes in leaf water content using Near- and Middle-Infrared reflectances. *Remote Sensing of Environment* 30(1): 43–54.

Identifying Crop Variability with Drones | by DroneDeploy | DroneDeploy's Blog | Medium (n.d.). Accessed: 17th November 2020 <https://medium.com/aerial-acuity/identifying-crop-variability-whats-the-difference-between-ndvi-false-ndvi-and-vari-plant-health-98c380381a33. >.

Iglhaut, J., Cabo, C., Puliti, S., Piermattei, L., O'Connor, J., and Rosette, J. (2019/15/September) Structure from Motion Photogrammetry in Forestry: a Review. *Current Forestry Reports*. Springer International Publishing.

Immitzer, M., Atzberger, C., and Koukal, T. (2012) Tree species classification with Random forest using very high spatial resolution 8-band worldView-2 satellite data. *Remote Sensing* 4(9): 2661–2693.

Jackson, R. D., and Huete, A. R. (1991) Interpreting vegetation indices. *Preventive Veterinary Medicine* 11(3–4): 185–200.

Jepsen, J. U., Hagen, S. B., Høgda, K. A., Ims, R. A., Karlsen, S. R., Tømmervik, H., and Yoccoz, N. G. (2009) Monitoring the spatio-temporal dynamics of geometrid moth outbreaks in birch forest using MODIS-NDVI data. doi:10.1016/j.rse.2009.05.006.

Karydas, C., Gewehr, S., Iatrou, M., Iatrou, G., and Mourelatos, S. (2017) Olive Plantation Mapping on a Sub-Tree Scale with Object-Based Image Analysis of Multispectral UAV Data; Operational Potential in Tree Stress Monitoring. *Journal of Imaging* 3(4): 57.

Kattenborn, T., Eichel, J., and Fassnacht, F. E. (2019) Convolutional Neural Networks enable efficient, accurate and fine-grained segmentation of plant species and communities from high-resolution UAV imagery. *Scientific Reports* 9(1): 17656.

Kendon, M., McCarthy, M., Jevrejeva, S., Matthews, A., and Legg, T. (2019) State of the UK climate 2018. *International Journal of Climatology* 39(S1): 1–55.

Khosravipour, A., Skidmore, A. K., and Isenburg, M. (2016) Generating spike-free digital surface models using LiDAR raw point clouds: A new approach for forestry applications. *International Journal of Applied Earth Observation and Geoinformation* 52(June): 104–114.

Klápště, P., Fogl, M., Barták, V., Gdulová, K., Urban, R., and Moudrý, V. (2020) Sensitivity analysis of parameters and contrasting performance of ground filtering algorithms with UAV photogrammetry-based and LiDAR point clouds. *International Journal of Digital Earth* 13(12): 1672–1694.

Knipling, E. B. (1970) Physical and physiological basis for the reflectance of visible and near-infrared radiation from vegetation. *Remote Sensing of Environment* 1(3): 155–159.

Koenderink, J. J., and van Doorn, A. J. (1991) Affine structure from motion. *Journal of the Optical Society of America. A, Optics and image science* 8(2): 377–85.

Kuster, T. M., Dobbertin, M., Günthardt-Goerg, M. S., Schaub, M., and Arend, M. (2014) A phenological timetable of oak growth under experimental drought and air warming. *PLoS ONE* 9(2).

Laar, A. van, and Akça, A. (2007) Remote Sensing In Forest Mensuration. In *Forest Mensuration*. Dordrecht: Springer Netherlands doi:10.1007/978-1-4020-5991-9_11.

Lausch, A., Erasmi, S., King, D. J., Magdon, P., and Heurich, M. (2016) Understanding forest health with remote sensing-Part I-A review of spectral traits, processes and remote-sensing characteristics. *Remote Sensing* 8(12): 1–44.

Leckie, D. G., Jay, C., Gougeon, F. A., Sturrock, R. N., and Paradine, D. (2004) Detection and assessment of trees with Phellinus weirii (laminated root rot) using high resolution multi-spectral imagery. *International Journal of Remote Sensing* 25(4): 793–818.

Lee, J., Cai, X., Lellmann, J., Dalponte, M., Malhi, Y., Butt, N., Morecroft, M., Schonlieb, C. B., and Coomes, D. A. (2016) Individual Tree Species Classification from Airborne Multisensor Imagery Using Robust PCA. *IEEE Journal of Selected Topics in Applied Earth Observations and Remote Sensing* 9(6): 2554–2567.

Lehmann, J. R. K., Nieberding, F., Prinz, T., and Knoth, C. (2015) Analysis of unmanned aerial system-based CIR images in forestry-a new perspective to monitor pest infestation levels. *Forests*. doi:10.3390/f6030594.

Lindberg, E., and Holmgren, J. (2017) Individual Tree Crown Methods for 3D Data from Remote Sensing. *Current Forestry Reports* : 19–31. doi:10.1007/s40725-017-0051-6.

Lisein, J., Michez, A., Claessens, H., and Lejeune, P. (2015) Discrimination of deciduous tree species from time series of unmanned aerial system imagery. *PLoS ONE* 10(11): 1–20.

Longuet-Higgins, H. C. (1987) Readings in Computer Vision: Issues, Problems, Principles, and Paradigms. In Fischler, M. A. and Firschein, O. (Eds.), . San Francisco, CA, USA: Morgan Kaufmann Publishers Inc.

Louhaichi, M., Borman, M. M., and Johnson, D. E. (2001) Spatially located platform and aerial photography for documentation of grazing impacts on wheat. *Geocarto International* 16(1): 65–70.

Lowe, D. G. (2004) Distinctive Image Features from Scale-Invariant Keypoints. *International Journal of Computer Vision* 60(2): 91–110.

Manfreda, S., McCabe, M. F., Miller, P. E., Lucas, R., Pajuelo Madrigal, V., Mallinis, G., et al. (2018) On the Use of Unmanned Aerial Systems for Environmental Monitoring. *Remote Sensing* 10(4).

Massey, M. E., and Welch, R. C. (1993) Monks Wood - The Experience of 40 Years 1953-93.

Mcgaughey, R. J. (2018) *FUSION/LDV: Software for LIDAR Data Analysis and Visualization*.

Meigs, G. W., Kennedy, R. E., and Cohen, W. B. (2011) A Landsat time series approach to characterize bark beetle and defoliator impacts on tree mortality and surface fuels in conifer forests. *Remote Sensing of Environment* 115(12): 3707–3718.

Melby, P. (2008) Insatiable Shipyards: The Impact of the Royal Navy on the World's Forests, 1200-1850. *Journal of Chemical Information and Modeling* 53(9): 287.

Meng, J., Li, S., Wang, W., Liu, Q., Xie, S., and Ma, W. (2016) Mapping forest health using spectral and textural information extracted from SPOT-5 satellite images. *Remote Sensing* 8(9).

Metz, C. E. (1978) Basic principles of ROC analysis. *Seminars in Nuclear Medicine* 8(4): 283–298.

Micheletti, N., Chandler, J. H., and Lane, S. N. (2015) Structure from Motion (SfM) Photogrammetry. *British Society for Geomorphology Geomorphological Techniques* 2(2).

Michez, A., Piégay, H., Lisein, J., Claessens, H., and Lejeune, P. (2016) Classification of riparian forest species and health condition using multi-temporal and hyperspatial imagery from unmanned aerial system. *Environmental monitoring and assessment* 188(3): 146.

Mijnsbrugge, K. Vander, Turcsán, A., Maes, J., Duchêne, N., Meeus, S., Steppe, K., and Steenackers, M. (2016) Repeated summer drought and re-watering during the first growing year of oak (quercus petraea) delay autumn senescence and bud burst in the following spring. *Frontiers in Plant Science* 7(MAR2016).

Minařík, R., and Langhammer, J. (2016) Use of a Multispectral Uav Photogrammetry for Detection and Tracking of Forest Disturbance Dynamics. *ISPRS - International Archives of the Photogrammetry, Remote Sensing and Spatial Information Sciences* XLI-B8(June): 711–718.

Mitchell, R. J., Bellamy, P. E., Ellis, C. J., Hewison, R. L., Hodgetts, N. G., Iason, G. R., Littlewood, N. A., Newey, S., Stockan, J. A., and Taylor, A. F. S. (2019) OakEcol: A database of Oak-associated biodiversity within the UK. *Data in Brief* 25: 104120.

Mitchell, R. J., Broome, A., Hewison, R. L., and Stokes, V. (2019) Protecting Oak Ecosystems: Managing oak woodlands to maximize support for oak associated biodiversity. Case study: Monkswood. (February): 1–7.

Mokros, M., and Surovy, P. (2019) UAV RTK / PPK Method - An Optimal Solution for Mapping Inaccessible UAV RTK / PPK Method — An Optimal Solution for Mapping Inaccessible Forested Areas ? (March). doi:10.3390/rs11060721.

Moura, M. M., de Oliveira, L. E. S., Sanquetta, C. R., Bastos, A., Mohan, M., and Corte, A. P. D. (2021) Towards amazon forest restoration: Automatic detection of species from uav imagery. *Remote Sensing* 13(13).

Murakami, P. F., Schaberg, P. G., and Shane, J. B. (2008) Stem girdling manipulates leaf sugar concentrations and anthocyanin expression in sugar maple trees during autumn. *Tree Physiology* 28(10): 1467–1473.

Myneni, R. B., Hall, F. G., Sellers, P. J., and Marshak, A. L. (1995) The interpretation of spectral vegetation indexes. *IEEE Transactions on Geoscience and Remote Sensing* 33(2): 481–486.

Näsi, R., Honkavaara, E., Blomqvist, M., Lyytikäinen-Saarenmaa, P., Hakala, T., Viljanen, N., Kantola, T., and Holopainen, M. (2018) Remote sensing of bark beetle damage in urban forests at individual tree level using a novel hyperspectral camera from UAV and aircraft. *Urban Forestry and Urban Greening* 30(December 2016): 72–83.

Näsi, R., Honkavaara, E., Lyytikäinen-Saarenmaa, P., Blomqvist, M., Litkey, P., Hakala, T., Viljanen, N., Kantola, T., Tanhuanpää, T., and Holopainen, M. (2015) Using UAV-based photogrammetry and hyperspectral imaging for mapping bark beetle damage at tree-level. *Remote Sensing* 7(11): 15467–15493.

Nuijten, R., Coops, N., Goodbody, T., and Pelletier, G. (2019) Examining the Multi-Seasonal Consistency of Individual Tree Segmentation on Deciduous Stands Using Digital Aerial Photogrammetry (DAP) and Unmanned Aerial Systems (UAS). *Remote Sensing* 11(7): 739.

O'Connor, J., Smith, M. J., and James, M. R. (2017) Cameras and settings for aerial surveys in the geosciences: Optimising image data. *Progress in Physical Geography* 41(3): 325–344.

Omari, K., White, H. P., Staenz, K., and King, D. J. (2013) Retrieval of forest canopy parameters by inversion of the proflair leaf-canopy reflectance model using the LUT approach. *IEEE Journal of Selected Topics in Applied Earth Observations and Remote Sensing* 6(2): 715–723.

Ortiz, S. M., Breidenbach, J., and Kändler, G. (2013) Early detection of bark beetle green attack using terraSAR-X and rapideye data. *Remote Sensing* 5(4): 1912–1931.

Oshiro, T. M., Perez, P. S., and Baranauskas, J. A. (2012) How many trees in a random forest? In *Lecture Notes in Computer Science (Including Subseries Lecture Notes in Artificial Intelligence and Lecture Notes in Bioinformatics)* (Vol. 7376 LNAI).

Pal, M. (2005) Random forest classifier for remote sensing classification. *International Journal of Remote Sensing* 26(1): 217–222.

Pauly, K. (2016) Towards Calibrated Vegetation Indices from UAS-derived Orthomosaics. *13th International Conference on Precision Agriculture* (August). doi:10.13140/RG.2.2.21842.35524.

Peñuelas, J., Filella, I., Biel, C., Serrano, L., and Save, R. (1993) The reflectance at the 950-970 nm region as an indicator of plant water status. *International Journal of Remote Sensing* 14(10): 1887–1905.

Peñuelas, Josep, and Filella, L. (1998) Visible and near-infrared reflectance techniques for diagnosing plant physiological status. *Trends in Plant Science* 3(4): 151–156.

Peppa, M. V., Hall, J., Goodyear, J., and Mills, J. P. (2019) Photogrammetric assessment and comparison of dji phantom 4 pro and phantom 4 rtk small unmanned aircraft systems. *International Archives of the Photogrammetry, Remote Sensing and Spatial Information Sciences - ISPRS Archives* 42(2/W13): 503–509.

Peterson, D. L., Aber, J. D., Matson, P. A., Card, D. H., Swanberg, N., Wessman, C., and Spanner, M. (1988) Remote sensing of forest canopy and leaf biochemical contents. *Remote Sensing of Environment* 24(1): 85–108.

Pham, L. T. H., Brabyn, L., and Ashraf, S. (2016) Combining QuickBird, LiDAR, and GIS topography indices to identify a single native tree species in a complex landscape using an object-based classification approach. *International Journal of Applied Earth Observation and Geoinformation* 50: 187–197.

Plesoianu, A., Stupariu, M. S., Sandric, I., and Stupariu, I. (2020) Individual Tree-Crown Detection and Species Classification in Very High-Resolution Remote Sensing Imagery Using a Deep Learning Ensemble Model. (July). doi:10.3390/rs12152426.

Potter, C., Li, S., Huang, S., and Crabtree, R. L. (2012) Analysis of sapling density regeneration in Yellowstone National Park with hyperspectral remote sensing data. *Remote Sensing of Environment* 121: 61–68.

Puliti, S., Gobakken, T., Ørka, H. O., and Næsset, E. (2017) Assessing 3D point clouds from aerial photographs for species-specific forest inventories. *Scandinavian Journal of Forest Research* 32(1): 68–79.

Qin, H., Zhou, W., Yao, Y., and Wang, W. (2022) Individual tree segmentation and tree species classification in subtropical broadleaf forests using UAV-based LiDAR, hyperspectral, and ultrahigh-resolution RGB data. *Remote Sensing of Environment* 280.

Raddi, S., Giannetti, F., Martini, S., Farinella, F., Chirici, G., Tani, A., Maltoni, A., and Mariotti, B. (2022) Monitoring drought response and chlorophyll content in Quercus by consumer-grade, near-infrared (NIR) camera: a comparison with reflectance spectroscopy. *New Forests* 53(2): 241–265.

Raparelli, E., and Bajocco, S. (2019) A bibliometric analysis on the use of unmanned aerial vehicles in agricultural and forestry studies. *International Journal of Remote Sensing* 40(24): 9070–9083.

Reich, P. B., Wright, I. J., Craine, J. M., Oleksyn, J., Westoby, M., and Walters, M. B. (2003) The Evolution of Plant Functional Variation: Traits, Spectra, and Strategies. 164(November 2002).

rgb_indices: RGB indices in uavRst: Unmanned Aerial Vehicle Remote Sensing Tools (n.d.). Accessed: 17th November 2020 <https://rdrr.io/cran/uavRst/man/rgb_indices.html. >.

Riggs, G. A., and Running, S. W. (1991) Detection of canopy water stress in conifers using the Airborne Imaging Spectrometer. *Remote Sensing of Environment* 35(1): 51–68.

Rouse, R. W. H., Haas, J. A. W., and Deering, D. W. (1973) *Monitoring vegetation systems in the Great Plains with ERTS*.

Rullan-Silva, C. D., Olthoff, A. E., Delgado de la Mata, J. A., and Pajares-Alonso, J. A. (2013) Remote monitoring of forest insect defoliation. A review. *Forest Systems* 22(3): 377–391.

Ruxton, G. D. (2006) The unequal variance t-test is an underused alternative to Student's t-test and the Mann-Whitney U test. *Behavioral Ecology* 17(4): 688–690.

Sampson, P. H., Zarco-Tejada, P. J., Mohammed, G. H., Miller, J. R., Noland, T. L., Morrison, I., Cameron, A., Weldon, T., and Fleming, R. (2003) *Hyperspectral Remote Sensing of Forest Condition: Estimating Chlorophyll Content in Tolerant Hardwoods*. *Forest Science* (Vol. 49).

Sandino, J., Pegg, G., Gonzalez, F., and Smith, G. (2018) Aerial mapping of forests affected by pathogens using UAVs, hyperspectral sensors, and artificial intelligence. *Sensors (Switzerland)* 18(4): 1–17.

Șandric, I., Irimia, R., Petropoulos, G. P., Anand, A., Srivastava, P. K., Pleșoianu, A., Faraslis, I., Stateras, D., and Kalivas, D. (2022) Tree's detection & health's assessment from ultra-high resolution UAV imagery and deep learning. *Geocarto International*. doi:10.1080/10106049.2022.2036824.

Sapp, M., Lewis, E., Moss, S., Barrett, B., Kirk, S., Elphinstone, J. G., and Denman, S. (2016) Metabarcoding of bacteria associated with the acute oak decline syndrome in England. *Forests* 7(5).

Sarrazin, M. J. D., van Aardt, J. A. N., Asner, G. P., McGlinchy, J., Messinger, D. W., and Wu, J. (2011) Fusing small-footprint waveform LiDAR and hyperspectral data for canopy-level species classification and herbaceous biomass modeling in savanna ecosystems. *Canadian Journal of Remote Sensing* 37(6): 653–665.

Sayn-Wittgenstein, L. (1978) *Recognition of Tree Species on Aerial Photographs*. Canadian Forestry Service, Department of the Environment.

Schiefer, F., Kattenborn, T., Frick, A., Frey, J., Schall, P., Koch, B., and Schmidtlein, S. (2020) Mapping forest tree species in high resolution UAV-based RGB-imagery by means of convolutional neural networks. *ISPRS Journal of Photogrammetry and Remote Sensing* 170: 205–215.

Seelig, H. D., Hoehn, A., Stodieck, L. S., Klaus, D. M., Adams, W. W., and Emery, W. J. (2008) The assessment of leaf water content using leaf reflectance ratios in the visible, near-, and short-wave-infrared. *International Journal of Remote Sensing* 29(13): 3701–3713.

Sellers, P. J., Berry, J. A., Collatz, G. J., Field, C. B., and Hall, F. G. (1992) Canopy reflectance, photosynthesis, and transpiration. III. A reanalysis using improved leaf

models and a new canopy integration scheme. *Remote Sensing of Environment* 42(3): 187–216.

Serifoglu Yilmaz, C., Yilmaz, V., and Gungor, O. (2018) Investigating the performances of commercial and non-commercial software for ground filtering of UAV-based point clouds. *International Journal of Remote Sensing* 39: 5016–5042.

Shi, Y., Skidmore, A. K., Wang, T., Holzwarth, S., Heiden, U., Pinnel, N., Zhu, X., and Heurich, M. (2018) Tree species classification using plant functional traits from LiDAR and hyperspectral data. *International Journal of Applied Earth Observation and Geoinformation* 73: 207–219.

Shi, Y., Wang, T., Skidmore, A. K., Holzwarth, S., Heiden, U., and Heurich, M. (2021) Mapping individual silver fir trees using hyperspectral and LiDAR data in a Central European mixed forest. *International Journal of Applied Earth Observation and Geoinformation* 98.

Shukla, P. R., Skea, J., Slade, R., Diemen, R. van, Haughey, E., Malley, J., M. Pathak, and Pereira, J. P. (2019) Climate Change and Land: an IPCC special report. *Climate Change and Land: an IPCC special report on climate change, desertification, land degradation, sustainable land management, food security, and greenhouse gas fluxes in terrestrial ecosystems*.

Siebring, J., Valente, J., Franceschini, M. H. D., Kamp, J., and Kooistra, L. (2019) Object-based image analysis applied to low altitude aerial imagery for potato plant trait retrieval and pathogen detection. *Sensors (Switzerland)* 19(24).

Silva, C. A., Crookston, N. L., Hudak, A. T., Vierling, L. A., Klauberg, C., and Maintainer, C. (2017) *Package 'rLiDAR' Type Package Title LiDAR Data Processing and Visualization Version 0.1.1*.

Sinclair, W. A. (1965) Comparisons of Recent Declines of White Ash, Oaks and Sugar Maple in Northeastern Woodlands. *The Cornell Plantations* 20(4): 62–67.

Skarlatos, D., and Kiparissi, S. (2012) Comparison of Laser Scanning, Photogrammetry and Sfm-Mvs Pipeline Applied in Structures and Artificial Surfaces. *ISPRS Annals of Photogrammetry, Remote Sensing and Spatial Information Sciences* I–3: 299–304.

Sketchley, R. (2019) Phytophthora ramorum in Larch UK Situation Report. *Forestry Commision England* (May): 1–7.

Smith, M. W., Carrivick, J. L., and Quincey, D. J. (2015) Structure from motion photogrammetry in physical geography. *Progress in Physical Geography* 40(2): 247–275.

Solberg, S., Næsset, E., Lange, H., and Bollandsås, O. (2012) Remote sensing of forest health.

Spruce, J. P., Sader, S., Ryan, R. E., Smoot, J., Kuper, P., Ross, K., Prados, D., Russell, J., Gasser, G., McKellip, R., and Hargrove, W. (2011) Assessment of MODIS NDVI time series data products for detecting forest defoliation by gypsy moth outbreaks. *Remote Sensing of Environment* 115(2): 427–437.

Spyropoulos, C. G., and Mavrommatis, M. (1978) Effect of Water Stress on Pigment Formation in Quercus Species. *Journal of Experimental Botany*. Oxford University Press.

Steele, R. C., and Welch, R. C. (1974) *Monks Wood. A Nature Reserve Record*. Nature Conservancy.

Stone, C., and Mohammed, C. (2017) Application of Remote Sensing Technologies for Assessing Planted Forests Damaged by Insect Pests and Fungal Pathogens: a Review. *Current Forestry Reports* 3(2): 75–92.

Strobl, C., Boulesteix, A.-L., Kneib, T., Augustin, T., and Zeileis, A. (2008) Conditional Variable Importance for Random Forests. *BMC bioinformatics* 9: 307.

Strobl, C., Boulesteix, A.-L., Zeileis, A., and Hothorn, T. (2007) Bias in random forest variable importance measures: Illustrations, sources and a solution. *BMC Bioinformatics* 8(1): 25.

Tansley, A. G. (1949) *The British Islands and Their Vegetation*. University Press.

Thomas, F. M., Blank, R., and Hartmann, G. (2002) Abiotic and biotic factors and their interactions as causes of oak decline in Central Europe. *Forest Pathology* 32(4–5): 277–307.

Thomas, Frank M. (2008) Recent advances in cause-effect research on oak decline in Europe. *CAB Reviews: Perspectives in Agriculture, Veterinary Science, Nutrition and Natural Resources* 3(July 2008).

Thompson, I., Mackey, B., Mcnulty, S., and Mosseler, A. (2009) *Forest Resilience, Biodiversity, and Climate Change. A Synthesis of the Biodiversity/Resilience/Stability Relationship in Forest Ecosystems. Technical Series*.

Townsend, M. (2013) Oak Processionary Moth in the United Kingdom. *Outlooks on Pest Management* 24(1).

Tu, Y.-H., Phinn, S., Johansen, K., and Robson, A. (2018) Assessing Radiometric Correction Approaches for Multi-Spectral UAS Imagery for Horticultural Applications. *Remote Sensing* 10(11): 1684.

Tucker, C. J. (1979) Red and photographic infrared linear combinations for monitoring vegetation. *Remote Sensing of Environment* 8(2): 127–150.

Tucker, C. J. (1980) Remote sensing of leaf water content in the near infrared. *Remote Sensing of Environment* 10(1): 23–32.

Tuominen, J., Lipping, T., Kuosmanen, V., and Haapane, R. (2009) Remote Sensing of Forest Health. *Geoscience and Remote Sensing* (May 2014). doi:10.5772/8283.

Ullman, S. (1979) The Interpretation of Structure from Motion. *Proceedings of the Royal Society of London. Series B. Biological Sciences* 203(1153): 405 LP – 426.

Verbesselt, J., Robinson, A., Stone, C., and Culvenor, D. (2009) Forecasting tree mortality using change metrics derived from MODIS satellite data. *Forest Ecology and Management* 258(7): 1166–1173.

Verrelst, J., Camps-Valls, G., Muñoz-Marí, J., Rivera, J. P., Veroustraete, F., Clevers, J. G. P. W., and Moreno, J. (2015/1/October) Optical remote sensing and the retrieval of terrestrial vegetation bio-geophysical properties - A review. *ISPRS Journal of Photogrammetry and Remote Sensing*. Elsevier B.V.

Vincini, M., Frazzi, E., and D'Alessio, P. (2008) A broad-band leaf chlorophyll vegetation index at the canopy scale. *Precision Agriculture* 9(5): 303–319.

Vincini, M., Frazzi, E., D'Alessio, P., and Stafford, J. (2007) Comparison of narrow-band and broad-band vegetation indices for canopy chlorophyll density estimation in sugar beet.

Vinod, V., Raj, R., Pingale, R., and Jagarlapudi, A. (2021) Estimating Leaf Water Content using Remotely Sensed Hyperspectral Data.

Wallace, L., Lucieer, A., Malenovskỳ, Z., Turner, D., and Vopěnka, P. (2016) Assessment of forest structure using two UAV techniques: A comparison of airborne laser scanning and structure from motion (SfM) point clouds. *Forests*. doi:10.3390/f7030062.

Walthert, L., Ganthaler, A., Mayr, S., Saurer, M., Waldner, P., Walser, M., Zweifel, R., and von Arx, G. (2021) From the comfort zone to crown dieback: Sequence of physiological stress thresholds in mature European beech trees across progressive drought. *Science of The Total Environment* 753: 141792.

Wan, H., Tang, Y., Jing, L., Li, H., Qiu, F., and Wu, W. (2021) Tree species classification of forest stands using multisource remote sensing data. *Remote Sensing* 13(1): 1–24.

Watts, A. C., Ambrosia, V. G., and Hinkley, E. A. (2012) Unmanned aircraft systems in remote sensing and scientific research: Classification and considerations of use. *Remote Sensing* 4(6): 1671–1692.

Welle, T., Aschenbrenner, L., Kuonath, K., Kirmaier, S., and Franke, J. (2022) Mapping Dominant Tree Species of German Forests. *Remote Sensing* 14(14).

Westoby, M. J., Brasington, J., Glasser, N. F., Hambrey, M. J., and Reynolds, J. M. (2012) 'Structure-from-Motion' photogrammetry: A low-cost, effective tool for geoscience applications. *Geomorphology* 179: 300–314.

White, J. C., Coops, N. C., Wulder, M. A., Vastaranta, M., Hilker, T., and Tompalski, P. (2016) Remote Sensing Technologies for Enhancing Forest Inventories: A Review. *Canadian Journal of Remote Sensing* 42(5): 619–641.

White, J. C., Wulder, M. A., Brooks, D., Reich, R., and Wheate, R. D. (2005) Detection of red attack stage mountain pine beetle infestation with high spatial resolution satellite imagery. *Remote Sensing of Environment* 96(3–4): 340–351.

Wigston, D. L. (1975) The distribution of Quercus robur L., Q. petraea (Matt.) Leibl. and their hybrids in south-western England: 1. The assessment of the taxonomic status of populations from leaf characters. *Watsonia* 10: 345–349.

Woodward, S., and Boa, E. (2013) Ash dieback in the UK: A wake-up call. *Molecular Plant Pathology* 14(9): 856–860.

Wulder, M. A., White, J. C., Coops, N. C., and Butson, C. R. (2008) Multi-temporal analysis of high spatial resolution imagery for disturbance monitoring. *Remote Sensing of Environment* 112(6): 2729–2740.

Xie, Z., Chen, Y., Lu, D., Li, G., and Chen, E. (2019) Classification of land cover, forest, and tree species classes with Ziyuan-3 multispectral and stereo data. *Remote Sensing* 11(2).

Yu, H., Yan, T., Yang, W., and Zheng, H. (2016) An integrative object-based image analysis workflow for uav images. *International Archives of the Photogrammetry, Remote Sensing and Spatial Information Sciences - ISPRS Archives* 2016-Janua(July): 1085–1091.

Yuan, Y., and Hu, X. (2016) Random forest and objected-based classification for forest pest extraction from uav aerial imagery. *International Archives of the Photogrammetry, Remote Sensing and Spatial Information Sciences - ISPRS Archives* 2016-Janua(July): 1093–1098.

Zhang, W., Qi, J., Wan, P., Wang, H., Xie, D., Wang, X., and Yan, G. (2016) An easy-to-use airborne LiDAR data filtering method based on cloth simulation. *Remote Sensing* 8(6).

Zhang, Z. (2016) Object-Based Tree Species Classification in Urban Ecosystems using Lidar and Hyperspectral Data. *Remote Sensing* 7(122): 1–16.

Zhong, H., Lin, W., Liu, H., Ma, N., Liu, K., Cao, R., Wang, T., and Ren, Z. (2022) Identification of tree species based on the fusion of UAV hyperspectral image and LiDAR data in a coniferous and broad-leaved mixed forest in Northeast China. *Frontiers in Plant Science* 13.

Appendix A - Accuracy assessment of photogrammetric surveys

Appendix A describes background investigations at a third study site, which aimed to determine achievable relative and absolute accuracy of photogrammetric surveys undertaken with the UAS (Bormatec Maja), and the optimal flight parameters required to achieve this.

A UAV survey was undertaken at Bradfield Wood, Suffolk, a 80-hectare diverse broadleaf forest. This survey was undertaken primarily in the scope of a separate study investigating ash dieback at the site and was used to provide a testbed to inform UAV specifications for the current study. The Sony a6000 sensor with a 16 mm lens (see Table 2-1) was utilised for this survey to provide high resolution RGB imagery. The assessment focused on testing and evaluating the PPK method for application in scenarios where GCP placement is prevented by dense vegetation. At Bradfield Wood 14 GCPs were placed throughout the site and independently surveyed with a RTK GNSS (Leica GS15), to better than one centimetre accuracy (see Figure A-1). These GCPs were solely used as validation (check points) of the photogrammetric products. The scene was reconstructed with the sensor's PPK location information alone, hence by a direct georeferencing approach.

Figure A-1 GCP survey for photogrammetric survey accuracy testing. Locations were surveyed with a Leica GS15 RTK GNSS to accuracy < 1 cm.

Due to the size of the site, three separate flights with the fixed wing UAV were required to fully cover the area. The unfavourable weather conditions (high wind) necessitated flights to be undertaken on two separate days. These challenging conditions allowed evaluation of the consistency of the achievable accuracy, hence the reliability. The raw GNSS log was post-processed with the RTKlib software using correction data from a CORS located in Newmarket, giving a ~ 30 km baseline. PPK corrected image locations were written to the imagery to utilise in the direct georeferencing approach. Images were photometrically processed in the SfM software Agisoft Metashape. Image locations were imported with the respective easting, northing and altitude accuracy estimation as calculated per image in the PPK process. The vertical datum was converted from Ordnance datum Newlyn to ellipsoidal heights to match the GCP vertical datum. GCPs were manually marked in five images (aiming for a mean pixel error across five images smaller than one pixel) and survey accuracy was set to 0.01 m. All 14 GCP locations were not incorporated as control points in the model generation, but were employed as check points. SfM processing was performed in Agisoft Metashape using a quarter of the original image scale for alignment (medium quality). Results were evaluated in terms of error estimates for 1) sensor locations and 2) GCP locations.

1284 images were taken in total for the survey, a GSD of 2.64 cm was yielded at an average flight height of 121 m AGL. The three separate flights were planned to provide a significant amount of overlap between them. The forested area of the site was covered with every point on the ground visible in more than nine images. All survey parameters are summarised in Table A-1. An illustration of image locations, their footprints and respective overlap is given in Figure A-2.

Table A-1 Survey and photogrammetric processing paramters for flights undertaken at Bradfield Wood with the aim of assessing the location accuracy of produced data.

Number of images:	1,284	Camera stations:	1,284
Flying altitude:	121 m	Tie points:	2,089,201
Ground resolution:	2.64 cm/pix	Projections:	5,485,479
Coverage area:	1.12 km²	Reprojection error:	1.67 pix

> 9
9
8
7
6
5
4
3
2
1

200 m
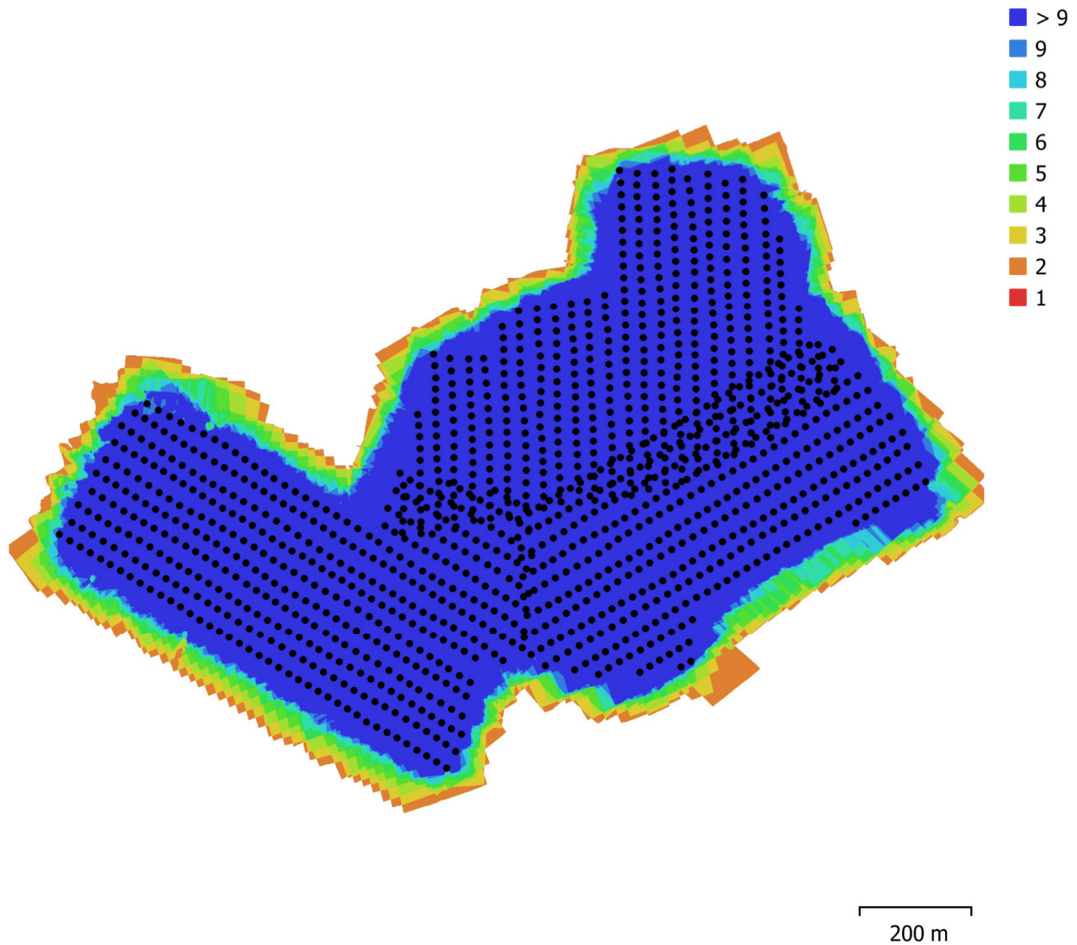
Figure A-2 Accuracy testing: camera locations and image overlap.

A.1 Accuracy testing: sensor error estimates

Across all 1284 images, a total error of 12.4 cm was estimated as the deviation of the calculated sensor location from the actual sensor location. The horizontal root mean square error (RMSE) is 4.3 cm with 11.6 cm vertical error. The error estimates for sensor locations are summarised in Table A-2. Reviewing the sensor locations with their respective error estimates, it becomes clear that higher errors were generated at the beginning of an individual flight, particularly in the first flight line (see Figure A-3). The lower accuracy during this flight phase is likely due to longer initialisation time of L1 GNSS receivers, compared to multi-band receivers.

Table A-2 Accuracy testing: RMSE of sensor location.

X error (cm)	Y error (cm)	Z error (cm)	XY error (cm)	Total error (cm)
3.22176	2.89759	11.6138	4.3331	12.3958
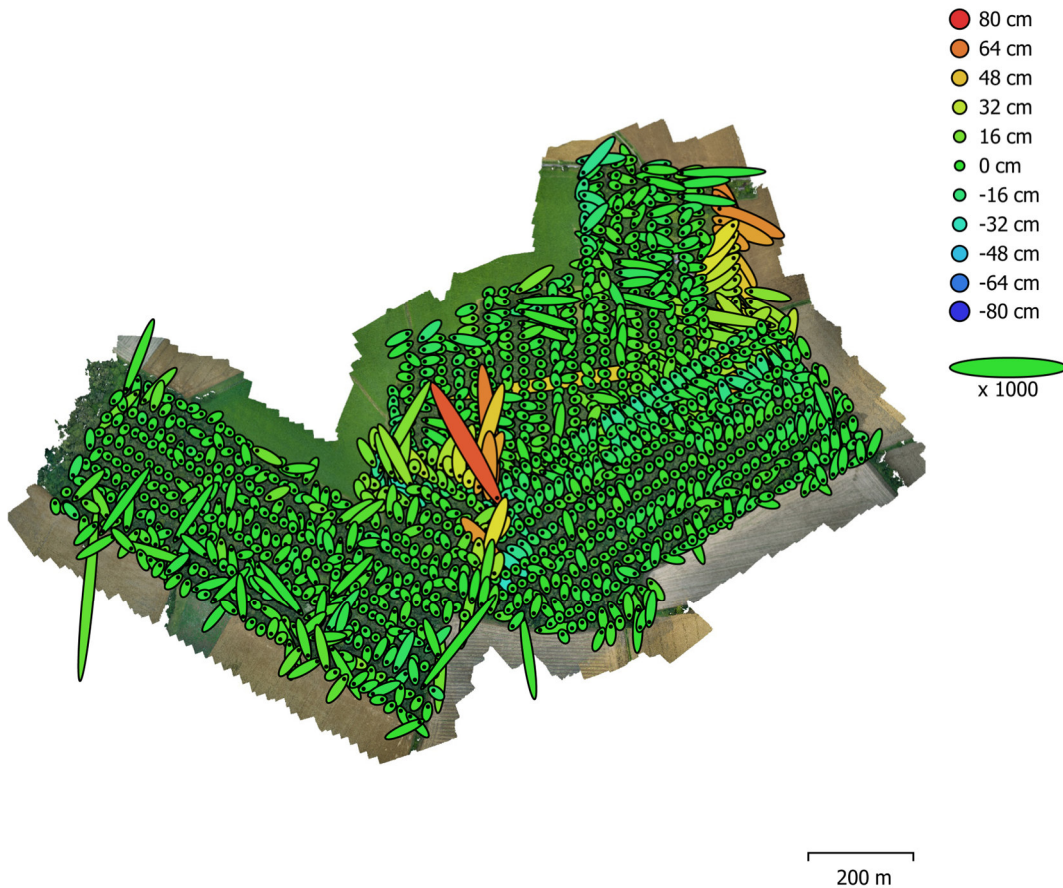
Figure A-3 Accuracy testing: sensor locations and error estimates. Z error is represented by ellipse colour. X,Y errors are represented by ellipse shape. Estimated sensor locations are marked with a black dot.

A.2 Accuracy testing: GCP error estimates

Across the 14 GCP locations, a total error of 91.7 cm was determined compared to the directly georeferenced model. This is calculated as the sum of overall XY horizontal RMSE estimated as 23.2 cm, plus the vertical RMSE of 88.7 cm (see Table A-3 and Table A-4). The maximum observed deviation of a GCP location to the model was -129.9 cm (see GCP 4, Z error), while the horizontal error of individual GCPs was often below one centimetre (see Table A-4). All GCPs show negative vertical error estimates revealing a downward shift of the entire model.

Table A-3 Accuracy testing: RMSE of surveyed GCP locations.

Count	X error (cm)	Y error (cm)	Z error (cm)	XY error (cm)	Total (cm)
14	9.71039	21.0815	88.7452	23.2104	91.7302

The visualisation of GCP errors (Figure A-4) shows that there appears to be an East-West tilt in the model compared to the height of surveyed GCP locations. GCPs in the western part of the site tend to be located further below the reconstructed scene than GCPs in the eastern section. For horizontal errors there is no clear pattern observable.
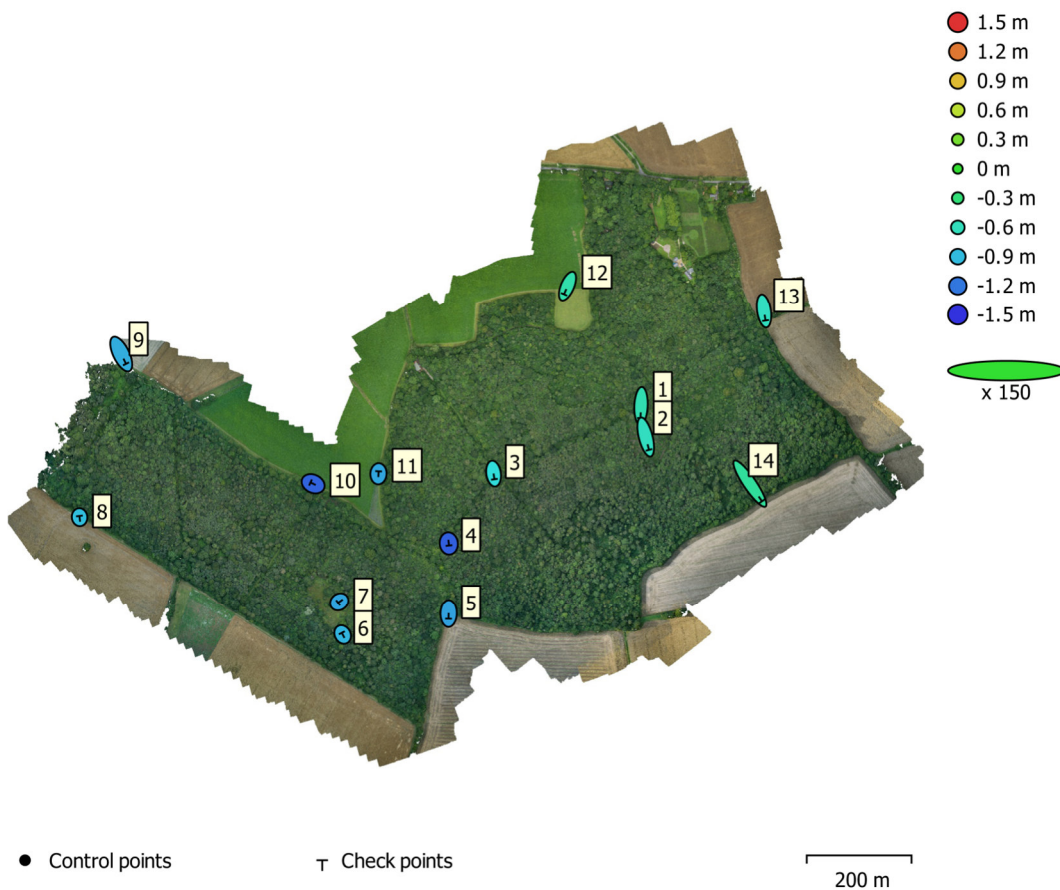
Figure A-4 Accuracy testing: GCP locations and error estimates. Z error is represented by ellipse colour. X,Y errors are represented by ellipse shape. All GCPs were incorporated as check points, thus solely used for validation.

Table A-4 Accuracy testing: Absolute errors of surveyed GCP locations compared to modelled GCP locations. GCPs are marked in five images with better than one pixel accuracy.

Label	X error (cm)	Y error (cm)	Z error (cm)	Total (cm)	Image (pix)
1	-1.35	-31.04	-55.48	63.60	0.48 (5)
2	8.41	-32.58	-61.53	70.13	0.88 (5)
3	2.10	-14.43	-73.67	75.10	0.47 (5)
4	0.55	-5.23	-129.89	130.00	0.79 (5)
5	-0.22	-13.68	-101.48	102.39	0.60 (5)
6	-2.14	4.13	-92.91	93.03	0.98 (5)
7	-2.99	-2.16	-99.86	99.93	0.74 (5)
8	-0.37	3.09	-88.45	88.51	0.33 (5)
9	12.17	-24.93	-96.42	100.33	0.36 (5)
10	-6.75	3.15	-128.38	128.59	0.25 (5)
11	0.33	6.34	-99.50	99.71	0.78 (5)
12	-8.82	-20.67	-52.91	57.49	0.40 (5)
13	3.82	-25.05	-61.58	66.59	0.56 (5)
14	30.70	-44.89	-45.69	71.03	0.57 (5)
Total	**9.71**	**21.08**	**88.74**	**91.7302**	**0.627**

A.3 Accuracy testing: summary

The direct georeferencing approach with the PPK system yielded horizontal errors < 50 cm and vertical errors < 100 cm. These errors are calculated by comparing the location of photogrammetrically derived products to independently surveyed GCPs. Overall, observed errors are acceptable in the context of forestry surveys. More so, considering that the present scenario is particularly challenging: The combination of three separate flights presumably decreased the achievable accuracy. It is expected that the absolute accuracy of a photogrammetric model using the PPK direct georeferencing method will be higher when using imagery from a single flight.

To assess the completeness of the photogrammetric model a dense point cloud was generated in Metashape using the low quality setting (1/8th image scale). No "holes" were observed in the model, thus indicating a complete reconstruction despite the challenging textural conditions. Conversely, re-running the same SfM processing parameters with the default five-metre horizontal, ten-metre vertical sensor location accuracy, produced multiple patches of missing data. This suggests that image matching is being supported by high accuracy sensor locations, which thus improves

photogrammetric performance for demanding UAV forest surveys. Although relative accuracy of the model is not directly measurable in this case, it is probable that the PPK direct georeferencing approach is beneficial here also. An indication of this benefit is given by the rather small deviations (4.3 cm horizontal, 11.6 cm vertical) of the initial image locations compared with image locations post-bundle adjustment (see Table A-2 and Figure A-3).

These results present a valuable source of information to inform the further UAV surveys undertaken in the scope of the research chapters within this thesis. Specifically, these independently validated data help to assess the need for GCPs and required flight characteristics to achieve high absolute and relative accuracies in photogrammetrically derived products.

Appendix B - Individual tree boxplots, Speculation Cannop

Appendix B presents the extracted pixel values for individual sample trees at the Speculation Cannop site as boxplots. Data distributions are shown per band for raw bands of the RGB and multispectral sensor and for derived vegetation indices. RGB data were collected on 05/05/2019 and 22/05/2019 and multispectral data were acquired on 05/07/2019 and 09/07/2019.
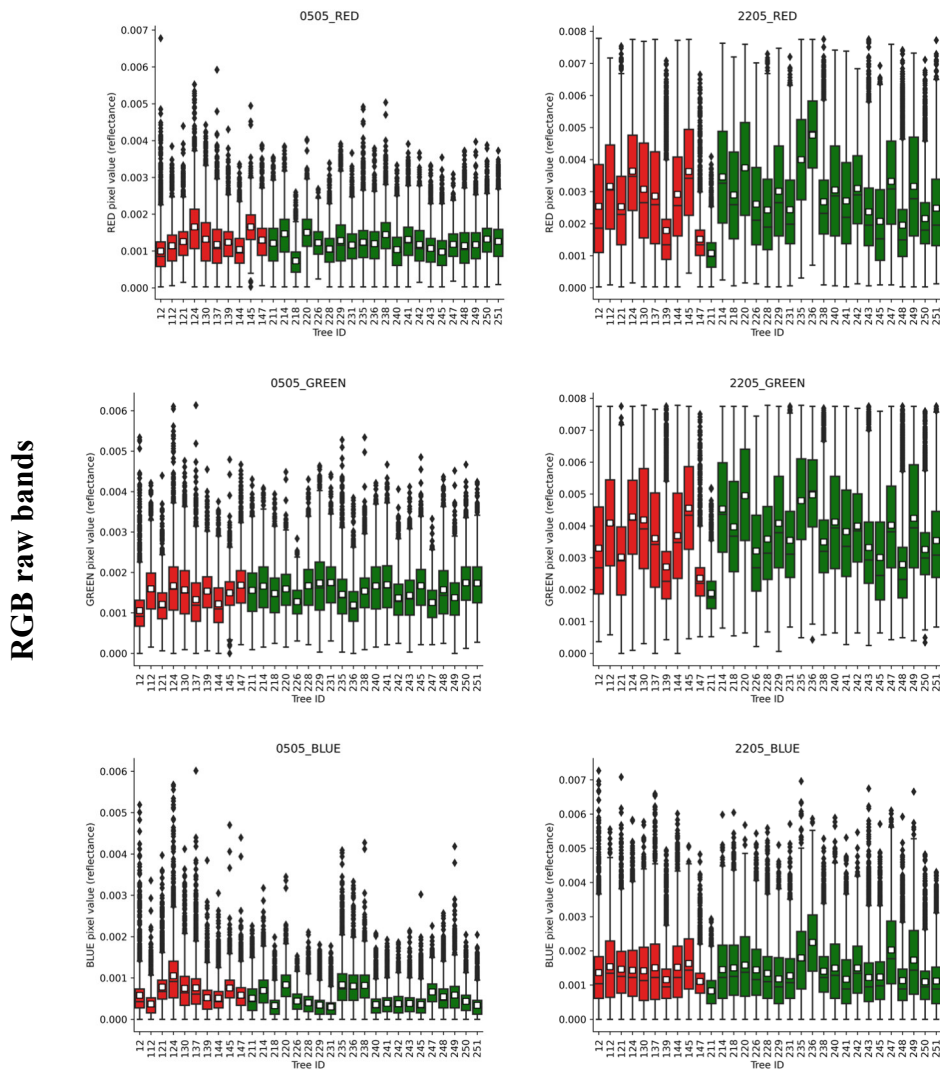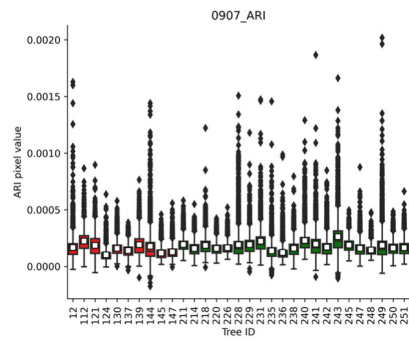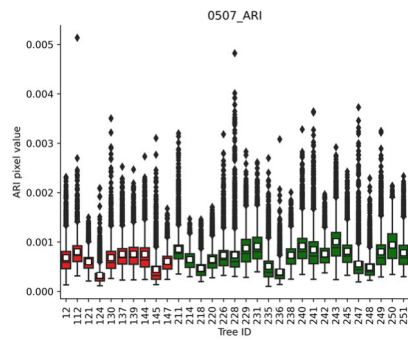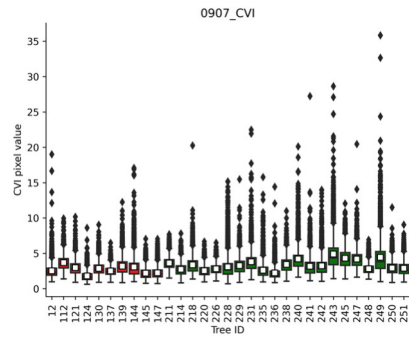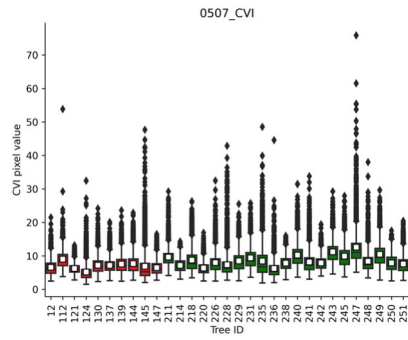
RGB vegetation indices
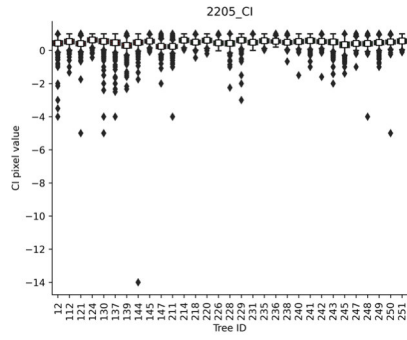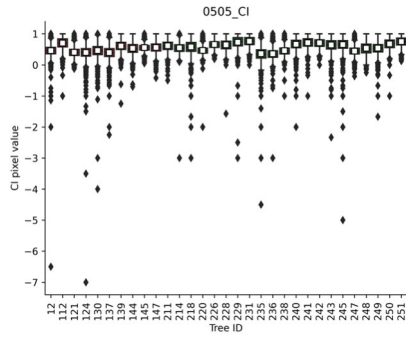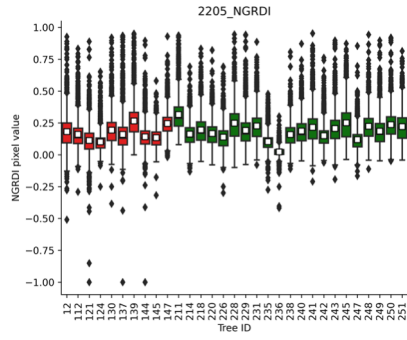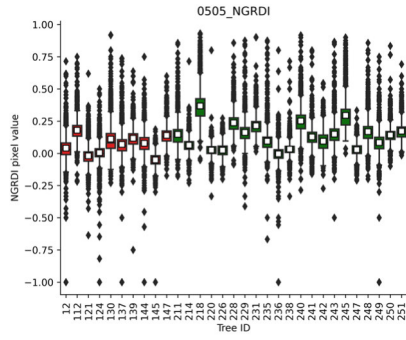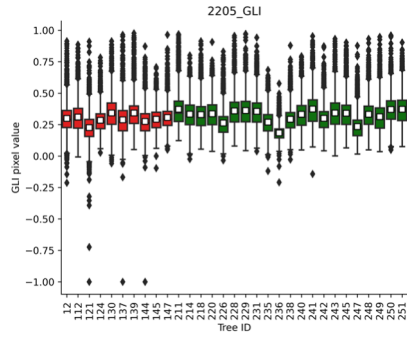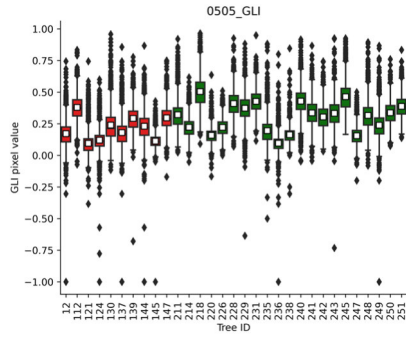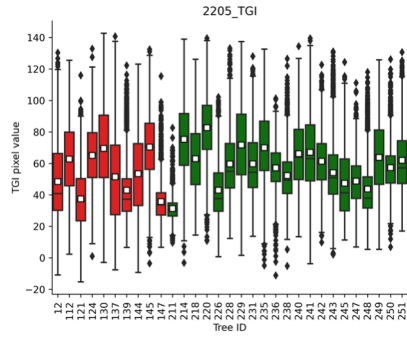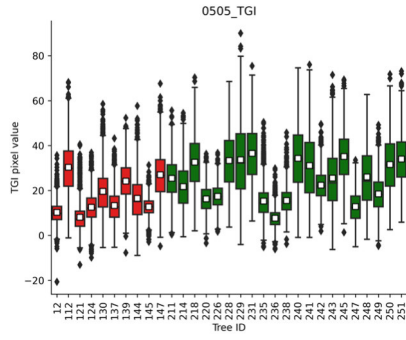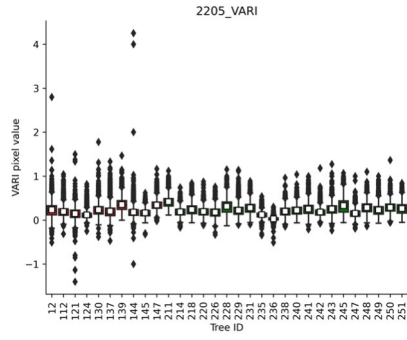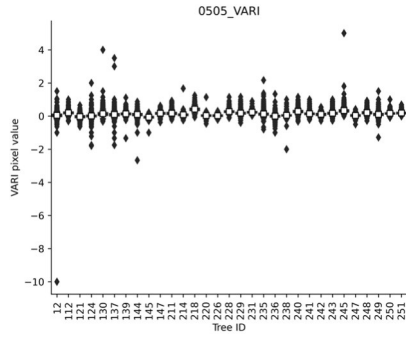
Multispectral raw bands
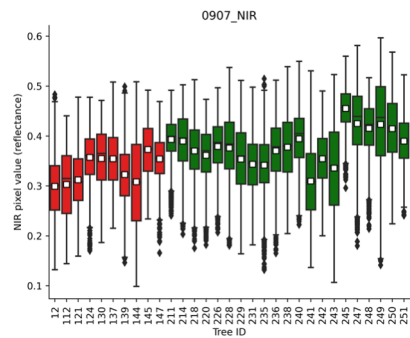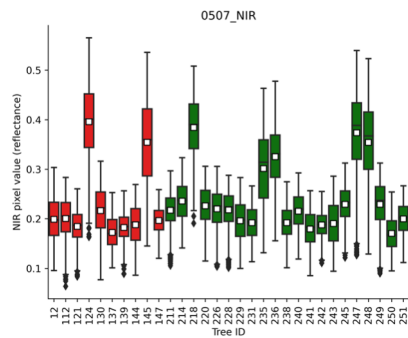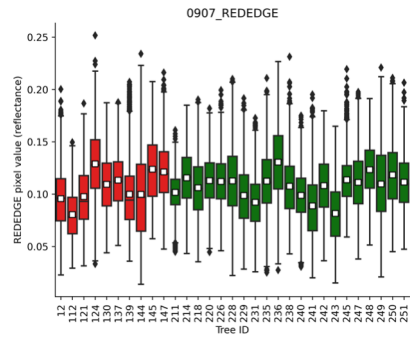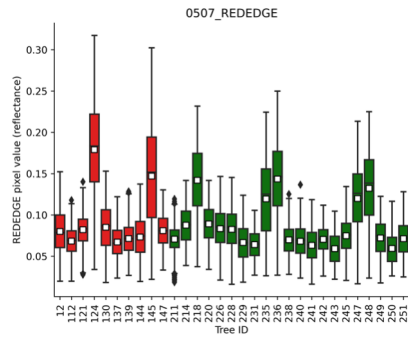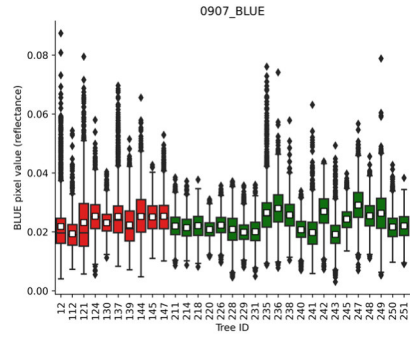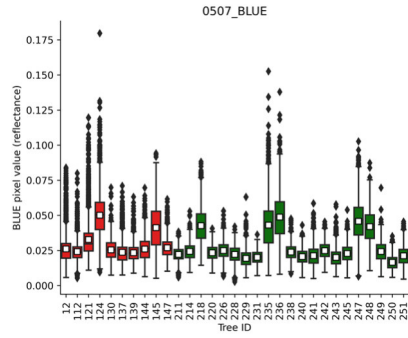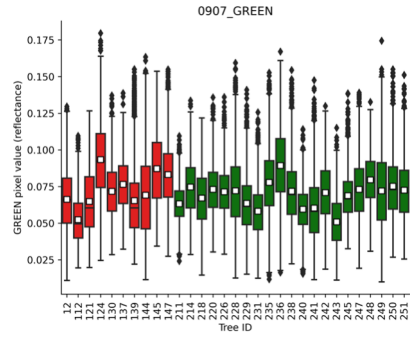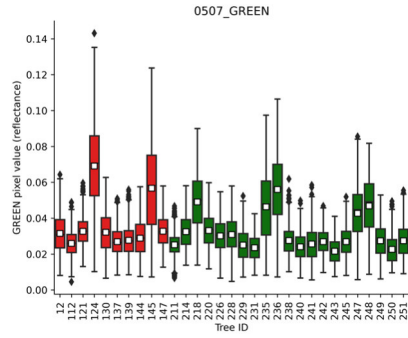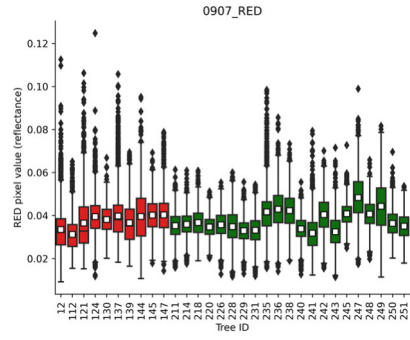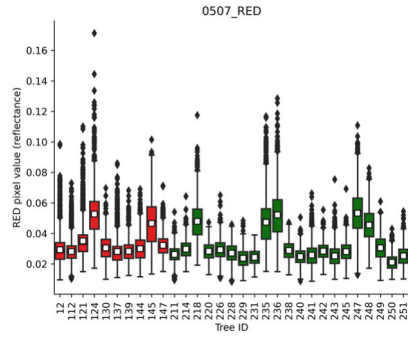
Multispectral vegetation indices
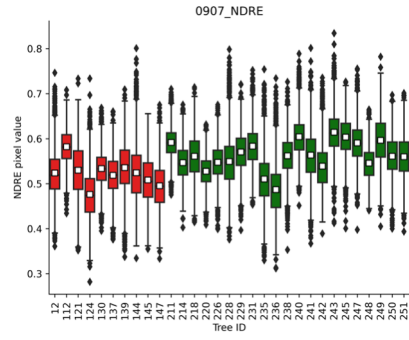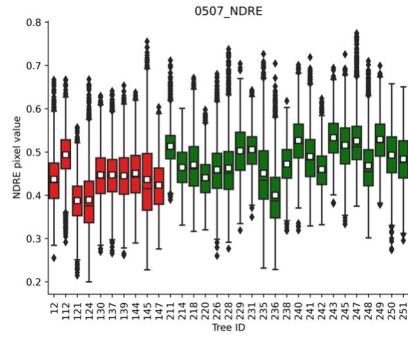
Appendix C illustrates the manually mapped individual tree crowns of sample trees at Speculation Cannop and their three-metre radius plots from which pixel values are extracted. Crown shapes and circular plots are overlaid on RGB, NDVI and NDRE background layers of the two multispectral flights undertaken at the Speculation Cannop site.
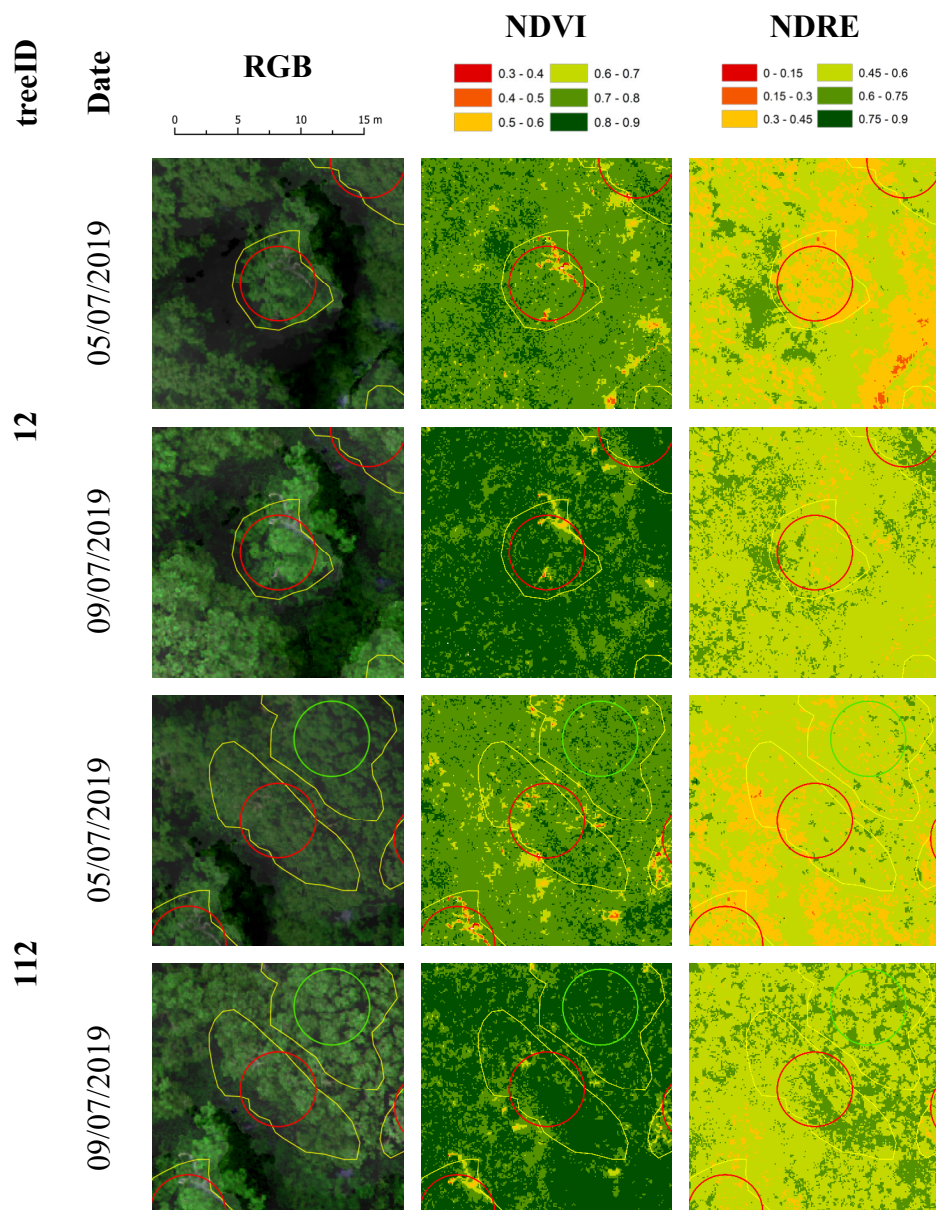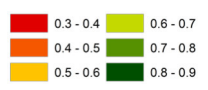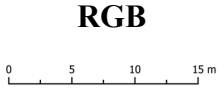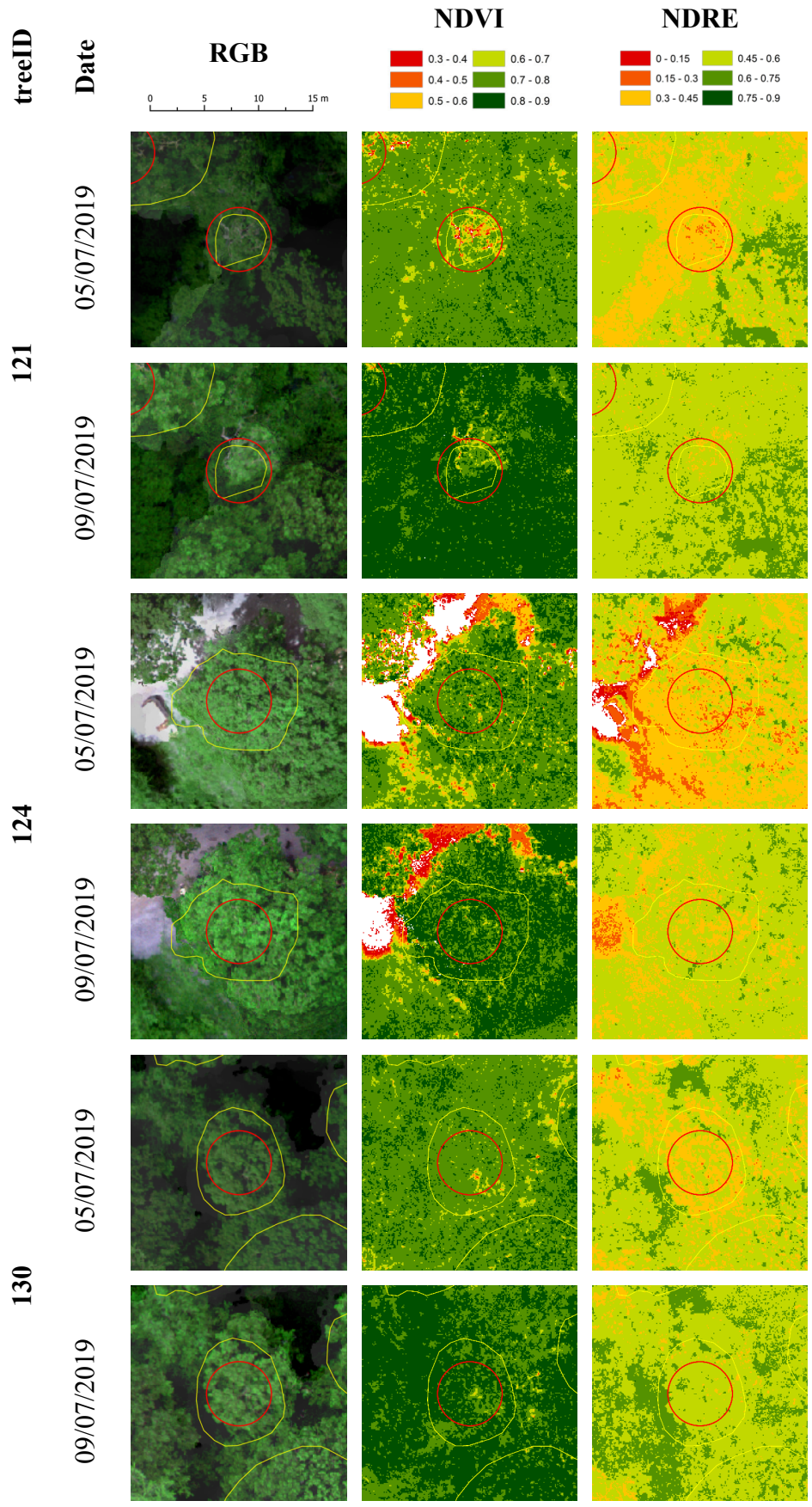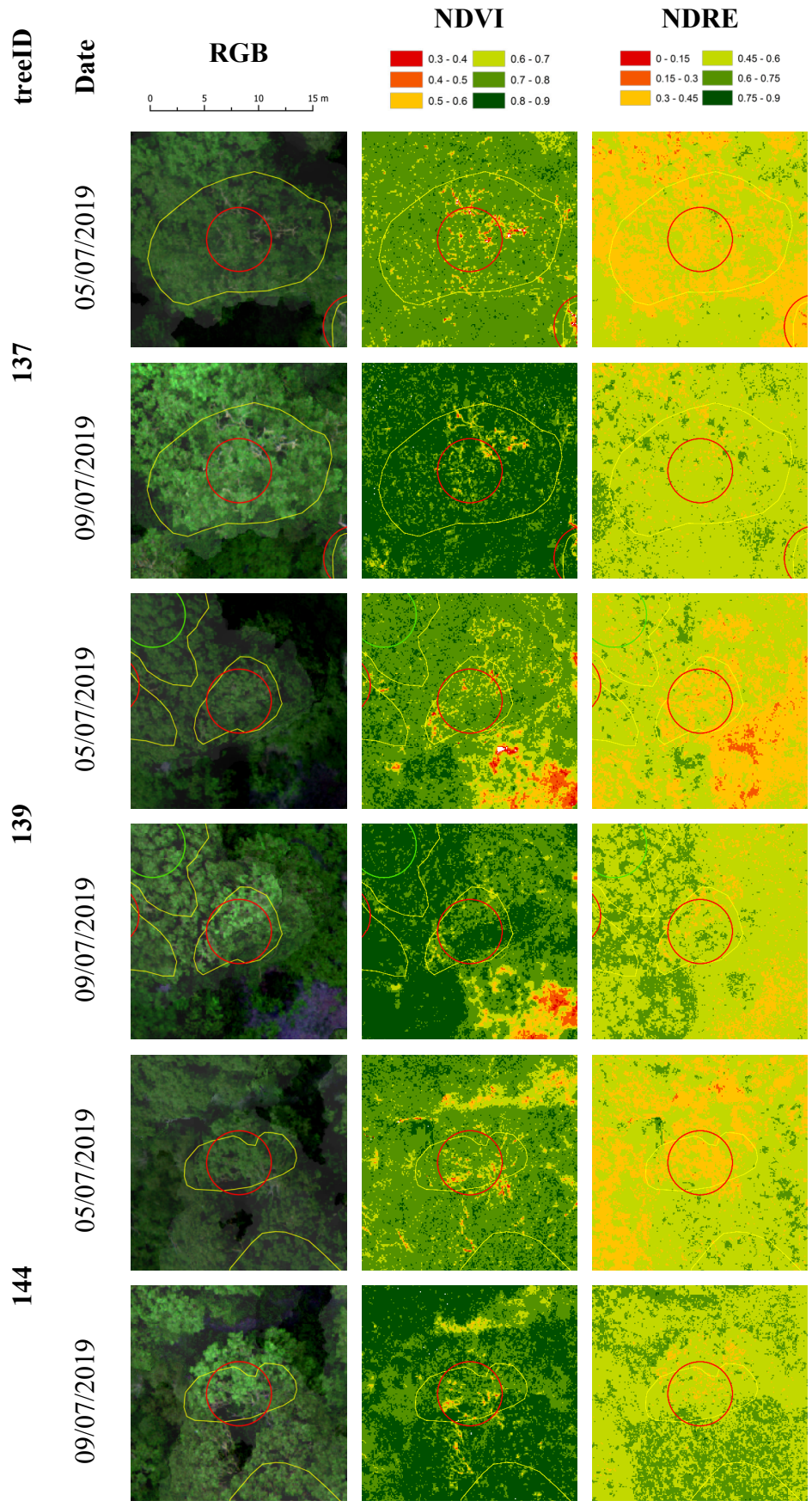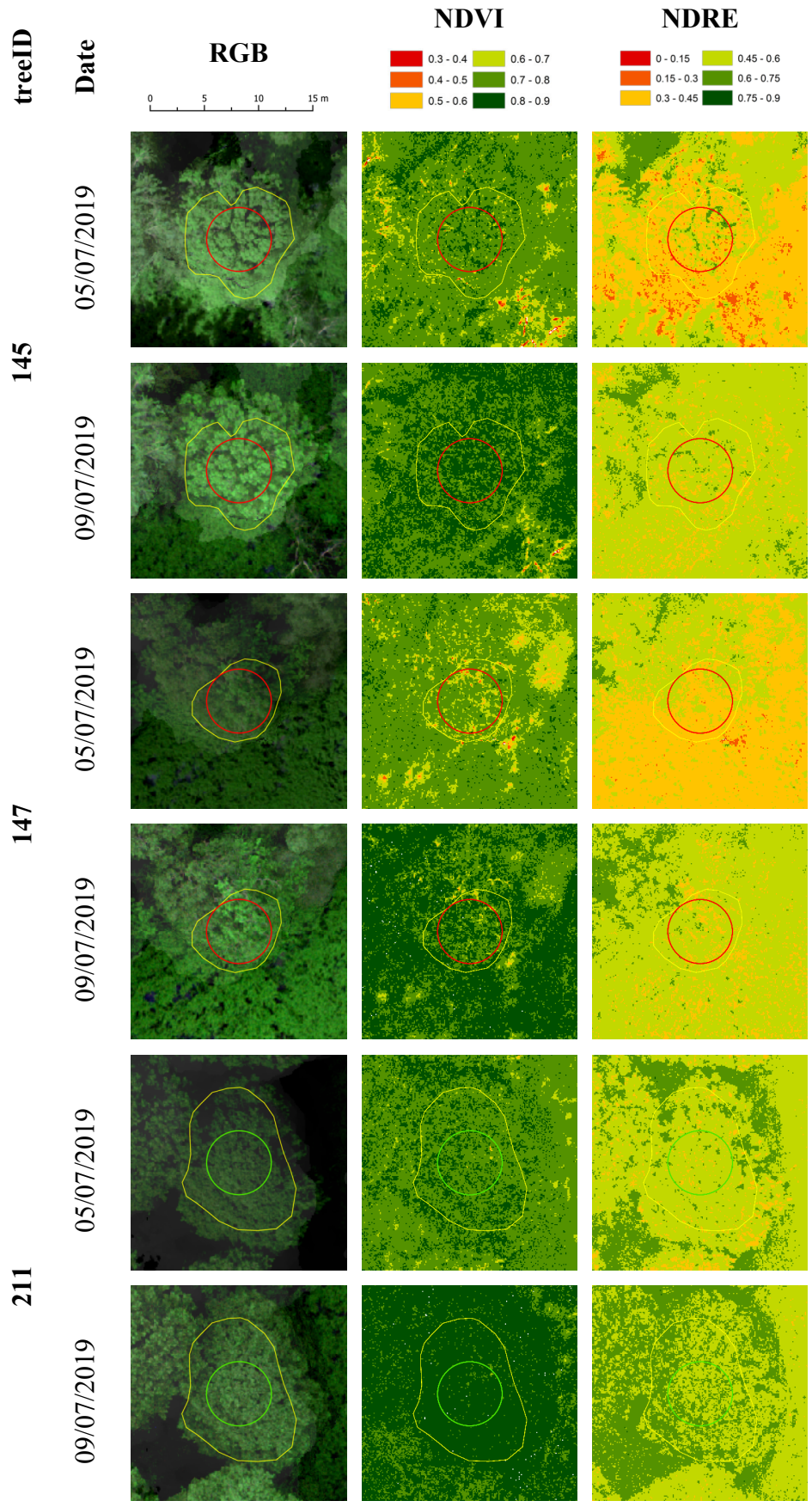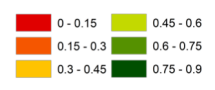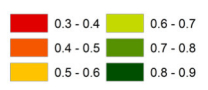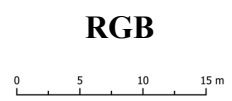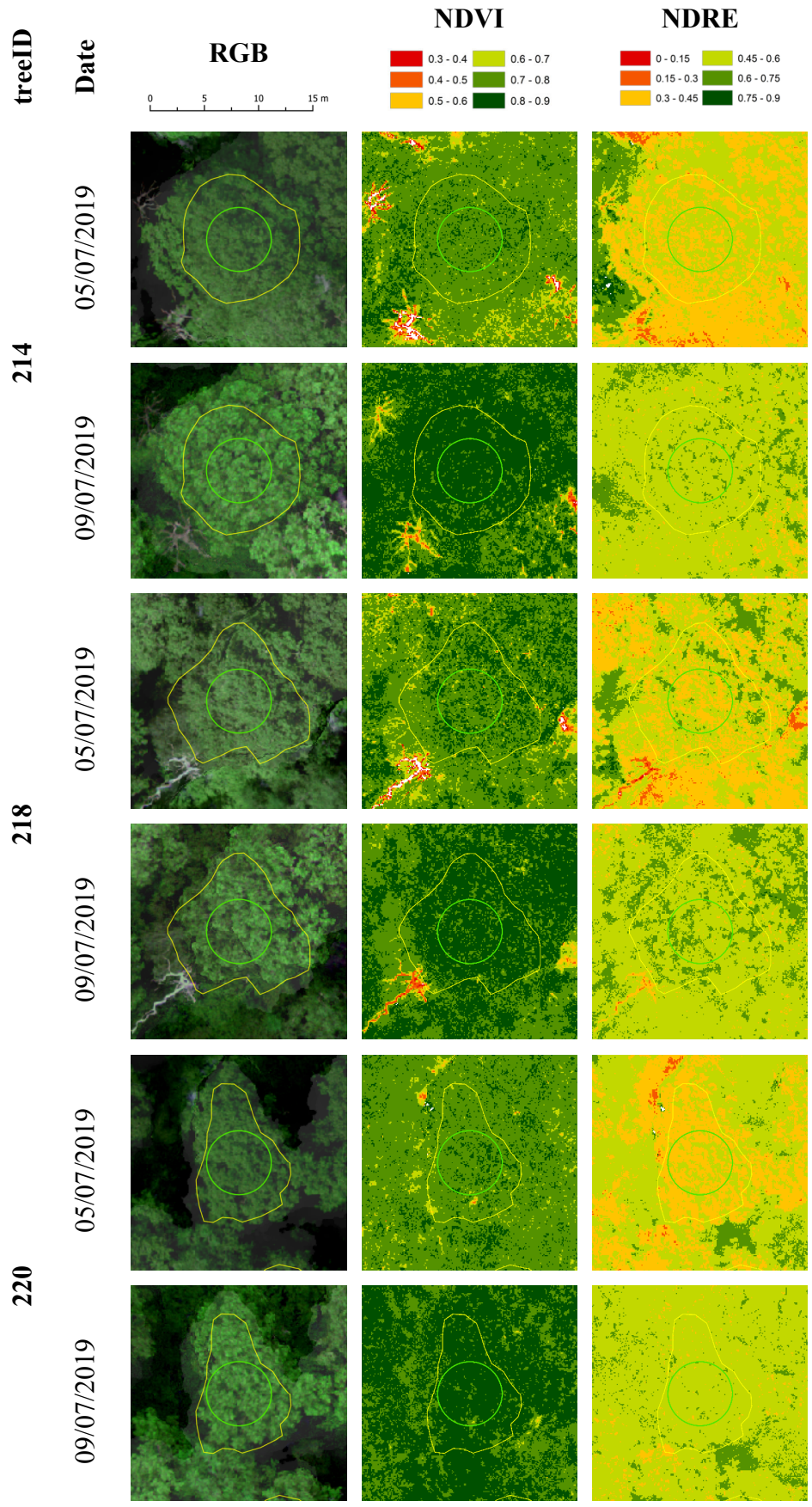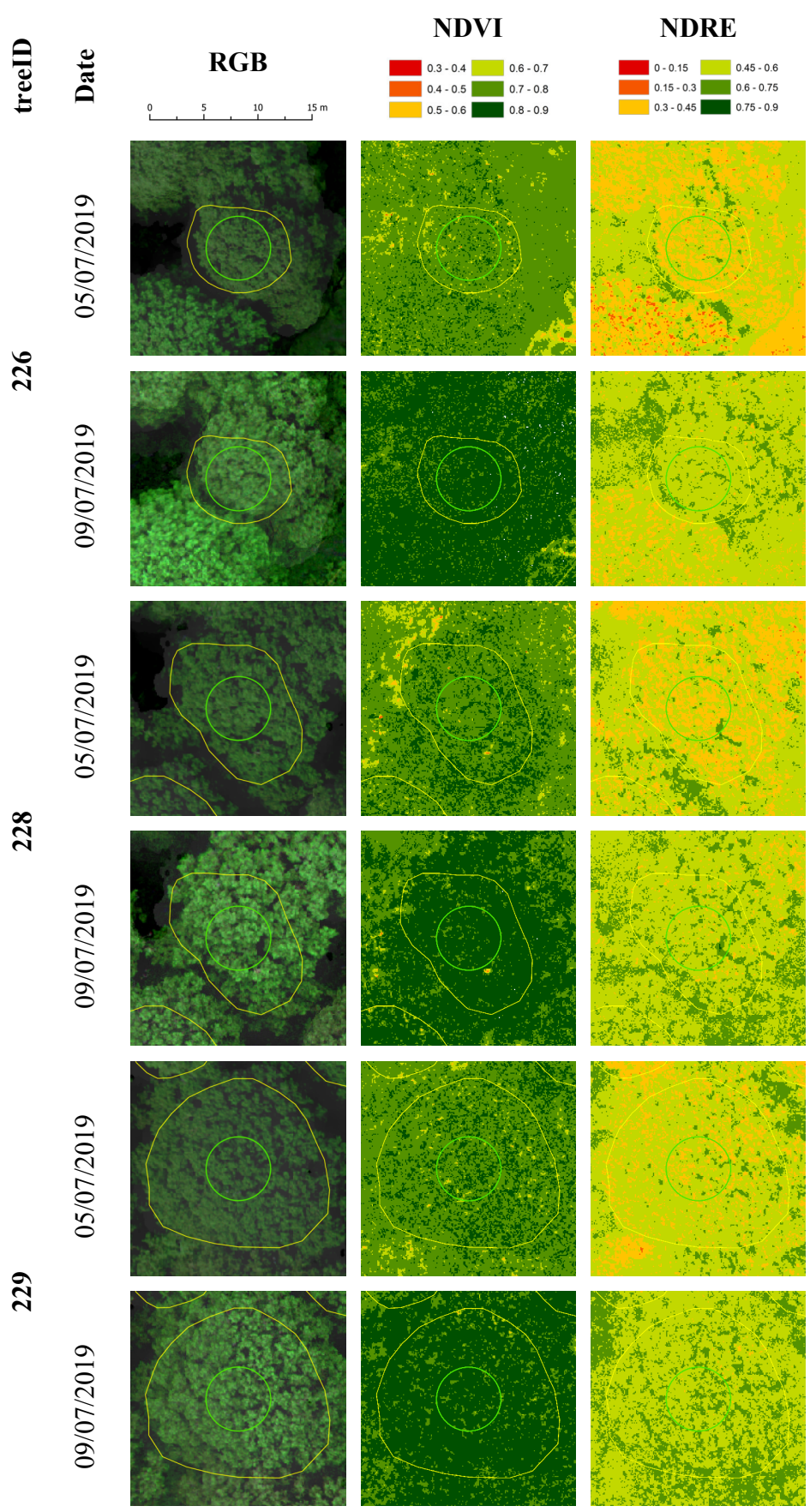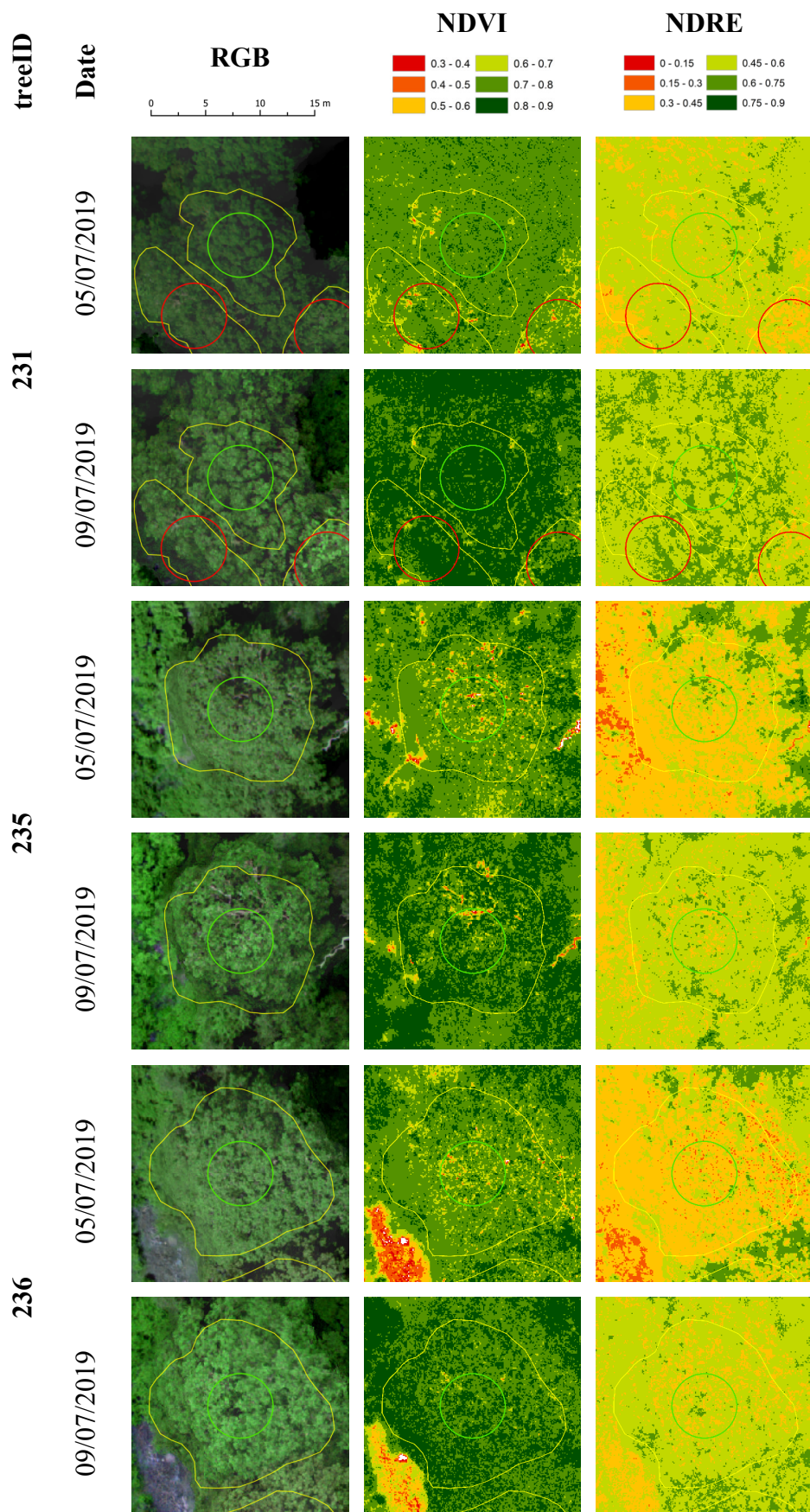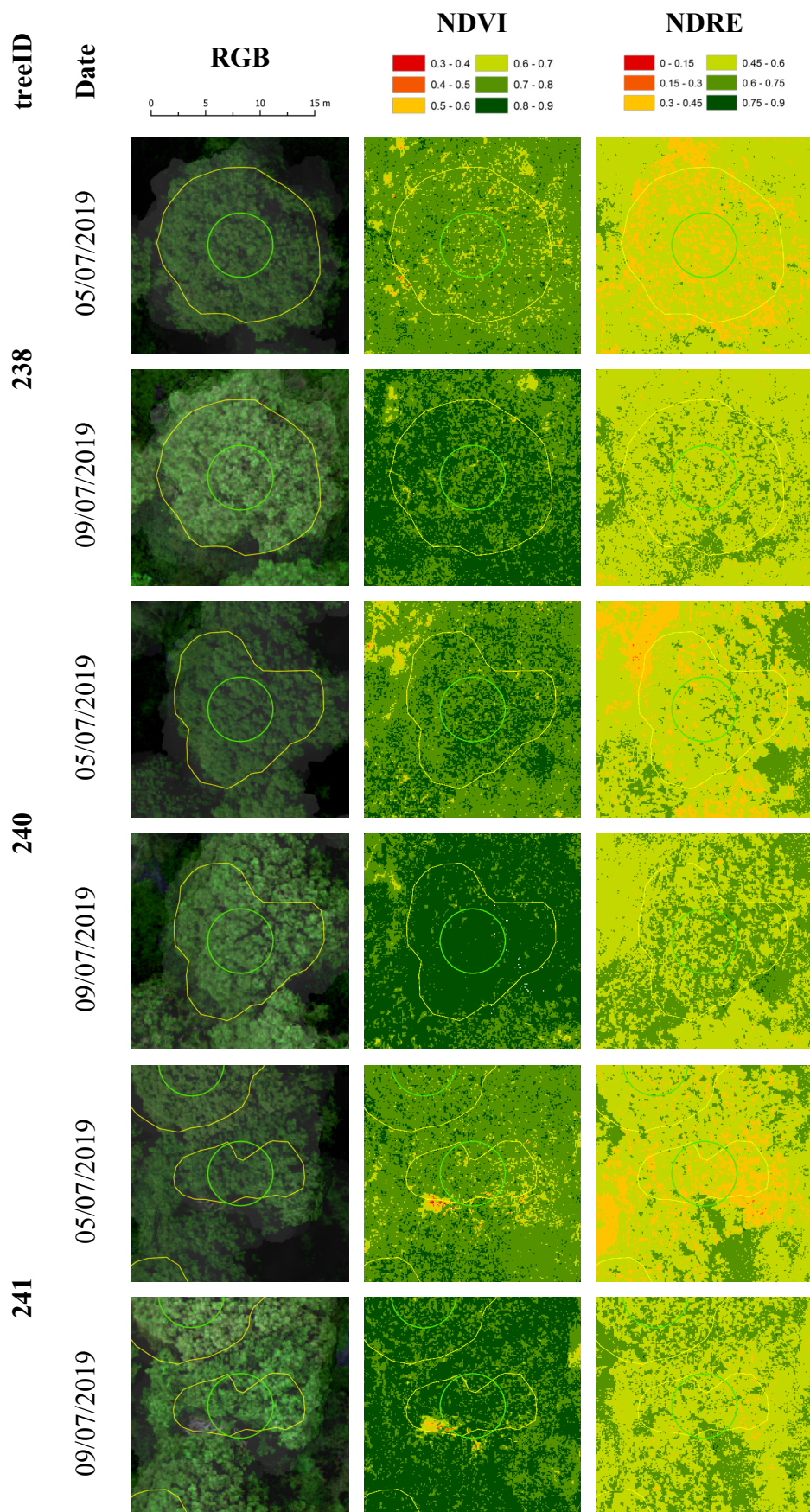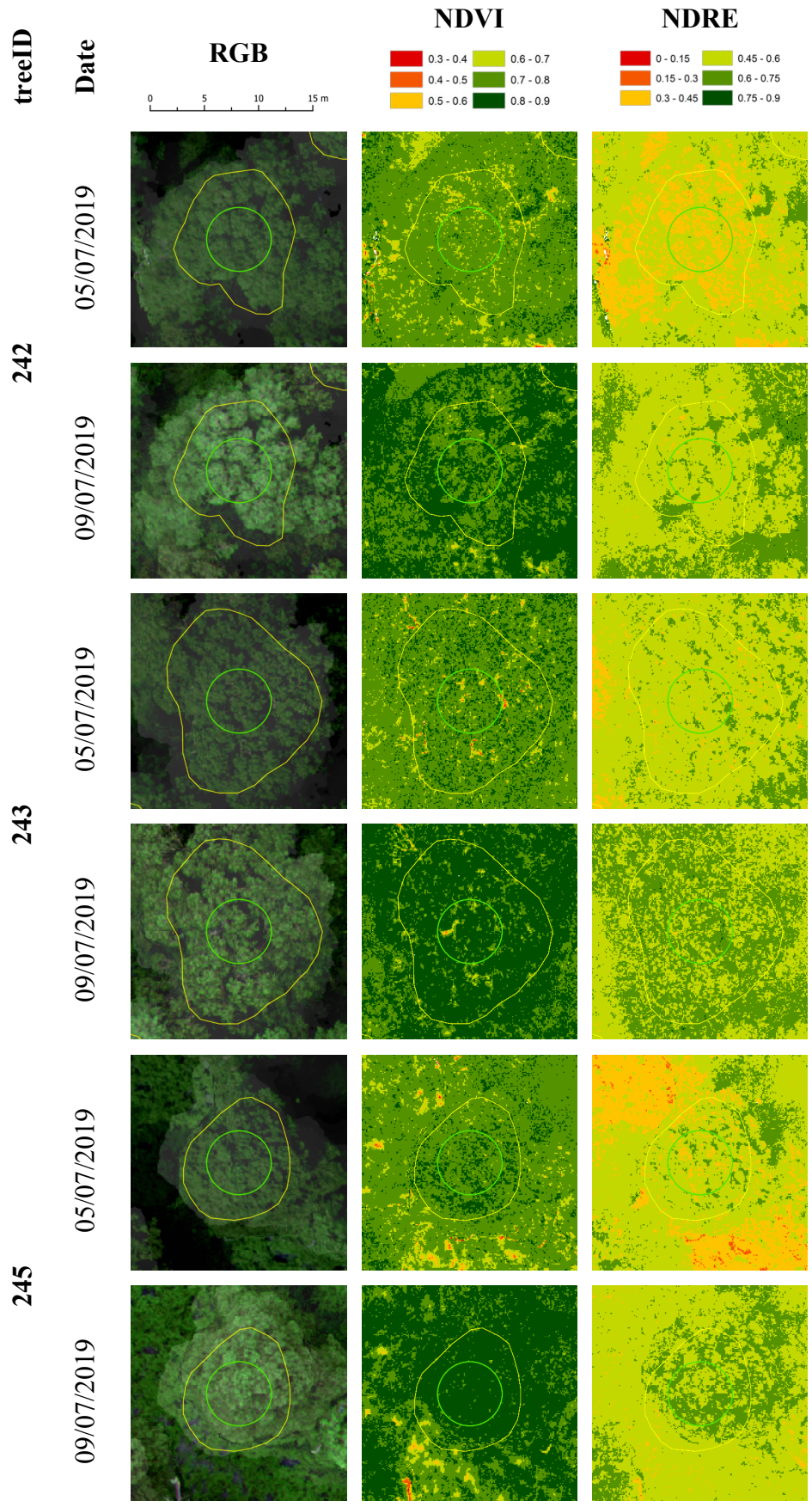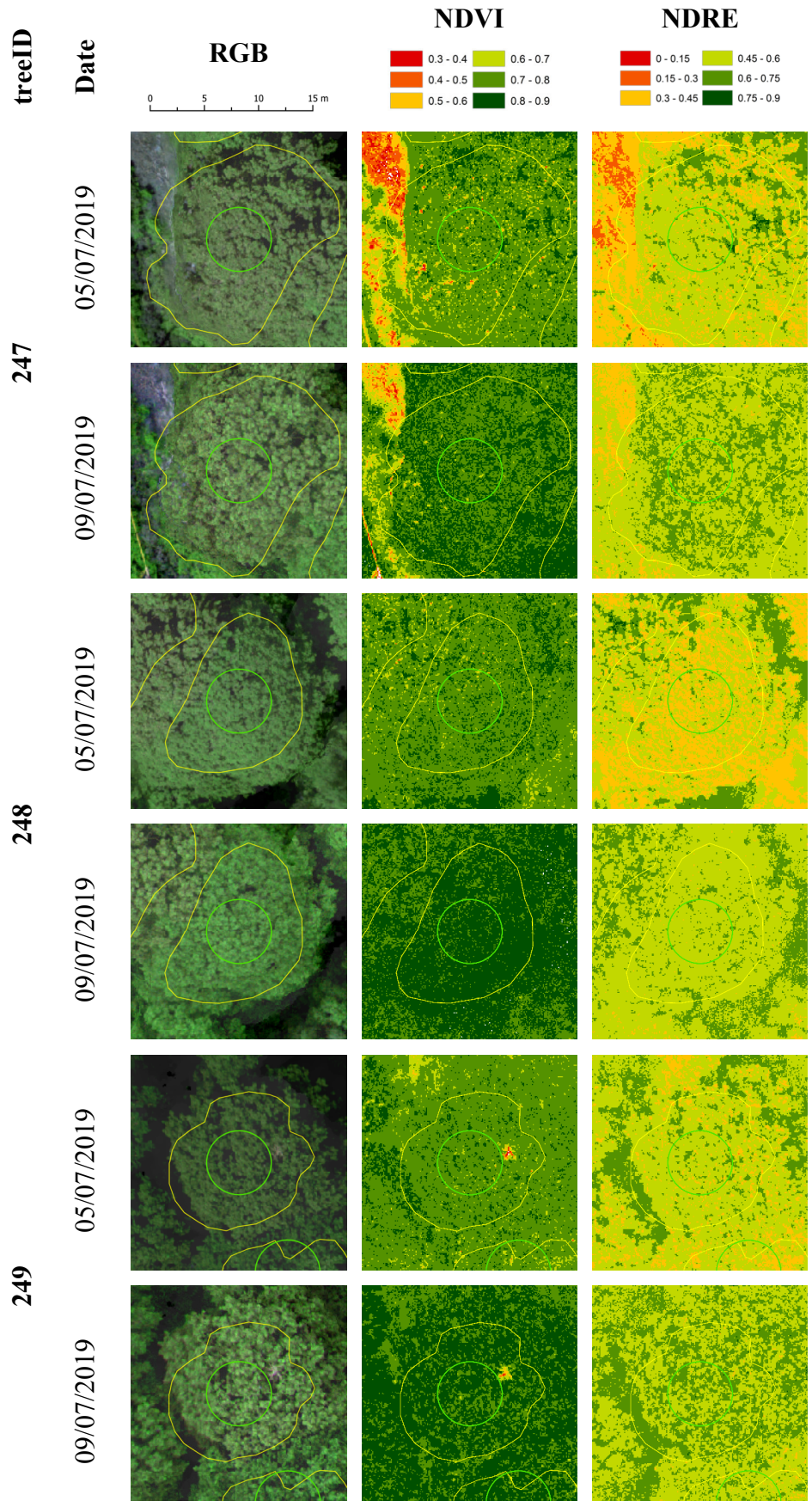
Appendix D Modelled decision thresholds for multispectral data

Appendix D depicts the decision threshold values for individual features determined in RF modelling for multispectral data at Speculation Cannop. Decision thresholds are obtained for every split in each decision tree and represent the modelled decision boundary between symptomatic and asymptomatic trees. Summary statistics are given for 100 iterations.

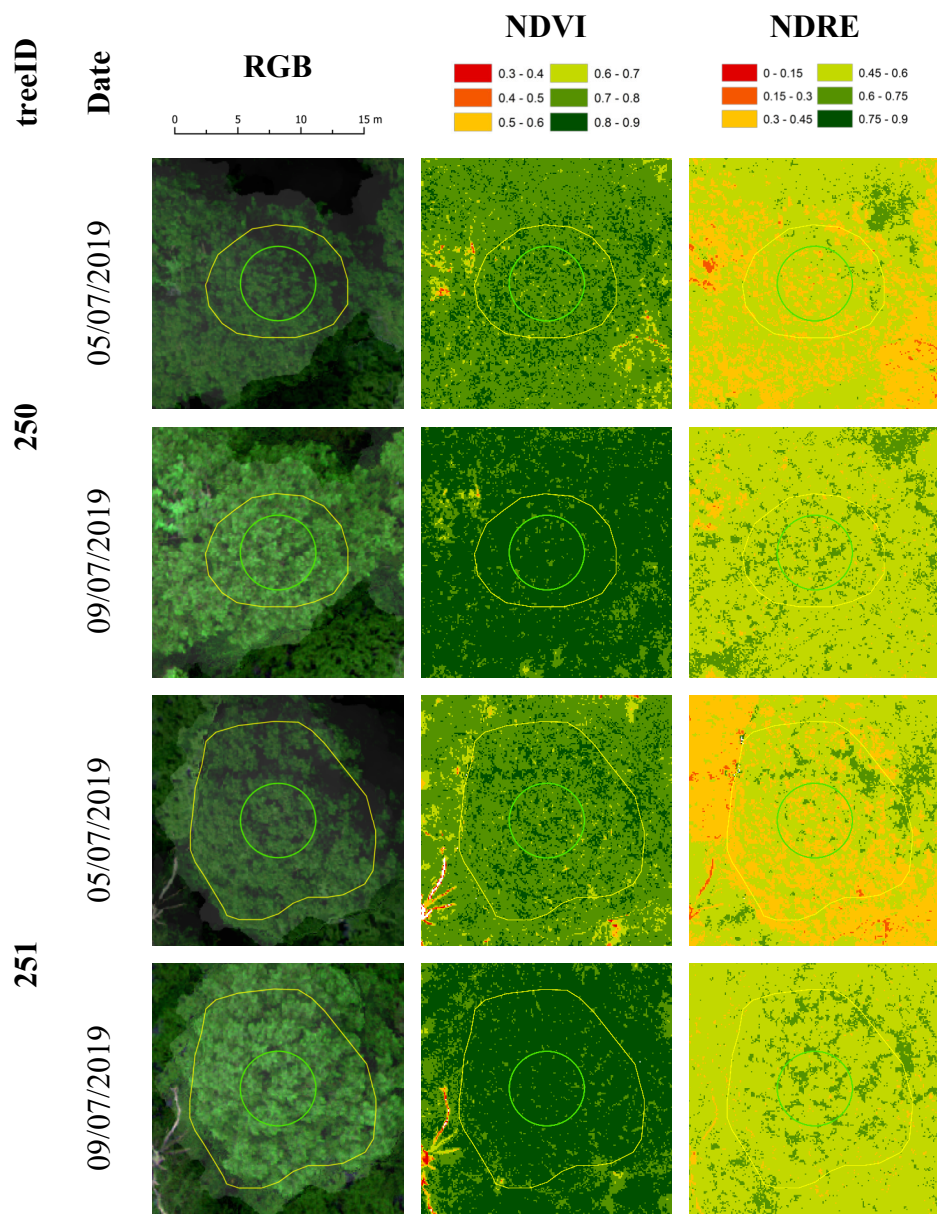| Feature	Mean	Std	Min	Max	Feature	Mean	Std	Min	Max
0507_RED_mean	0.129	0.004	0.125	0.129	0907_RED_mean	0.262	0.006	0.256	0.269
0507_GREEN_mean	0.183	0.014	0.165	0.183	0907_GREEN_mean	0.363	0.005	0.356	0.368
0507_BLUE_mean	0.125	0.000	0.125	0.125	0907_BLUE_mean	0.259	0.007	0.250	0.265
0507_REDEDGE_mean	0.198	0.018	0.185	0.198	0907_REDEDGE_mean	0.407	0.012	0.381	0.417
0507_NIR_mean	0.293	0.015	0.285	0.293	0907_NIR_mean	0.507	0.040	0.468	0.555
0507_NDVI_mean	0.832	0.010	0.825	0.832	0907_NDVI_mean	0.817	0.009	0.805	0.826
0507_NDRE_mean	0.436	0.004	0.435	0.436	0907_NDRE_mean	0.470	0.013	0.457	0.494
0507_CCCI_mean	0.125	0.000	0.125	0.125	0907_CCCI_mean	0.323	0.014	0.313	0.348
0507_CVI_mean	0.085	0.000	0.085	0.085	0907_CVI_mean	0.062	0.007	0.054	0.069
0507_ARI_mean	0.122	0.009	0.105	0.122	0907_ARI_mean	0.160	0.006	0.148	0.165
0507_RED_0.1	0.082	0.018	0.065	0.082	0907_RED_0.1	0.163	0.008	0.150	0.176
0507_GREEN_0.1	0.098	0.005	0.095	0.098	0907_GREEN_0.1	0.214	0.015	0.183	0.222
0507_BLUE_0.1	0.075	0.000	0.075	0.075	0907_BLUE_0.1	0.159	0.017	0.136	0.176
0507_REDEDGE_0.1	0.107	0.008	0.095	0.107	0907_REDEDGE_0.1	0.244	0.010	0.223	0.250
0507_NIR_0.1	0.181	0.007	0.175	0.181	0907_NIR_0.1	0.331	0.022	0.302	0.361
0507_NDVI_0.1	0.771	0.013	0.760	0.771	0907_NDVI_0.1	0.754	0.021	0.736	0.789
0507_NDRE_0.1	0.311	0.006	0.305	0.311	0907_NDRE_0.1	0.366	0.020	0.338	0.390
0507_CCCI_0.1	0.095	0.000	0.095	0.095	0907_CCCI_0.1	0.252	0.001	0.252	0.254
0507_CVI_0.1	0.042	0.005	0.035	0.042	0907_CVI_0.1	0.037	0.003	0.035	0.045
0507_ARI_0.1	0.070	0.005	0.065	0.070	0907_ARI_0.1	0.119	0.001	0.119	0.120
0507_RED_0.2	0.103	0.027	0.085	0.103	0907_RED_0.2	0.191	0.011	0.175	0.210
0507_GREEN_0.2	0.121	0.011	0.105	0.121	0907_GREEN_0.2	0.242	0.022	0.220	0.270
0507_BLUE_0.2	0.102	0.017	0.085	0.102	0907_BLUE_0.2	0.195	0.010	0.182	0.205
0507_REDEDGE_0.2	0.144	0.009	0.130	0.144	0907_REDEDGE_0.2	0.284	0.019	0.254	0.315
0507_NIR_0.2	0.232	0.004	0.230	0.232	0907_NIR_0.2	0.411	0.029	0.366	0.448
0507_NDVI_0.2	0.801	0.013	0.765	0.801	0907_NDVI_0.2	0.782	0.011	0.772	0.797
0507_NDRE_0.2	0.347	0.008	0.330	0.347	0907_NDRE_0.2	0.396	0.013	0.384	0.414
0507_CCCI_0.2	0.097	0.004	0.095	0.097	0907_CCCI_0.2	0.276	0.001	0.274	0.281
0507_CVI_0.2	0.053	0.004	0.045	0.053	0907_CVI_0.2	0.044	0.001	0.042	0.046
0507_ARI_0.2	0.080	0.005	0.075	0.080	0907_ARI_0.2	0.129	0.002	0.126	0.133
0507_RED_0.3	0.116	0.028	0.105	0.116	0907_RED_0.3	0.223	0.017	0.184	0.233
0507_GREEN_0.3	0.151	0.012	0.140	0.151	0907_GREEN_0.3	0.291	0.027	0.262	0.327
0507_BLUE_0.3	0.105	0.000	0.105	0.105	0907_BLUE_0.3	0.224	0.006	0.217	0.229
0507_REDEDGE_0.3	0.174	0.016	0.145	0.174	0907_REDEDGE_0.3	0.323	0.021	0.297	0.341
0507_NIR_0.3	0.256	0.008	0.245	0.256	0907_NIR_0.3	0.443	0.030	0.412	0.484
0507_NDVI_0.3	0.817	0.019	0.785	0.817	0907_NDVI_0.3	0.813	0.010	0.806	0.827
0507_NDRE_0.3	0.375	0.000	0.375	0.375	0907_NDRE_0.3	0.428	0.018	0.401	0.438
0507_CCCI_0.3	0.111	0.005	0.105	0.111	0907_CCCI_0.3	0.293	0.001	0.290	0.295
0507_CVI_0.3	0.059	0.005	0.055	0.059	0907_CVI_0.3	0.049	0.001	0.045	0.050
0507_ARI_0.3	0.086	0.004	0.085	0.086	0907_ARI_0.3	0.134	0.003	0.130	0.137
0507_RED_0.4	0.122	0.005	0.115	0.122	0907_RED_0.4	0.245	0.006	0.241	0.253
0507_GREEN_0.4	0.164	0.008	0.155	0.164	0907_GREEN_0.4	0.305	0.015	0.294	0.337
0507_BLUE_0.4	0.115	0.000	0.115	0.115	0907_BLUE_0.4	0.243	0.008	0.235	0.248
0507_REDEDGE_0.4	0.196	0.016	0.165	0.196	0907_REDEDGE_0.4	0.345	0.021	0.316	0.378
0507_NIR_0.4	0.277	0.011	0.255	0.277	0907_NIR_0.4	0.497	0.030	0.444	0.523
0507_NDVI_0.4	0.829	0.011	0.820	0.829	0907_NDVI_0.4	0.823	0.008	0.816	0.838
0507_NDRE_0.4	0.398	0.006	0.395	0.398	0907_NDRE_0.4	0.450	0.014	0.427	0.471
0507_CCCI_0.4	0.117	0.004	0.115	0.117	0907_CCCI_0.4	0.310	0.008	0.297	0.321
0507_CVI_0.4	0.065	0.000	0.065	0.065	0907_CVI_0.4	0.054	0.001	0.052	0.055
0507_ARI_0.4	0.095	0.005	0.085	0.095	0907_ARI_0.4	0.140	0.001	0.139	0.142

Feature	Mean	Std	Min	Max	Feature	Mean	Std	Min	Max
0507_RED_0.5	0.127	0.005	0.120	0.135	0907_RED_0.5	0.266	0.005	0.260	0.271
0507_GREEN_0.5	0.190	0.011	0.165	0.205	0907_GREEN_0.5	0.359	0.014	0.334	0.370
0507_BLUE_0.5	0.125	0.000	0.125	0.125	0907_BLUE_0.5	0.253	0.001	0.252	0.254
0507_REDEDGE_0.5	0.225	0.016	0.185	0.240	0907_REDEDGE_0.5	0.372	0.010	0.350	0.378
0507_NIR_0.5	0.300	0.021	0.265	0.335	0907_NIR_0.5	0.520	0.029	0.475	0.559
0507_NDVI_0.5	0.842	0.007	0.835	0.855	0907_NDVI_0.5	0.831	0.009	0.818	0.847
0507_NDRE_0.5	0.425	0.000	0.425	0.425	0907_NDRE_0.5	0.476	0.009	0.455	0.482
0507_CCCI_0.5	0.120	0.005	0.115	0.125	0907_CCCI_0.5	0.330	0.006	0.325	0.339
0507_CVI_0.5	0.074	0.003	0.065	0.075	0907_CVI_0.5	0.060	0.004	0.054	0.067
0507_ARI_0.5	0.106	0.006	0.095	0.115	0907_ARI_0.5	0.147	0.001	0.146	0.149
0507_RED_0.6	0.142	0.004	0.135	0.145	0907_RED_0.6	0.276	0.012	0.247	0.289
0507_GREEN_0.6	0.206	0.011	0.190	0.225	0907_GREEN_0.6	0.395	0.003	0.390	0.397
0507_BLUE_0.6	0.133	0.004	0.125	0.135	0907_BLUE_0.6	0.276	0.004	0.273	0.281
0507_REDEDGE_0.6	0.237	0.022	0.195	0.265	0907_REDEDGE_0.6	0.432	0.015	0.409	0.444
0507_NIR_0.6	0.325	0.019	0.285	0.355	0907_NIR_0.6	0.569	0.015	0.548	0.593
0507_NDVI_0.6	0.854	0.010	0.845	0.865	0907_NDVI_0.6	0.840	0.008	0.826	0.855
0507_NDRE_0.6	0.458	0.015	0.440	0.480	0907_NDRE_0.6	0.493	0.012	0.474	0.506
0507_CCCI_0.6	0.128	0.005	0.125	0.135	0907_CCCI_0.6	0.339	0.011	0.320	0.343
0507_CVI_0.6	0.085	0.000	0.085	0.085	0907_CVI_0.6	0.066	0.007	0.056	0.075
0507_ARI_0.6	0.126	0.010	0.115	0.135	0907_ARI_0.6	0.154	0.001	0.152	0.156
0507_RED_0.7	0.150	0.010	0.145	0.165	0907_RED_0.7	0.286	0.011	0.279	0.294
0507_GREEN_0.7	0.222	0.017	0.195	0.245	0907_GREEN_0.7	0.427	0.003	0.423	0.432
0507_BLUE_0.7	0.143	0.004	0.135	0.145	0907_BLUE_0.7	0.287	0.014	0.256	0.297
0507_REDEDGE_0.7	0.249	0.023	0.215	0.265	0907_REDEDGE_0.7	0.472	0.005	0.464	0.478
0507_NIR_0.7	0.340	0.017	0.305	0.365	0907_NIR_0.7	0.581	0.011	0.548	0.585
0507_NDVI_0.7	0.860	0.009	0.845	0.875	0907_NDVI_0.7	0.851	0.009	0.839	0.864
0507_NDRE_0.7	0.485	0.000	0.485	0.485	0907_NDRE_0.7	0.524	0.012	0.497	0.532
0507_CCCI_0.7	0.137	0.004	0.135	0.145	0907_CCCI_0.7	0.358	0.010	0.347	0.371
0507_CVI_0.7	0.095	0.000	0.095	0.095	0907_CVI_0.7	0.068	0.009	0.062	0.084
0507_ARI_0.7	0.134	0.009	0.125	0.145	0907_ARI_0.7	0.165	0.004	0.160	0.168
0507_RED_0.8	0.164	0.007	0.155	0.170	0907_RED_0.8	0.318	0.006	0.313	0.325
0507_GREEN_0.8	0.240	0.011	0.215	0.255	0907_GREEN_0.8	0.462	0.014	0.428	0.470
0507_BLUE_0.8	0.158	0.007	0.145	0.165	0907_BLUE_0.8	0.305	0.021	0.270	0.328
0507_REDEDGE_0.8	0.292	0.013	0.260	0.305	0907_REDEDGE_0.8	0.511	0.009	0.505	0.529
0507_NIR_0.8	0.356	0.032	0.310	0.395	0907_NIR_0.8	0.632	0.000	0.632	0.632
0507_NDVI_0.8	0.873	0.007	0.865	0.885	0907_NDVI_0.8	0.859	0.008	0.851	0.874
0507_NDRE_0.8	0.527	0.009	0.515	0.535	0907_NDRE_0.8	0.555	0.003	0.553	0.557
0507_CCCI_0.8	0.151	0.005	0.145	0.155	0907_CCCI_0.8	0.373	0.009	0.369	0.391
0507_CVI_0.8	0.105	0.000	0.105	0.105	0907_CVI_0.8	0.084	0.010	0.070	0.096
0507_ARI_0.8	0.159	0.015	0.145	0.185	0907_ARI_0.8	0.179	0.006	0.172	0.189
0507_RED_0.9	0.184	0.004	0.180	0.195	0907_RED_0.9	0.348	0.026	0.303	0.378
0507_GREEN_0.9	0.265	0.019	0.225	0.285	0907_GREEN_0.9	0.519	0.015	0.494	0.535
0507_BLUE_0.9	0.173	0.009	0.155	0.185	0907_BLUE_0.9	0.355	0.009	0.345	0.366
0507_REDEDGE_0.9	0.290	0.023	0.260	0.325	0907_REDEDGE_0.9	0.559	0.007	0.551	0.566
0507_NIR_0.9	0.393	0.014	0.380	0.430	0907_NIR_0.9	0.689	0.005	0.671	0.691
0507_NDVI_0.9	0.879	0.005	0.875	0.885	0907_NDVI_0.9	0.873	0.004	0.870	0.879
0507_NDRE_0.9	0.585	0.000	0.585	0.585	0907_NDRE_0.9	0.590	0.005	0.585	0.595
0507_CCCI_0.9	0.165	0.000	0.165	0.165	0907_CCCI_0.9	0.412	0.004	0.409	0.417
0507_CVI_0.9	0.130	0.005	0.125	0.135	0907_CVI_0.9	0.113	0.009	0.086	0.117
0507_ARI_0.9	0.195	0.013	0.165	0.205	0907_ARI_0.9	0.197	0.017	0.180	0.225

Appendix E provides equations for adopted texture metrics. In CHAPTER 5 a set of eight Haralick features (Haralick *et al.*, 1973) are calculated from a grey level co-variance matrix (GLCM). Here $g(i,j)$ refers to the frequency of elements in the GLCM with the index i,j. Further, μ and σ are defined as follows:

$$\mu = (weighted\ pixel\ average) = \sum_{i,j} i \cdot g(i,j) = \sum_{i,j} j \cdot g(i,j),$$

$$\sigma = (weighted\ pixel\ variance) = \sum_{i,j} (i-\mu)^2 \cdot g(i,j) = \sum_{i,j} (j-\mu)^2 \cdot g(i,j)$$

Eight Haralick texture metrics were calculated in Orfeo ToolBox, using the default GLCM offset of one pixel. Equations are stated according to the documentation provided in the Orfeo Cookbook (https://www.orfeo-toolbox.org/CookBook):

$$Energy = \sum_{i,j} g(i,j)^2$$

$$Entropy = -\sum_{i,j} g(i,j) \log_2 g(i,j)$$

$$Correlation = \sum_{i,j} \frac{(i-\mu)(j-\mu)g(i,j)}{\sigma^2}$$

$$InverseDifferenceMoment = \sum_{i,j} \frac{1}{1+(i-j)^2} g(i,j)$$

$$Inertia = \sum_{i,j} (i-j)^2 g(i,j)$$

$$ClusterShade = \sum_{i,j} \big((i-\mu)+(j-\mu)\big)^3 g(i,j)$$

$$ClusterProminence = \sum_{i,j} \big((i-\mu)+(j-\mu)\big)^4 g(i,j)$$

$$Haralick'sCorrelation = \frac{\sum_{i,j}(i,j)g(i,j)-\mu_t^2}{\sigma_t^2}$$

where μ_t and σ_t are the mean and standard deviation of the row sums

Appendix F - Feature importance scores, Monks Wood

Appendix F lists the determined mean feature importances of all features within individual models used in the assessment of AOD at Monks Wood. Importances are sorted by importance in descending order. Results are presented for RF trees = 100, CV = 3-fold and permutation iterations = 10.

Feature	mean	Feature	mean	Feature	mean	Feature	mean
Jul17_ws3_ClusterProminance_std	0.011	Oct17_ws3_Correlation_std	0.036	May18_ws3_ClusterProminance_std	0.099	Jul18_ARI_std	0.112
Jul17_ws3_Entropy_std	0.010	Oct17_ws3_HarlickCorrelation_mean	0.032	May18_NIR_std	0.041	Jul18_NDVI_std	0.058
Jul17_ARI_std	0.006	Oct17_ws3_ClusterProminance_mean	0.013	May18_RE_std	0.034	Jul18_NIR_std	0.032
Jul17_NDRE_mean	0.004	Oct17_G_mean	0.005	May18_bright_std	0.019	Jul18_RE_mean	0.031
Jul17_CCCI_mean	0.002	Oct17_ws3_IDM_mean	0.003	May18_ARI_std	0.018	Jul18_R_std	0.022
Jul17_G_std	0.001	Oct17_ARI_mean	0.002	May18_G_std	0.016	Jul18_ws3_Correlation_std	0.020
Jul17_R_mean	0.001	Oct17_R_mean	0.001	May18_CCCI_std	0.013	Jul18_ws3_Energy_std	0.018
Jul17_RE_std	0.001	Oct17_ws3_Entropy_mean	0.001	May18_ws3_ClusterProminance_mean	0.007	Jul18_ws3_Entropy_std	0.014
Jul17_NIR_mean	0.001	Oct17_NDVI_std	0.001	May18_NDRE_std	0.005	Jul18_ws3_HarlickCorrelation_std	0.012
Jul17_ARI_mean	0.001	Oct17_ARI_std	0.000	May18_ws3_HarlickCorrelation_std	0.001	Jul18_B_std	0.010
Jul17_B_mean	0.001	Oct17_B_std	0.000	May18_ws3_ClusterShade_std	0.001	Jul18_ws3_ClusterShade_mean	0.010
Jul17_bright_mean	0.000	Oct17_B_mean	0.000	May18_ws3_Correlation_std	0.000	Jul18_B_mean	0.010
Jul17_ws3_ClusterShade_std	0.000	Oct17_ws3_ClusterProminance_std	0.000	May18_B_mean	0.000	Jul18_RE_std	0.008
Jul17_RE_mean	0.000	Oct17_ws3_Energy_mean	-0.001	May18_ws3_IDM_mean	0.000	Jul18_bright_std	0.007
Jul17_B_std	0.000	Oct17_NIR_mean	-0.001	May18_NDVI_mean	-0.001	Jul18_R_mean	0.006
Jul17_CVI_std	0.000	Oct17_ws3_Inertia_mean	-0.001	May18_ws3_ClusterShade_mean	0.000	Jul18_bright_mean	0.002
Jul17_ws3_Correlation_std	0.000	Oct17_NDRE_mean	-0.001	May18_ws3_Entropy_mean	0.000	Jul18_G_mean	0.002
Jul17_ws3_Energy_mean	0.000	Oct17_RE_mean	-0.001	May18_CVI_mean	0.000	Jul18_ws3_ClusterShade_std	0.002
Jul17_ws3_ClusterShade_mean	0.000	Oct17_bright_mean	-0.001	May18_NDRE_mean	0.000	Jul18_G_std	0.002
Jul17_ws3_IDM_mean	-0.001	Oct17_CVI_std	-0.001	May18_ws3_Inertia_mean	0.000	Jul18_ARI_mean	0.001
Jul17_ws3_Inertia_mean	-0.001	Oct17_ws3_ClusterShade_mean	-0.002	May18_ws3_Energy_mean	0.000	Jul18_ws3_Inertia_mean	0.001
Jul17_ws3_Entropy_mean	-0.001	Oct17_bright_std	-0.003	May18_R_mean	0.000	Jul18_ws3_Correlation_mean	0.001
Jul17_CVI_mean	-0.001	Oct17_ws3_ClusterShade_std	-0.003	May18_ws3_Correlation_mean	0.000	Jul18_ws3_HarlickCorrelation_mean	0.001
Jul17_ws3_ClusterProminance_mean	-0.001	Oct17_CCCI_mean	-0.003	May18_ARI_mean	0.000	Jul18_NDVI_mean	0.001
Jul17_CCCI_std	-0.001	Oct17_NDRE_std	-0.003	May18_CCCI_mean	0.000	Jul18_ws3_ClusterProminance_mean	0.001
Jul17_NDVI_mean	-0.001	Oct17_ws3_IDM_std	-0.004	May18_ws3_IDM_std	-0.001	Jul18_ws3_Entropy_mean	0.000
Jul17_NDRE_std	-0.001	Oct17_G_std	-0.006	May18_ws3_Energy_std	-0.001	Jul18_ws3_Energy_mean	0.000
Jul17_NDVI_std	-0.001	Oct17_CVI_mean	-0.007	May18_NDVI_std	-0.001	Jul18_NIR_mean	0.000
Jul17_G_mean	-0.001	Oct17_RE_std	-0.009	May18_ws3_Inertia_std	-0.001	Jul18_ws3_IDM_mean	0.000
Jul17_bright_std	-0.003	Oct17_R_std	-0.009	May18_ws3_Entropy_std	-0.002	Jul18_CCCI_mean	0.000
Jul17_R_std	-0.007	Oct17_CCCI_std	-0.010	May18_ws3_HarlickCorrelation_mean	-0.002	Jul18_CVI_mean	0.000
Jul17_ws3_HarlickCorrelation_mean	-0.008	Oct17_ws3_Inertia_std	-0.011	May18_G_mean	-0.002	Jul18_NDRE_std	-0.001
Jul17_ws3_Correlation_mean	-0.008	Oct17_NDVI_mean	-0.012	May18_B_std	-0.005	Jul18_CCCI_std	-0.001
Jul17_ws3_IDM_std	-0.011	Oct17_ws3_Entropy_std	-0.015	May18_R_std	-0.005	Jul18_NDRE_mean	-0.001
Jul17_ws3_Energy_std	-0.012	Oct17_ws3_Correlation_mean	-0.023	May18_RE_mean	-0.012	Jul18_CVI_std	-0.002
Jul17_ws3_Inertia_std	-0.028	Oct17_ws3_Energy_std	-0.029	May18_NIR_mean	-0.012	Jul18_ws3_ClusterProminance_std	-0.003
Jul17_ws3_HarlickCorrelation_std	-0.029	Oct17_NIR_std	-0.104	May18_bright_mean	-0.014	Jul18_ws3_IDM_std	-0.008
Jul17_NIR_std	-0.047	Oct17_ws3_HarlickCorrelation_std	-0.117	May18_CVI_std	-0.068	Jul18_ws3_Inertia_std	-0.009